Damage Detection in Civil Structures Using High-Frequency Seismograms

Thesis by

Vanessa Heckman

In Partial Fulfillment of the Requirements

for the Degree of

Doctor of Philosophy

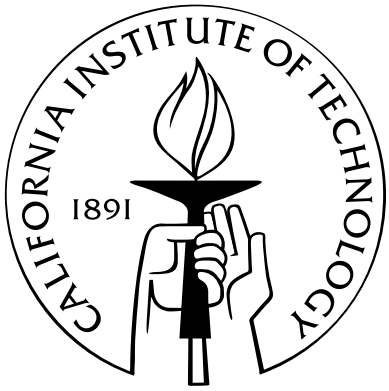

California Institute of Technology

Pasadena, California

2014

(Defended September 27, 2013)

To my parents and brother.

Acknowledgements

I would like to thank my adviser, Tom Heaton, for sharing his enthusiasm and wisdom with me throughout the years. I will always happily remember discussing research results with him in his office, and I am very appreciative of his willingness to meet with me to discuss research for hours at a time and for keeping his door always open.

To Monica Kohler for, in many ways, serving as a second adviser to me. She's been a great role model throughout the years, and I've learned a lot from her professionally, especially as an experimentalist and a technical writer.

To Rob Clayton for welcoming me to his group meetings and serving as a geophysics mentor to me in my earlier years of graduate school when I went to my first conference, undoubtedly the largest conference I will ever attend (the AGU). Thanks also for his patience.

To Jim Beck, for discussions related to math and history of science. Also for his guidance in research topics in damage detection and in daring to teach mathematics to engineers.

To Victor Tsai for his feedback during my thesis talk.

To Masumi Yamada, for welcoming me to Uji Campus, Kyoto University for my EAPSI project and making my summer research experience a special one. I will always look up to Masumi as an amazing researcher and speaker.

To John Hall, my adviser during college, for taking the time to cultivate my passion for civil engineering.

To Ken Pickar, for welcoming our group of CE students into his entrepreneurship class and taking the time to meet with us to provide an honest, well-informed opinion on our project.

To Swami Krishnan, for his involvement in public outreach programs with me.

To Joann Stock for welcoming me on the seismic field trips, especially to the Salton Sea (where I got to create my first 'earthquake' from a borehole explosion).

To Luke Wang and Bill Iwan for their mentorship.

To Kaushik Bhattacharya for meeting with me during college to discuss Timoshenko.

To Brad Aagaard for developing his amazing code PyLith and for helping to get it up and running on the GPS and CE computing clusters. I am confident that his endeavors in creating this program will reward many researchers to come.

To Case Bradford for taking the time to work with me on the Millikan library project when I was still an undergraduate.

To Carolina Oseguera and Chris Silva, who kept Thomas running and yet still found the time to be supportive of the students.

To Raul for fixing the equipment for class and for telling me stories about the old CE department as he was doing so.

Also a special thanks to all of the friends I made through my involvement with the EERI student leadership council. Nima, Erica, David, Tim, Maria, Karthik, Evgueni, Jeff, Manny, Jasmine, Charlie, Michael, Andreas, we did it! To the UC Memphis faculty for letting us borrow their shake table. To the staff at EERI and President-Elect Tom Tobin, it was a pleasure working with you. To Ashraf at CSI for daring to dream big and inspiring others to do so. To the friends I made through my involvement in APSS and EAPSI, especially Christiana, Emily, Austin, and Ben.

A special thanks to my friends in the CE and GPS departments, who have been my coffee buddies throughout the years: Matt, Dan, Anna, Ahmed, In Ho, Trevor, Ramses, Stephen, Michael, Song, Hemanth, Mohsen, Navneet, Surendra, Nathalie, Grant, Arnar, Swetha, Dan, Dani, June. To the Painter group and Tirrell lab members: Ari, Amir, Jasper, Jeffs. J.D., Rob, Dvin. To my art class friends Christine and Patrick. Tiffany, Tim, Iram, Juhwan, Alice, Lydia, and Sangita. To Cedric and Ming, who encouraged me to reattend Caltech for graduate school. To my high school friends Omid, Zach, Logan, and Natasha.

Finally, thank you to my family for their love and support: my parents, Nate, Brett and the kitties.

Abstract

The dynamic properties of a structure are a function of its physical properties, and changes in the physical properties of the structure, including the introduction of structural damage, can cause changes in its dynamic behavior. Structural health monitoring (SHM) and damage detection methods provide a means to assess the structural integrity and safety of a civil structure using measurements of its dynamic properties. In particular, these techniques enable a quick damage assessment following a seismic event. In this thesis, the application of high-frequency seismograms to damage detection in civil structures is investigated.

Two novel methods for SHM are developed and validated using small-scale experimental testing, existing structures *in situ*, and numerical testing. The first method is developed for pre-Northridge steel-moment-resisting frame buildings that are susceptible to weld fracture at beam-column connections. The method is based on using the response of a structure to a nondestructive force (i.e., a hammer blow) to approximate the response of the structure to a damage event (i.e., weld fracture). The method is applied to a small-scale experimental frame, where the impulse response functions of the frame are generated during an impact hammer test. The method is also applied to a numerical model of a steel frame, in which weld fracture is modeled as the tensile opening of a Mode I crack. Impulse response functions are experimentally obtained for a steel moment-resisting frame building *in situ*. Results indicate that while acceleration and velocity records generated by a damage event are best approximated by the acceleration and velocity records generated by a colocated hammer blow, the method may not be robust to noise. The method seems to be better suited for damage localization, where information such as arrival times and peak accelerations can also provide indication of the damage location. This is of significance for sparsely-instrumented

civil structures.

The second SHM method is designed to extract features from high-frequency acceleration records that may indicate the presence of damage. As short-duration high-frequency signals (i.e., pulses) can be indicative of damage, this method relies on the identification and classification of pulses in the acceleration records. It is recommended that, in practice, the method be combined with a vibration-based method that can be used to estimate the loss of stiffness. Briefly, pulses observed in the acceleration time series when the structure is known to be in an undamaged state are compared with pulses observed when the structure is in a potentially damaged state. By comparing the pulse signatures from these two situations, changes in the high-frequency dynamic behavior of the structure can be identified, and damage signals can be extracted and subjected to further analysis. The method is successfully applied to a small-scale experimental shear beam that is dynamically excited at its base using a shake table and damaged by loosening a screw to create a moving part. Although the damage is aperiodic and nonlinear in nature, the damage signals are accurately identified, and the location of damage is determined using the amplitudes and arrival times of the damage signal. The method is also successfully applied to detect the occurrence of damage in a test bed data set provided by the Los Alamos National Laboratory, in which nonlinear damage is introduced into a small-scale steel frame by installing a bumper mechanism that inhibits the amount of motion between two floors. The method is successfully applied and is robust despite a low sampling rate, though false negatives (undetected damage signals) begin to occur at high levels of damage when the frequency of damage events increases. The method is also applied to acceleration data recorded on a damaged cable-stayed bridge in China, provided by the Center of Structural Monitoring and Control at the Harbin Institute of Technology. Acceleration records recorded after the date of damage show a clear increase in high-frequency short-duration pulses compared to those previously recorded. One undamage pulse and two damage pulses are identified from the data. The occurrence of the detected damage pulses is consistent with a progression of damage and matches the known chronology of damage.

Contents

List of Figures

List of Tables

Chapter 1

Introduction

> The Earth is a lovely and more or less placid place. Things change, but slowly. We can lead a full life and never personally encounter a natural disaster more violent than a storm. And so we become complacent, relaxed, unconcerned. But in the history of Nature, the record is clear. Worlds have been devastated. On the landscapes of other planets where the records of the past have been preserved, there is abundant evidence of major catastrophes. It is all a matter of time scale. An event that would be unthinkable in a hundred years may be inevitable in a hundred million. Even on the Earth, even in our own century, bizarre natural events have occurred.
>
> - Carl Sagan
>
> Cosmos, Series 1 Episode 4 (Heaven and Hell) (Sagan et al., 1980)

Natural catastrophes typically operate on timescales that are much longer than the lifetime of a person. The same concepts that apply to impact events[1], to which Carl Sagan was referring, apply to earthquakes. Small earthquakes happen on a daily basis, while large earthquakes are relatively rare. The number of earthquakes of a given magnitude occurring in any given region and time period follows the Gutenberg-Richter power law (Gutenberg and Richter, 1965); in a seismically active region, in the time it takes for 100 earthquakes of magnitude 5 to occur, about 10 magnitude 6 earthquakes and a single magnitude 7 earth-

[1] An Earth impact event is a collision of an astronomical object, such as a meteor or a comet, with the Earth. The Torino Impact Hazard Scale is used to assess asteroid and comet impact hazard (Binzel, 2000).

quake will have occurred. Without having personally experienced a large earthquake or having any family or friends who have experienced a large earthquake, we can develop a false sense of security, underestimating the seismic risk of a region. However, natural history knows that there are slumbering giants underground that stir from time to time.

We are at a unique point in history where we have developed a good understanding of earthquakes as well as technologies that can be used to increase seismic preparedness and resilience. We thus have an obligation to both prepare for earthquakes in seismically active regions, and to continue to better our understanding through the analysis of the many moderate-sized earthquakes and few large earthquakes that occur worldwide. From a seismological perspective, this knowledge leads to better models of the seismic risk of a region as well as earthquake early warning systems. From a civil engineering perspective, this knowledge leads to the design of safer structures and better seismic assessment and retrofitting of existing structures. This thesis, in partial fulfillment of the requirements for a Ph.D. in Civil Engineering at Caltech, contributes to the body of knowledge related to seismic resilience by presenting a damage-detection method to help assess the safety of a structure after an earthquake.

Seismic Hazard: Earthquakes

The most seismically active region on Earth is the circum-Pacific seismic belt, also known as the "Ring of Fire." This region forms an arc that traces plate boundaries in the Pacific Ocean across the borders of four continents, Australia, Asia, North America, and South America. Faults located at plate boundaries are capable of producing massive earthquakes, some of which are followed by devastating tsunamis. Nearly all of the largest earthquakes since 1900 (of M 8.5 and above) have occurred within the circum-Pacific seismic belt, and a number of these happened recently: the M 9.1 2004 Sumatra-Andaman earthquake, the M 9.0 2011 Tohoku earthquake, the M 8.8 2010 Chile earthquake, the M 8.6 2005 Nias earthquake, and the M 8.5 2007 Sumatra earthquake (Park et al., 2005; USGS, 2012). As the return periods of these earthquakes are long, few written records exist, and clues existing in nature, such as formation and dating of sedimentation layers, must be used to determine

Figure 1.1: **1906 San Francisco Earthquake and Fire.** The M 7.9 1906 San Francisco earthquake was followed by four nights of destructive fires that destroyed much of the city and left over half of its residents homeless. **a**, The fire at Third and Mission, **b**, Close-up of building on fire. Images courtesy of the George W. Housner collection.

when previous events of a similar size occurred at a given fault.

There is paleoseismic evidence that great plate-boundary earthquakes occur periodically off the northwestern coast of the contiguous United States. This seismically active region, called the Cascadia subduction zone, is created by the subduction of the Pacific oceanic crust below the North American tectonic plate. Based on its shared characteristics with other subduction zones, Heaton and Hartzell (1987) recognized the potential for the Cascadia subduction zone to produce a great earthquake (of magnitude 8 or larger) or a giant earthquake (of magnitude 9 or larger) that would result in strong shaking and large local tsunamis. From field analysis, Atwater and Hemphill-Haley (1997) verified that about once every five hundred years, the Cascadia fault produces a great earthquake that is followed by a devastating tsunami. The last such earthquake happened about 300 years ago in 1700. Goldfinger et al. (2012) found that these 500-year earthquakes are due to full-margin rupture, and estimates the magnitude to be 9 or larger. The same study estimates the probability of a giant earthquake in the next 50 years at 7-11% and the probability of a magnitude 8 or larger earthquake caused by rupture of the southern portion of the fault zone at 18% or 32-43%, depending on the model used.

A continental transform fault, the San Andreas fault extends for nearly a thousand miles from its southernmost point located south of Los Angeles close to the Salton Sea, tracing northward along the coast through San Francisco, to its northernmost point, the Mendocino Triple Junction off the coast of Cape Mendocino in northern California. Unlike the Cascadia fault, both moderate and large earthquakes on the San Andreas fault and its sister faults pose a seismic threat due to their close proximity to cities in California. A number of notable earthquakes have occurred on the San Andreas fault in the 20th and 21st century, the largest of which is the infamous 1906 San Francisco earthquake. With an estimated moment-magnitude of 7.9 according to Thatcher et al. (1997) and an estimated surface wave magnitude of 7.75 according to Wald et al. (1993), the earthquake was followed by four nights of destructive fires, documented in Figure 1.1, that destroyed much of the city and left over half of its residents homeless. According to the 2008 UCERF (Uniform California Earthquake Rupture Forecast) Version 2 report, the probability of a magnitude 6.7 or larger

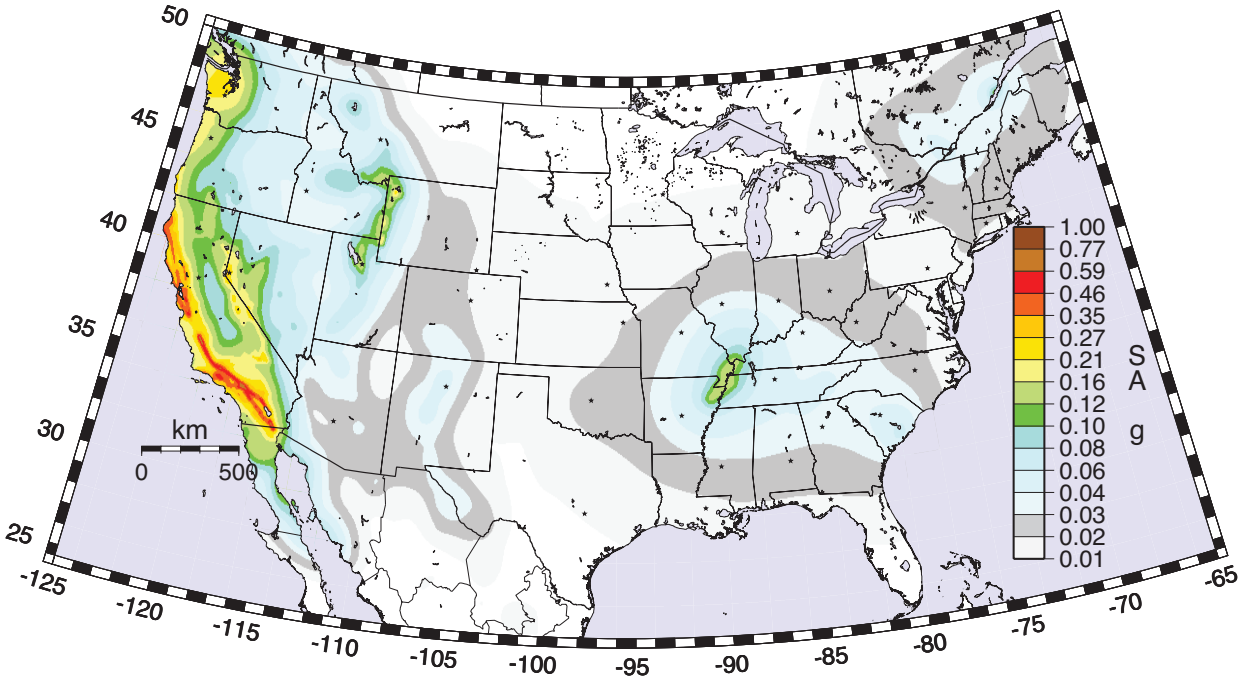

Figure 1.2: **2008 U.S. Geological Survey National Seismic Hazard Map: 1.0-Second Spectral Acceleration with 10% Probability of Occurrence in 50 Year PE, BC rock.** Hazard maps, as well as other important factors such as site soil characteristics and occupancy, are incorporated into seismic provisions in building code. Figure courtesy of the U.S. Geological Survey.

earthquake occurring in California in the next 30 years is greater than 99%, with an average repeat time of 5 years (Field et al., 2009). The estimated probability of a magnitude 7.0 earthquake is 94%, with an average repeat time of 11 years. The probability of a magnitude 7.5 earthquake is 46% with a repeat time of 48 years. It is only a matter of time until one of these earthquakes occurs near a city. Fortunately, California is a seismically-proactive state, thanks in part to programs like ShakeOut that serve to increase public awareness, professional organizations like EERI, SEAOSC, and ASCE that bring together civil engineers, and well-known Californian universities that advance the field of earthquake engineering.

Seismic Risk: Civil Structures

The U.S. Geological Survey (USGS) routinely publishes United States National Seismic Hazard Maps that estimate earthquake ground motions for various probability levels, an example of which is shown in Figure 1.2 (Petersen et al., 2008). Hazard maps, as well as

other important factors such as site soil characteristics and occupancy, are incorporated into seismic provisions in building code (BSSC, 2003; ICC, 2000). Earthquake mitigation is as much a social and economic issue as it is an engineering issue. According to Jennings (2013) in his book review of 'Earthquakes and Engineers: An International History written by Robert K. Reitherman' and published in 2012, "the development of earthquake engineering was not a smooth, continuous process, nor was it one always advanced by damaging earthquakes, but rather, it was influenced by more complex interactions with society;" for example, it wasn't until after the M 6.4 1933 Long Beach earthquake that significant changes were made to California's building code. Unreinforced masonry buildings performed very poorly in the 1933 Long Beach Earthquake, some examples of which are shown in Figure 1.3 (Reitherman, 2012). Even today, adoption of a model seismic building code is uneven across and within states, including areas with high levels of seismic hazard. In addition to the adoption of a model code, the code must also be enforced. This is generally the responsibility of local government building officials. Undoubtedly, public policies that mitigate seismic risk must include steps to educate and raise public awareness in addition to developing effective land-use regulations and building codes.

The largest seismic risk in the United States today stems from older structures that were designed in accordance to the building code at the time of construction and have not been retrofitted to correct for seismic vulnerabilities that were discovered post-construction. In extreme cases, proactive measures are taken against unsafe building types or practices. One such example is unreinforced masonry structures, whose construction was prohibited by building codes in California in 1933. A 1986 URM Law was passed requiring local governments in Seismic Zone 4 to inventory URM buildings, establish loss reduction programs, and report their progress and recommended that local governments establish seismic retrofit standards, adopt mandatory strengthening programs, and enact measures to reduce the number of occupants in URM buildings (SSC, 2004). As of 2004, 25,900 URM buildings with an average size of 10,000 square feet have been inventoried in Zone 4 regions in California, and 55% of those inventoried have been retrofitted. To put this figure into context, there were about 12 million buildings in California in 2004.

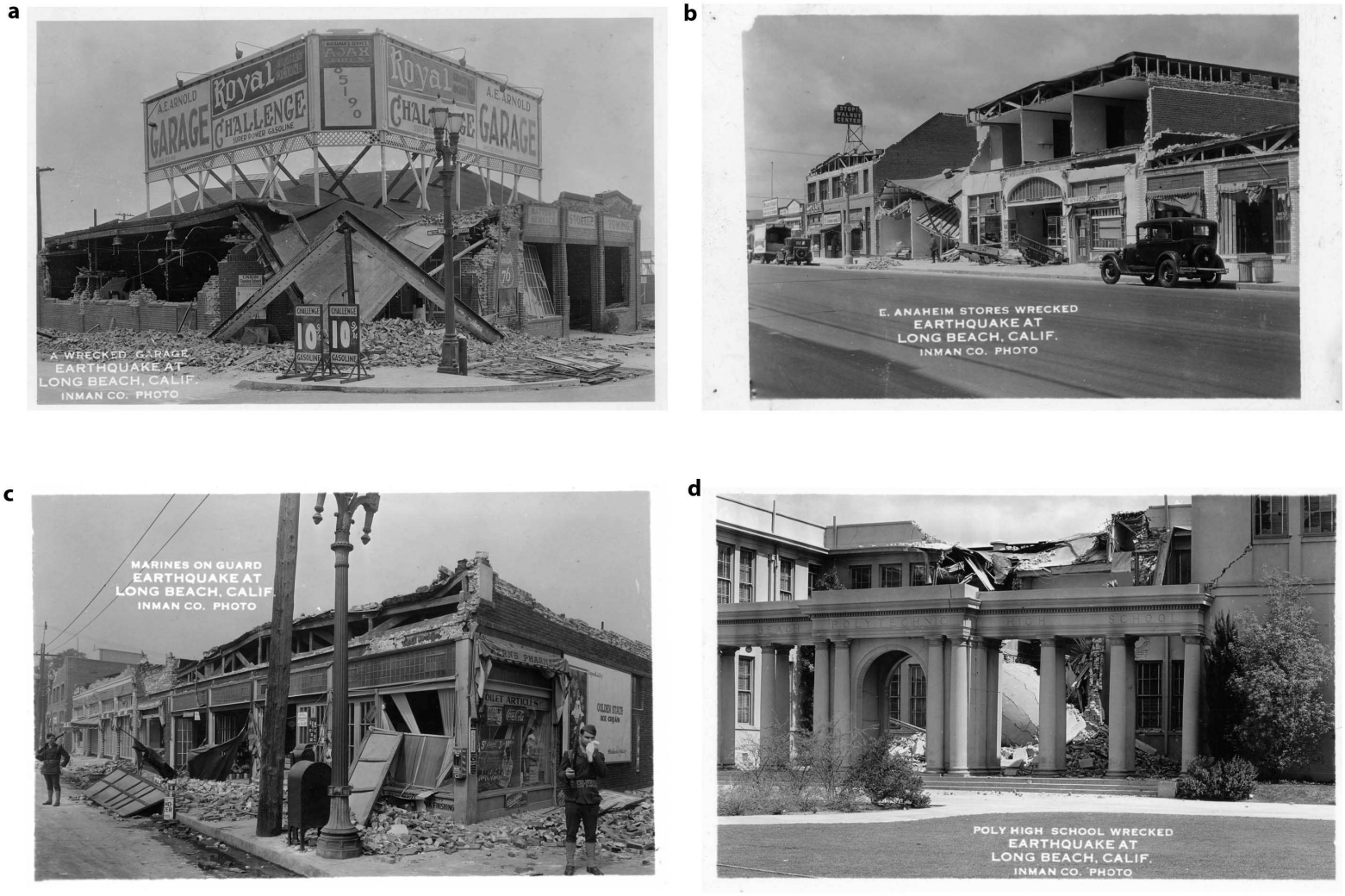

Figure 1.3: **1933 Long Beach Earthquake: Collapse of Unreinforced Masonry Buildings**] Postcards documenting the collapse of unreinforced masonry buildings during the 1933 Long beach earthquake, including **a**, a garage at Ocean Blvd, **b**, East Anaheim stores, **c**, a pharmacy, and **d**, the Long Beach Polytechnic High School. Images courtesy of the George W. Housner collection.

Another source of seismic risk is newer structures that incorporate a novel feature such as a structural system, material, or construction technique, whose performance has not yet been validated by a major earthquake. Moderate-sized earthquakes can serve as canaries, revealing problems with existing types of structures at the cost of relatively little damage and little to no loss of life. A frequently-cited example, the 1994 Northridge earthquake exposed the brittle nature of welded beam-column connections in steel moment-resisting frame buildings. These connections were designed to behave as plastic hinges in the case of heavy seismic loading, but were instead observed to have undergone brittle fracture, even in buildings that experienced only moderate levels of shaking. A FEMA-sponsored partnership of SEAOC, ATC, and CUREe, the SAC Joint Venture was carried out from 1994 to 2000 to develop guidelines and standards for the repair or upgrading of damaged steel moment frame buildings, the design of new steel buildings, and the identification and rehabilitation of at-risk steel buildings. These buildings were not found to present enough of a hazard to warrant taking measures similar to those taken against unreinforced masonry structures, though the building code was updated and other mitigation steps were taken.

The remainder of this chapter is comprised of the following: Section 1.1 presents a discussion of structural damage for building types in the United States, with a focused discussion of types of damage that can be detected using high-frequency seismograms, and Section 1.2 contains a literature review of existing structural health monitoring and damage detection methods.

1.1 Structural Damage

In order to assess the potential for structural health monitoring and damage detection systems for seismic mitigation, we must first understand the types of structural damage that occur during earthquakes. Structural damage can be defined as a change to the structure that adversely affects its performance, thereby reducing its structural integrity. Structural damage generally weakens the structure's vertical or lateral force-resisting-systems. Other types of damage are classified as nonstructural. Examples include the falling of slabs from

a hanging ceiling or a crack propagating through stucco covering a stud wall. The general design philosophy in the United States, similar to that used in Japan and Chile, is to prevent collapse for larger, less frequent earthquakes, while deeming small levels of damage acceptable for moderate-sized earthquakes that are expected to occur during the lifespan of the structure.

The impact of recent earthquakes in Haiti, China, and Chile support the fact that buildings that haven't been designed or constructed to be seismically resistant are the ones that are most at risk from earthquakes. The M 7.0 2010 Haiti earthquake left more than 300,000 people dead and 1.3 million homeless, according to Haiti (2010). An EERI reconnaissance team evaluated building performance in Port Au Prince and nearby areas. They found that nearly all of the severe damage and collapse occurred in buildings that were constructed without considering the effects of earthquakes; the majority of buildings that were designed for earthquakes and constructed well did not collapse (DesRoches et al., 2011). The M 7.9 2008 Sichuan earthquake killed over 69,000 people and left 5 million homeless. The following factors contributing to the poor performance of buildings: the high intensity of ground motion that was above that anticipated by Chinese seismic design code, the poor construction quality of buildings in terms of materials and seismic design, the large number of unreinforced masonry buildings and similar brittle structures, the practice of using heavy solid clay bricks for infill walls and non-structural elements, and the many structures that have large openings at their ground floor creating a soft-story (Zhao et al., 2009).

In contrast to these earthquakes is the M 8.8 2010 Maule, Chile earthquake and tsunami, that together resulted in over 500 deaths. Like the United States and Japan, Chile is seismically-resilient country, with strong public policy programs and building codes that improve seismic safety. According to Moehle and Frost (2012), "like many other economically developed countries in the world, including the United States, Chile is also a nation of income equality, and the 2010 Maule, Chile earthquake demonstrated both the effectiveness and the shortcomings of modern earthquake risk reduction programs." Most of the building damage was contained to unreinforced masonry and adobe single-family dwellings that were built without the assistance of a professional engineer and typically constructed of a quality to

withstand only the types of earthquakes experienced in the region in the past 100 years (Astroza et al., 2012).

1.1.1 Structural Damage to Buildings in the United States

The overall seismic performance and typical seismic issues for 15 model building types (classified by the lateral load resisting system) commonly found in the United States is repeated here from The Rapid Visual Screening of Buildings for Potential Seismic Hazards Handbook, Version 2 (ATC, 2002).

The most hazardous building type is **unreinforced masonry**, and seismic issues can stem from insufficient floor anchorage, excessive diaphragm deflection, low shear resistance, and slender walls. Steel frame buildings with unreinforced masonry infill are also hazardous due to the falling hazard the infill poses. When sufficiently reinforced, **reinforced masonry** can perform well in moderate earthquakes, but poor construction techniques can pose problems. Another seismic hazard is the existence of older **tilt-up** buildings that have not been retrofitted. While construction practices are now improved in California, older tilt-ups are likely to have weak connections between the walls and diaphragms as well as between the concrete panels. Failure of these connections during an earthquake can lead to collapse of wall panels and the roof. **Steel frame buildings with concrete shear walls** tend to perform well during earthquakes, and their seismic vulnerabilities include shear cracking around openings in shear walls, wall shear failure at construction joints, and bending failure from insufficient chord steel lap lengths. **Precast concrete frames** can vary widely in performance, generally depending on the strength and ductility of the structure. Typical seismic issues include poorly designed connections between prefabricated elements, accumulated internal stresses from shrinkage, a loss of vertical support due to inadequate bearing area, insufficient connection between floor elements and columns, and corrosion of metal connectors between prefabricated elements, in addition to the problems experienced by shear wall buildings. The best seismic performance is generally by **wooden stud wall buildings** and **light metal buildings** due to the fact that they are lightweight and typically low-rise.

The most common seismic issue encountered is sliding of the building initiating from an inadequate connection between the building and the foundation. **Steel frame buildings** generally behave in a satisfactory manner due to their strength, flexibility, and lightness, but as mentioned previously, steel moment-frames in particular are vulnerable to fracture at welded connections.

1.1.2 1994 Northridge Earthquake: Lessons Learned

The M 6.7 Northridge Earthquake occurred at 4:31am on January 17, 1994. It resulted in the deaths of 57 people, roughly 9,000 injuries, and cost over $24 billion (in 1994 $) in damage, mitigation, and public assistance (not including repair costs outside of insurance coverage) (Eguchi et al., 1998). The damage to different building types is summarized below.

Steel Frame Buildings

During the 1994 Northridge earthquake, structural damage, notably fracture of steel frames, occurred in more than 100 buildings designed for the ground motions produced by the earthquake (Updike, 1996). Instead of behaving as plastic hinges as they were designed, the beam-column connections underwent brittle fracture that was initiated at the weld. Reliable post-earthquake damage evaluations were made difficult by the fact that damage to the connections was generally not accompanied by overt indicators such as damage to architectural elements or permanent building drifts. Steel moment-frame buildings had performed well in previous earthquakes, and they were a preferred building type for seismically active areas. More than 20 such structures were subjected to and survived the 1906 San Francisco earthquake and fire; many of these buildings are still in service today (Hamburger et al., 2009). The 1994 Northridge earthquake was "the first severe seismic field test of modern steel structures", and while significant problems were noted, the structures performed as expected and no structural collapse occurred (Krawinkler et al., 1996).

The nature of the weld fracture was determined through a variety of field and laboratory experiments. By analyzing data from 51 moment-frame buildings that represent 330

inspected frames consisting of a total of 5,120 beam-to-column connections, Youssef et al. (1995) found that about half of all of the connections at one level of the frame reported no damage, and another third reported weld damage only. In both laboratory tests (a number of which where conducted prior to the Northridge earthquake) and analyzed specimens that were located in buildings impacted by the earthquake, fracture initiated in the weld metal of the bottom flange groove weld, and the crack either remained in the weld or extended into the column (Engelhardt and Sabol, 1997). Detailed analysis of sixteen fractured welded connections was conducted by (Kaufmann et al., 1997). The most frequent fracture type resulted in fracture which penetrated across the column flange. Other fractures were observed to penetrate into the beam flange or the flange welds and the heat-affected zones of these welds (Brockenbrough and Merritt, 2006). The location and source of fracture initiation was the same for all samples, near the midwidth of the weld (near the column web centerline) where limited access for welding results in a higher incidence of weld root incomplete fusion. The mechanism of crack propagation in all samples was cleavage fracture. Fracture initiated from the weld root within the weld metal.

According to SAC (2000), the issues and conditions that led to the brittle failure of typical moment-resisting connections in Northridge were:

- The weld technique used at the bottom flange and the column flange can often result in poor quality welding, and defects can serve as crack initiators.

- Significantly higher shear stresses than are modeled occur at the beam flanges at the connection. The stress concentrations result in severe strength demands at the root of the complete joint penetration welds between the beam flanges and column flanges, a region that often includes discontinuities and slag inclusions, where cracks can initiate.

- The weld access hole that is created to ensure a continuous weld across the beam flange leads to strain concentrations in the beam flange at the weld access hole that can lead to low-cycle fatigue and the initiation of ductile tearing of the beam flanges.

- The restraint of motion of the steel material at the center of the beam-flange-to-column-

flange joint results in high stresses on the welded joint.

- The design practice of using relatively weak panel zones led to an increase in local kinking of the column flanges adjacent to the beam flange-to-column-flange joint which increased the stress and strain demands on the region.

- It is difficult to perform a visual inspection of welded joints, and ultrasonic testing does not reliably detect flaws at the bottom beam flange weld root.

- In the mid-1960s, the construction industry moved to the use of a welding process and welding consumables that produced welds with low toughness. Excessive deposition rates, commonly employed by welders, further compromised the toughness of the weld. Brittle fracture could initiate in welds with large defects, at stresses approximating the yield strength of the beam steel, before ductile deformation could occur.

- For economical reasons related to the increased cost of labor, the industry began constructing buildings with larger members and fewer moment-connections. As member sizes increased, strain demands, related to the span-to-depth-ratio, on the welded connections also increased.

- The use of scrap-based production in steel mills in the 1980s led to beams having yield strengths that were higher than those for previously used A36 beams. An increase in base metal yield strength contributes to brittle behavior if the weld metal in the beam-flange-to-column flange joints becomes under-matched.

Some of the resulting modifications made to building code in the design and welding of moment connections include the use of cover plates and other types of connection, the use of dogbone cutouts in the beam flanges close to the connection, the use of higher toughness weld metals, removal of backing bars and weld tabs, and closer adherence to good welding and inspection practices (Engelhardt and Sabol, 1997). The interested reader is directed to 'Seismic Design of Steel Special Moment Frames: A Guide for Practicing Engineers' which is written for practicing structural engineers to assist in their understanding and application of

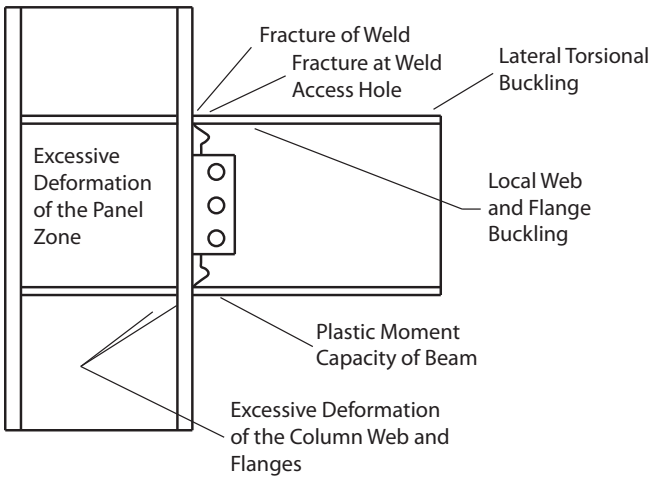

Figure 1.4: **Typical Failure Modes for Welded-Flange-Bolted-Web Connections.** This figure was adapted from a similar figure in FEMA (2000).

the ASCE 7, AISC 341, and AISC 358 documents in steel special moment frame design. The primary goals for special moment frame design are: 1) design for strong-column/weak-beam configurations that distribute inelastic response over several stories; 2) design for lateral seismic drifts that avoid the P-Δ instability under gravity loads; and 3) detailed design for ductile flexural response in yielding regions (Hamburger et al., 2009).

A FEMA-sponsored partnership of SEAOC, ATC, and CUREE, the SAC Joint Venture, existed from 1994 to 2000 to develop guidelines and standards for the repair or upgrading of damaged steel moment frame buildings, the design of new steel buildings, and the identification and rehabilitation of at-risk steel buildings. The interested reader is directed to the comprehensive set of reports and technical briefs were published by FEMA and NEHRP, some of which are listed below:

- FEMA-350: Recommended Seismic Design Criteria for New Steel Moment-Frame Buildings.
- FEMA-351: Recommended Seismic Evaluation and Upgrade Criteria for Existing Welded Steel Moment-Frame Buildings.
- FEMA-352: Recommended Postearthquake Evaluation and Repair Criteria for Welded Steel Moment-Frame Buildings.

- FEMA-353: Recommended Specifications and Quality Assurance Guidelines for Steel Moment-Frame Construction for Seismic Applications.
- FEMA-355A: State of the Art Report on Base Metals and Fracture.
- FEMA-355B: State of the Art Report on Welding and Inspection.
- FEMA-355C: State of the Art Report on Systems Performance of Steel Moment Frames Subject to Earthquake Ground Shaking.
- FEMA-355D: State of the Art Report on Connection Performance.
- FEMA-355E: State of the Art Report on Past Performance of Steel Moment-Frame Buildings in Earthquakes.
- FEMA-355F: State of the Art Report on Performance Prediction and Evaluation of Steel Moment-Frame Buildings.
- NEHRP Seismic Design Technical Brief No. 1: Seismic Design of Reinforced Concrete Special Moment Frames: A Guide for Practicing Engineers.
- NEHRP Seismic Design Technical Brief No. 2: Seismic Design of Steel Special Moment Frames: A Guide for Practicing Engineers.

In order to determine if a building has sustained connection damage it is necessary to remove architectural finishes and fireproofing and perform detailed inspections of the connections. As physical inspection of these connections in buildings is an expensive, obtrusive, and time-consuming process, FEMA offers reimbursements for preliminary post-earthquake assessment for eligible structures with pre-Northridge welded beam-column connections (FEMA, 2007). Most steel moment-frame buildings constructed during the period 1960-1994 employed connections of a type that is vulnerable to brittle connection fracture, making them vulnerable to upcoming earthquakes.

Other Building Types

Other building types generally performed as expected, with the earthquake presenting an opportunity to validate retrofitting practices for wooden, masonry, and concrete buildings. Reinforced concrete shear-wall buildings performed well with respect to life safety and prevention of collapse (Osteraas et al., 1996). Retrofitted nonductile concrete frames also performed adequately. Except for parking structures, post-1967 buildings that relied on shear walls or ductile frames for their lateral load-resisting system performed well. However, there were indications that lateral deformation requirements of gravity columns are inadequate to prevent potential failure. Modern parking structures with precast elements underwent much more damage than expected, with a general pattern of failure of columns that in some cases led to collapse. Tilt-up buildings, especially older ones, suffered a lot of damage in the Northridge earthquake. Of the 1,200 tilt-up buildings in the San Fernando Valley, over 400 had significant structural damage, including partial roof collapse and collapse of exterior walls (CSSC, 1994). There was a high monetary value to the amount of damage to wooden buildings, but little loss of life. The damage was generally due to poor design and construction practices, with buildings with soft-stories or cripple walls suffering the most damage (Hall et al., 1996). Retrofitted masonry buildings performed well, while unreinforced masonry buildings suffered extensive damage. As seems to have been too frequently the case, 'neither the distinction between life safety and control of monetary loss nor the probable variability of performance among buildings is well understood by the general public' (Somers et al., 1996).

1.1.3 Using High-Frequency Seismograms for Damage Detection

High-frequency seismograms have the potential to be used for damage detection in structures where the presence of damage results in the generation of high-frequency signals. High-frequency generally refers to frequencies above the predominant modal response of the structure, although this may depend on the context. High-frequency signals can occur at the moment damage occurs, as in the acoustic emission that occurs during crack propagation.

High-frequency signals can also occur after damage has been created, as in the case of an opening and closing crack, known as a 'breathing crack.' From an analysis of the literature, two potential applications for damage detection using high-frequency seismograms include the detection of weld fracture in steel moment-resisting frame buildings, and the continuous monitoring of high-frequency signals in structures exposed to extreme conditions, such as bridges, which tend to have higher-frequency sources than buildings due to traffic and environmental loading.

There is some support in literature for the idea that high-frequency signals can be used for damage detection in sparsely instrumented steel moment-frame buildings. Rodgers and Mahin (2007) conducted both numerical and experimental testing on a one-third scale, two-story, one-bay steel moment frame. On the experimental structure, twelve accelerometers were installed, and the data were recorded with a time step of 0.01 s. The authors found that short-duration high-frequency signals are present in acceleration records at the moment of fracture, with the time of the fracture determined from beam-end strain gauges. The sign of the high-frequency signal was found to be consistent with that predicted by the equations of motion and analysis, and the high frequency content and amplitude of these signals made them easily distinguishable from the predominant response of the structure to shaking. According to Rodgers et al. (2007), fracture damage causes 'sudden' changes in local stiffness and deflected shape, 'sudden' changes in global acceleration, and a 'sudden' release of energy in the form of elastic waves. In a separate study, the authors analyze data collected from 24 buildings following the Northridge earthquake and use the presence of transient signals in the acceleration records as well as other information about the buildings to determine if weld fracture occurred, with a 67% success rate.

1.2 Structural Health Monitoring and Damage Detection Methods

Structural health monitoring can be defined as the measurement of the operating and loading environment and the critical responses of a structure to track and evaluate symptoms of operational incidents, anomalies, and/or deterioration or damage indicators that may affect operation, serviceability, or safety reliability (Aktan et al., 2000). The basic idea behind structural health monitoring is that the dynamic properties of a structure are a function of its physical properties, and changes in the physical properties of the structure, including the introduction of structural damage, can lead to changes in its dynamic properties. By monitoring the behavior of a civil structure over time, its dynamic properties can be monitored and used to assess its structural integrity. In the event of detected changes in its dynamic properties, the level of damage can be assessed in what is typically formulated as an inverse problem.

The nature of structural damage can be linear (i.e., the material properties of the structure change, however the response of the structure remains linear-elastic) or nonlinear (i.e., loose connections that rattle, or a crack in a beam that opens and closes based on its bending configuration) (Doebling et al., 1996). According to Rytter (1993), a robust damage detection method should be able to: Level 1) identify damage, Level 2) localize damage, Level 3) assess the level of damage, and Level 4) assess the consequence (e.g., give information about the actual safety of the structure given a certain damage state).

The key components of a structural health monitoring system include the type of excitation (forced or ambient), the physical quantities to be measured (e.g., modal values and temperature), the number and types of sensors (e.g., accelerometers, fiber-optic cables, strain gauges, anemometer, etc.), data acquisition system, and data processing. Methods of actively exciting a structure include forced vibration with a (hydraulic, mechanical eccentric mass, or electrodynamic) shaker, impact excitation with an impact hammer, step relaxation using a tensioning device such as a cable, or a hydraulic shake table (Sohn et al., 2004).

Ambient excitation is defined as the excitation experienced by a structure under its normal operating conditions, which can consist of forces from traffic, wind, and microseisms.

While there is a wealth of research in the field of structural health monitoring, there has been a seemingly slow adoption of these methods in industry. This may, in part, be due to a misconnect between the developers of SHM methods and the intended users. Researchers generally focus on the technical aspects of the problem, such as how to locate damage from limited information, and in most studies a damage detection method is tailored to a single building. On the other hand, building owners are generally concerned with the financial aspects of damage detection, such as knowing information about the likelihood of damage, cost of repair, and extension of serviceability. There is clearly room for incorporation of structural health monitoring and damage detection methods into seismic risk management, assessment, and mitigation. This topic is beyond the scope of this thesis. However, one potentially high-impact application for SHM could be the monitoring of national highway bridges. As of 2011, of the total 605,102 highway bridges in the U.S., Moore (2013) rates 67,526 (11 %) as structurally deficient and (13 %) as functionally obsolete.

Only damage detection methods which have relevance to this thesis are mentioned below. Extensive reviews of structural health monitoring methods have been presented by Sohn et al. (2004), Doebling et al. (1996), Doebling et al. (1998), and Friswell (2007).

1.2.1 Vibration-Based Techniques

The term 'vibration-based techniques' is loosely defined to include methods that rely on changes in the global vibration characteristics of the structure, including modal frequencies, mode shapes, and changes in measured flexibility/stiffness coefficients for structural health monitoring and damage assessment. Most of the literature encompasses vibration-based techniques that are typically applied to numerical or small-scale experimental cases.

Generally only the lowest modes are excited under ambient conditions. According to Friswell (2007), an advantage to using low-frequency vibration measurements is that low-frequency modes are generally global, and few vibration sensors are typically needed to

be installed on the structure to monitor these modes. The downside is that the spatial wavelengths of the modes are typically far larger than the extent of the damage. This results in a low spatial resolution in damage identification schemes. On the other hand, using high-frequency excitation uses highly local modes that are able to locate damage, but only in a close proximity to the sensor and actuator.

1.2.1.1 Natural Frequency Based Methods

Damage detection methods that rely only on changes in the natural frequencies of a structure are inherently limited for a few reasons (Doebling et al., 1996). Foremost, natural frequencies typically have low sensitivity to various types of structural damage, and either very precise measurements of frequency or very large levels of damage are required to detect damage. Even when these conditions are met, other factors (e.g., changes in the material properties of the structure caused by changes in weather, or changes in the mass of the structure) may be responsible for observed changes in natural frequencies.

In this case, the forward problem consists of calculating frequency shifts from a known type of damage; the inverse problem consists of calculating the damage parameters from the measured frequency shifts. Though multiple frequency shifts can provide spatial information about structural damage, damage localization that relies solely on modal frequencies is difficult as there is often an insufficient number of frequencies with significant enough change to uniquely determine the location of damage. One common method is to develop a sensitivity relation, whereby a linear relation is developed between the natural frequencies (or changes in natural frequencies) and physical quantities in the model, such as changes in stiffness.

1.2.1.2 Mode Shape Based Methods

Some commonly-applied techniques that are based on changes in mode shape make use of the Modal Scale Factor (MSF), Modal Assurance Criterion (MAC), and Coordinated Modal Assurance Criterion (COMAC). Mode shape derivatives, i.e., curvature, are also used, as they exhibit a direct relationship to bending strain for beams, plates and shells (Doebling

et al., 1996). Methods based on changes in mode shapes are generally combined with outlier methods, forward modeling using a known type of damage, or model updating.

Modal Scale Factor

A suitable scalar-based method of comparison for two mode shape vectors is to plot each pair of elements in the mode shape vectors, on an x-y plot (Ewins, 2000). The slope of the best straight line is called the modal scale factor, and it is defined as (for reference modal vector ϕ):

$$MSF(\psi, \phi) = \frac{\psi^T \bar{\phi}}{\phi^T \bar{\phi}},$$

where $\bar{\phi}$ denotes the complex conjugate of ϕ. If the mode shapes are similar, they should lie close to a straight line. If the mode shape vectors are mass-normalized, this straight line should have a slope of 1. if the points lie close to a straight line with a slope that is not one, then one of the mode shapes is not mass-normalized or there is scaling error in the data.

Modal Assurance Criterion

The modal assurance criterion (MAC), is a simple tool used commonly in the fields of mechanical and aerospace engineering to provide a measure of consistency (degree of linearity) between estimates of a modal vector. The modal assurance criterion is defined as a scalar constant relating the degree of consistency (linearity) between one modal vector and another reference modal vector as follows:

$$MAC(\psi, \phi) = \frac{|\psi^T \bar{\phi}|^2}{(\phi^T \bar{\phi})(\psi^T \bar{\psi})}. \tag{1.1}$$

The modal assurance criterion ranges in value from zero to one. If its value is close to one, it is an indication that the modal shape vectors are consistent. If other explanations can be ruled out (i.e., the modal vectors have been incompletely measured, are primarily coherent noise, or are the result of a forced excitation other than the desired input), then it can be assumed that the modal vectors represent the same modal vector with different arbitrary

scaling (Allemang, 2003). Allemang (2003) further points out that the modal assurance criterion is most sensitive to large differences.

The partial modal assurance criterion (PMAC) is defined as a spatially limited version of the modal assurance criterion where only a subset of the modal vector is used.

Coordinated Modal Assurance Criterion

The COMAC technique is based on the same principle as the MAC and is essentially a measure of the correlation between the reference and the measured mode shapes for a given common coordinate (Marwala, 2010). The coordinated modal assurance criterion (COMAC), for the n^{th} mode shape recorded at the m^{th} receiver, attempts to identify which measurement degrees-of-freedom contribute negatively to a low value of MAC:

$$COMAC[m] = \frac{\sum_{n=1}^{N} \psi_m^n \bar{\phi}_m^n}{\left(\sum_{n=1}^{N} \psi_m^n \bar{\psi}_m^n\right)\left(\sum_{n=1}^{N} \phi_m^n \bar{\phi}_m^n\right)}.$$

If the mode shape vectors are used then the COMAC becomes a vector.

1.2.1.3 Flexibility/Stiffness Based Methods

The flexibility matrix is defined as the inverse of the static stiffness matrix, and it relates the applied static force to the resultant displacement. Each column of the flexibility matrix represents the displacement of the structure to a unit force applied at the associated degree-of-freedom. Analogously, as the stiffness matrix relates the applied force to the displacement of the model, each column of the stiffness matrix represents the amount of force that must be applied to the model to maintain a unit displacement at the corresponding degree of freedom.

The formulation of the flexibility matrix is approximate in the case that not all of the modes of the structure can be measured. Typically, only the lowest frequency modes are measured, related to the tendency of the source to consist of lower-frequency energy. The flexibility is most sensitive to changes in the lower frequency modes of the structures due to its inverse relationship to the frequencies; the stiffness matrix is most sensitive to the

highest frequencies. Damage is detected by using modal values to compute the flexibility or stiffness matrix of a potentially damaged structure, and comparing these values with those determined when the structure was in an undamaged state.

1.2.1.4 Parameter Estimating and Updating

In model identification methods, a model for the structure is formulated, and static or dynamic data is used to update model parameters such as natural frequencies, mode shapes, mass, stiffness, and damping matrices. Generally a constrained optimization problem based on the equations of motions, the nominal model, and the measured data is used. Damage detection, localization, and estimation of severity is generally performed by comparing the updated values to the nominal values. The procedure is generally to: 1) identify an objective function, 2) define constraints, and 3) define a numerical scheme to implement the optimization.

Matrix updating methods that use a closed-form direct solution to compute the damaged model matrices or the perturbation matrices are known as optimal matrix update methods. The problem is generally formulated as a Lagrange multiplier or penalty-based optimization. Methods that are based on the solution of a first-order Taylor series that minimizes an error function of the matrix perturbations are known as sensitivity-based update methods. Some common objective functions include: 1) the modal force error, with constraints that preserve the matrix symmetry of the perturbation matrices, sparsity, and positive-definiteness, 2) the mean-squared-error computed in the time domain, 3) the mean-squared error computed in the frequency domain using the transfer function.

Damage detection techniques using finite element model updating often leads to updating of a large number of damage parameters, especially when the structure has many structural members (Sohn et al., 2004). There are techniques that can help with solving for a large number of system or damage parameters, e.g., the Hamiltonian Markov chain method has been shown to aid in solving higher-dimensional Bayesian model updating problems (Cheung and Beck, 2009).

1.2.2 Acoustic Methods

Acoustic damage detection methods typically rely on the comparison of a recent signal to an archived baseline response function, known as a template. The template is recorded at a time when the structure is undamaged. The sensor network must have a high sampling rate to capture the propagation of waves throughout the structure. Acoustic techniques have been explored experimentally and numerically for thin plates and beams (Park et al., 2007; Wang et al., 2004; Wang and Rose, 2003), which serve as waveguides that effectively carry information from the location of structural damage to a receiver. This information, namely differences in waveform and amplitude between the current signal and the template, are used to diagnose damage.

Acoustic methods can be passive or active, and sensor networks can be permanently installed or temporary. Giurgiutiu and Cuc (2005) reviews current techniques, including embedded ultrasonic non-destructive evaluation (NDE), which uses a transmitter to interrogate the structure while a receiver records the structural response. 1) Pitch-catch: a pulse is emitted by a transmitter and travels through the material to a receiver. Differences in guided wave shape, phase, and amplitude are used to detect damage in the medium between the transmitter and receiver. 2) Pulse-echo: a pulse is emitted by a transmitter, which also acts as a receiver to detect damage in the form of additional echoes. 3) Time-reversal: a signal sent by a transmitter arrives at a receiver, where the signal is time-reversed and reemitted. Structural damage that causes linear reciprocity to break down leads to discrepancy between the original signal and the final signal received by the transmitter. 4) Migration: recorded waves are back-propagated through the material by systematically solving the wave equation to image reflectors in the medium.

1.2.2.1 Guided-Wave Methods

Guided-wave testing is an active form of structural health monitoring that relies on a network of sensors and actuators to probe the structure with a controlled high-frequency vibration. The vibration excites stress waves that essentially become trapped within nearby structural

members, such as beams or plates, hence the term "guided wave." A baseline response, recorded when the structure is known to be in an undamaged state, serves as a reference signal to which future responses, when the structure is not known to be undamaged, can be compared. Features that potentially indicate damage are extracted from the recorded signal, typically by removing the baseline response from the recorded response in the time-domain or in the time-frequency domain. Finally, a chosen technique (e.g., a neural network coupled with an FEM model or seismic migration) is used to detect and locate damage and estimate its severity. A review of guided-wave structural health monitoring methods is presented by Raghavan and Cesnik (2007).

A transducer is a device that converts a signal of one form of energy into another form of energy. The most popular types of transducers used in guided-wave testing are piezo-electric and can act as both sensors, which detect vibration by converting a mechanical signal into an electrical signal, and actuators, which generate vibration by converting an electrical signal into a mechanical signal. Other types of transducers are also available, including those based on fiber optic, microelectromechanical (MEMS), and nanotube technologies.

The two main techniques used to produce vibration are dubbed "pulse-echo" and "pitch-catch." In pulse-echo setups, the sensor is co-located with the actuator, and in pitch-catch setups, the sensor is located away from the actuator. Differences between a recorded signal and a prerecorded baseline are used to detect damage. In pulse-echo setups, damage is detected by the presence of additional features in a signal that are caused by waves reflecting off a damaged region, such as a crack, which acts as a reflector. In pitch-catch setups, damage is detected by changes in the recorded signal from the baseline signal that could denote damage in the medium between the actuator and sensor. A time-reversal method is experimentally verified by Park et al. (2007) with an experimental setup that consists of a pair of piezoelectric patch transducers that are attached to a composite plate. In the first step of the method, a Lamb wave is emitted by the first transducer. The signal recorded at the second transducer is time-reversed and retransmitted by the second transducer. The resulting signal recorded at the first transducer is compared to the initially emitted Lamb wave. The Lamb wave is designed, using Mindlin plate theory, in such a way that the

reconstructed signal will be very close to the emitted signal. Nonlinearities between the two transducers that are due to damage should result in differences between the original emitted signal and the final resulting signal. This method bypasses the need for a prerecorded baseline.

For most applications, a dense network of actuators and sensors is needed for damage localization (e.g., multiple actuators and sensors located on each plate). Furthermore, most studies take place in a laboratory setting, and the robustness of these systems still need to be vetted *in situ* against the noisy conditions that would be encountered on an actual structure. Finally, many of these methods are based on theoretical formulations for simple geometries, such as a simply supported plate. However, in the real world, these elements would be likely fixed to other members, and hence they would have radically different boundary conditions than those considered in lab. For these reasons, these methods are not yet industry-ready.

1.2.3 Time-Frequency Signal Analysis

There are two basic approaches to time-frequency analysis. The first is to divide the signal into slices in time and to analyze the frequency content of each of these slices separately (e.g., Wigner-Wille transform). The second is to filter the signal at different frequency bands and window the frequency bands to analyze their energy content as a function of time and frequency. Other time-frequency analysis techniques include, but are not limited to, wavelet analysis, and empirical mode decomposition combined with Hilbert transform (Sohn et al., 2004). Time-frequency analysis can aid in damage detection by better distinguishing a damage signal temporally and spectrally.

1.2.3.1 Analytic Signal

The analytic signal (also known as analytic representation or analytic associate) $x_a(t)$ of a real-valued signal $x(t)$ is defined as

$$x_a(t) = x(t) + i\mathcal{H}\left\{x(t)\right\},$$

where the Hilbert transform $\mathcal{H}\{x(t)\}$ of a signal $x(t)$ is given by:

$$\mathcal{H}\{x(t)\} = \mathcal{F}^{-1}\{(-isgnf)\mathcal{F}\{x(t)\}\}.$$

The negative frequency components of real signals are superfluous, as $X(-f) = X^*(f)$ for $f > 0$, where $X(f)$ is the Fourier transform of $x(t)$. By converting to the analytic signal, the negative frequency components are set to zero with no loss of information, but at the expense of transitioning to a complex-valued signal.

1.2.3.2 Time-Frequency Distributions

Boashash (2003) presents a comprehensive reference of time-frequency signal analysis, and two time-frequency distributions discussed in the book are summarized here. Generally speaking, the time-frequency distribution $\rho_{x_a}(t, f)$ of the analytic signal $x_a(t)$ aims to represent the energy, temporal, and spectral characteristics of $x_a(t)$ in the (t, f) plane. By using the analytic signal rather than the real-valued signal when constructing a time-frequency distribution, spurious terms caused by interference between the positive- and negative-frequency components can be avoided.

Spectrogram

A spectrogram can be used to analyze the time-varying spectrum of frequencies in a signal, effectively estimating the energy density of the signal in the time-frequency plane by partitioning the signal in the time domain and analyzing the frequency content of each window.

The spectrogram is constructed from a signal $x(\tau)$ and a chosen time-limited, real, even window $w(\tau)$ by multiplying the signal by a window centered at time $\tau = t$ and taking the squared magnitude of the Fourier transform of the resulting signal;

$$S_x^w(t, \omega) = |\mathcal{F}_{\tau->\omega}\{x(\tau)w(\tau - t)\}|^2.$$

There is a trade-off between time and frequency resolution in accordance with the 'uncertainty relationship.' Using a shorter window $w(\tau)$ allows for better localization of the spectrum in time, but also makes for a decrease in resolution in frequency. Using a longer window $w(\tau)$ allows for better resolution of the signal in frequency, at the expense of a poorer localization of the signal in time.

Wigner-Ville Distribution

The Wigner-Ville distribution of an analytic signal $x_a(t)$ is given by:

$$W_{x_a}(t,\omega) = \mathcal{F}_{\tau->\omega}\left\{x_a(t+\tau/2)x_a^*(t-\tau/2)\right\}.$$

According to Boashash (2003), the Wigner-Ville distribution has a number of advantages, including but not limited to the following: realness, time-shift invariance, frequency-shift invariance, time marginal (integration over frequency gives the instantaneous power), frequency marginal (integration over time gives the energy spectrum), and preservation of the instantaneous frequency and time delay. Its limitations include the artifacts, or cross-terms, which appear midway between multicomponent signals.

1.2.4 Other Methods

Other inspection methods, such as visual inspection, magnetic particle inspection, radiography, eddy current, ultrasonic, and thermal field are not covered here. Neither are aerial and satellite methods that detect post-disaster damage at the scale of an entire city or region. Machine learning methods, such as neural networks, have also not been touched upon; although the main disadvantage to using this approach is the lack of experimental training data, there has been some recent success in applying pattern recognition to acoustic emission signals obtained from databases of empirical data (Friswell, 2007). Finally, hybrid techniques have not been mentioned. However, a hybrid SHM system is the most promising as each method has its own strengths and weaknesses, and augmenting a vibration-based technique with a high-frequency time-domain technique could make for a more robust detection of

damage.

1.2.5 Validation and Comparative Studies

There is a (fortunate) lack of seismic data recorded in instrumented U.S. civil structures that were structurally damaged during an earthquake. This is due to the absence of a recent large earthquake in the United States, the ability of structural engineers, improvements in building codes and seismic design maps, and the relatively small percentage of densely instrumented buildings. Without a wealth of real-world data for validating and benchmarking damage detection methods, numerical and experimental testing are key in providing insight and direction for developing structural health monitoring and damage detection methods.

1.2.5.1 Publicly-Available Datasets for the Purpose of Benchmarking

There exist a few publicly-available datasets for the purpose of validating and benchmarking structural health monitoring, particularly damage detection methods. These datasets, as well as the methods that have been used to study them, are summarized below.

The most extensively-studied SHM benchmark was created by the International Association for Structural Control (IASC) of the American Society for Civil Engineers (ASCE) structural health monitoring task group. The benchmark problem was carried out in two phases, Phase I (a numerical study) and Phase II (an experimental study).

IASC-ASCE SHM Benchmark: Phase I

A special issue on Phase I of the IASC-ASCE Structural Health Monitoring Benchmark to date was published in the Journal of Engineering Mechanics (Volume 130, Issue 1, pp. 1-104). The issue contains a brief introduction by Bernal and Beck (2004) of the benchmark and methods applied to the Phase I benchmark problem in the special issue, a description of the benchmark problem by Johnson et al. (2004), as well as seven papers each presenting the application of an SHM technique to the benchmark problem (Bernal and Gunes, 2004; Caicedo et al., 2004; Hera and Hou, 2004; Lam et al., 2004; Lus et al., 2004; Yang et al.,

2004; Yuen et al., 2004). The results published in these papers and other studies subsequently performed on the benchmark problem are discussed below.

Phase I of the IASC-ASCE SHM benchmark problem is described in detail by Johnson et al. (2004) and is summarized here for convenience. The numerically-modeled structure used for the benchmark is a four-story, two-bay by two-bay steel-frame quarter-scale structure (2.5 m by 2.5 m plan and 3.6 m height) located at the Earthquake Engineering Research Laboratory at the University of British Columbia. Damage is introduced either to a diagonal brace (by reducing the stiffness or removing the brace) or to a beam-column connection (by changing the connection from a moment connection to a simple connection).

Participants in the benchmark are tasked with detecting damage using a 12-DOF shear building as the identification model. Data is numerically simulated using either a 12-degree-of-freedom or a 120-degree-of-freedom analytical structural finite-element model. Using two models to generate the data provides participants with a means of studying modeling error. The output "noise level" is the RMS of the sensor noises, generated using independent Gaussian pulse processes, as a percentage of the maximum RMS acceleration responses; the noise level is 10% for the benchmark problem. Six different cases are considered by varying the excitation source (wind or shaker), model used to generate the data (12 DOF or 120 DOF), and number of sensors (accelerometers) used for the output.
Six different damage patterns are considered, and they are defined as:

Damage Pattern I: No stiffness in the braces of the first story.

Damage Pattern II: No stiffness in any of the braces of the first and third stories.

Damage Pattern III: No stiffness in one brace in the first story.

Damage Pattern IV: No stiffness in one brace in the first story and in one brace in the third story.

Damage Pattern V: The same as damage pattern iv, but with a floor beam at the first level partially unscrewed so that the beamcolumn connection can only transmit forces and cannot sustain any bending moments.

Damage Pattern VI: Two-thirds stiffness, i.e., a one-third stiffness loss in one brace in the first story.

The six cases are defined as:

Case 1: 12-DOF model used to generate data, symmetric mass distribution on roof, ambient excitation, both a known and unknown input, Damage Patterns I and II.

Case 2: 120-DOF model used to generate data, symmetric mass distribution on roof, ambient excitation, both a known and unknown input, Damage Patterns I and II.

Case 3: 12-DOF data generation model, symmetric mass distribution with a shaker diagonal on roof, unknown input for the data, Damage Patterns I and II.

Case 4: 12-DOF data generation model, asymmetric mass distribution, shaker excitation, unknown input, Damage Patterns I, II, III, IV, and VI.

Case 5: 120-DOF data generation model, asymmetric mass distribution, shaker excitation, unknown input, Damage Patterns I, II, III, IV, V, and VI.

Case 6: 120-DOF data generation model, asymmetric mass distribution, shaker excitation, unknown input, limited sensors to those on the second and fourth floors, Damage Patterns I, II, III, IV, V, and VI.

Yuen et al. (2004) apply a two-stage method that is based on a modal identification technique and model parameter updating using a Bayesian model identification method. In the first stage, the MODE-ID modal identification procedure is used to estimate modal parameters from the response data when the structure is in either an undamaged or a possibly damaged state. In the second stage, the estimated modal parameters are used in a Bayesian model updating method to determine the most probable values of the stiffness parameters. Yuen et al. (2004) note that in all of the benchmark cases, the damage can be identified solely on the basis of the maximum posterior value of the stiffness parameters, however the authors recommend that the probability of damage in each story instead be calculated as a

probability of the fractional reduction in interstory stiffness. The damage probability curves are also presented in the study. The uncertainty in estimating the damping ratios is much higher than in estimating the natural frequencies, and in the case of an unknown excitation, additional information, such as the spectral level of excitation, is needed to better identify the damping ratios. Only the (lower) modes that contribute significantly to the motion can be identified. The reduction in accelerometers resulted in larger uncertainties of the estimated stiffness parameters, as well as a few spurious increases in stiffness and false positives (estimated decreased stiffnesses in undamaged floors). Yuen et al. (2004) note that in the event that the "known" mass matrix is inaccurate, significant bias can be introduced in the resulting estimates. By relaxing the conditions on the mass matrix to include some uncertainty, robustness is gained at the expense of a small loss of precision.

A single-step Bayesian modal identification approach is considered by Lam et al. (2004). The basic concept is to identify a set of optimal model parameters based on maximizing the posterior probability density function (PDF) for the parameters, which is a product of the prior PDF for the parameters as well as a PDF giving the probability of the spectral data given some values for the parameters. The excitation is assumed to be wide-band and able to be modeled as white noise. First, spectral estimates are formed from the cross-correlations of the responses. A subset of the spectral estimates, i.e., a range within a specified frequency band, is used for parameter estimation using a Bayesian approach. The estimated parameters include the model stiffness parameters as well as the modal parameters (modal frequencies, damping ratios, mode shapes, modal forcing spectral density terms, and the covariance matrix of the prediction error). The posterior probability distribution function of the parameters is formulated. It incorporates the subset of the spectral data and the prior probability distribution function for the stiffnesses and is maximized in a single-step to yield the most likely estimates for the parameters. According to Lam et al. (2004), unlike a two-step minimization, a one-step minimization ensures that the structural model corresponding to the optimal stiffness parameters is the optimal structural model within the chosen class of models. The methodology did not fail to detect damage in any of the benchmark cases considered, although in some cases the identified damage extent was slightly overestimated

for cases with modeling error, often within the margin of statistical error.

Caicedo et al. (2004) estimate interstory stiffness values by applying the natural excitation technique (NExT) method, in conjunction with the eigensystem realization algorithm (ERA) and a least squares optimization. The modal parameters are estimated by applying ERA to cross-correlation functions, which are computed from the forced vibration data and treated as free vibration data. This technique is applicable for problems in which the excitation is broadband and random, and the ratio of masses is known. There is some art in choosing the reference signal, which cannot lie at a node at any of the considered modes. This method was found to be robust to noise, modeling error (Case 2), and coupling due to asymmetry in the mass distribution (Case 4), with typical errors in the identified stiffness values for the members less than 1%. For Case 6, as half of the sensors were removed, an iterative procedure was used to estimate the eigenvectors and stiffness terms. The approach provides an indication of the location of the damage, but may include some false positives, which indicate that damage occurs in some locations where damage is not present. The authors note that when an iterative approach is used, a single sensor would be adequate to determine the eigenvectors, eigenvalues, and stiffnesses of the structure. If the number of sensors is limited, this technique could be applied by independently relocating the available sensors on a structure while keeping the reference channel at the same position.

A flexibility-based method is employed by Bernal and Gunes (2004) to locate and quantify damage. The method consists of the following steps: 1) compute the state-space realization from the measured signal, 2) extract the flexibility matrices from the matrices of the realization (using the ERA-OKID algorithm when the input is known and the Sub-ID subspace technique when the input is stochastic), 3) compute the change in flexibility from the undamaged to the damaged state, 4) apply the damage locating vector (DLV) technique to localize the damage, and 5) quantify the damage. The steps of DLV localization is as follows: 1) compute the change in flexibility, 2) obtain a singular value decomposition of DF, 3) compute the stresses in an undamaged model of the structure, 4) reduce the internal stresses in every element to a single characterizing stress, 5) compute the svn index, 6) check if the svn index is lower than a threshold value, 7) compute the normalized stress index vector, 8)

compute the vector of weighted stress indices, and finally 9) the weighted stress indices that are less than 1, which include the potentially damaged elements. Arbitrary viscous damping is considered. The authors further partitioning the shear beam into four sections per floor in an attempt to locate damage at the element level. When there are at least three sensors per level one can dene the interstory stiffness and center of stiffness positions from the modal data and use the changes in these quantities to determine the level, location, and extent of the damage without the need for an explicit model. The authors note that the approach may not be robust in eld conditions, because the truncation of the modal space is likely to be too large to allow accurate computation of the physical parameters.

Lus et al. (2004) apply a two-step approach that consists of finding a first-order minimal state space realization of the system using only the input-output measurements, and then extracting the physical parameters (mass, damping, and stiffness parameters) of the underlying second-order system. An Observer/Kalman filter identification (OKID) algorithm is used to identify the Markov parameters of the system, which are used in the eigensystem realization algorithm to realize the discrete-time first-order system matrices. The initial state space model is further refined by minimizing the output error between the measured and predicted response using a nonlinear optimization approach based on sequential quadratic programing techniques. Finally, the physical parameters of the FE model are determined from the state-space model, and damage is determined by comparing these values with those recorded when the structure was in an undamaged state.

Two time-frequency analysis methods are applied by Yang et al. (2004) to detect the occurrence of damage spikes as well as changes over time in the structure's modal properties (frequencies and damping ratios). The first method, based on filtering using the empirical mode decomposition (EMD), is used to to extract high-frequency damage spikes that occur at the instant that damage occurs. Structural damage results in a sudden change of structural stiffness that causes a discontinuity in acceleration in the vicinity of the location of damage. Yang et al. (2004) found that for Damage Patterns I and II, the damage spikes can always be detected when the measured data has zero or little added noise. A Monte Carlo simulation is performed for ten sample cases, and it is estimated that the probability of detecting the

damage spike, with 10% noise added, is about 30%. The authors note that there is some art in choosing the intermittency frequency, i.e., the cutoff frequency for filtering, which should be above the modal frequencies but below the frequency of the damage spike. As the damage spike is only present in the acceleration records on the damaged floors in this study, it is relatively simple to qualitatively determine the floor at which the damage occurred. For Damage Patterns III, IV, and V, the damage spikes are submerged with the noise in the y-component sensor data. The authors conclude that the detection of damage time instants and damage locations through the identification of damage spikes is influenced significantly by the severity of damages and the noise-to-signal ratio. The second method, a Hilbert-Huang approach based on the EMD and Hilbert transform, is combined with the random decrement method to determine the natural frequencies and damping ratios of the structure before and after damage. The authors note that only a single record is needed to determine these modal values, but a full array of sensors should be installed in order to identify the damage locations.

A wavelet-based technique is used by Hera and Hou (2004) to detect damage spikes in the acceleration data. The supplied MATLAB program for the benchmark problem is slightly modified to introduce damage in the middle of a response history by piecing together two segments of response data, one directly before damage, one directly after damage, while satisfying continuity conditions in velocity and displacement. In this example, even when all diagonal braces are broken between two floors, damage spikes are only observed in the acceleration records immediately above and below that floor. Localization of damage to a story is achieved using patterns in the spatial distribution of spikes. Hera and Hou (2004) find that the effectiveness and reliability of the proposed approach depends on damage severity and measurement noise level. One advantage to this technique is that it is not dependent on knowledge of the structure's modal response and only relies on the spatial distribution of sensors. However, structural information may still be needed in order to properly interpret the results from the wavelet analysis. Although the severity of damage was seen to have a predictable change on the amplitudes of the spikes, the authors did not present a way of quantifying the severity of damage depending on the data.

Later studies published on Phase I of the IASC-ASCE benchmark study include a two-stage eigensensitivity-based finite element model updating method by Wu and Li (2006) and a method based on the change of strain energy in each structural element in both the damaged and undamaged state by Sharifi and Banan (2008).

IASC-ASCE SHM Benchmark: Phase II and Phase IIe

Phase II consists of experimental testing of the model located at the Earthquake Engineering Research Laboratory at the University of British Columbia (UBC). The experimental setup is described by Dyke et al. (2003) and is summarized here for convenience. The 4-story 2-bay by 2-bay (2.5 m x 2.5 m x 3.6 m)steel-frame (grade 300W steel) scale model is located at the Earthquake Engineering Research Laboratory at the University of British Columbia (UBC). Acceleration data is recorded using three sources of excitation (ambient vibrations, impact hammer tests, and electrodynamic shaker tests), with nine cases of damage simulated by removing bracing within the structure or by loosening bolts connecting beams to columns. The benchmark provides a great example for the comparison of the numerical data with the experimental data, and a common framework (dataset and objectives) with which to accurately compare the performance of different SHM and DD methods.

Ching and Beck (2004) apply a two-step probabilistic structural health monitoring approach; the modal parameters and their uncertainties are estimated in the first step, and they are used in the second step to determine the probability that stiffness reductions exceed a prescribed damage threshold. In the cases where damage is simulated by removing braces, all damage was successfully detected with both the hammer excitation or the ambient vibration excitation. No false alarms were detected using hammer excitation, but some false detections were found using ambient vibration excitation. In cases where damage is introduced by loosening the bolts connecting beams to columns, only the hammer excitation data were considered for determining the mode shapes, as they had the best quality. Most damage cases were detected, but there were many false detections, most likely due to the difficulty of estimating the rotational stiffness as the stiffness matrix of the structure was found to be dominated by the columns.

IMAC Benchmark

An earlier benchmark problem was initiated at the 15^{th} International Modal Analysis Conference (IMAC XV), and consisted of numerical data simulating a finite element model of a one-third scale steel frame structure subjected to uncorrelated shaker inputs at its roof (Black and Ventura, 1998). Three different damage configurations (including one blind example) were created by removing members or changing member properties, and 5% noise was added to the output signals, 16 acceleration time-histories. One damage detection study was published on this dataset, in which the Damage Index Method was applied to localize and estimate the level of damage (Park et al., 1998).

Center of Structural Monitoring and Control at the Harbin Institute of Technology Benchmark I and II

Finally, a real-world benchmark problem was recently made available by the Center of Structural Monitoring and Control (SCM) at the Harbin Institute of Technology using data recorded on an instrumented cable-stayed bridge in China (Li et al., 2010, 2012, 2013). First opened to traffic in 1987, the bridge is one of the first built cable-stayed bridges in mainland China. According to Li et al. (2013), the bridge was repaired between 2005 and 2007 for cracks observed at the bottom of a girder segment over the mid-span, and corroded stay cables (especially those near the anchors). During this time, the bridge was also upgraded with an SHM system that includes more than 150 sensors, including 14 uniaxial accelerometers, 1 biaxial accelerometer, an anemoscope, a temperature sensor, and optical fiber Bragg grating sensors. Two benchmark problems are proposed, based on the bridge. The first benchmark problem is to assess the condition of the stay cables based on the strains measured over the period of one week in January, 2008 and the fatigue properties of the deteriorated steel wires as determined from fatigue testing on some specimens taken from the cables near the bottom anchorages. Specifically, researchers are asked to assess the fatigue life prediction model of parallel wire cables, as well as the residual fatigue life assessment of deteriorated cables. The second benchmark problem is to detect, localize, and quantify damage using acceleration measured from January to August 2008. Li et al. (2013) presume that the bridge was dam-

aged gradually over this time period by overloading. The benchmark study is a blind test, as no further information about the damage is supplied. Lastly, a finite-element model has also been made available for this benchmark problem. As this benchmark problem was only recently made available, no papers have yet been published on this dataset.

1.2.5.2 Datasets Used in this Thesis for the Purpose of Validation

In this thesis, numerical testing, small-scale experimental testing, and full-scale experimental testing is conducted for the purpose of developing and testing damage detection methods for civil structures instrumented with a seismic array. In Chapter 2, a novel damage detection method that relies on approximating connection fracture as a hammer blow is experimentally tested using a small-scale steel frame. Experimental impact hammer data is also obtained in an instrumented steel moment-resisting-frame building. In Chapter 3, an instrumented small-scale experimental shear beam is subjected to a repeatable pulse at its base using a shake table. The experiment is repeated with the beam in different damage configurations. A novel damage detection method, that relies on the detection of repeating high-frequency short-duration pulses, is successfully applied to the structure. Numerical studies in Chapter 4 further investigate the feasibility of the proposed damage detection method for weld fracture, as well as exploring a time-reversed reciprocal method for a frame. Finally, high-frequency data from the SCM benchmark bridge in China, as well as a test bed data set using a nonlinear frame provided by the Los Alamos National Laboratory are studied in Chapter 5. In the Appendix, experimental data from a densely-instrumented high-rise building located in Osaka is used to obtain the impulse response function of the building. A numerical model is developed, based on the design parameters for the structure, and is subsequently damaged and studied.

Chapter 2

Experimental Study: Damage Detection Method for Weld Fracture of Beam-Column Connections in Steel Moment-Resisting-Frame Buildings

Automated damage detection methods have application to instrumented structures that are susceptible to types of damage that are difficult or costly to detect. The presented method has application to the detection of brittle fracture of welded beam-column connections in steel moment-resisting frames (MRFs), where locations of potential structural damage are known *a priori*. The method makes use of a prerecorded catalog of impulse response function (IRF) templates and a cross-correlation method to detect the occurrence, location, and time of structural damage in an instrumented building. The method is designed to recognize elastic waves radiated by the original brittle fracture event, where the event is not known to have occurred with certainty and the resulting damage may not be visible. An experimental study is conducted to provide insight into applying the method to a real structure. A series of hammer blows and bolt fractures is used to excite a small-scale steel frame to test whether cross-correlation techniques and catalogued IRF templates can be used to identify the occurrence and location of an assumed-unknown event. To investigate this method for a full-scale structure *in situ*, IRFs are experimentally obtained from a densely-instrumented

steel moment-resisting frame building. The recorded IRFs are easily observed over the ambient noise of the building. Results support the idea of using a nondestructive force to localize damage using high-frequency seismograms, though the method might be prone to false negatives (i.e., missed detections) when used to detect the presence of damage.

2.1 Introduction

Acoustic damage detection methods rely on the comparison of a recent signal to an archived baseline response function, known as a template. The template is recorded at a time when the structure is undamaged. The sensor network has a sampling rate that is high enough to capture the propagation of waves throughout the structure. Acoustic techniques have been explored experimentally and numerically for thin plates and beams, which serve as waveguides that effectively carry information from the location of structural damage to a receiver (Giurgiutiu and Cuc, 2005; Park et al., 2007; Wang et al., 2004; Wang and Rose, 2003). This information, namely differences in waveform and amplitude between the current signal and the template, is used to diagnose damage. Acoustic methods can be passive or active, and sensor networks can be permanently installed or temporary. Existing methods include pitch-catch, pulse-echo, time-reversal, and migration. In this paper, a complementary acoustic method is presented that makes use of a prerecorded catalog of IRFs and a cross-correlation method to passively detect the original failure event. This technique is different from existing acoustic methods as it is designed to use the elastic waves radiated by the original brittle failure event to both identify and localize damage. It is similar to the matched filter method, which has been successfully used in other fields to detect repeating small-magnitude earthquakes in noisy data (Anstey, 1964; Gibbons and Ringdal, 2006). The method has yet to be explored in the context of acoustic damage detection of civil structures.

2.2 Description of Proposed Damage Detection Method

The proposed method makes use of a prerecorded catalog of IRFs for an instrumented building to detect structural damage during a later seismic event. Continuous data collected on a passive network are screened for the presence of waveform similarity to one of the IRF templates. The method is outlined below.

1. Identify probable points of failure in an instrumented building before structural damage has occurred. As pre-Northridge steel MRFs are susceptible to the brittle failure of welded beam-column connections, these would be the locations of probable failure for this type of building.

2. At each labeled location, apply a short-duration high-frequency pulse (e.g. using a force transducer hammer). The response of the building at each instrument site is the IRF specific to that source location-receiver pair. The IRFs are archived in the catalog of templates to be used later to screen the high-frequency seismogram for a damage signal.

3. Screen data recorded at a later time for the presence of a damage event using the prerecorded templates. For each possible source location k, perform a running cross-correlation between the IRF templates for that source location and a moving window of the seismogram that recorded the shaking event, stacking over the receivers. Cross-correlation between the k^{th} IRF template g_i^k recorded by the i^{th} receiver and the seismogram x_i recorded by the i^{th} receiver is given by:

$$C_i^k(t) = \frac{\int_0^T g_i^k(\tau) x_i(t+\tau) \mathrm{d}\tau}{\left(\int_0^T (g_i^k(\tau))^2 \mathrm{d}\tau \int_0^T (x_i(t+\tau))^2 \mathrm{d}\tau \right)^{1/2}}. \tag{2.1}$$

   Time T is the duration of the template, and the cross-correlation is normalized by the autocorrelation values for the given time window. Compute the stacked cross-

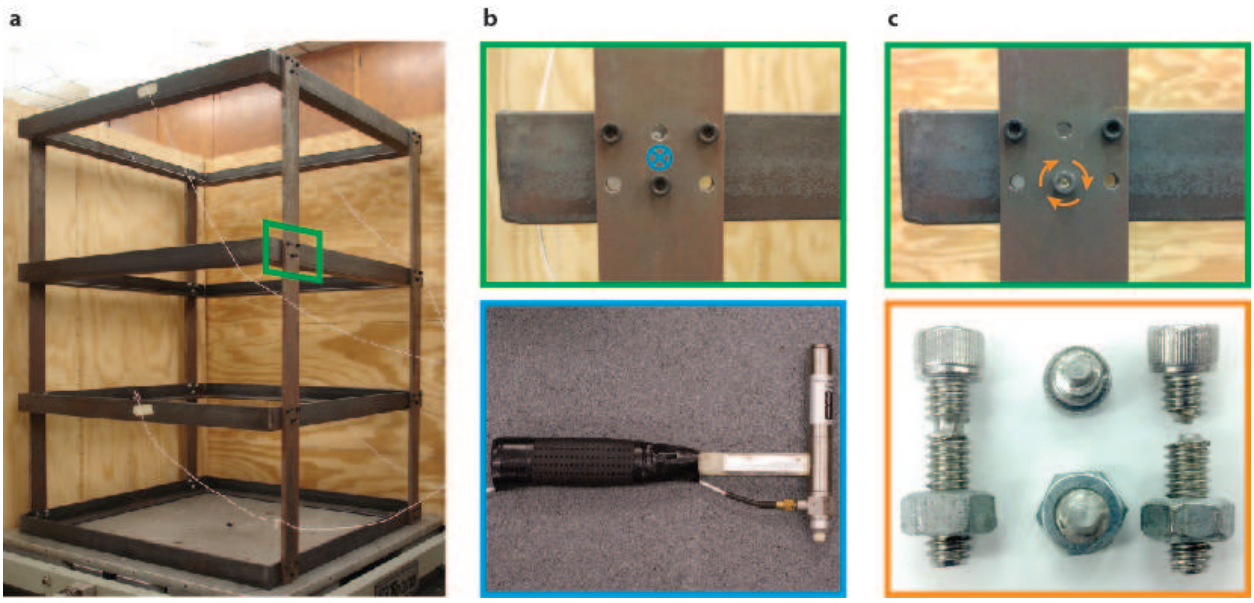

Figure 2.1: **Steel Frame: Experimental Setup.** **a**, The steel frame consists of three floors above ground and one floor at its base that is attached to a stationary shake table. The connections are moment-resisting, with three bolts firmly connecting the beams to columns. **b**, A force-transducer hammer is used to apply an impulsive force to a beam-column connection at the mark shown in blue, along an axis that points into the page. **c**, Bolt fracture is introduce by first substituting a bolt with a notch machined into it into a connection at the indicated location in orange. The bolt is torqued until it fractures.

correlation function by summing over the R receiver locations:

$$C^k(t) = \frac{1}{R} \sum_{i=1}^{R} C_i^k(t). \tag{2.2}$$

4. If damage occurred at or near the k^{th} source location, the stacked cross-correlation function given by Equation 2.2 should peak at a value close to unity at the correct time of the structural damage event. In the case of multiple locations of damage, then the stacked cross-correlation functions should each peak at a value close to unity at the corresponding times, provided the correct IRF templates are used. This procedure could be extended to the three-dimensional or discrete case.

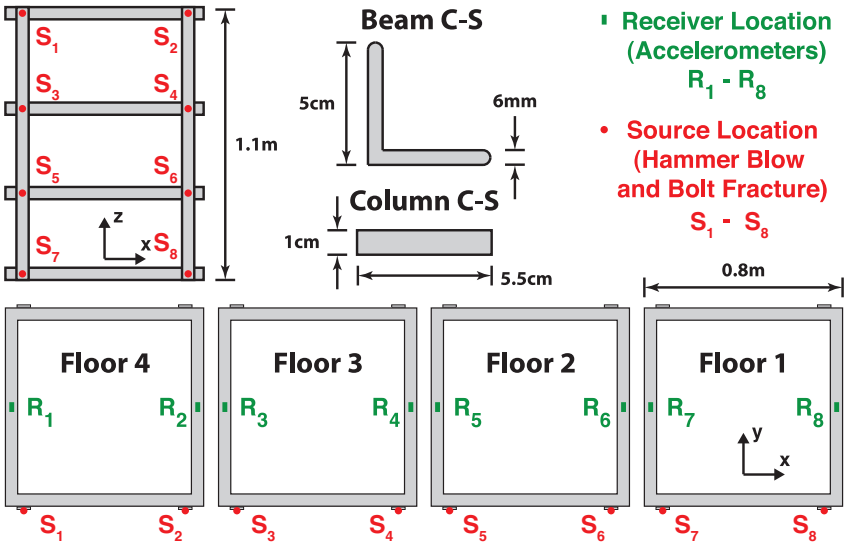

Figure 2.2: **Steel Frame: Receiver Locations.** The steel frame is instrumented with eight accelerometers in a layout that is similar to a instrumentation layout one might expect to find in the vibration monitoring of an actual building. The receivers record acceleration along the y-axis.

2.3 Experimental Study: Small-Scale Steel Frame

To study the feasibility of the proposed method, experimental tests were conducted on the small-scale steel frame shown in Figure 2.1. Three different configurations of damage state and source mechanism were tested: impulsive hammer blow applied to the undamaged frame, bolt fracture, and impulsive hammer blow applied to a frame with a damaged beam-column connection. The similarities and differences between the three cases were analyzed using waveform cross-correlation normalized by the autocorrelation value and stacked over the eight receiver locations. Results were averaged over the total number of trials.

2.3.1 Experimental Setup

A small-scale steel frame instrumented with eight uniaxial (y-axis) accelerometers, shown in Figure 2.1, was subjected to hammer blows and bolt fracture at beam-column connections. A sample frequency of 100 kHz and record duration of 2 seconds were used. The experimental setup included the following equipment (the corresponding specification sheets can be found in the Appendix A):

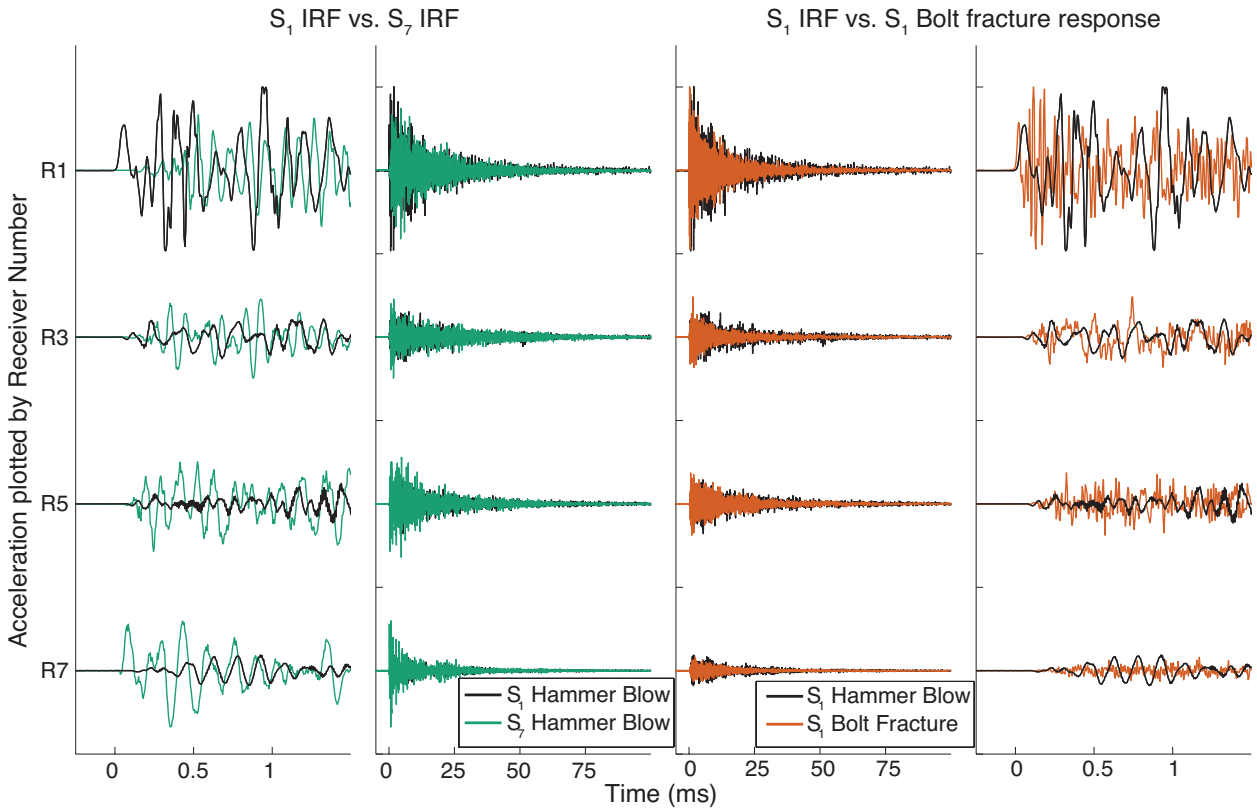

Figure 2.3: **Steel Frame: Example Accelerations.** A comparison of the IRFs for two hammer blows that were applied at different locations (S_1 and S_7) for the undamaged frame is shown on the left. A comparison of a prerecorded IRF with the response of the frame to bolt fracture at the same location (S_1) is plotted on the right. As can be seen from the comparison of IRFs, the arrival times and the relative amplitudes differ significantly between the two records, with the highest amplitudes and first arrivals occurring at the receiver location closest to the source location. As can be seen from the comparison of IRF with the response to colocated damage, the arrival times and the relative amplitudes are similar.

- Small-scale steel frame with a pinned base and bolted beam-column connections.
- High-sensitivity low-mass accelerometers and power supply.
- Force transducer hammer and power supply.
- USB multifunction data acquisition device.
- Laptop for data logging.

2.3.2 Experimental Results and Discussion

IRFs were generated by using a force transducer hammer to apply an impulsive force load along the y-axis to each of the eight beam-column connections (S_1-S_8) shown in Figures 2.1 and 2.2. IRFs were obtained by exciting the frame using a hammer blow and recording the resulting acceleration. Seven trials were repeated at each source location. In order to determine whether these prerecorded IRFs could be used as an approximation to the frames response to structural damage (i.e., a fracture event) at the same source location, bolt fracture was also used to excite the structure in response to a damage event. A notched stainless steel socket cap screw was introduced into a beam-column connection. The screw replaced the bottom bolt shown in Figure 2.1. It was then loaded by torque tightening to the point of failure, and the response of the frame to the fracture was recorded on the eight accelerometers. Three trials were repeated at each of the four source locations S_1, S_3, S_5, and S_7. Finally, a tap test was conducted using the damaged frame; damage was introduced to the frame at a connection by removing all three bolts. These damage IRFs were compared with the pre-recorded IRFs.

As can be seen from the example acceleration time series shown in Figure 2.3, the response of the frame to bolt fracture consists of more high-frequency energy than does the IRF. The relative amplitudes and arrival times of the two responses are observed to be similar when the source is generated at the same location. The relative amplitudes are shown in Figure 2.4. Both the amplitudes and arrival times of the responses could be used for damage localization. The arrival times and amplitudes between IRFs generated by hammer blows applied at different source locations differ significantly.

The maximum amplitude of the stacked cross-correlation record is used as an indicator of how similar two responses are. Cross-correlations were first calculated at each receiver location, using the recorded pair of acceleration time series and autocorrelation normalization, as in Equation 2.1. The cross-correlations were then stacked over all eight receivers, as in Equation 2.2. Example cross-correlations are presented in Figure 2.5, where the cross-correlations of the IRFs generated by an impulsive hammer blow applied at location S_1 is

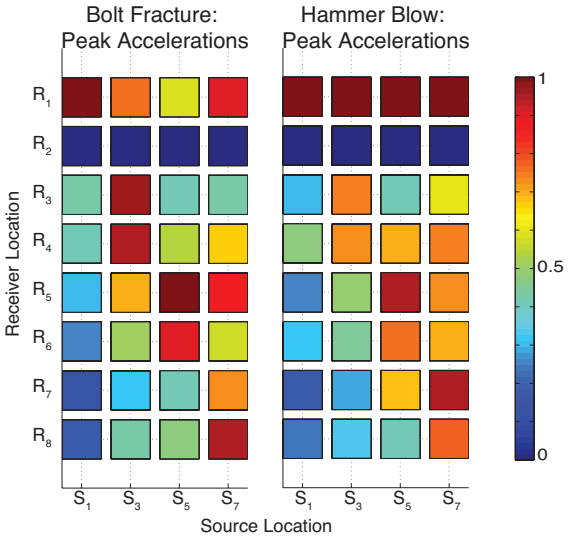

Figure 2.4: **Steel Frame: Comparison of Peak Accelerations in Response to Bolt Fracture and IRFs. a,** The peak acceleration is calculated for a given trial by taking the maximum absolute value of each of the eight acceleration records (at locations R_1-R_8); the eight recorded peak accelerations are then normalized to range between zero and one for each trial. Peak accelerations are averaged over the number of trials and shown above. A total of three trials were conducted at each of the four source locations (S_1, S_3, S_5, S_7). **b,** Similarly, the peak accelerations are computed for the IRFs applied at the same source locations. Again, a total of five trials is averaged for each of the four source locations (S_1, S_3, S_5, S_7). There is general agreement of peak accelerations between the response to the two colocated different source mechanisms. The data recorded at location R_2 were corrupted, and were thus omitted.

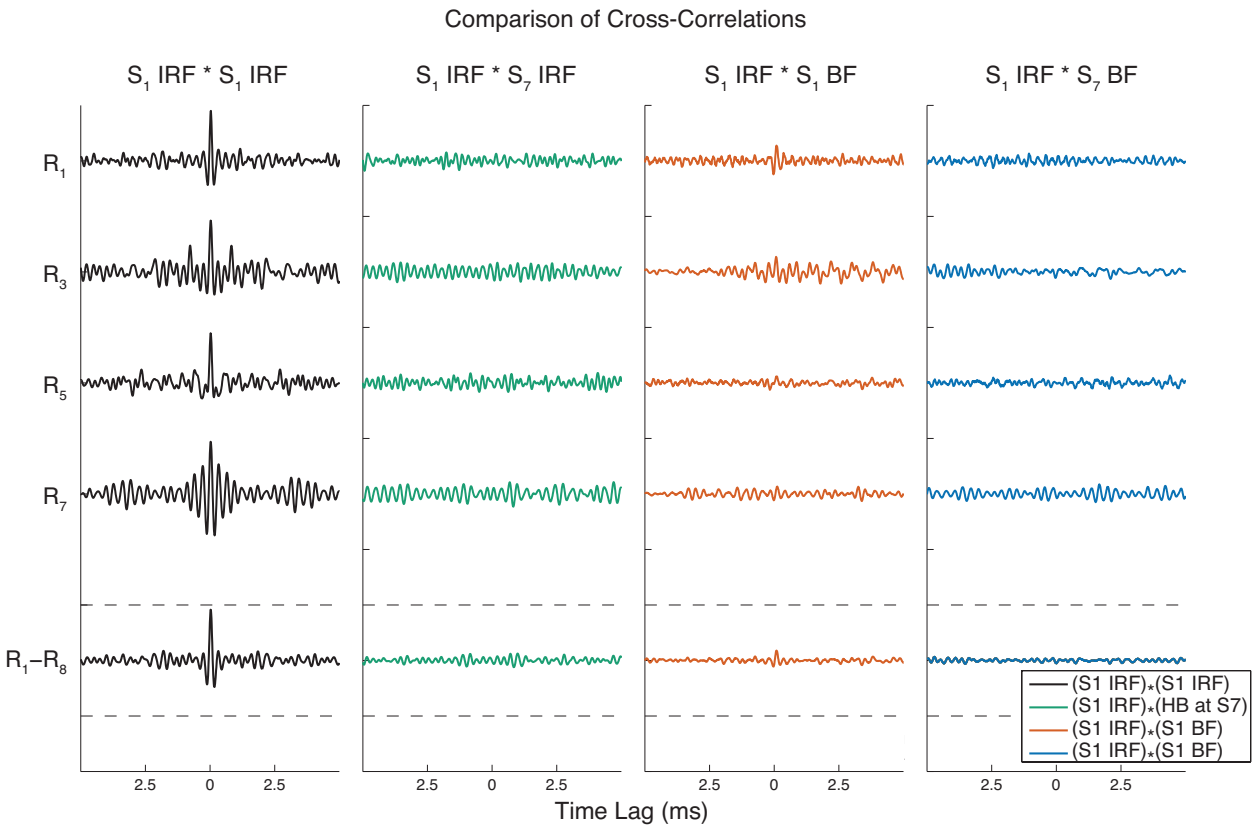

Figure 2.5: **Steel Frame: Example Cross-Correlations.** Example cross-correlations are shown using the impulse response function generated by a hammer blow applied at S_1 with (left) a second impulse response function generated by a hammer blow applied at S_1, (left-middle) the impulse response function generated by a hammer blow applied at S_7, (right-middle) the response of the frame to bolt fracture at location S_1, and (right) the response of the frame to bolt fracture at location S_7. The stacked cross-correlations are plotted on the bottom, with dashed black lines referencing values of 1 and -1. The maximum value of the stacked cross-correlation for each of the four illustrated cases is 0.91, 0.13, 0.18, and 0.07, respectively. Normalized waveform cross-correlations are performed using the entire acceleration time series.

cross-correlated with the following records: 1) a second IRF generated by a hammer blow applied at S_1, 2) an IRF generated by a hammer blow applied at S_7, 3) the response of the frame to bolt fracture at S_1, and 4) the response of the frame to bolt fracture at S_7. The maximum value of the stacked cross-correlation for each of the four illustrated cases is 0.91, 0.13, 0.18, and 0.07, respectively.

To determine the degree of similarity between the IRFs, the cross-correlation of every possible pair was computed and is presented in Table 2.1. The pair of IRFs have a cross-correlation value near to one when their sources are colocated and a value close to zero when

their sources are applied at different locations. The time delay from the cross-correlation is compared to the relative time difference of the hammer blows in Table 2.1, and a high level of precision is observed in determining the moment at which the hammer blow was applied, typically to within 10 μs.

Cross-correlations were also computed between the prerecorded IRFs and the frame's response to bolt fracture. This was done in order to determine the degree of similarity between the two responses. Specifically, the frame's prerecorded IRFs were cross-correlated with the response of the frame to bolt fracture. Each possible pair of bolt failure source location and IRF source location was considered, and the correlation values are presented in Table 2.3. The response of the frame to bolt fracture correlates best with the response of the frame to the colocated hammer blow. However, these correlation values are not close to unity; they range from 0.17 to 0.19. This experimental analysis suggests that the method may not be very robust in the case of damage detection.

Correlation values were improved by weighting the individual cross-correlation records proportionally to the amplitude of the response to bolt failure at each recorded location prior to stacking them. The maximum value of the amplitude of the stacked cross-correlation was determined, and these values are tabulated in Table 2.4. The correlation values along the diagonal range from 0.2 to 0.45. The modified Equation 2.2 is:

$$C^k(t) = \frac{\sum_{i=1}^{R} \max|x_i| C_i^k(t)}{R\left(\sum_{i=1}^{R} \max|x_i|^2\right)^{1/2}}. \tag{2.3}$$

If the envelopes are used instead of the waveforms for cross-correlation, then the terms along the diagonal are close to unity, but so are the off-diagonal terms, albeit only slightly smaller than the diagonal values. This form of cross-correlation would be feasible in the cases with accelerations that have larger differences in arrival times and shorter length of pulses. Other signal processing techniques that were applied in various combinations were not found to significantly improve the correlation values, and they include:

- Filtering - high-pass or low-pass.

- Polarity/phase - using the analytic signal, envelope, or amplitude.
- Shortening the length of the template and adjusting the normalization scheme accordingly.
- Integrating or differentiating the record.
- Recording the maximum value of the amplitude of the stacked cross-correlation.
- Cross-correlating with the IRFs recorded on the damaged frame.
- Creating a template using two IRFs applied in opposite directions.

Correlation values calculated using the responses to bolt fracture, found in Table 2.7, can serve as a rough upper bound estimate for the maximum correlation values one might expect to obtain by using waveform cross-correlation of an IRF with the response to bolt fracture. The correlation values for the response of the frame to colocated bolt fracture range from 0.7 to 0.87. These values demonstrate the surprisingly high level of consistency between the response of the frame to bolt fracture between different trials. This also indicates that, in the case where the damage signal is generated by a repeating source, the initially-detected signal can be used to as a template to detect the next occurrence of the damage signal in the time series.

Finally, IRFs for a damaged frame were obtained by performing a tap test on the frame with a damaged beam-column connection. Damage was introduced by removing all three bolts from a connection (S_1, S_3, S_5, or S_7), with the stiffness of the frame rigidly holding the beam and column in place. An impulsive hammer blow was applied to each of the eight source locations, for each of the four damaged connection cases. This was performed a total of three times. To highlight differences in structural response before and after damage occurred, the prerecorded IRFs were cross-correlated with the response of the damaged frame to an impulsive hammer blow applied at the same source location, for each of the four damaged connection cases. Results were averaged over 15 total trials and are presented in Table 2.6. There are significant differences between the response of the frame before

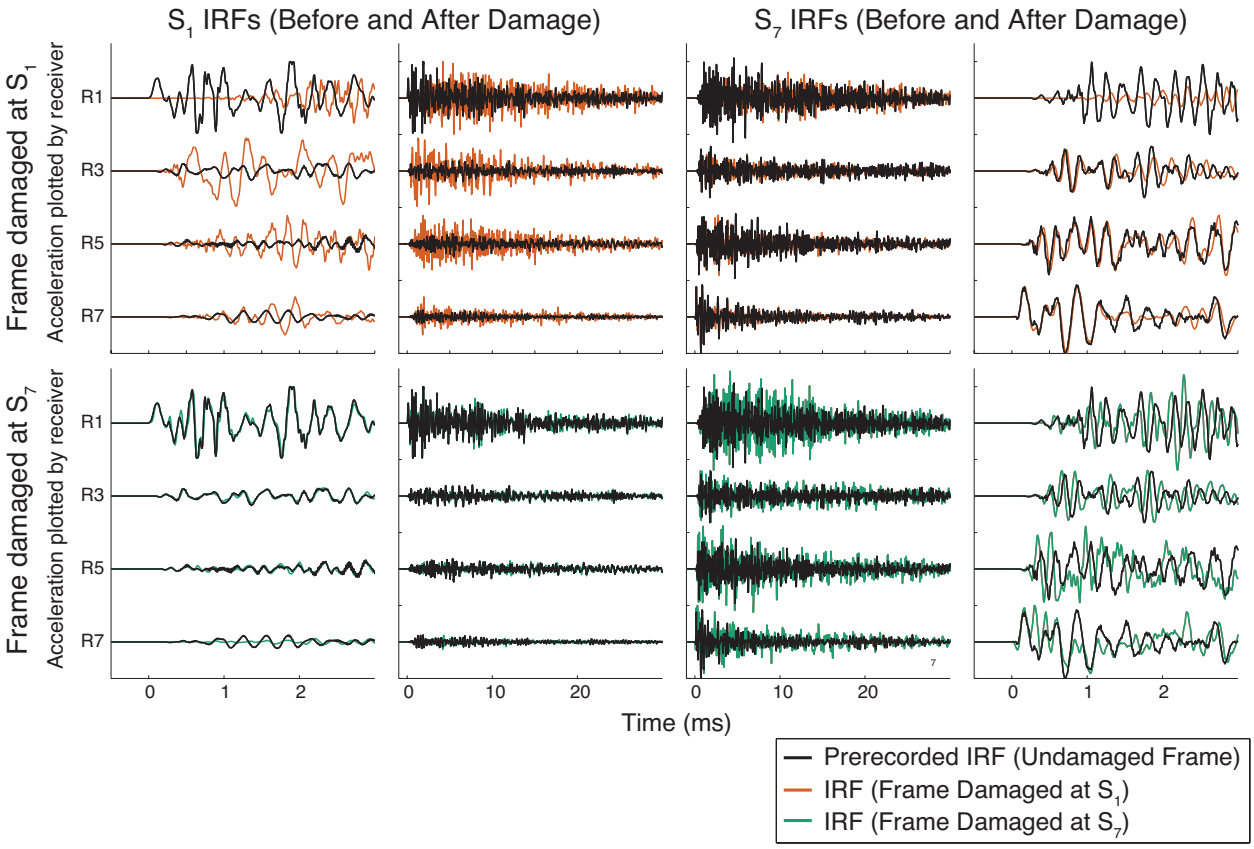

Figure 2.6: **Steel Frame: Comparison of IRFs Before and After Damage.** Prerecorded IRFs are compared with IRFs generated when the frame is in a damaged state. The first two columns plot accelerations generated by a hammer blow applied at location S_1; the second two columns plot accelerations generated from a hammer blow applied at location S_7. The color of the signal indicates the damage state of the frame, with undamaged shown in black, damaged at S_1 shown in orange, and damaged at S_7 shown in green. As can be surmised from the plots in Columns 1 and 4, the initial pulse propagates through the medium undisturbed until it passes through the region of damage. At this point, the response of the damaged frame begins to diverge from the response of the undamaged frame. A high-frequency signal is generated when the hammer blow is applied at the damaged source location, resulting in larger accelerations on all floors. The relative amplitudes of acceleration have been preserved for each trial.

damage was introduced and the response of the frame after damage was introduced, with typical correlation values of 0.5. For comparison, these values range from 0.78-0.85 for the undamaged case. Furthermore, the observed correlation values along the diagonal are much lower than are the values of the off-diagonal terms, and they range from 0.11 to 0.41. This means that the IRF of the damaged frame is observed to differ the most from the pre-recorded IRF when the source is applied at the location of damage. As seen in Figure 2.6, the damaged connection is observed to act as a high-frequency source when the hammer blow is applied to the damaged connection. The high-frequency signal is presumably generated by slight mechanical impact and slippage within the interface between the column and the beam. This relative motion is very small as the frame is very stiff and no motion is detected by visual observation. The fact that the lowest cross-correlation value occurs for damage introduced at the top of the column supports this hypothesis. The column is less stiff at the damaged location than it is in other cases, due to the free boundary at the top floor. The introduction of damage changes the boundary conditions at the damaged connection, as the screws of the undamaged connections tightly secure together the beam and column. The frame is rigid enough that even by removing the bolts from a particular connection, the beam and column are firmly held in place. When damage is introduced to a beam-column connection at one of the lower floors, the stiffness of the column near the damaged connection is relatively large as the column is bolted together with the floors immediately above and below the damaged connection. When damage is introduced to the top floor, the stiffness of the column is not as high, as it is only screwed together with the lower floor and has a free boundary at the top. Hence, it is more flexible and is able to experience larger motions at the beam-column interface. A visual comparison of the different correlation values can be found in Figure 2.7.

2.3.3 Blind Tap Test

A blind tap test was performed to confirm whether the prerecorded IRFs could be used to determine where and when a later hammer blow occurred. A number of tap tests were

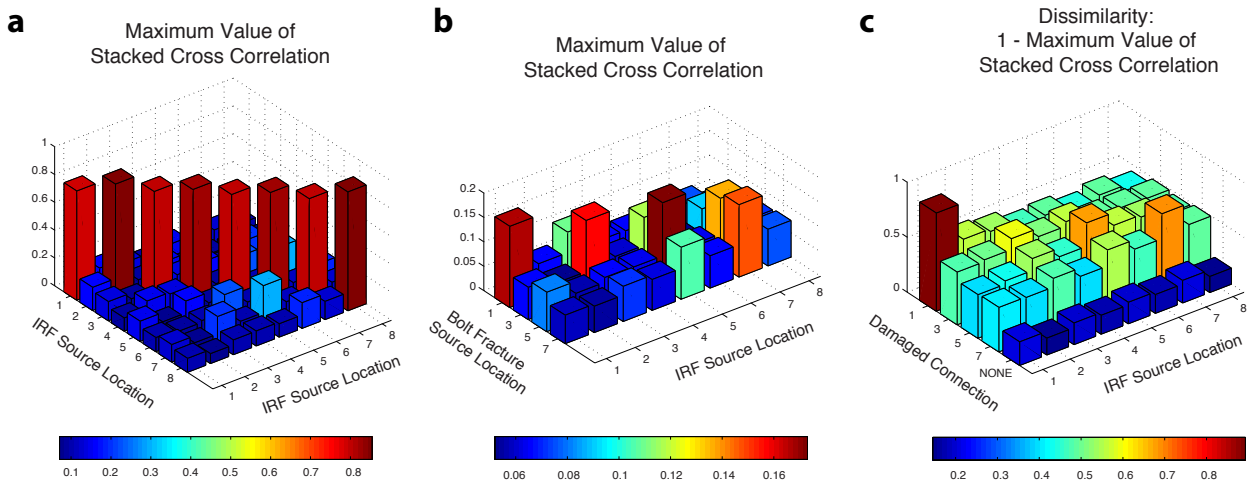

Figure 2.7: **Steel Frame: Comparison of Correlation Values Before, During, and After Damage.** **a,** The correlation values using the IRFs recorded before damage (see Table 2.1) are plotted. There is a high degree of similarity between pairs with colocated sources. **b,** The correlation values generated using the prerecorded IRFs and responses to bolt fracture are much smaller for the values generated using two colocated IRFs (see Table 2.3). Values along the diagonal range between 0.15 and 0.20. These values can be improved to 0.20 and 0.45 if, before stacking, the cross-correlations at a given receiver are scaled proportionally to the amplitude of the peak absolute acceleration recorded at that receiver in the response to bolt failure. **c,** The dissimilarity values (one minus the peak stacked correlation values) using the IRFs recorded before and after damage (see Table 2.6) are plotted. There is a high degree of dissimilarity between pairs with colocated sources, and especially when the source is applied at the damaged location.

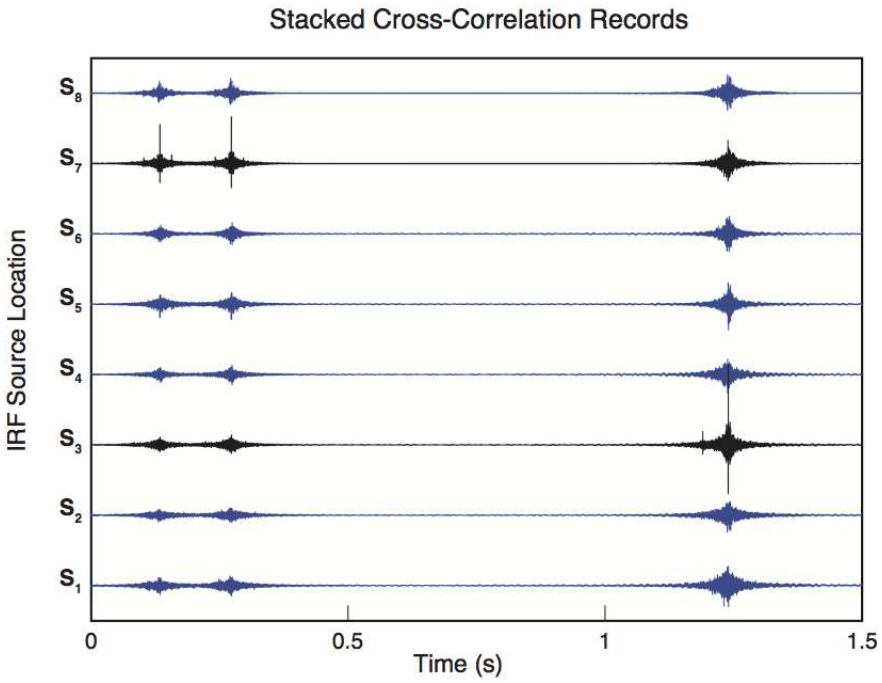

Figure 2.8: **Steel Frame: Blind Tap Test Using Hammer Blows.** A blind tap test is conducted using an acceleration time series containing the response of the frame to three hammer blows applied to unknown locations. A number of tap tests were performed, and one of the tests was selected at random and analyzed. The stacked cross-correlation values, computed using the test data and one of the IRFs, is used to determine where the hammer blow was applied. The actual locations were revealed only after the selection had been made. As can be determined from the stacked correlations shown above, the hammer blows were applied at locations S_7, S_7, and S_3 at times 0.15 s, 0.30 s, and 1.25 s, respectively.

performed, and one of the tests was selected at random and analyzed to see if the source locations could be correctly determined. The blind tap test, shown in Figure 2.8 below, was performed using three hammer blows applied in unknown locations. Stacked cross-correlations between the test data and each IRF (one for each source location) were computed and compared to determine the three locations. Three cross-correlation peaks stand out in the comparison: S_7, S_7, and S_3. The actual locations were revealed after the selection had been made. The determined locations were indeed the three locations used for the blind test.

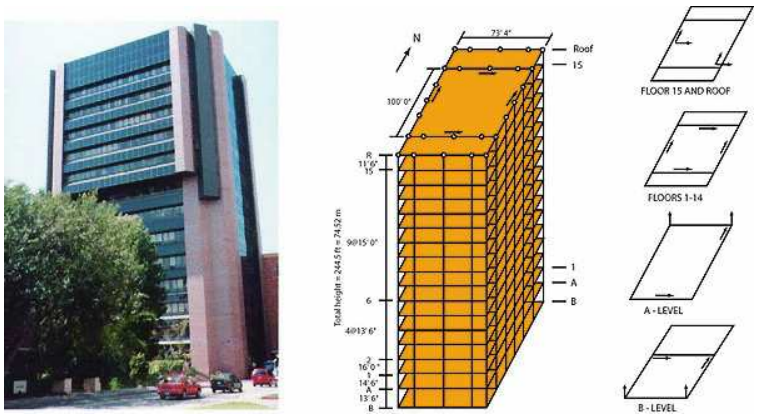

Figure 2.9: **Factor Building: Instrumentation.** A 16-story moment-resisting frame building located at UCLA, the Factor Building is densely instrumented with a 72-channel accelerometer network. Image courtesy of Kohler et al. (2009).

2.4 Experimental Study: Steel Moment-Resisting Frame Building

A 16-story moment-resisting frame building located at UCLA, the Factor Building is densely instrumented with a 72-channel accelerometer network (see Figure 2.9). IRFs were experimentally obtained using a rubber mallet to excite the building at a few locations close to moment-resisting connections. Both 500 sps and 100 sps data was recorded. The IRFs were obtained by recording the acceleration response of the building to hammer blows applied at the following locations:

15^{th} Floor NW: Two hammer blows were applied next to the northwest corner below a major moment-resisting connection.

15^{th} Floor SW: Two hammer blows were applied next to the southeast corner, base of column, below major moment-resisting connection.

3^{rd} Floor: One hammer blow was applied at the stairs.

Each of the five IRFs is clearly observable over the ambient response of the structure, at both 500 sps and downsampled to 100 sps. The IRF generated by applying a hammer blow at the northwest corner of the 15^{th} floor, shown Figure 2.10, has a high signal-to-noise ratio

(SNR) for the acceleration records on the the 3^{rd} floor through the 16^{th} floor stations located on the west side of the building with a northward orientation. The SNR for this record is lower for acceleration records located on the other side of the building, as seen in Figure 2.11. Reasons for this include the distance to the source, and the effectiveness of the beams and columns in transmitting the high-frequency energy generated by the hammer blow to other regions of the building. While the column to which the hammer blow was applied may be efficient at transmitting the high-frequency energy to lower floors on the same side of the building, this does not indicate that the energy will travel well around corners or between structural members.

IRF templates, shown in Figure 2.11, are formed using the recorded accelerations at all floors within a short duration (0.2 seconds) after the hammer blow was applied. The largest amplitude acceleration and first arrival time occurs at the receiver located closest to the source location. To measure the degree of similarity between IRFs, correlation values are calculated. Waveform cross-correlation was performed using templates with a length of 0.2 seconds. Results were stacked and normalized, so that the resulting correlation values range between zero and one. Colocated IRFs have the highest correlation values close to 0.5. These values could be improved by only including signals with a high SNR in the IRF template rather than all existing records, and also by forming the IRF templates by stacking using a few trials conducted at each location. Although the 15 NW IRF and 15 SE IRF were generated by using hammer blows applied at the same floor, the IRFs differ significantly, with a maximum correlation value of 0.10. This means that it is possible to distinguish between locations within a single floor using this method.

2.5 Conclusion

An experimental study was conducted to provide insight into a damage detection method that makes use of a prerecorded catalog of IRF templates and a cross-correlation method to detect the occurrence and location of structural damage in an instrumented building. Impulsive hammer blows and bolt fracture were applied to a small-scale steel frame to test the

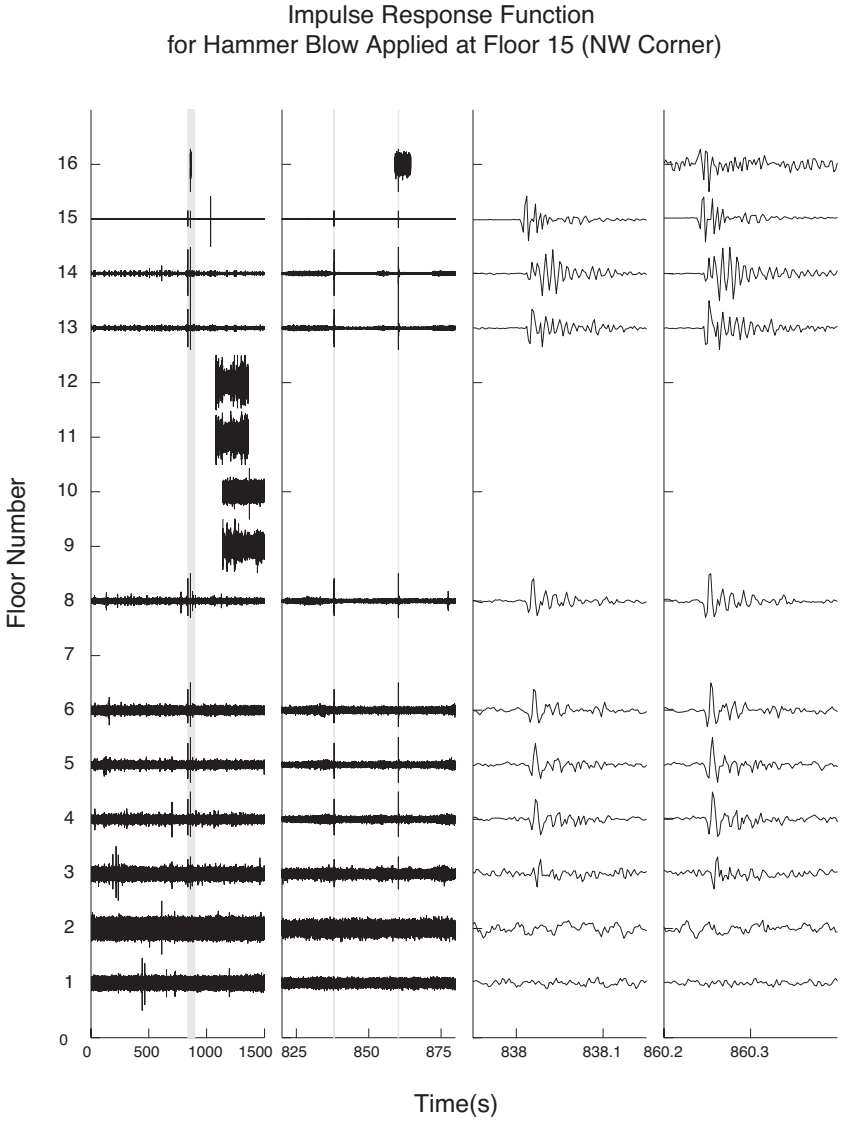

Figure 2.10: **Factor Building: Example IRF.** An IRF was generated using a rubber mallet to apply a hammer blow next to the northwest corner below a major moment-resisting connection. In the first column, 25 minutes of data are shown, with a minute-long segment shaded in gray. This minute-long segment is expanded in the second column, where the two IRFs, highlighted in gray, are clearly observable over the ambient response of the structure. The recorded IRFs of the structure to two hammer blows at this location are plotted for Floors 1-16 using the seismometers located at the west position with an orientation pointing north and recording at 500 sps. There is a high degree of consistency between the two trials, with high signal-to-noise ratios from the 3^{rd} floor through the 16^{th} floor. Each acceleration record was normalized to better view the waveform, and the relative amplitudes were not preserved. Some of the sensors were not recording at the time of testing, and those records are missing from the figure.

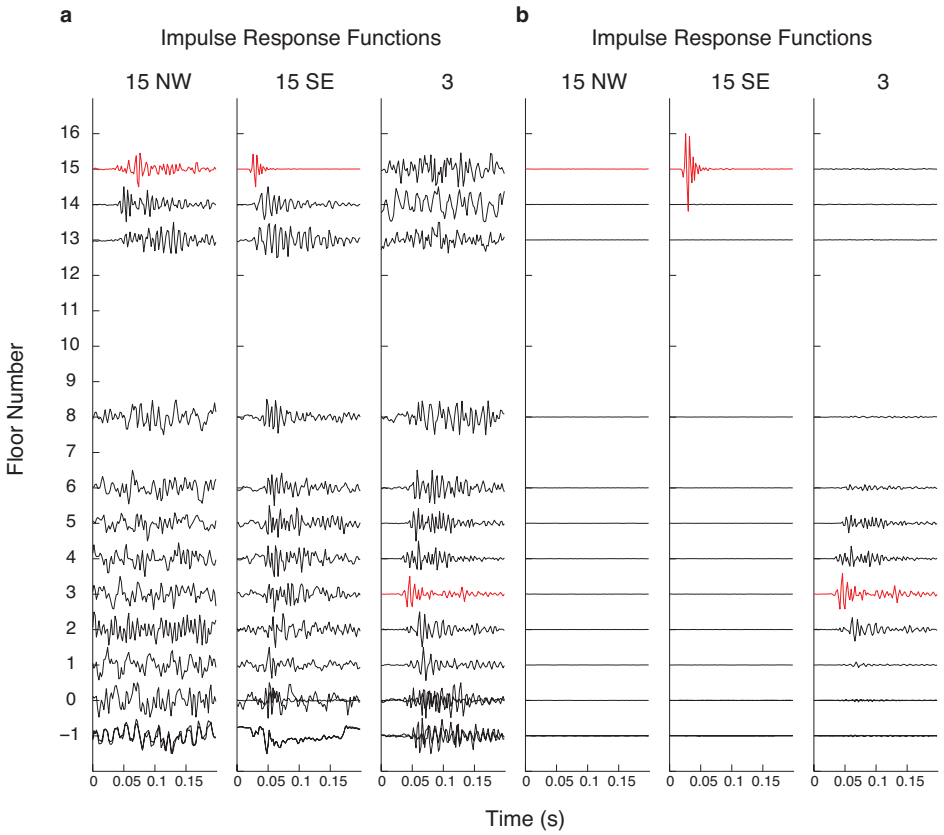

Figure 2.11: **Factor Building: Comparison of Impulse Response Functions.** Impulse response functions were experimentally obtained for a steel-moment-resisting frame building *in situ* by applying a hammer blow near to a moment-resisting-beam-column connection using a rubber mallet. Both 100 sps and 500 sps data were recorded, and the IRF is clearly visible in both cases; the 500 sps data is plotted above. A high signal-to-noise ratio (SNR) is obtained for stations located close to the hammer blow on the same side of the building. The stations shown above are located on the south side of the building and oriented eastward. The SNR could be improved by stacking the IRFs. There is a clear difference in arrival times and amplitudes between IRFs generated by hammer blows applied at different source locations. In **a**, each record has been normalized to better view the waveforms. In **b**, the set of acceleration records generated by a hammer blow have been normalized using the same value, so that the relative amplitudes have been preserved. The largest amplitudes are recorded on the closest seismometers to the hammer blow, on the same floor. The station on the same floor to which the hammer blow was applied is highlighted in red.

feasibility of applying the method to a building. The similarity between structure responses was evaluated using a cross-correlation method. The main findings of this chapter are:

1. IRFs were successfully obtained for an existing steel moment-resisting-frame building *in situ*. Not only were the IRFs clearly observable over ambient noise, the waveforms were also very consistent between trials with colocated sources, with correlation values typically greater than 0.8. For IRFs generated by hammer blows at different locations, significant differences were observed in arrival times, peak accelerations, and waveforms using eight accelerometers recording at 100 kHz. The data supports the idea of using hammer blow data to localize damage to a single column within a story. A sampling rate of 100 sps, though preferably 500 sps, seems to be high enough to capture the IRFs in the Factor building.

2. The application of the proposed damage detection method to the small-scale frame suggests that the IRF is not a robust approximation of the response to bolt failure. The method may also be suitable for damage localization, especially if it is combined with information about the arrival times and peak accelerations. While the IRFs cross-correlated well with each other and the responses to bolt fracture cross-correlated well with each other when the sources were colocated, the IRFs and responses to bolt fracture did not. However, in all considered cases, the IRF that had the highest correlation value with the response of the frame to bolt failure was the colocated IRF. Improvements in the correlation values were made by using an amplitude-dependent normalization that scaled with the maximum amplitude of acceleration at each receiver in response to bolt fracture. Information, such as arrival times and peak accelerations, can also be indicators of where damage occurred; this is of significance for sparsely-instrumented structures.

3. The response of the frame to bolt fracture was observed to be surprisingly consistent between trials (correlation values of 0.70-0.85 for responses with colocated sources). This suggests that the mechanism that occurs at the moment of bolt failure is consistent between trials, and a hammer blow does not well-characterize this source. This also

implicates that if a building were to undergo damage that resulted in the creation of a repeating source, a repeating high-frequency, short-duration signal might be observed in the acceleration time series. This could be generated by damage cases such as in the case of a breathing crack that repeatedly opens and closes, or a change in boundary conditions that increases the flexibility of a member and allows for the excitation of traveling waves.

4. The pre-recorded IRFs differed significantly from the IRFs that were recorded when the frame was in a damaged state, with typical cross-correlation values of 0.5, as compared to pre-damage values of 0.8. By comparing the generation of waves propagating through the frame, it was seen that the response of the damaged structure to a hammer blow applied at a given location begins to diverge from the response of the undamaged structure only after the elastic waves recorded at a given receiver location passed through the region of damage. This phenomenon is similar to the guided wave methods used in acoustic damage detection methods, and it also has potential to be used for damage detection in larger-scale structures. It would be necessary to use a repeatable mechanism to excite the structure over time, preferably under similar environmental conditions, and differences between the baseline signal and the subsequent recorded signal would be used to indicate damage. Damage might be located through an inverse problem approach that makes use of a finite-element model.

5. The application of a hammer blow to a damaged connection resulted in a low correlation value with the pre-recorded IRF generated by a colocated hammer blow. In this case, the damaged connection was observed to also act as a high-frequency source, most likely due to motion generated at the interface of the beam and column. Applying a hammer blow to a cracked beam or column in a real building may or may not result in high-frequency energy generated at the crack interface. Presumably, if a beam has a crack and the two sides of the crack are not held firmly together, e.g., a vertical crack in a beam, a hammer blow applied in the vicinity of the crack could result in mechanical slippage and impact caused by the relative motion at the crack interface. If, on the

other hand, the crack is firmly held closed, as might be the case for a horizontal crack in a column, high-frequency energy might not be generated at the crack interface in response to a nearby hammer blow.

6. As the responses to bolt fracture correlated just as well with pre-recorded IRFs as they did with the post-damage IRFs, it may be desirable to record the IRFs after an earthquake has occurred, when the building is in a potentially damaged state. In this way, there is an additional chance of detecting any high-frequency energy that is generated within a cracked interface at a damaged connection. (Also, if the building is never subjected to a large earthquake, there will be no need to conduct the hammer blow trials in the first place.) One advantage of having previously-recorded IRFs, however, is that they can be directly compared with post-earthquake IRFs, in order to detect damage in the frame by differences between them.

IRF: Hammer Blow Source Location			IRF: Hammer Blow Source Location							
			S_1	S_2	S_3	S_4	S_5	S_6	S_7	S_8
S_1	μ		**0.85**	0.22	0.12	0.10	0.12	0.09	0.09	0.10
	σ		**0.06**	0.01	0.02	0.01	0.01	0.01	0.01	0.01
	N		**21**	49	49	49	49	49	49	49
S_2	μ		0.22	**0.83**	0.10	0.12	0.10	0.10	0.10	0.09
	σ		0.01	**0.06**	0.01	0.03	0.01	0.01	0.01	0.01
	N		49	**21**	49	49	49	49	49	49
S_3	μ		0.12	0.10	**0.86**	0.12	0.19	0.12	0.19	0.12
	σ		0.02	0.01	**0.05**	0.01	0.01	0.01	0.01	0.01
	N		49	49	**21**	49	49	49	49	49
S_4	μ		0.10	0.12	0.12	**0.83**	0.09	0.18	0.11	0.15
	σ		0.01	0.03	0.01	**0.05**	0.01	0.02	0.01	0.02
	N		49	49	49	**21**	49	49	49	49
S_5	μ		0.12	0.10	0.19	0.09	**0.82**	0.11	0.17	0.14
	σ		0.01	0.01	0.01	0.01	**0.05**	0.01	0.03	0.01
	N		49	49	49	49	**21**	49	49	49
S_6	μ		0.09	0.10	0.12	0.18	0.11	**0.78**	0.13	0.16
	σ		0.01	0.01	0.01	0.02	0.01	**0.06**	0.01	0.04
	N		49	49	49	49	49	**21**	49	49
S_7	μ		0.09	0.10	0.19	0.11	0.17	0.13	**0.80**	0.18
	σ		0.01	0.01	0.01	0.01	0.03	0.01	**0.06**	0.02
	N		49	49	49	49	49	49	**21**	49
S_8	μ		0.10	0.09	0.12	0.15	0.14	0.16	0.18	**0.80**
	σ		0.01	0.01	0.01	0.02	0.01	0.04	0.02	**0.04**
	N		49	49	49	49	49	49	49	**21**

Table 2.1: **Steel Frame: Correlation Values (Undamaged Frame IRFs).** IRFs were generated by using a force transducer hammer to apply an impulsive force load along the y-axis to each of the eight beam-column connections (S_1-S_8). The correlation values are close to unity when the IRFs are colocated. A total of seven hammer blows were delivered at each source location. Cross-correlations were first calculated at each receiver location, using the two different records and autocorrelation normalization. The cross-correlations were then stacked over all eight receivers. The maximum amplitude of the stacked cross-correlation is recorded, averaged over the total number of pairs (21 total for pairs consisting of two identical source locations and 49 total for pairs consisting of two distinct source locations), and presented above. Waveform cross-correlation was performed using the entire record. Values calculated using responses with colocated sources are highlighted in bold.

IRF: Hammer Blow Source Location		IRF: Hammer Blow Source Location							
		S_1	S_2	S_3	S_4	S_5	S_6	S_7	S_8
S_1	μ_t	**-7**	1370	-1900	2500	-620	-840	2600	470
	σ_t	**15**	15	2300	930	840	2700	5900	2200
	N	**21**	49	49	49	49	49	49	49
S_2	μ_t	1370	**5**	-2100	2500	-2100	-1600	-2100	900
	σ_t	15	**17**	1800	3900	2400	5400	1600	5800
	N	49	**21**	49	49	49	49	49	49
S_3	μ_t	-1900	-2100	**-20**	-1200	190	-40	600	-2000
	σ_t	2300	1800	**33**	2000	250	2100	30	1900
	N	49	49	**21**	49	49	49	49	49
S_4	μ_t	2500	2500	-1200	**14**	-140	330	-830	420
	σ_t	930	3900	2000	**24**	2700	27	2000	58
	N	49	49	49	**21**	49	49	49	49
S_5	μ_t	-620	-2100	190	-140	**4**	950	280	-2300
	σ_t	840	2400	250	2700	**23**	2700	69	1100
	N	49	49	49	49	**21**	49	49	49
S_6	μ_t	-840	-1600	-40	330	950	**-3**	1300	520
	σ_t	2700	5400	2100	27	2700	**25**	890	760
	N	49	49	49	49	49	**21**	49	49
S_7	μ_t	2600	-2100	600	-830	280	1300	**-1**	1400
	σ_t	5900	1600	30	2000	69	890	**23**	332
	N	49	49	49	49	49	49	**21**	49
S_8	μ_t	470	900	-2000	420	-2300	520	1400	**7**
	σ_t	2200	5800	1900	58	1100	760	332	**12**
	N	49	49	49	49	49	49	49	**21**

Table 2.2: **Steel Frame: Time Errors in Correlations (Undamaged Frame IRFs).** The accompanying time error (in units μs) from the previous table's cross-correlation values are presented above. The time error is computed as the difference between the time lag of the stacked cross-correlation and the difference in times at which the force was applied, as measured by the force transducer hammer. A very small time error, typically less than 10 μs, is observed. Values calculated using responses with colocated sources are highlighted in bold.

Bolt Fracture Source Location			IRF: Hammer Blow Source Location							
			S_1	S_2	S_3	S_4	S_5	S_6	S_7	S_8
S_1		μ	**0.19**	0.08	0.13	0.08	0.08	0.07	0.09	0.06
		σ	**0.05**	0.09	0.01	0.01	0.07	0.01	0.01	0.01
		N	**15**	15	15	15	15	15	15	15
S_3		μ	0.08	0.06	**0.18**	0.07	0.14	0.06	0.10	0.06
		σ	0.01	0.01	**0.02**	0.01	0.01	0.01	0.01	0.01
		N	15	15	**15**	15	15	15	15	15
S_5		μ	0.09	0.07	0.08	0.07	**0.19**	0.07	0.16	0.08
		σ	0.01	0.00	0.01	0.01	**0.03**	0.01	0.02	0.01
		N	15	15	15	15	**15**	15	15	15
S_7		μ	0.07	0.06	0.08	0.07	0.13	0.08	**0.17**	0.08
		σ	0.01	0.00	0.01	0.01	0.03	0.01	**0.03**	0.01
		N	15	15	15	15	15	15	**15**	15

Table 2.3: **Steel Frame: Correlation Values (IRFs and Response to Bolt Fracture).** IRFs were generated by using a force transducer hammer to apply an impulsive force load along the y-axis to each of the eight beam-column connections (S_1-S_8). A total of five hammer blows were delivered at each source location. Damage was introduced through bolt fracture at one of the connections (S_1,S_3,S_5,S_7). Three trials were repeated for each source location. Cross-correlations were first calculated at each receiver location, using the two different records and autocorrelation normalization. The cross-correlations were then stacked over all eight receivers. The maximum amplitude of the stacked cross-correlation is recorded, averaged over the total number of pairs. Waveform cross-correlation was performed using the entire record. Values calculated using responses with colocated sources are highlighted in bold.

Bolt Fracture Source Location			IRF: Hammer Blow Source Location							
			S_1	S_2	S_3	S_4	S_5	S_6	S_7	S_8
		μ	**0.45**	0.18	0.35	0.17	0.20	0.16	0.23	0.16
	S_1	σ	**0.07**	0.03	0.02	0.02	0.03	0.02	0.03	0.01
		N	**15**	15	15	15	15	15	15	15
		μ	0.13	0.11	**0.30**	0.11	0.22	0.10	0.17	0.10
	S_3	σ	0.02	0.02	**0.05**	0.02	0.03	0.02	0.02	0.01
		N	15	15	**15**	15	15	15	15	15
		μ	0.11	0.08	0.08	0.09	**0.25**	0.10	0.25	0.10
	S_5	σ	0.02	0.01	0.02	0.02	**0.06**	0.02	0.05	0.02
		N	15	15	15	15	**15**	15	15	15
		μ	0.05	0.05	0.07	0.06	0.09	0.06	**0.20**	0.09
	S_7	σ	0.01	0.01	0.02	0.01	0.03	0.01	**0.06**	0.02
		N	15	15	15	15	15	15	**15**	15

Table 2.4: **Steel Frame: Correlation Values Using Peak Acceleration Normalization (IRFs and Response to Bolt Fracture).** IRFs were generated by using a force transducer hammer to apply an impulsive force load along the y-axis to each of the eight beam-column connections (S_1-S_8). A total of five hammer blows were delivered at each source location. Damage was introduced through bolt fracture at one of the connections (S_1,S_3,S_5,S_7). Three trials were repeated for each source location. Cross-correlations were first calculated at each receiver location, using the two different records and autocorrelation normalization. The cross-correlation computed using the records at a given receiver was further scaled by the peak amplitude of the acceleration recorded at that receiver, given by Equation 2.3. The maximum amplitude of the stacked cross-correlation is recorded, averaged over the total number of pairs, and divided by the square root of the sum of the squared peak amplitudes. Waveform cross-correlation was performed using the entire record. Values calculated using responses with colocated sources are highlighted in bold.

Bolt Fracture Source Location			Bolt Fracture Source Location			
			S_1	S_3	S_5	S_7
S_1		μ	**070**	0.10	0.08	0.09
		σ	**0.02**	0.01	0.01	0.01
		N	**3**	9	9	9
S_3		μ	0.10	**0.83**	0.08	0.08
		σ	0.01	**0.06**	0.01	0.01
		N	9	**3**	9	9
S_5		μ	0.08	0.08	**0.87**	0.11
		σ	0.01	0.01	**0.03**	0.01
		N	9	9	**3**	9
S_7		μ	0.09	0.08	0.11	**0.85**
		σ	0.01	0.01	0.01	**0.05**
		N	9	9	9	**3**

Table 2.5: **Steel Frame: Correlation Values (Response to Bolt Fracture).** Damage was introduced through bolt fracture at one of the connections (S_1,S_3,S_5,S_7). Three trials were repeated for each source location. Cross-correlations were first calculated at each receiver location, using the two different records and autocorrelation normalization. The cross-correlations were then stacked over all eight receivers. The maximum amplitude of the stacked cross-correlation is recorded, averaged over the total number of pairs. Waveform cross-correlation was performed using the entire record. Values calculated using responses with colocated sources are highlighted in bold.

Damaged Location		IRF: Hammer Blow Source Location							
		S_1	S_2	S_3	S_4	S_5	S_6	S_7	S_8
–	μ	**0.78**	0.85	0.80	0.83	0.81	0.83	0.80	0.85
	σ	**0.05**	0.09	0.01	0.01	0.07	0.01	0.01	0.01
	N	**15**	15	15	15	15	15	15	15
S_1	μ	**0.11**	0.44	0.46	0.53	0.51	0.56	0.51	0.56
	σ	**0.05**	0.09	0.01	0.01	0.07	0.01	0.01	0.01
	N	**15**	15	15	15	15	15	15	15
S_3	μ	0.52	0.50	**0.41**	0.48	0.44	0.51	0.51	0.51
	σ	0.01	0.01	**0.02**	0.01	0.01	0.01	0.01	0.01
	N	**15**	15	15	15	15	15	15	15
S_5	μ	0.60	0.57	0.46	0.54	**0.33**	0.45	0.47	0.53
	σ	0.01	0.00	0.01	0.01	**0.03**	0.01	0.02	0.01
	N	**15**	15	15	15	15	15	15	15
S_7	μ	0.60	0.60	0.52	0.60	0.45	0.54	**0.31**	0.50
	σ	0.01	0.00	0.01	0.01	0.03	0.01	**0.03**	0.01
	N	**15**	15	15	15	15	15	15	15

Table 2.6: **Steel Frame: Correlation Values (IRFs Before and After Damage)** IRFs were generated by using a force transducer hammer to apply an impulsive force load along the y-axis to each of the eight beam-column connections (S_1-S_8). A total of five hammer blows were delivered at each source location. IRFs for a damaged frame were obtained by performing a tap test on the frame with a damaged beam-column connection. Damage was introduced by removing all three bolts from the connection (S_1, S_3, S_5, or S_7), with the stiffness of the frame rigidly holding the beam and column in place. An impulsive hammer blow was applied to each of the eight source locations, for each of the four damaged connection cases. This was performed a total of three times. The prerecorded IRFs were cross-correlated with the response of the damaged frame to an impulsive hammer blow applied at the same source location, for each of the four damaged connection cases. Results were averaged over 15 total trials. Waveform cross-correlation was performed using the entire record. Values calculated using responses with colocated sources are highlighted in bold.

	Hammer Blow Source Location				
	15 NW (I)	15 NW (II)	15 SE (I)	15 SE (II)	3
15 NW (I)	-	**0.51**	0.10	0.08	0.04
15 NW (II)	**0.51**	-	0.10	0.09	0.05
15 SE (I)	0.10	0.10	-	**0.46**	0.06
15 SE (II)	0.08	0.09	**0.46**	-	0.05
3	0.04	0.05	0.06	0.05	-

Table 2.7: **Steel Moment-Resisting Frame Building: Correlation values (IRFs).** A hammer blow was applied at one of three locations (near a moment-connection at the northwest corner of the 15th floor, near a moment-connection at the southeast corner, and on the third floor stairwell). Waveform cross-correlation was performed using templates with a length of 0.2 seconds. Results were stacked and normalized, so that the resulting correlation values ranged between zero and one. Colocated IRFs have the highest correlation values. The highest correlation value between the 15 NW IRFs and the 15 SE IRFs is 0.10, which is quite low considering that the IRF sources are located on the same floor. This means that it is possible to distinguish between locations within a single floor using this method. The diagonal values in the table above have been omitted, for the same source, they are all equal to one. These results could be improved if only signals with a high signal-to-noise ratio are computed in the template, or if the template is formed by stacking over multiple trials. Values calculated using responses with colocated sources are highlighted in bold.

Chapter 3

Experimental Shear Beam

By studying the effects of damage on the dynamic behavior of small-scale structures, one can form a better understanding of the effects of damage on actual buildings, thus aiding in the development of damage detection methods for large-scale structures. To this end, the effect of damage on the dynamic response of a civil structure is investigated experimentally using a small-scale (0.75 meter tall) shear beam. Damage is introduced into the shear beam by loosening the bolts connecting the columns to the floor, and a shake table is used to apply a consistent pulse at the base of the beam. The structural response is analyzed in both the time and frequency domains. The introduction of damage results in predictable changes in vertical shear wave propagation within the beam, as well as the surprising presence of repeating short-duration high-frequency signals that are presumably due to mechanical slippage and impact at the damaged floor.

The shear beam used in this study does not serve as a representative small-scale version of a real building, but rather serves as a mechanical system to which a damage detection method can be applied for establishing proof of concept. In fact, the shear beam used in this study is much stiffer than a typical full-scale five-story building. In tall buildings, a phenomenon known as the P-Δ effect can occur when the building undergoes a significant amount of lateral displacement, while considering the effects of gravity. The lateral movement of a story mass to a deformed position generates second-order overturning moments that are equal to the sum of the story weights P times the lateral displacements Δ (Wilson, 2004). The contribution to moment from the lateral force is equal to the force times the story height.

Such a phenomenon cannot occur in the test specimen.

It is also worth mentioning that various sampling rates were used in the experiments, depending on the objectives. When the experimental objective is to determine the modal characteristics of the system, a lower sampling rate is used to record a longer segment of data. When the objective is to capture the high-frequency signals emitted by the damage events, a higher sampling rate, typically of 1 or 5 ksps but sometimes as high as 150 ksps, is used at the expense of recording a shorter segment of data. This is analogous to the strategy used in the continuous vibration monitoring of actual structures. Typically a lower sampling rate is used during ambient loading conditions, and a higher sampling rate is used in the event of an earthquake. As we will see in later chapters from the analysis of data recorded in existing full-scale structures *in situ*, a sampling rate of 100 sps seems to be high enough to detect high-frequency signals originating from structural damage events. For the structure used in this chapter, 'high-frequency' seismograms refers to signals of frequencies above 25 Hz, the fifth modal frequency of the structure.

3.1 Experimental Setup and Method

The five-story aluminum structure is fixed at its base to a shake table, as shown in the experimental setup in Figure 3.1. A high-sensitivity low-mass piezoelectric accelerometer is attached at each floor. Each accelerometer is connected to a data acquisition system and data logger (laptop computer). A list of the equipment and their specification sheets can be found in the Appendix. The dimensions of the structure can be found in Figure 3.2.

The shake table is used to supply a consistent pulse at the base of the shear beam that excites the structure over a broad range of frequencies. By using a repeatable source, differences in the dynamic response of the structure between trials due to differences in the source are minimized, and the effect of damage on the dynamic response of the structure can be more readily analyzed. As is apparent from Figure 3.3, the modal response of the structure is highly consistent between trials, though the introduction of damage results in the presence of transient signals that generally originate at the damaged floor. These transient

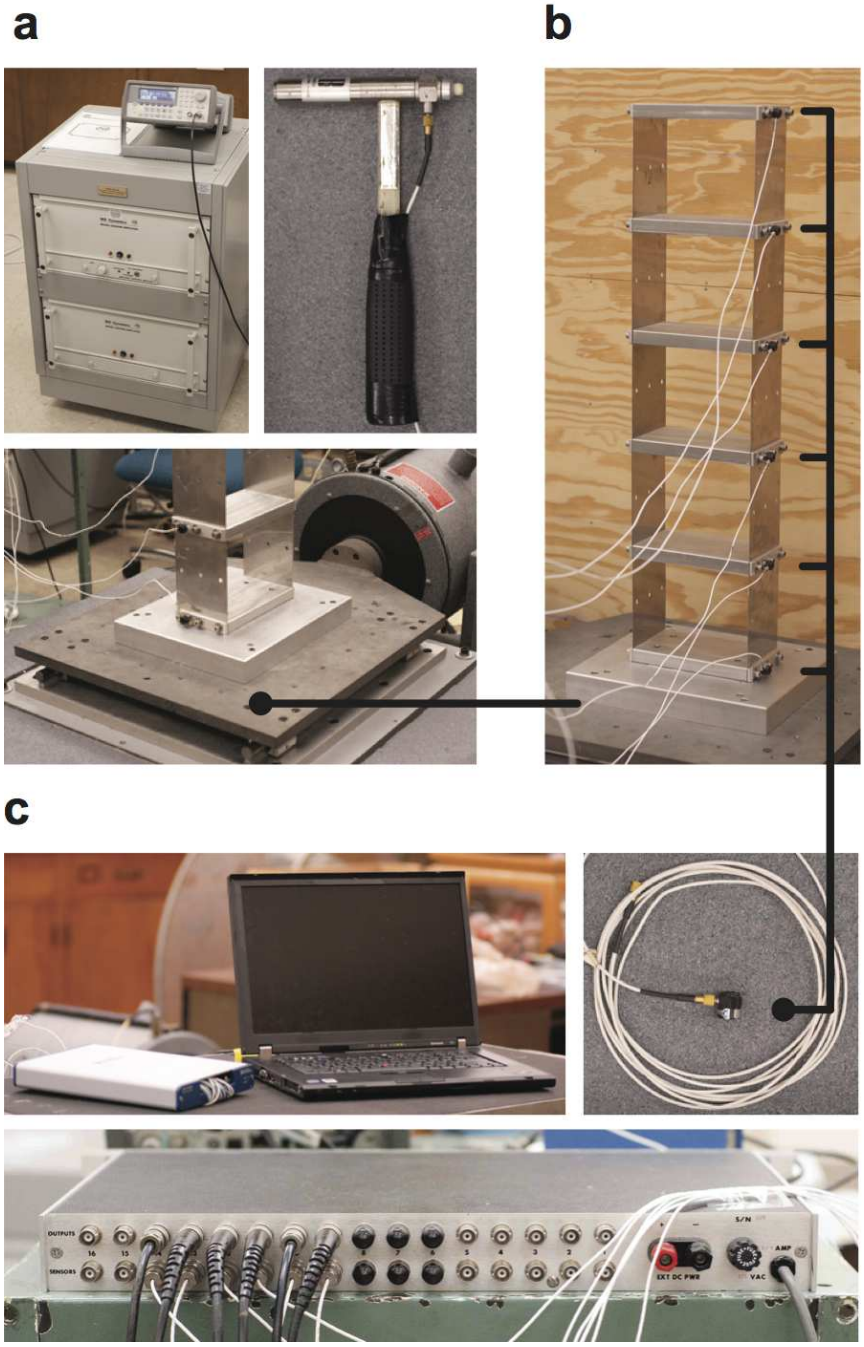

Figure 3.1: **Uniform Shear Beam Experimental Setup. a,** Input sources include an impulse hammer and a shake table. A signal generator and power amplifier are used in conjunction with the shake table to supply a consistent pulse at the base of the shear beam. **b,** The aluminum shear beam is firmly attached at its base to a shake table and is instrumented via an accelerometer attached to each of the five floors as well as the base. **c,** The low-mass piezoelectric accelerometers are connected to a power supply and signal conditioner, and a data acquisition device and laptop are used to record and store the data.

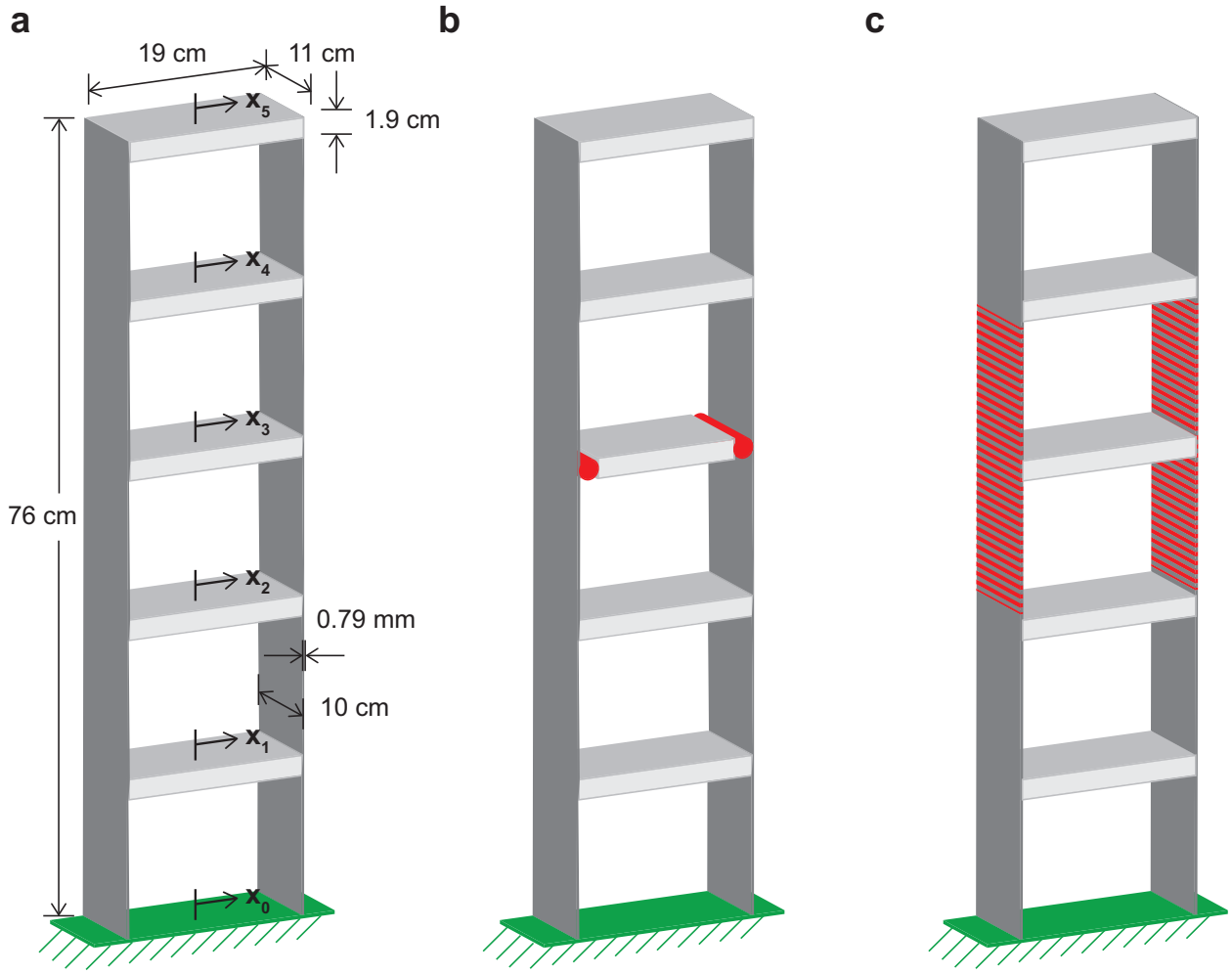

Figure 3.2: **Uniform Shear Beam Models. a,** The shear beam consists of two columns and six masses. Each column is constructed from five rectangular aluminum plates that are firmly connected to each floor by three screws per column. The masses are solid rectangular prisms. The shear beam is firmly screwed into a shake table. The bottom mass is screwed into the shake table platform, and thus is not accounted for in the five-degree-of-freedom model. Damage is introduced by loosening the screws connecting the columns to a floor mass. To model damage, two different frameworks are considered: damage to the connection and damage to the columns. **b,** In Damage Model I, the undamaged moment connection is replaced by a semi-rigid connection. **c,** In Damage Model II, the undamaged columns above and below the damaged floor are replaced by columns with reduced stiffness. In Damage Levels 1, 2, and 3, damage is introduced to the shear beam by incrementally loosening the 6 screws attaching the 2 columns to one of the five floors. Damage Level 1, 2, and 3 corresponds to a 1/6, 2/6, and 3/6 turn of each screw at the damaged floor, respectively. The amount of space created by loosening the screws is very small. The length of the gap created on one side is equal to 0.21 mm (0.0083”), 0.42 mm (0.017”), and 0.64 mm (0.025”) for Damage Levels 1, 2, and 3, respectively.

signals are clearly observed over the modal response of the structure, and are presumably caused by mechanical slippage and impact at the loosened connections.

Structural damage is introduced into the shear beam by loosening the six screws attaching the two vertical the columns to a floor, shown in Figure 3.2, have been loosened. Three levels of damage are created by incrementally loosening the screws at the damaged floor. Damage levels one, two, and three correspond to a rotation of each screw by 1/6 turns (60°), 2/6 turns (120°), and 3/6 turns (180°), respectively. The type of screw used is a 1/4-20 screw, which has 20 turns in one inch. The amount of space created by loosening the screws is very small. The length of the gap created on one side is equal to 0.21 mm (0.0083"), 0.42 mm (0.017"), and 0.64 mm (0.025") for Damage Levels 1, 2, and 3, respectively. By introducing damage incrementally, it is possible to study changes in the behavior of the small-scale structure for a progression of damage.

3.2 Theoretical Model: Linear Multi-Degree of Freedom System

The frame is modeled as a linear, uniaxial, five-degree of freedom system. Each floor in the model is constrained to displace along the horizontal x-axis; the vertical displacement and rotation of each floor is neglected. Masses are lumped at each floor and accounted for in the M matrix, columns contribute to the K matrix via their lateral stiffness, and either proportional or modal damping C is considered. The differential equations of motion for the model are given by:

$$M\ddot{x}(t) + C\dot{x}(t) + Kx(t) = f(t). \tag{3.1}$$

Let the displacement at the n^{th} floor be denoted by $x_n(t)$, the displacement at the ground be denoted by $x_0(t)$, and the external force applied to the n^{th} floor be denoted by $f_n(t)$. Then

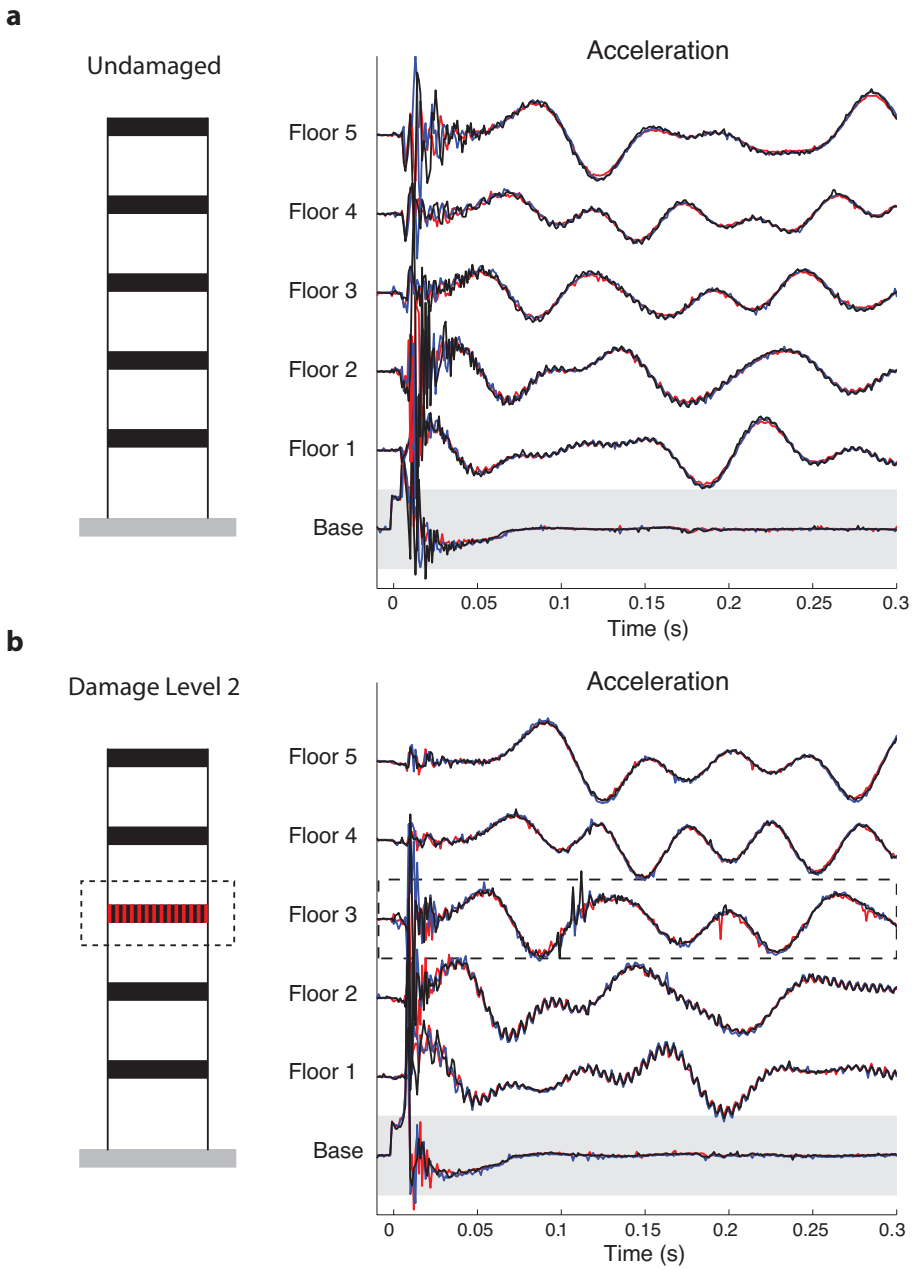

Figure 3.3: **Consistency Between Trials. a.** The undamaged shear beam is subjected to a pulse at its base via a shake table. Three separate trials are compared in each plot, and considerable agreement is shown between trials. **b.** The damaged (Damage Level 2 at Floor 3) shear beam is subjected to a pulse at its base via a shake table. Again, there is considerable agreement shown between trials. There are minor differences in the occurrence of the transient signals, such as those present in the third floor accelerations at times 0.12 seconds and 0.2 seconds. These transient signals are presumably caused by mechanical slippage and impact at the loosened connections, and the signals are clearly observed over the modal response of the structure. There is also a less efficient transmission of high-frequency motion through the third floor, as can be seen by the amplitudes of the high-frequency acceleration that accompany the initial pulse generated by the shake table at time 0.015 seconds; the high-frequency energy seems to become trapped within the first and second floors. The relative amplitudes in each plot have been preserved, as the acceleration time series have been scaled proportional to the maximum amplitude of the initial pulse at the ground floor.

the displacement vector $x(t)$ and the force vector $f(t)$ are given by:

$$\begin{aligned} x(t) &= \begin{pmatrix} x_1(t) & x_2(t) & x_3(t) & x_4(t) & x_5(t) \end{pmatrix}^T, \\ f(t) &= \begin{pmatrix} f_1(t) & f_2(t) & f_3(t) & f_4(t) & f_5(t) \end{pmatrix}^T. \end{aligned}$$

A schematic of both the undamaged and damaged shear beam models is shown in Figure 3.2.

3.2.1 Undamaged Frame

Assuming moment connections and uniform properties, the mass and stiffness matrices for the undamaged frame are populated.

$$\begin{aligned} M &= m \begin{pmatrix} 1 & 0 & 0 & 0 & 0 \\ 0 & 1 & 0 & 0 & 0 \\ 0 & 0 & 1 & 0 & 0 \\ 0 & 0 & 0 & 1 & 0 \\ 0 & 0 & 0 & 0 & 1 \end{pmatrix}, \\ K &= k \begin{pmatrix} 2 & -1 & 0 & 0 & 0 \\ -1 & 2 & -1 & 0 & 0 \\ 0 & -1 & 2 & -1 & 0 \\ 0 & 0 & -1 & 2 & -1 \\ 0 & 0 & 0 & -1 & 1 \end{pmatrix}. \end{aligned}$$

The model parameters used for the floor mass m and interstory shear stiffness k are determined both theoretically, by using the properties of aluminum and the dimensions of the experimental model, and experimentally. The experimental value for the mass m is obtained by disconnecting and weighing one of the floors of the structure and is measured to be 0.9355 kg. The corresponding theoretical value is found by multiplying the volume of a

floor by the density of aluminum (2.7 g/cm^3) and is calculated to be 1.008 kg. The weight of the columns is neglected. The stiffness value k is determined theoretically by approximating the column as an Euler-Bernoulli beam, using the material properties of aluminum and the geometry of the experimental model, and is calculated to be 2.993 10^3 N/m.

Let λ_n and ϕ_n, for n = 1,2,3,4,5, denote the distinct eigenvalues and eigenvectors (normalized with respect to the mass matrix) of $M^{-1}K$.

$$\begin{aligned}
\Phi &= \begin{pmatrix} \phi_1 & \phi_2 & \phi_3 & \phi_4 & \phi_5 \end{pmatrix}, \\
\lambda_n &= \omega_n^2 \\
&= (2\pi f_n)^2, \\
M_g &= \Phi^T M \Phi \\
&= I_{5x5}, \\
K_g &= \Phi^T K \Phi \\
&= \begin{pmatrix} \omega_1^2 & 0 & 0 & 0 & 0 \\ 0 & \omega_2^2 & 0 & 0 & 0 \\ 0 & 0 & \omega_3^2 & 0 & 0 \\ 0 & 0 & 0 & \omega_4^2 & 0 \\ 0 & 0 & 0 & 0 & \omega_5^2 \end{pmatrix}.
\end{aligned}$$

The generalized coordinate vector $x(t)$ is expressed in terms of the principal coordinate displacement vector $p(t)$. By converting from generalized coordinates x to principal coordinates p, the differential equations of motions can be uncoupled.

$$\begin{aligned}
x(t) &= \Phi p(t), \\
p(t) &= \Phi^{-1} x(t), \\
p(t) &= Ip(t) \\
&= \Phi^T M \Phi p(t) \\
&= \Phi^T M x(t).
\end{aligned}$$

Assume modal damping, with a modal damping value for the n^{th} mode shape denoted by ζ_n. The damping matrix C and the damped natural frequencies ω^d are given by:

$$
\begin{aligned}
C_{modal} &= \begin{pmatrix} 2\zeta_1\omega_1 & 0 & 0 & 0 & 0 \\ 0 & 2\zeta_2\omega_2 & 0 & 0 & 0 \\ 0 & 0 & 2\zeta_3\omega_3 & 0 & 0 \\ 0 & 0 & 0 & 2\zeta_4\omega_4 & 0 \\ 0 & 0 & 0 & 0 & 2\zeta_5\omega_5 \end{pmatrix} \\
&= \Phi^T C \Phi, \\
C_{modal} &= I C_{modal} I \\
&= \Phi^T M \Phi C_{modal} \Phi^T M \Phi \\
&= \Phi^T (M \Phi C_{modal} \Phi^T M) \Phi, \\
C &= M \Phi C_{modal} \Phi^T M \\
&= \Phi^{-T} C_{modal} \Phi^{-1}, \\
\omega_n^d &= \omega_n \sqrt{1 - \zeta_n^2}.
\end{aligned}
\tag{3.2}
$$

Modal damping is assumed for the numerical model, and the values are also determined experimentally by integrating to obtain the displacement, applying the logarithmic decrement method to estimate modal damping for the first mode and the half-power bandwidth method to estimate modal damping for higher modes (Cole, 1971). The theoretical values for damping are calculated assuming 2% proportional modal damping.

The differential equations of motion, Equation 3.1, are uncoupled by transforming to principal coordinates and multiplying the equation by Φ^T:

$$
\begin{aligned}
\Phi^T M \Phi \ddot{p}(t) + \Phi^T C \Phi \dot{p}(t) + \Phi^T K \Phi p(t) &= \Phi^T f(t), \\
M_g \ddot{p}(t) + C_{modal} \dot{p}(t) + K_g p(t) &= \Phi^T f(t).
\end{aligned}
$$

Letting $g_n(t)$ denote the n^{th} generalized force term (the n^{th} component of the vector

$\Phi^T f(t)$), each of the five uncoupled equations is written as:

$$\ddot{p}_n(t) + 2\zeta_n\omega_n\dot{p}_n(t) + \omega_n^2 p_n(t) = g_n(t). \tag{3.3}$$

3.2.2 Damaged Frame

Damage is introduced at a given floor by loosening the screws connecting the columns to the floor. Damage is only introduced to one floor at a time; the other four floors and base remain undamaged. In Damage Levels 1, 2, and 3, all six screws connecting the columns to a floor are loosened, by 1/6, 2/6, and 3/6 turn, respectively. The amount of space created by loosening the screws is very small. By loosening the screws to create damage, a short gap of length 0.21 mm (0.008"), 0.42 mm (0.017"), and 0.64 mm (0.025") is created on either side of the damaged floor for Damage Levels 1, 2, and 3, respectively.

Damage to the system is modeled either as damage to the connection or as damage to the columns: I) in Damage Model I, the original moment connection at the damaged floor is replaced by a semi-rigid connection, and II) in Damage Model II, a reduction in inter-story shear stiffness is introduced in the columns directly above and below the damaged floor. Schematics of the damage models are shown in Figure 3.2.

The damage models are used to estimate the amount of damage from a static tilt test and from a dynamic impulse test, and give insight into the mechanism of damage, as an exact physical explanation for quantifying the amount of damage is unavailable. The percent change in inter-story stiffness in an actual building due to structural damage could range from a small percentage, in the case of damage to a few structural members at a floor, to a large percentage, in the case of severe damage to a floor. It is important to quantify the loss of stiffness that is present in the damaged shear beam in order to evaluate whether the amount of damage is analogous to realistic losses of inter-story shear stiffness that could be encountered in an actual civil structure, due to failure of structural members on that story during an earthquake, or due to the progression of damage in a structure due to environmental loading.

3.2.2.1 Damage Model I

In Damage Model I, a reduction in stiffness is introduced at the beam-column connections at the damaged floor by replacing the moment connections with semi-rigid connections. The system still obeys the differential equations of motions given by Equation 3.1, but the changes in boundary conditions at each floor are manifested in the stiffness matrix. The stiffness matrix is updated according to the new lateral stiffness calculated while taking the new boundary conditions into account. The mass matrix remains the same, but damping is expected to increase, and is determined experimentally. In the matrices below, K_m^I represents the stiffness matrix for the structure with damage to the m^{th} floor and assuming Damage Model I. The level of damage is parameterized by introducing the scalar κ to represent a torsion spring at the damaged connection, thus representing a semi-rigid connection. The values for stiffness are calculated by approximating the column as a Euler-Bernoulli beam, introducing a torsion spring at the damaged connection, and assuming a small angle of rotation at the connection.

$$K_1^I = k\begin{pmatrix} 2 & -1 & 0 & 0 & 0 \\ -1 & \frac{13+2\kappa}{8+\kappa} & -1 & 0 & 0 \\ 0 & -1 & 2 & -1 & 0 \\ 0 & 0 & -1 & 2 & -1 \\ 0 & 0 & 0 & -1 & 1 \end{pmatrix}, K_2^I = k\begin{pmatrix} \frac{13+2\kappa}{8+\kappa} & -1 & \frac{3}{8+\kappa} & 0 & 0 \\ -1 & 2 & -1 & 0 & 0 \\ \frac{3}{8+\kappa} & -1 & \frac{13+2\kappa}{8+\kappa} & -1 & 0 \\ 0 & 0 & -1 & 2 & -1 \\ 0 & 0 & 0 & -1 & 1 \end{pmatrix},$$

$$K_3^I = k\begin{pmatrix} 2 & -1 & 0 & 0 & 0 \\ -1 & \frac{13+2\kappa}{8+\kappa} & -1 & \frac{3}{8+\kappa} & 0 \\ 0 & -1 & 2 & -1 & 0 \\ 0 & \frac{3}{8+\kappa} & -1 & \frac{13+2\kappa}{8+\kappa} & -1 \\ 0 & 0 & 0 & -1 & 1 \end{pmatrix}, K_4^I = k\begin{pmatrix} 2 & -1 & 0 & 0 & 0 \\ -1 & 2 & -1 & 0 & 0 \\ 0 & -1 & \frac{13+2\kappa}{8+\kappa} & -1 & \frac{3}{8+\kappa} \\ 0 & 0 & -1 & 2 & -1 \\ 0 & 0 & \frac{3}{8+\kappa} & -1 & \frac{5+\kappa}{8+\kappa} \end{pmatrix},$$

$$K_5^I = k \begin{pmatrix} 2 & -1 & 0 & 0 & 0 \\ -1 & 2 & -1 & 0 & 0 \\ 0 & -1 & 2 & -1 & 0 \\ 0 & 0 & -1 & \frac{5+2\kappa}{4+\kappa} & -\frac{1+\kappa}{4+\kappa} \\ 0 & 0 & 0 & -\frac{1+\kappa}{4+\kappa} & \frac{1+\kappa}{4+\kappa} \end{pmatrix}.$$

To work with a more manageable stiffness parameter that ranges from 0 to 1, introduce stiffness parameter γ:

$$\kappa = \frac{\gamma}{1-\gamma}. \tag{3.4}$$

As γ ranges from 0 to 1, the connection changes from a simple connection (no torsional stiffness, i.e., $\kappa = 0$) to a moment connection (infinite torsional stiffness, i.e., $\kappa \to \infty$). For a moment connection, the stiffness matrices simplify to those for the undamaged case. For a simple connection, the stiffness matrices simplify to those shown below:

$$K_1^I|_{\kappa=0} = k \begin{pmatrix} 2 & -1 & 0 & 0 & 0 \\ -1 & 13/8 & -1 & 0 & 0 \\ 0 & -1 & 2 & -1 & 0 \\ 0 & 0 & -1 & 2 & -1 \\ 0 & 0 & 0 & -1 & 1 \end{pmatrix}, K_2^I|_{\kappa=0} = k \begin{pmatrix} 13/8 & -1 & 3/8 & 0 & 0 \\ -1 & 2 & -1 & 0 & 0 \\ 3/8 & -1 & 13/8 & -1 & 0 \\ 0 & 0 & -1 & 2 & -1 \\ 0 & 0 & 0 & -1 & 1 \end{pmatrix},$$

$$K_3^I|_{\kappa=0} = k \begin{pmatrix} 2 & -1 & 0 & 0 & 0 \\ -1 & 13/8 & -1 & 3/8 & 0 \\ 0 & -1 & 2 & -1 & 0 \\ 0 & 3/8 & -1 & 13/8 & -1 \\ 0 & 0 & 0 & -1 & 1 \end{pmatrix}, K_4^I|_{\kappa=0} = k \begin{pmatrix} 2 & -1 & 0 & 0 & 0 \\ -1 & 2 & -1 & 0 & 0 \\ 0 & -1 & 13/8 & -1 & 3/8 \\ 0 & 0 & -1 & 2 & -1 \\ 0 & 0 & 3/8 & -1 & 5/8 \end{pmatrix},$$

$$K_5^I|_{\kappa=0} = k \begin{pmatrix} 2 & -1 & 0 & 0 & 0 \\ -1 & 2 & -1 & 0 & 0 \\ 0 & -1 & 2 & -1 & 0 \\ 0 & 0 & -1 & 5/4 & -1/4 \\ 0 & 0 & 0 & -1/4 & 1/4 \end{pmatrix}.$$

3.2.2.2 Damage Model II

In Damage Model II, a reduction in inter-story shear stiffness is introduced in the columns directly above and below the damaged floor. Unlike Damage Model I, the moment connection is assumed to be undamaged, but the columns immediately above and below are assumed to have the same reduced lateral stiffness, with a value that is denoted by k_d. The stiffness parameter for this model is chosen to be the ratio k_d/k, and it also ranges from 0 (no stiffness) to 1 (no loss in stiffness).

$$K_1^{II} = k \begin{pmatrix} 2k_d/k & -k_d/k & 0 & 0 & 0 \\ -k_d/k & k_d/k+1 & -1 & 0 & 0 \\ 0 & -1 & 2 & -1 & 0 \\ 0 & 0 & -1 & 2 & -1 \\ 0 & 0 & 0 & -1 & 1 \end{pmatrix}, K_2^{II} = k \begin{pmatrix} 1+k_d/k & -k_d/k & 0 & 0 & 0 \\ -k_d/k & 2k_d/k & -k_d/k & 0 & 0 \\ 0 & -k_d/k & 1+k_d/k & -1 & 0 \\ 0 & 0 & -1 & 2 & -1 \\ 0 & 0 & 0 & -1 & 1 \end{pmatrix},$$

$$K_3^{II} = k \begin{pmatrix} 2 & -1 & 0 & 0 & 0 \\ -1 & 1+k_d/k & -k_d/k & 0 & 0 \\ 0 & -k_d/k & 2k_d/k & -k_d/k & 0 \\ 0 & 0 & -k_d/k & 1+k_d/k & -1 \\ 0 & 0 & 0 & -1 & 1 \end{pmatrix},$$

$$K_4^{II} = k \begin{pmatrix} 2 & -1 & 0 & 0 & 0 \\ -1 & 2 & -1 & 0 & 0 \\ 0 & - & 1+k_d/k & -k_d/k & 0 \\ 0 & 0 & -k_d/k & 2k_d/k & -k_d/k \\ 0 & 0 & 0 & -k_d/k & k_d/k \end{pmatrix}, K_5^{II} = k \begin{pmatrix} 2 & -1 & 0 & 0 & 0 \\ -1 & 2 & -1 & 0 & 0 \\ 0 & -1 & 2 & -1 & 0 \\ 0 & 0 & -1 & 1+k_d/k & -k_d/k \\ 0 & 0 & 0 & -k_d/k & k_d/k \end{pmatrix}.$$

In Section 3.3.2, these models are used to estimate the reduction in stiffness that is caused by damage.

3.3 Experimental Results

The following experimental results are presented.

Section 3.3.1 A set of experiments is conducted to verify the linearity of the damaged and undamaged frame.

Section 3.3.2 A series of static tilt tests is performed. The stiffness of the damaged and undamaged frames is estimated, and the amount of damage at each damage level (expressed as a ratio of stiffnesses) is computed as a ratio of stiffnesses.

Section 3.3.3 A series of dynamic testing is performed with the frame damaged at each floor at Damage Levels 1-3. Experimental results are shown for the undamaged frame, and the damaged frame, at three different levels of damage. The raw and filtered acceleration records are used for the time series analysis. Four repeated trials are conducted for each damage case. The set of experiments was conducted with sampling rates of 1 ksps, 5 ksps, and 150 ksps.

Section 3.3.4 A damage detection method is discussed, and a series of dynamic tests are conducted in which damage is sequentially introduced to the frame, one bolt at a time. A damage-detection method is presented and used to identify potential damage in the frame.

Section 3.3.5 A comparison of the experimental and theoretical data is presented, for the frequency domain (i.e., mode shapes and modal frequencies) for the undamaged frame.

3.3.1 Linearity of the Damaged and Undamaged Shear Beam

Before applying techniques developed for a linear system, it is necessary to first verify that the shear beam behaves as a linear system. A linear system is one in which the doubling of the magnitude of the excitation force results in a doubling of the response, and the response to two simultaneous inputs equals the sum of the responses to each independent input.

One way to test linearity is by inputing a pure sinusoidal signal at the base of the shear beam. If the structure behaves linearly, then the response of the structure will consist of a signal of only the input frequency. If the structure behaves nonlinearly, then either harmonic distortion or frequency modulation will occur, and harmonics or sidebands will be present in the frequency response of the structure (Farrar et al., 2007). As the shake table used is not capable of inputing a pure sinusoidal wave, a different approach must be taken. According to Ewins (1984), signs of nonlinear behavior include the following: 1) natural frequencies vary with position and strength of excitation, 2) distorted frequency response plots, and 3) unstable or unrepeatable data. The structure is thus subjected to a pulse at its base, and the natural frequencies and modeshapes are analyzed for changes.

As seen in Figure 3.4, across a range in shake table gains from 2 to 6, there is no variation in the observed natural frequencies and little variation in the observed modeshapes for the undamaged shear beam. For the damaged shear beam (Damage Level 1 introduced at the third floor), there is a slight decrease in the observed natural frequencies above a shake table gain of 4. In order to remain within the linear response range of the shear beam, while maintaining a high signal-to-noise ratio (which increases with an increased shake table gain), a shake table gain of either 3 or 4 is used for the experiments in this chapter. There is a possibility that the shaking of the structure causes the bolts to slightly loosen, however only small variations in observed natural frequencies are observed between repeated trials.

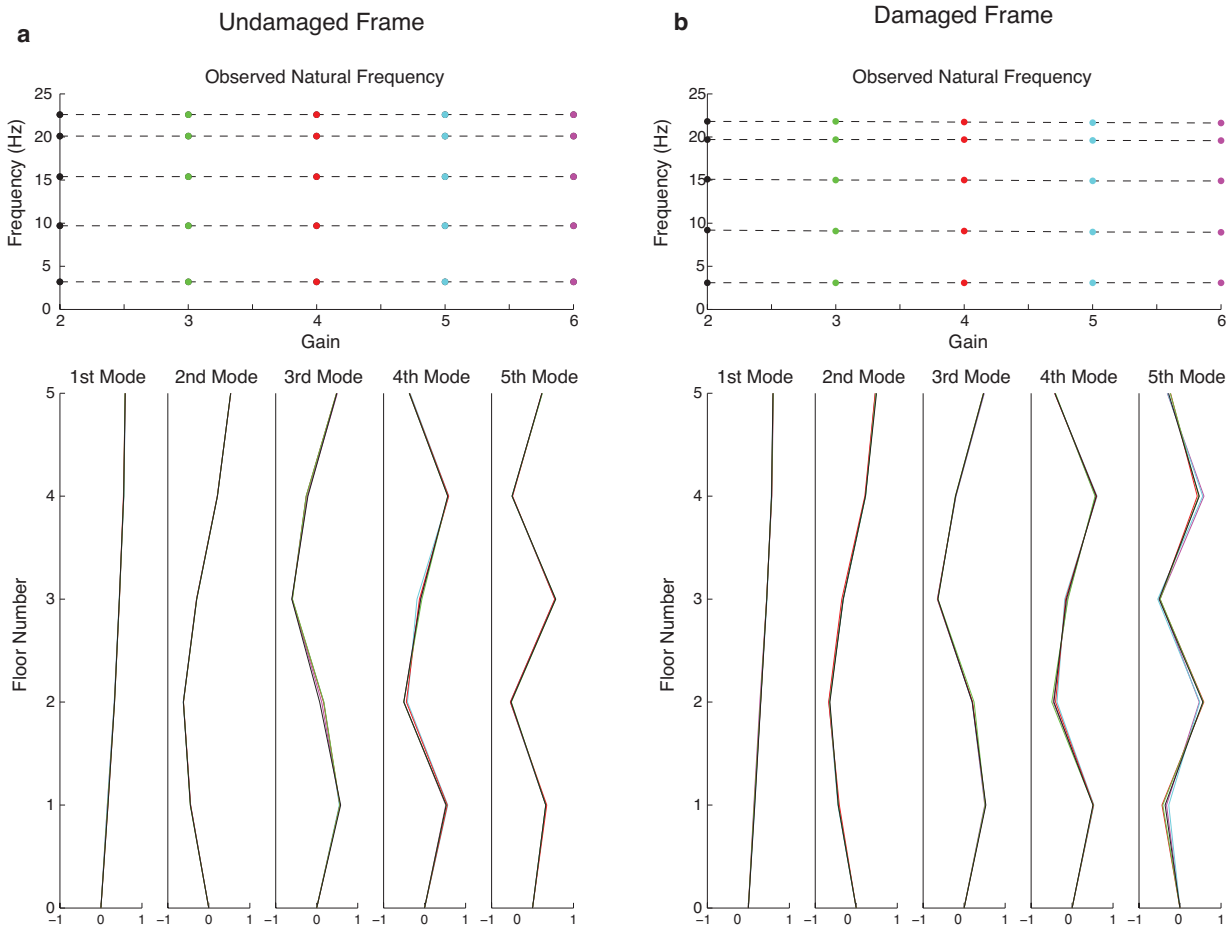

Figure 3.4: **Verification of System Linearity. a.** The undamaged shear beam is subjected to a series of pulses at its base, over a range of shake table gains, and the modal properties are compared. There is no change in the observed natural frequencies over the frequency range of interest, and the mass-normalized modeshapes are also consistent. **b.** Damage (Damage Level I) is introduced at the third floor, and the damaged shear beam is subjected to a similar series of pulses. The frequencies are unchanged until a gain of 4, after which there is a slight decrease in two of the natural frequencies. The modeshapes are consistent between rounds.

3.3.2 Static Testing:

Stiffness Parameter Estimation via a Tilt Test

The stiffness and stiffness parameters are determined experimentally by performing a tilt test. Complementing the dynamic testing of the structure, the tilt test provides an additional method to estimate the stiffness for the small-scale structure by using its static response. The undamaged model is rotated from $-30°$ to $30°$ using a tilt table that rotates the structure at precise angles, shown in Figure 3.5. The lateral force on each floor due to gravity can be calculated using the measured mass of each floor. The structure is in static equilibrium; its velocity and acceleration equals zero, and the resulting displacement at the top floor, $x_{5\,tilt}$, is recorded. The differential equation of motion, Equation 3.1, for the static case is:

$$Kx = f. \tag{3.5}$$

Solving for x by multiplying the equation by K^{-1} and substituting in the experimentally-measured value m_{exp} for m yields:

$$\begin{aligned}
x_{tilt}(\theta) &= \frac{mg\sin\theta}{k}\begin{pmatrix} 2 & -1 & 0 & 0 & 0 \\ -1 & 2 & -1 & 0 & 0 \\ 0 & -1 & 2 & -1 & 0 \\ 0 & 0 & -1 & 2 & -1 \\ 0 & 0 & 0 & -1 & 1 \end{pmatrix}^{-1}\begin{pmatrix} 1 \\ 1 \\ 1 \\ 1 \\ 1 \end{pmatrix} \\
&= \frac{mg\sin\theta}{k}\begin{pmatrix} 1 & 1 & 1 & 1 & 1 \\ 1 & 2 & 2 & 2 & 2 \\ 1 & 2 & 3 & 3 & 3 \\ 1 & 2 & 3 & 4 & 4 \\ 1 & 2 & 3 & 4 & 5 \end{pmatrix}\begin{pmatrix} 1 \\ 1 \\ 1 \\ 1 \\ 1 \end{pmatrix} \\
&= \frac{mg\sin\theta}{k}\begin{pmatrix} 5 & 9 & 12 & 14 & 15 \end{pmatrix}^{T}, \\
k &= \frac{15mg\sin\theta}{x_{5\,tilt}}.
\end{aligned} \tag{3.6}$$

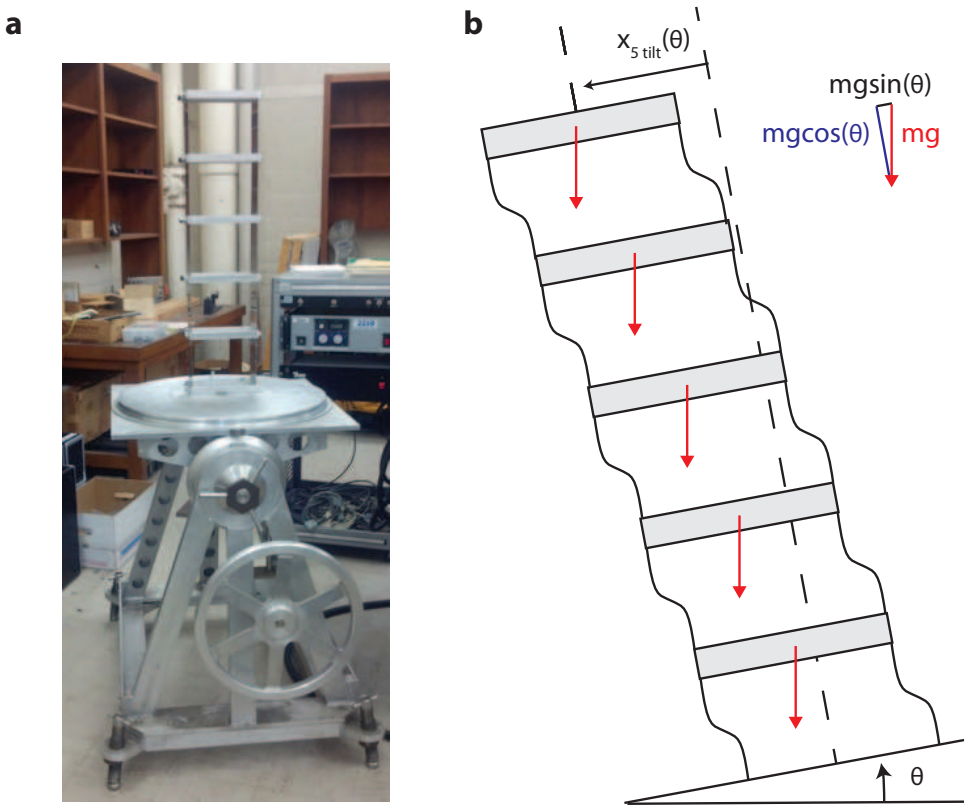

Figure 3.5: **Static Testing: Tilt Table and Schematic a,** The test structure is firmly fixed at its base to a tilt table that precise controls the angle of tilt. The resulting relative displacement at the top of the structure is determined for various angles between $-30°$ and $30°$. **b** The lateral force is determined from the tilt angle and weight of the structure

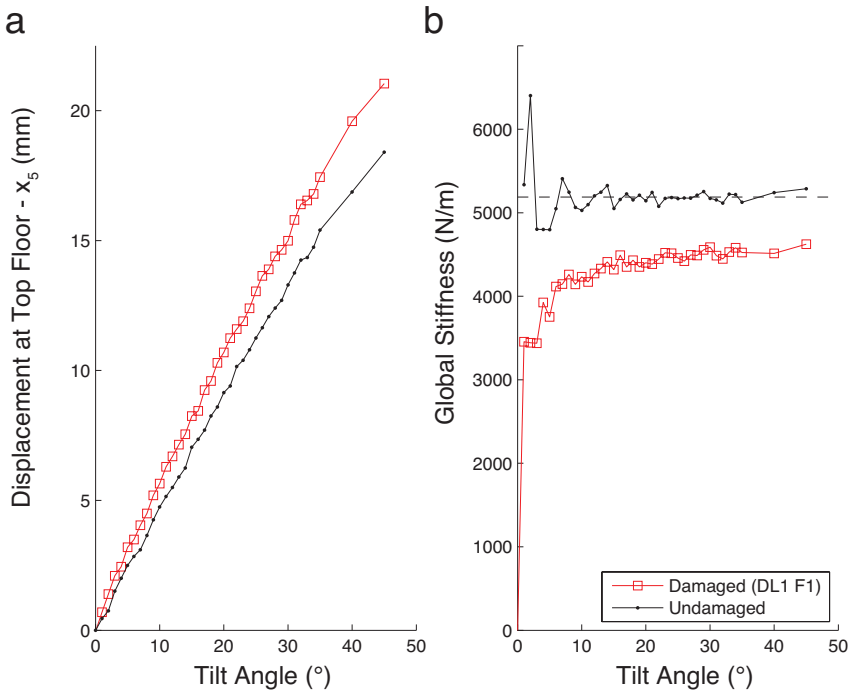

Figure 3.6: **Tilt Test: Damaged vs. Undamaged (Example).** The resulting roof displacement for the undamaged and damaged (Damage Level 1 introduced at Floor 1) frame is shown to the left. To the right, the global stiffness, calculated using Equation 3.6, is plotted for each point. As expected, the damaged structure experiences larger displacements and hence has reduced global stiffness than the undamaged structure. The mean value of the global stiffness, $k_{exp} = 5.19x10^3 N/m$, for the undamaged case is indicated by the dashed line.

When performing a matrix inversion, it is important to check the condition number. The condition number is used to estimate the accuracy of the results of the inversion and, for a matrix, is equal to the ratio of the largest singular value to the smallest singular value. The condition number for K is calculated to be 45, or $10^{3.8}$, which is a reasonably small value. This means that about four digits of accuracy might be lost in addition to the loss of precision from arithmetic methods; the larger the condition number, the more ill-conditioned the system (Cheney and Kincaid, 2012).

A set of tilt tests is performed for each of the 15 damaged configurations of the structure in order to assess the change in stiffness and corresponding value of the stiffness parameter that accompanies the level and location of damage. The displacement at the top floor, $x_{5\,tilt}$, is recorded when the damaged shear beam is rotated through various angles between $-30°$

and 30°. The stiffness at the undamaged floors is assumed to be equal to the experimentally-obtained undamaged stiffness k_{exp}. For each data point, the stiffness parameter is solved for using Equation 3.5, and the stiffness parameter depends on which model of damage is used. For Damage Model I, the stiffness parameter estimated is γ, given by Equation 3.4; for Damage Model II, the stiffness parameter estimated is the ratio of the reduced stiffness value to the undamaged stiffness value k_d/k.

As inverting the stiffness matrices for the damaged frame is more difficult than it was for the undamaged case, the inversion is formulated as a numerical optimization problem. For damage introduced at the n^{th} floor, using stiffness matrix K for the undamaged system with stiffness value k_{exp}, and assuming Damage Model I, the stiffness parameter γ is estimated as:

$$\gamma_{tilt} \;=\; \arg\min_{\gamma\in[0\,1]} |x_{5\,tilt} - \begin{pmatrix}0 & 0 & 0 & 0 & 1\end{pmatrix} K^{-1}_{damaged}(k_{exp},\gamma) f_g|^2.$$

The term 'arg min' simply means the value of γ within the range of [0 1] that minimizes the argument to the right of the expression. Stiffness matrix $K_{damaged}$ is written as $K^{-1}_{damaged}(k_{exp},\gamma)$ to emphasize its dependence on the parameters. The force vector f_g is a 5x1 vector of forces due to gravity, with each term equal to $m_{exp}g$.

Similarly, assuming Damage Model II under the same conditions, the stiffness parameter k_d/k is estimated as:

$$(k_d/k)_{tilt} \;=\; \frac{1}{k_{exp}} \arg\min_{k_d\in[0\,k_{exp}]} |x_{5\,tilt} - \begin{pmatrix}0 & 0 & 0 & 0 & 1\end{pmatrix} K^{-1}_{2\_n}(k_{exp},k_d) f_g|^2.$$

The estimated values for the stiffness parameters, listed in Table 3.2 and plotted in Figure 3.7, can be used as reference values in relating differences observed in the dynamic response of the structure to the reduction in stiffness of the frame. Moderate levels of damage are created by the slight loosening of the bolts. If damage is modeled as a loss of stiffness in the connection, as in Damage Model I, then as expected, higher values of γ are observed for lower levels of damage. This means that the damaged connection behaves more like a simple

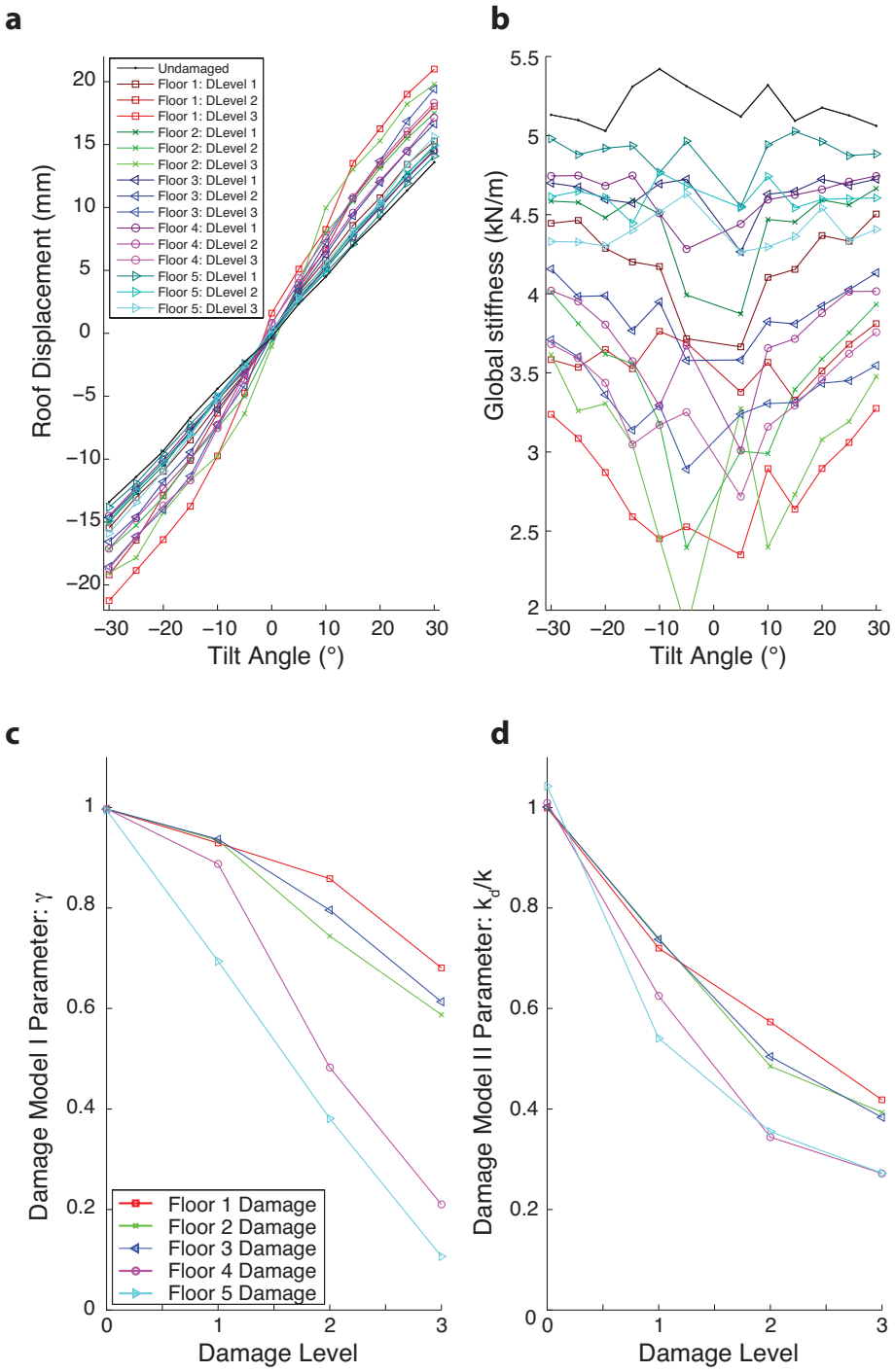

Figure 3.7: **Tilt Test: Damaged vs. Undamaged (All Cases). a,** The undamaged or damaged (Levels 1-3, Floors 1-5) structure is tilted at various angles between -30° and 30°, and the resulting roof displacement is recorded. **b,** The global stiffness is determined using Equation 3.6. As expected, the undamaged model has the highest global stiffness, with the global stiffness decreasing from Levels 1 to 2 and 3. **c** Damage Model I is assumed, and the tilt angle and recorded displacement are used to solve for the stiffness parameter, as in Equation 3.7. **d** Damage Model II is assumed, and the tilt angle and recorded displacement are used to solve for the stiffness parameter, as in Equation 3.7. As expected, the stiffness parameter decreases with increasing damage. The stiffness parameters for damage introduced to Floors 4 and 5 are lower than those estimated for damage to Floors 1, 2, and 3.

connection and less like a moment connection for higher levels of damage than it does for lower levels of damage. If instead damage is modeled as a loss of interstory stiffness adjacent to the damaged floor, then higher values of k_d/k are observed for lower levels of damage. This means that, for lower levels of damage, the stiffness of the damaged columns is closer to that of the undamaged columns, and the column stiffness decreases for higher levels of damage.

Level of	Model Type	Damaged Floor				
Damage	and Parameter	1	2	3	4	5
Undamaged	DM I: γ	1.00	1.00	1.00	1.00	1.00
	DM II: k_d/k	1.00	1.00	1.00	1.01	1.04
Level 1	DM I: γ	0.93	0.93	0.94	0.89	0.69
	DM II: k_d/k	0.72	0.74	0.74	0.63	0.54
Level 2	DM I: γ	0.86	0.74	0.80	0.48	0.38
	DM II: k_d/k	0.57	0.49	0.50	0.34	0.36
Level 3	DM I: γ	0.68	0.59	0.61	0.21	0.11
	DM II: k_d/k	0.42	0.39	0.38	0.27	0.27

Table 3.1: **Estimated Stiffness Parameters from the Tilt Test.** To quantify the amount of damage introduced to the frame in Damage Levels 1-3, a static tilt test is performed, and a model for damage is assumed. The tilt angle and resulting rotation is used with the model to determine the amount of stiffness in the damaged connection. Moderate levels of damage are created by the slight loosening of the bolts.

.

In addition to the expected trend of decreasing stiffness with increasing levels of damage, there appears to be a trend of decreasing stiffness for damage to increasing floor numbers for a given level of damage. We expect stiffness values to be uniform across different floors for the same level of damage. The general trends in the table suggest that there is a phenomenon that exists in the real system, such as rotation or a nonlinear stiffness mechanism, that is not captured by the simple damage models.

Finally, if damage is introduced by the loosening of only one screw, then the amount of

displacement at the top floor for a given angle of rotation is observed to equal the amount of displacement at the top floor for the undamaged frame. This means that there is no observed loss of inter-story stiffness for this damage case.

3.3.3 Dynamic Testing: Damage Levels 1, 2, and 3

The shear beam is excited by a repeatable pulse at its base by a shake table. By using a repeatable pulse at the base, the baseline response of the frame in an undamaged configuration can be directly compared to the response of the frame for levels of increasing damage. Differences in the dynamic response of the structure between trials due to differences in the source are minimized, and the effect of damage on the dynamic response of the structure can be more readily analyzed.

As mentioned previously, in Damage Levels 1, 2, and 3, damage is introduced to the shear beam by incrementally loosening the six screws attaching the two columns to one of the five floors. Damage Levels 1, 2, and 3 correspond to a 1/6, 2/6, and 3/6 turn of each screw at the damaged floor, respectively. The amount of space created by loosening the screws is very small. The length of the gap created on one side is equal to 0.21 mm (0.0083”), 0.42 mm (0.017”), and 0.64 mm (0.025”) for Damage Levels 1, 2, and 3, respectively.

A schematic of the typical dynamic response recorded at 1 ksps is shown in Figure 3.8. The pulse at the base of the structure excites a shear wave that travels up the height of the building and is reflected at the top. The response of the structure can be filtered into its low-frequency and high-frequency components. The low-frequency component consists of the predominant modal response of the structure that includes the five lowest modes. The high-frequency component consists of the initial slip of the shake table as well as mechanical slippage and impact that occurs at the damaged floor. When the screws are loosened, the gap allows for motion of the columns and washers.

The unfiltered dynamic response of the frame in all 15 damaged cases (three levels of damage, five different damage locations) is plotted against the undamaged case in Figure 3.9. A few features in the damaged data stand out. The low-frequency response of the

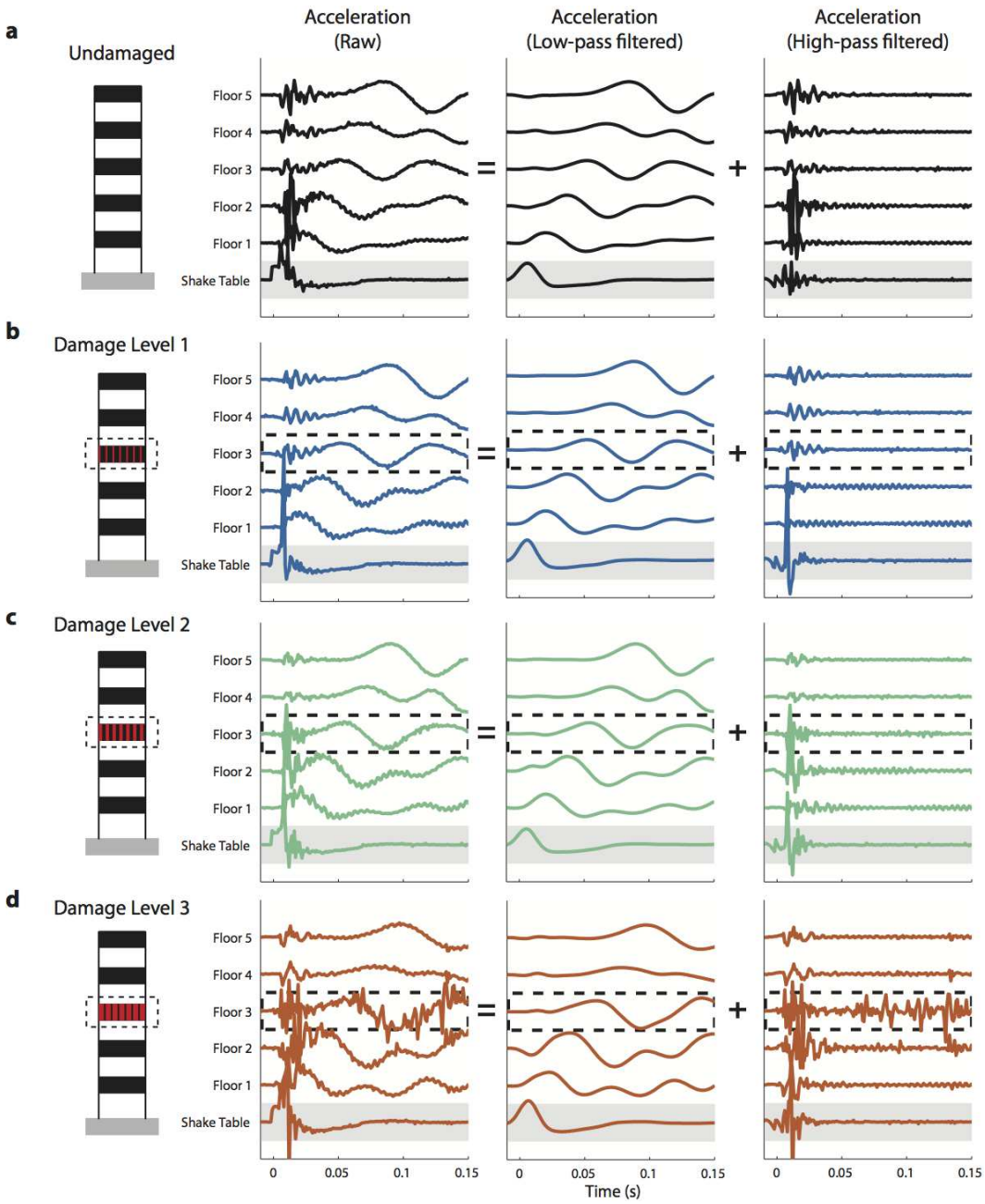

Figure 3.8: **Dynamic Testing: Explanatory Schematic.** The shear beam is excited by a repeatable pulse at its base by a shake table. Three different levels of damage are introduced into one floor of the the shear beam; in this case Floor 3 is damaged. A total of six accelerometers instrument the shear beam, one attached to each floor and one attached to the shake table; the sampling rate is 1 ksps. By using a repeatable pulse at the base, the response of the frame in an **a** undamaged configuration can be directly compared to the response of the frame for levels of increasing damage (**b** Damage Level 1, **c** Damage Level 2, **d** Damage Level 3). The response of the structure is filtered into its low-frequency and high-frequency components. The low-frequency response of the structure consists of the predominant modal response (first five modes) and is obtained using a 4^{th} order Butterworth filter with a 50 Hz cutoff frequency. The high-frequency response is obtained by applying a 4^{th} order high-pass Butterworth filter. The high-frequency components decay much more rapidly than do the low-frequency components. The primary sources of the high-frequency signals are the initial slip of shake table as well as mechanical slippage and impact at the damaged floor. These data were recorded at a rate of 5 ksps.

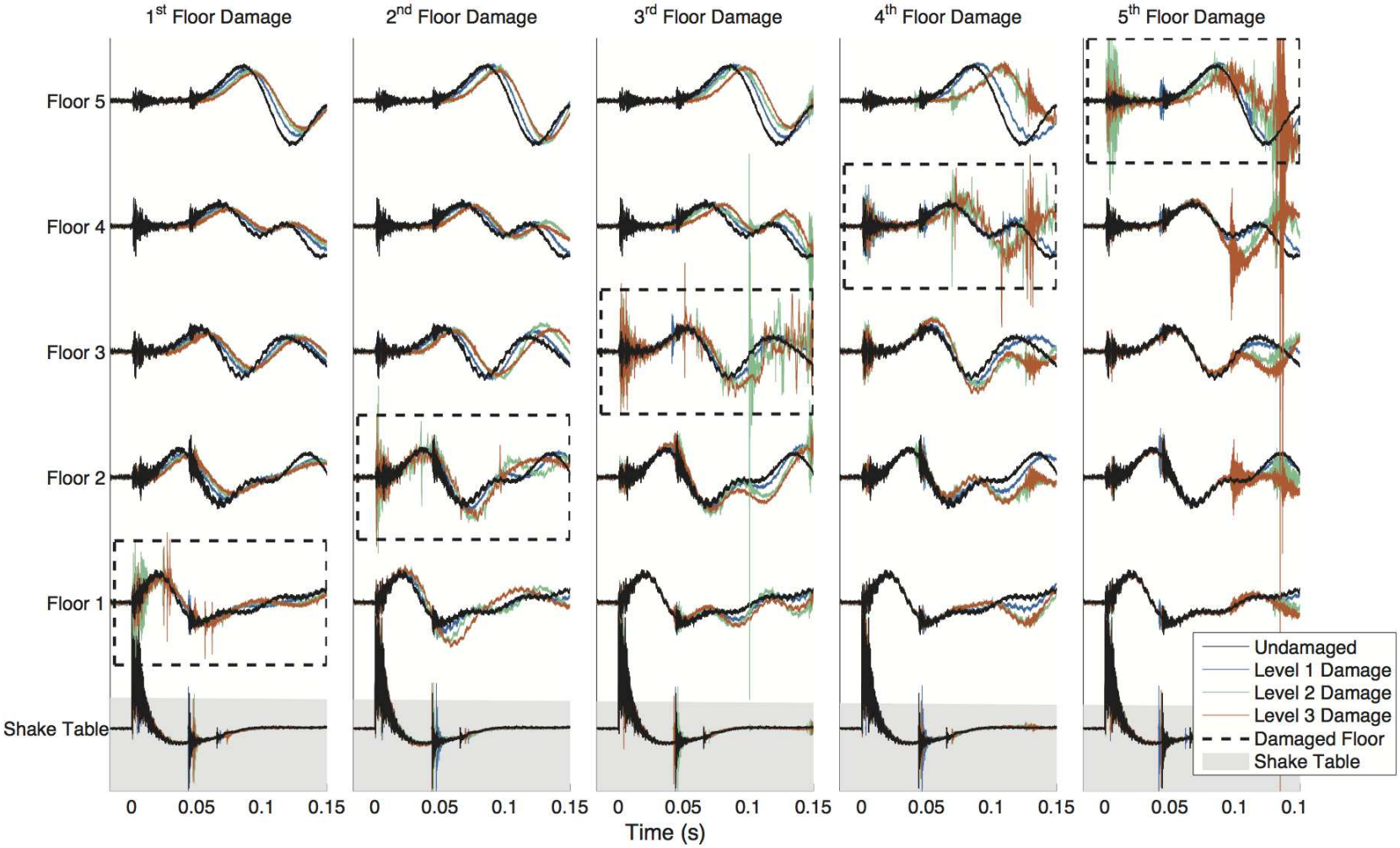

Figure 3.9: **Raw Acceleration Records: Damaged vs. Undamaged.** Features in both the low-frequency response of the structure and the high-frequency response of the structure are indicative of damage. A delay in arrival time occurs as the low-frequency shear wave propagates through the damaged region, and a reflected wave generated at the damage interface results in a slightly higher amplitude recorded below the damaged floor. The high-frequency pulse generated by the initial motion of the shake table is observed to have decreased as it is transmitted from the damaged floor to the above floors. The high-frequency energy seems to become trapped within this undamaged floor, where mechanical vibrations of the loose connections also result in large high-frequency accelerations. Additional short-duration high-frequency pulses are recorded as the structure continues to deform.

structure is indicative of damage. Much like a vertical SH wave traveling through a low velocity layer, the shear wave that propagates through the structure is slowed down when it passes through the region of damage, which consists of the damaged floor and the columns immediately above and below that floor. The low velocity zone results in increasing delays in arrival times for increasing levels of damage in records obtained above the damaged floor. A reflected wave is generated at the interface between the undamaged frame and the damaged frame, which results in slightly larger amplitudes in the shear wave pulse at the floor just below the damaged interface.

According to Timoshenko, a body's reaction to a suddenly applied force is not present at all parts of the body at once. The remote portions of the body remain unaffected during early times. Deformation propagates through the body in the form of elastic waves (Timoshenko, 1951). This concept can be applied to elastic waves that travel through the damaged region. The response of the damaged frame does not begin to differ from the response of the undamaged frame until elastic waves have had time to propagate through the damaged region and reach the location of a receiver. In this sense, there is some amount of time that passes before information of damage has been disseminated throughout the medium.

The high-frequency response of the structure is also highly indicative of damage. The initial pulse of the shake table generates a high-frequency pulse across all five floors in addition to exciting the predominant modal response of the structure. In the damaged frame, it appears that there is a decreased transmission of this high frequency energy from the damaged floor to the above floors. The energy appears to essentially become trapped at the level of the damaged floor, where the excitation of the loose connections generates mechanical vibrations that result in short-duration high-frequency accelerations (pulses) recorded on the damaged floor. As the structure continues to deform in free vibration, additional pulses are recorded. These pulses occur more often as the level of damage progresses.

Using the uniform shear beam model outlined in the Appendix, the arrival time delays (plotted in Figure 3.10) are estimated from the low-pass filtered data shown in Figure 3.20. The ratio of inter-story lateral stiffness, $k_{damaged}/k_{undamaged}$, is calculated as the the ratio of the squares of the computed inter-story shear wave speeds, $\beta^2_{damaged}/\beta^2_{undamaged}$. The mean

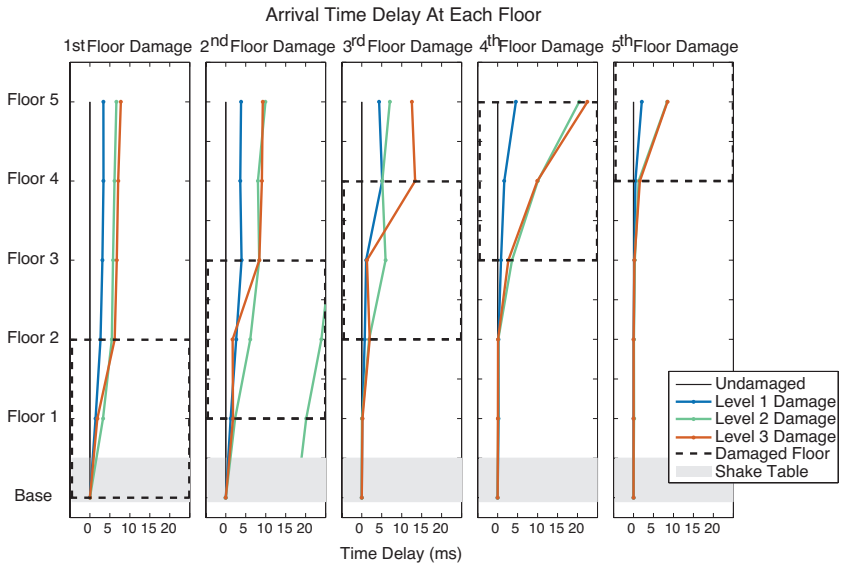

Figure 3.10: **Arrival Time Delays: Damaged Frame.** The arrival time delays are estimated from the low-pass filtered data, and are calculated relative to the arrival times obtained for the undamaged frame. Little to no change in arrival times is observed for floors below the damaged region. An increase in the arrival time delay occurs during the region of damage, and that increase in arrival time remains constant in floors above the damaged region.

values (and standard deviations) of the estimated inter-story lateral stiffness immediately beneath the damaged floor for Damage Levels 1, 2, and 3, respectively, are 0.93 (0.03), 0.70 (0.1), and 0.82 (0.23). The mean values (and standard deviations) of the estimated inter-story lateral stiffness immediately above the damaged floor for Damage Levels 1, 2, and 3, respectively, are 0.94 (0.03), 0.67 (0.09), and 0.80 (0.24). The mean values (and standard deviations) of the estimated inter-story lateral stiffness in floors not immediately above or below the damaged floor are calculated to be 0.99 (0.03), 0.95 (0.07), and 0.96 (0.05). The calculated stiffness ratios are much higher than those computed during the static testing. The estimate could be improved by taking a different approach, such as assuming a damped mass-spring model, using the shake table motion as input, and calculating the maximum likelihood estimates of model parameters that determine the best least-squares fit to the recorded floor accelerations. By using the entire time series, this approach would take much more information from the data into account in calculating the inter-story lateral stiffnesses. The amplitudes of the initial shear wave pulse (Figure 3.17) can also be used for a quick assessment of damage detection, but the presence of the transient pulses can make amplitude

estimation more difficult.

Level of Damage	Damaged Floor	Lateral Stiffness between Floors				
		$0-1$	$1-2$	$2-3$	$3-4$	$4-5$
Undamaged	1	1.00	1.00	1.00	1.00	1.00
Level 1	1	0.92^b	0.92^a	0.97	0.98	1.00
	2	0.93	0.91^b	0.91^a	1.02	0.99
	3	0.99	0.96	0.98^b	0.74^a	1.04
	4	0.99	1.00	0.96	0.95^b	0.84^a
	5	1.00	1.00	0.99	0.98	0.91^b
Level 2	1	0.81^b	0.86^a	0.98	0.98	0.97
	2	0.86	0.77^b	0.86^a	1.02	0.89
	3	1.00	0.89	0.73^b	1.05^a	0.89
	4	0.99	1.00	0.78	0.58^b	0.42^a
	5	0.99	1.00	0.99	0.94	0.60^b
Level 3	1	0.89^b	0.73^a	0.97	0.98	0.96
	2	0.89	1.01^b	0.57^a	0.96	0.99
	3	0.99	0.89	1.04^b	0.22^a	1.05
	4	1.00	1.00	0.83	0.53^b	0.29^a
	5	1.00	1.00	0.99	0.91	0.61^b

Table 3.2: **Estimated Damage Parameters from Dynamic Testing.** The ratio of inter-story lateral stiffness, $k_{damaged}/k_{undamaged}$, is calculated as the the ratio of the squares of the computed inter-story shear wave speeds, $\beta^2_{damaged}/\beta^2_{undamaged}$. A uniform shear beam model is assumed. The mean values (and standard deviations) of the estimated inter-story lateral stiffness immediately beneath the damaged floor for Damage Levels 1, 2, and 3, respectively, are 0.93 (0.03), 0.70 (0.1), and 0.82 (0.23). The mean values (and standard deviations) of the estimated inter-story lateral stiffness immediately above the damaged floor for Damage Levels 1, 2, and 3, respectively, are 0.94 (0.03), 0.67 (0.09), and 0.80 (0.24). The mean values (and standard deviations) of the estimated inter-story lateral stiffness in floors not immediately above or below the damaged floor are calculated to be 0.99 (0.03), 0.95 (0.07), and 0.96 (0.05).
^{a} = Immediately above damaged floor
^{b} = Immediately below damaged floor

3.3.4 Dynamic Testing: Damage Detection Method Based on Pulse Identification

It has become apparent that 1) the presence of short-duration high-frequency signals (call them pulses) can be indicative of damage, 2) some types of damage result in the generation of a new high-frequency source mechanism in the structure, and 3) the response of a structure is consistent between trials when a similar source mechanism is applied at the same location. Information about repeating pulses present in the acceleration time series has potential use for damage detection. A schematic of the idea is illustrated in Figure 3.11. The basic idea is to compare pulses observed in the acceleration time series when the structure is in a potentially damaged state to pulses observed when the structure was known to be in an undamaged state. By comparing the pulses in these two situations, a change in this type of high-frequency dynamic behavior of the structure can be identified. The approximate location of the damage source can be determined from the arrival times and amplitudes of the pulses. These regions can be analyzed in the context of potential nearby sources of high-frequency excitation, including the possibility of damage. Pulses can be generated by various mechanisms related to damage, including acoustic emission generated by the propagation of a crack tip, elastic waves generated by mechanical impact of loose parts, or multi-modal traveling waves that can occur during the dynamic loading of flexible structural members such as the propagation of a flexural wave through a beam. Pulses can also be generated by environmental mechanisms, such as a car driving over a bump on a bridge, the collapse of a bookshelf during an earthquake, or an impact hammer. Hence, it is preferable to have a baseline recording to which possible damage features can be compared.

A series of dynamic tests is conducted on the shear beam in order to experimentally test this method. In Damage State A, damage is introduced to the frame by loosening a single screw. In Damage State B, the frame is further damaged by loosening a screw at a second location. A static tilt test was performed on the structure with a single screw loosened, and the resulting roof displacements due to tilt did not deviate from those recorded for the undamaged frame; the same global stiffness was recorded, and no loss in interstory stiffness

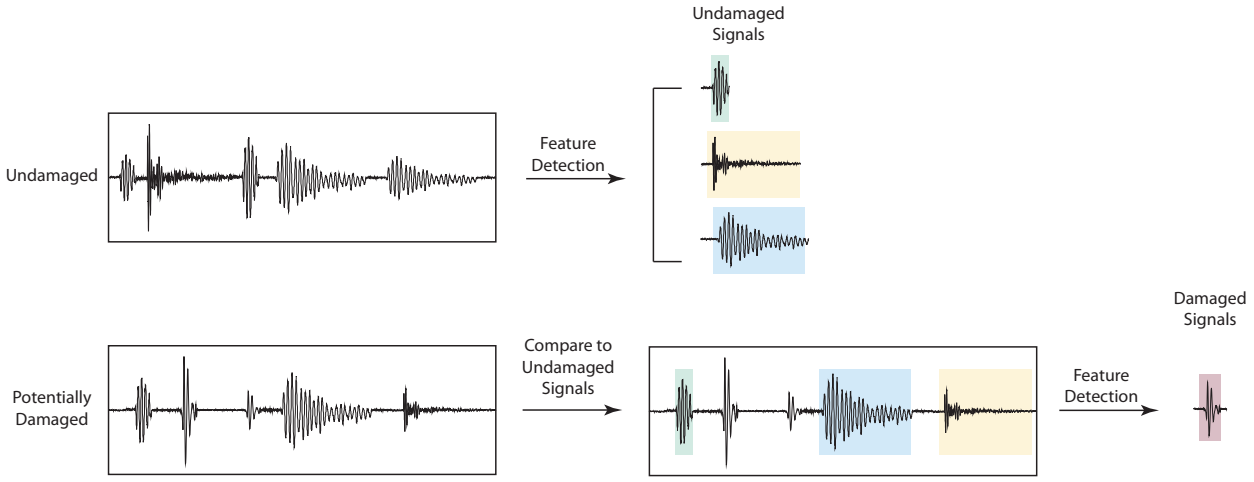

Figure 3.11: **Shear Beam: Damage Detection Method Using the Detection of Repeating Pulses.** By comparing pulses observed in the acceleration time series when the structure is in a potentially undamaged state to pulses observed when the structure was known to be in an undamaged state, changes in the dynamic behavior of the structure that could indicate damage can be identified.

was observed. The frame is subjected to a repeatable pulse at its base when it is in both an undamaged and a damaged state. The recorded accelerations, both unfiltered and high-pass filtered, are shown in Figure 3.12. The loosening of the screw allows the washer located between the head of the screw and the frame to move during loading, enough to impact the head of the bolt, on one side, or the floor column, on the other side.

In the undamaged data, shown in Figure 3.12, two distinct pulse signals are identified in the undamaged acceleration time series, and their occurrence in the time series is plotted in gray. The pulses result from the motion of the shake table, which is itself a stick-slip event of sorts. The matched filter method is applied for each identified pulse to detect its repeating presence in the high-pass filtered acceleration time series. This is done by performing a running cross-correlation that is normalized by the autocorrelation values, as given by Equations 2.1 and 2.2. Only the accelerations recorded on Floors 1-5 are used in calculating the correlation values. A threshold value of 1/3 is chosen, and whenever the cross-correlation value exceeds the threshold, the pulse is said to have been detected in the data. There is some art in choosing the threshold value; an increase in the probability of false negatives accompanies higher threshold values, and a decrease in the probability of false positives accompanies lower threshold values. The first identified signal, T_1^{UD}, occurs twice

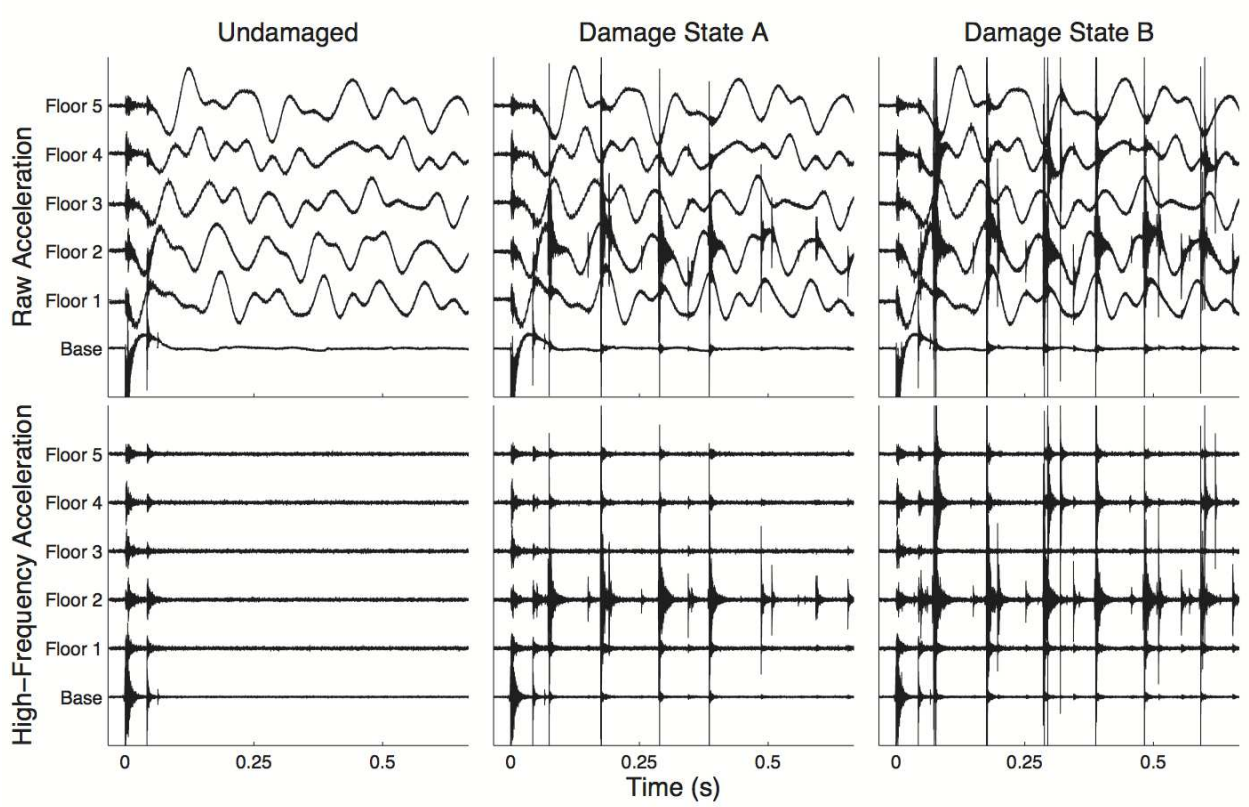

Figure 3.12: **Shear Beam: Raw and High-Frequency Accelerations.** The unfiltered and high-pass filtered (Butterworth filter, 4th order, 250 Hz) are shown above for the undamaged frame, frame with one loosened screw (Damage State A), frame with two loosened screws (Damage State B). The motion of the shake table results in a transient pulse present across all five floors. Damage results in the presence of many high-frequency pulses. The relative amplitudes have been preserved.

in the data set. The second identified signal, T_2^{UD}, occurs three times, two times during which it is embedded in T_1^{UD}.

In Damage State A, shown in Figure 3.13, the undamaged signals T_1^{UD} and T_2^{UD} are clearly identified in the data at the correct time (when the shake table supplies the initial pulse). From the remaining unidentified pulses in the Damage State A acceleration records, three damage signals, T_1^{DA}, T_2^{DA}, and T_3^{DA} are detected. These damage signals are methodically identified. First, the first unidentified pulse that appears to consist of a single event is classified as a damage signal T_1^{DA}. Similar pulses are detected in the Damage State A acceleration records by applying the matched filter method and using a threshold value of 1/3 to identify signals in the record that have a higher correlation value. The procedure is repeated using the remaining unidentified pulses until all pulses have been classified. The damage signal templates were formed using only one of the pulses, but averaging the template over the detected occurrences could improve the signal-to-noise ratio of the damage signal. The final set of three identified damage signals is used to screen the undamaged data. This is done to determine whether one of the damage signals is present in the undamaged data set, which would suggest that it be reclassified as an undamaged signal. Damage signals T_1^{DA}, T_2^{DA}, and T_3^{DA} are not detected in the undamaged data.

The identified damage signals all have the largest amplitudes and first arrival times on the Floor 2, and damage can be concluded to have originated at this floor. Damage was, in fact, introduced to this floor, to a screw on the opposite side of the accelerometers. An interesting phenomenon is observed by noting trends in the Floor 2 raw acceleration record when damage signals T_1^{DA} (yellow) and T_3^{DA} (blue) occur. T_1^{DA} (yellow) only occurs near the local maxima in the Floor 2 acceleration records, when the second floor is at its minimum displacement along the axis of shaking and is changing direction. T_3^{DA} (blue) only occurs after the local minima in the Floor 2 acceleration records, when the floor is at a maximum displacement and is beginning to change directions. Hence, two different signals are generated by two mechanisms resulting from the same source, namely the impact of the washer against either the head of the bolt or the side of the column. The damage events are nonlinear and aperiodic in nature. As the second damage signal T_2^{DA} only occurs once and has a similar

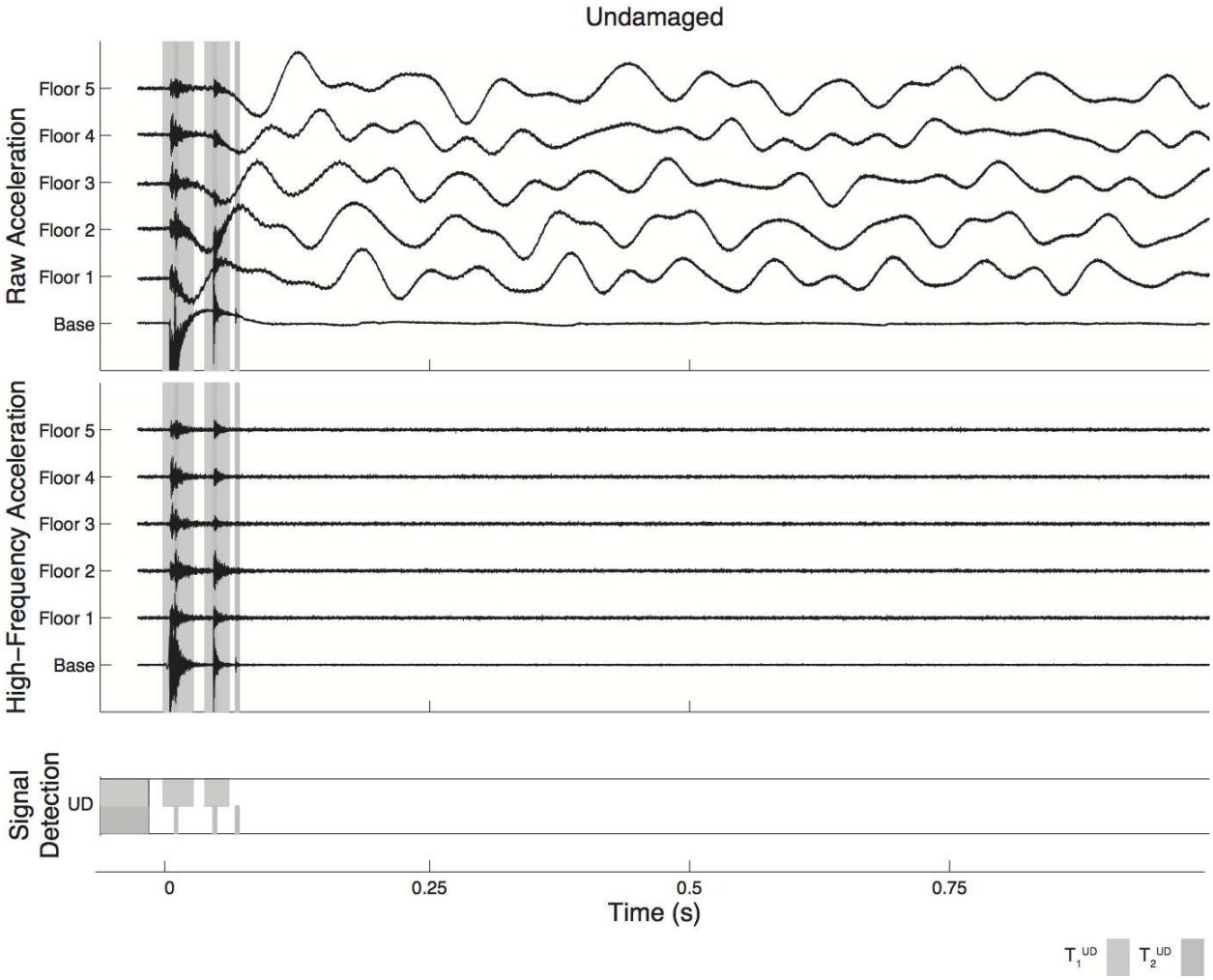

Figure 3.13: **Acceleration Pulses: Undamage Signals.** Two different pulse signals are identified in the undamaged acceleration time series, and their occurrence in the time series is plotted in gray. The pulses are due to the input pulse supplied by the shake table. A threshold value of 1/3 is chosen, and only Floors 1-5 are used in the analysis. The first identified signal, T_1^{UD}, occurs twice in the data set. The second identified signal, T_2^{UD}, occurs three times, two times during which it is embedded in the first identified signal.

waveform and time of occurrence to T_3^{DA}, it is likely that the second and third identified damage signals are generated by the same mechanism.

A second screw is loosened in Damage State B, and the acceleration records are plotted in Figure 3.15. Again, the initial pulse of the shake table is identified using the prerecorded undamaged signals T_1^{UD} and T_2^{UD}. Two of the Damage State A damage signals are also detected. From the remaining unidentified pulses in Damage State B, three different damage signals are detected, T_1^{DB} (yellow), T_2^{DB} (dark blue), and T_3^{DB} (red). Damage signal T_1^{DB} seems to initiate at Floor 2, and it occurs at similar points in the time history as T_3^{DA}. By looking for the presence of T_1^{DB} in the Damage State A data, we find that the damage signal T_1^{DB} is detected twice, while T_2^{DB} and T_3^{DB} are not detected. We conclude that T_3^{DA} and T_1^{DB} must be generated by the same source and mechanism. Both T_2^{DB} and T_3^{DB} originate and have the largest peak accelerations on the fourth floor. Moreover, they seem to occur at the local minima and maxima, respectively, in the Floor 4 acceleration records. Hence, we conclude that damage signals T_2^{DB} and T_3^{DB} are caused by two different mechanisms at the same source, namely a washer at Floor 4 impacting the head of the bolt or the side of the column. Damage was, in fact, introduced to this floor, to a screw on the same side as the accelerometers.

3.3.5 Comparison of Experimental and Theoretical Models: Undamaged Frame

There is considerable agreement between the numerical model and experimental data for the undamaged frame. A comparison of modeshapes is presented in Figure 3.16 and Table 3.3. The numerical model is computed using parameters obtained experimentally as well as parameters obtained numerically based on the material properties of aluminum and the geometry of the model. As there is much better agreement between the data and the model using the experimental parameters than there is between the data and the model using the numerical parameters, the subsequent numerical analysis is conducted using the model with the experimental parameters.

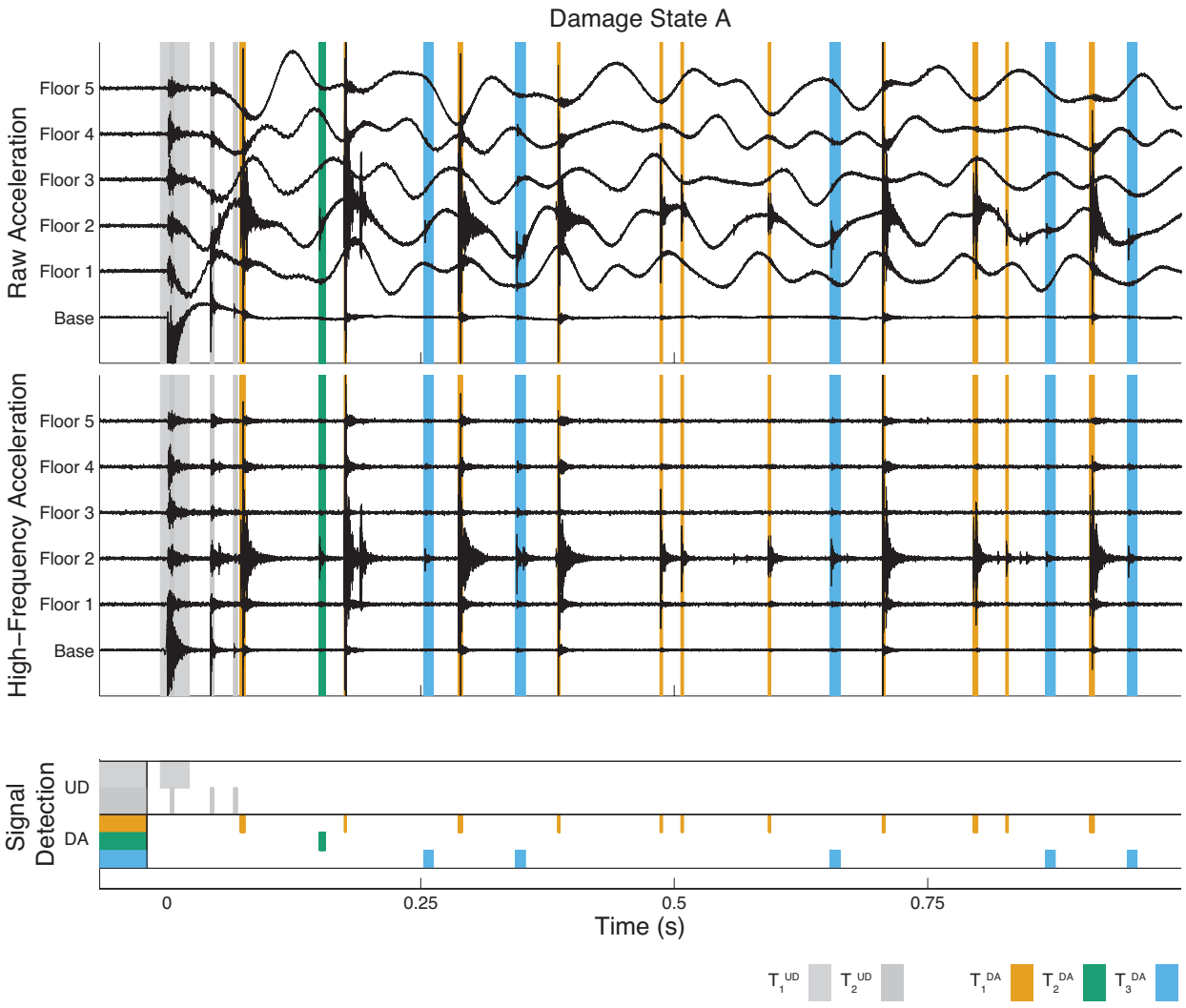

Figure 3.14: **Acceleration Pulses: Damage Signals (Damage State A).** The pulses generated by the shake table are accurately identified using the prerecorded undamaged signals T_1^{UD} and T_2^{UD}, and their occurrence is highlighted in gray. Undamaged signal T_1^{UD} is detected once in the data set, and T_2^{UD} is detected three times, one time during which it is embedded in T_1^{UD}. Damage signals are generated by a washer between the head of the loosened screw and the frame that is able to move when the screw is loosened. Three damage signals, T_1^{DA} (orange, 11 occurrences), T_2^{DA} (green, 1 occurrence), and T_3^{DA} (blue, 5 occurrences) are detected based on the unidentified pulses. The damage signals all have the largest amplitudes and first arrival times on the Floor 2, and damage can be concluded to have originated at this floor. Damage signals T_1^{DA} and T_3^{DA} appear to be caused by different mechanisms. An interesting phenomenon is observed by noting trends in the Floor 2 raw acceleration record when damage signals T_1^{DA} (yellow) and T_3^{DA} (blue) occur. Damage signal T_1^{DA} (yellow) only occurs near the local maxima in the Floor 2 acceleration records, when the second floor is at its minimum displacement along the axis of shaking and is changing direction. T_3^{DA} (blue) only occurs after the local minima in the Floor 2 acceleration records, when the floor is at a maximum displacement and is beginning to change directions. Hence, two different signals are generated by two mechanisms resulting from the same source, namely the impact of the washer against either the head of the bolt or the side of the column. The damage events are nonlinear and aperiodic in nature. It is likely that the second and third identified damage signals are generated by the same mechanism.

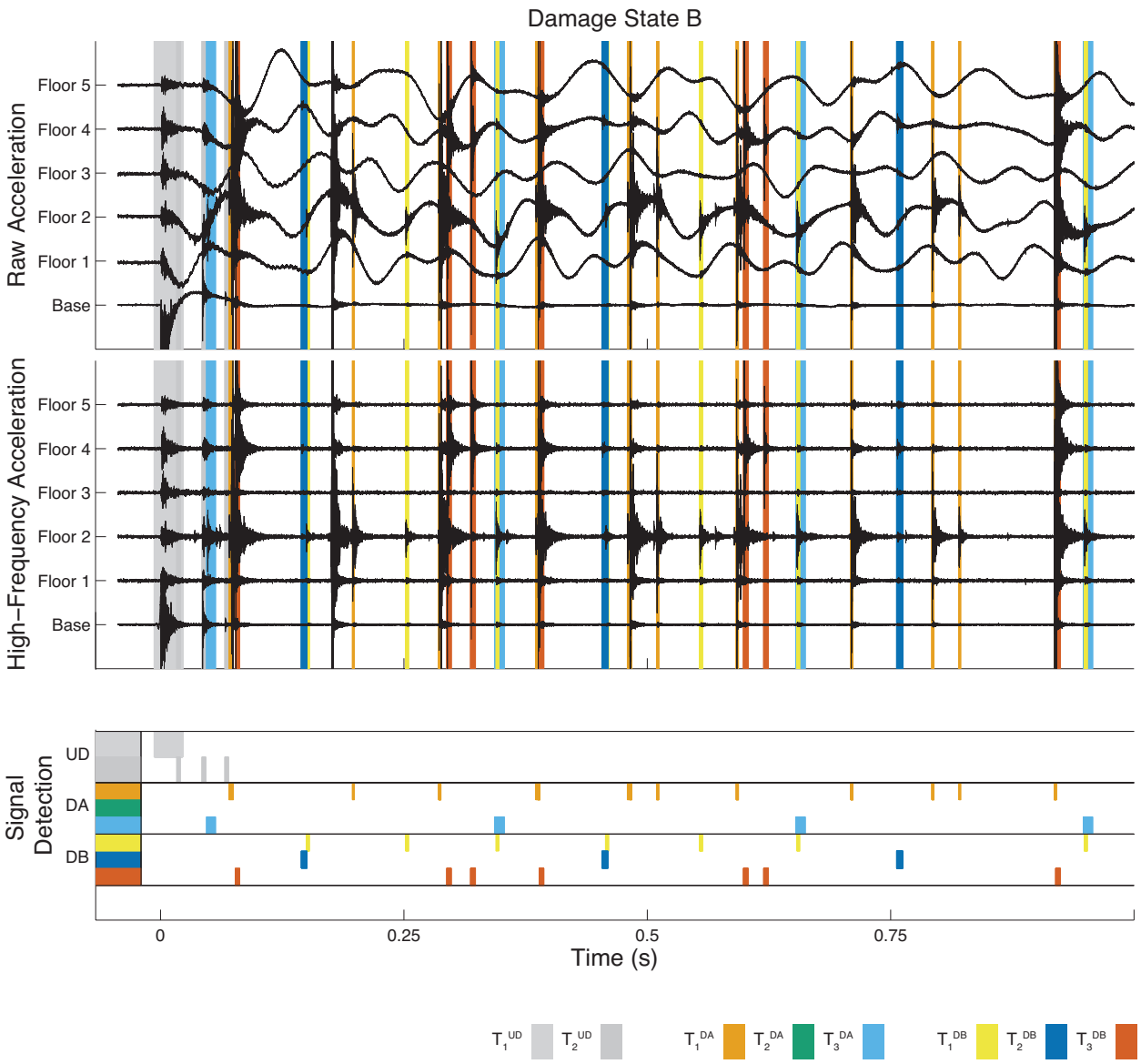

Figure 3.15: **Acceleration Pulses: Damage Signals (Damage State B).** The initial pulse of the shake table is identified using the prerecorded undamaged signals, and the occurrence of the undamaged signals is highlighted in gray. Again, the first undamaged signal T_1^{UD} appears once in the data set, and the second undamaged signal T_2^{UD} occurs three times, one time during which it is embedded in the first signal. Two of the Damage State A damage signals are detected, with 11 detected occurrences of T_1^{DA} (orange) and four detected occurrences of T_3^{DA} (light blue). From the remaining unidentified pulses in Damage State B, three different damage signals are detected. Damage signal T_1^{DB} (yellow) occurs seven times, T_2^{DB} (dark blue) occurs three times, and T_3^{DB} (red) occurs seven times. Damage signal T_1^{DB} seems to initiate at Floor 2, and it occurs at similar points in the time history as T_3^{DA}. Hence, it is likely that this signal is caused by the same source and mechanism that causes T_3^{DA}. This is tested by looking for the presence of T_3^{DA} in the Damage State A data. In the Damage State A data, the damage signal T_3^{DA} shows up two times, while T_1^{DA} and T_2^{DA} show up zero times, and we conclude that T_3^{DA} and T_1^{DB} are generated by the same source and mechanism. Both T_2^{DB} and T_3^{DB} originate and have the largest peak accelerations on the fourth floor. Moreover, they seem to occur at the local maxima and minima in the Floor 4 acceleration records. Hence, we conclude that damage signals T_2^{DB} and T_3^{DB} are caused by two different mechanisms at the same source, namely a washer at Floor 4 impacting the head of the bolt or the side of the column.

There is considerable consistency in the response of the structure between different experimental trials. The raw acceleration waveforms recorded in three different trials are compared in Figure 3.3 for both a damaged and undamaged frame. Both the shape and amplitude of the resulting accelerations show considerable consistency for the shear wave that propagate within the structure. There is greater agreement between different trials for the undamaged frame than there is for the damaged frame. There is a seemingly stochastic occurrence of transient signals in the undamaged trial that may be due to slipping and impact between different structural members in the shear beam that lead to momentarily high accelerations.

Mode	Observed	Experimental Parameters		Numerical Parameters	
		Undamped	Damped	Undamped	Damped
1	3.27 Hz	3.38 Hz	3.38 Hz	2.47 Hz	2.47 Hz
2	9.62 Hz	9.85 Hz	9.82 Hz	7.20 Hz	7.19 Hz
3	15.27 Hz	15.52 Hz	15.45 Hz	11.36 Hz	11.31 Hz
4	19.97 Hz	19.94 Hz	19.79 Hz	14.59 Hz	14.49 Hz
5	22.43 Hz	21.74 Hz	21.54 Hz	16.64 Hz	16.49 Hz

Table 3.3: **Natural Frequencies of the Undamaged Shear Beam.** The 'Observed' natural frequencies are those experimentally observed during dynamic testing of the structure with an impulse input at the base. The theoretical natural frequencies are computed using a five-degree-of-freedom model. Both the experimentally-determined parameters (weighing the floor mass, static tilt test to determine the global stiffness value) and theoretically-determined parameters (using the geometry and material properties of aluminum) are used. Proportional modal damping is assumed, with 2% for the first mode. Good agreement is shown between the observed data and the theoretical data (using the experimentally-determined parameters).

The natural frequencies (Figure 3.18 and Table 3.4), damping values (Table 3.5), and mode shapes (Figure 3.19) for the damaged frame are obtained using the eigensystem realization algorithm (ERA) (Juang and Pappa, 1985). The ERA consists of two major parts, basic formulation of the minimum-order realization and modal parameter identification. Note that the process of constructing a state space representation from experimental data is called system realization. As expected, with increasing damage, there is a decrease in natural fre-

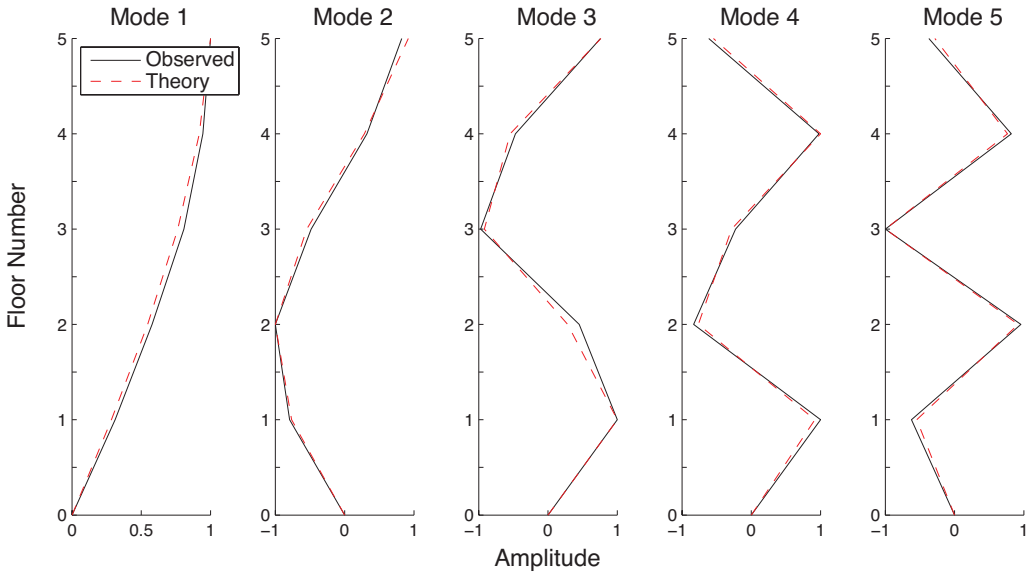

Figure 3.16: **Shear Beam: Analytical vs. Experimental Modeshapes.** There is good agreement between the observed and modeled modeshapes of the undamaged uniform shear beam. The theoretical mode shapes were computed using experimentally-obtained parameters.

quencies and and increase in damping.

3.4 Conclusion

The effect of damage on the dynamic response of a civil structure was investigated experimentally using a small-scale (0.75 meter tall) shear beam. Damage was introduced into the shear beam by loosening the bolts connecting the columns to the floor, and a shake table was used to apply a consistent pulse at the base of the beam. The main findings of this chapter are outlined below:

1. A dynamic pulse was input at the base of the shake table. High-frequency acceleration records could be used to immediately determine the presence and location of damage, based on the presence of short-duration high-frequency signals caused by mechanical impact and slippage. Low-frequency acceleration records could also be used to immediately determine the location of damage (i.e., which floor), based on the delayed arrival times and amplitudes of the initial shear wave.

2. A damage detection method that is based on detecting pulses in both the undamaged and potentially damaged acceleration records was found to be successful in detecting the nonlinear, aperiodic occurrences of damage signals. The arrival times and amplitudes were used to determine which floor was damaged. The advantage this strategy has over current strategies is that it can detect early onset damage. It is also based on the physical mechanism of damage in the structure, namely wave propagation, and energy formulations or the combination of the method with a time-reversed reciprocal method could give more information about the damage mechanism. The obvious disadvantage is that if there are no pulses (due to not using a high-enough sampling rate, or the absence of such a signal), the method will not work. Another disadvantage is that the method cannot be used to determine the amount of damage (e.g., loss of stiffness), it can only detect the occurrence of signals that may indicate damage. The method could be combined with a vibration-based method.

3. A static tilt test was performed to estimate the severity of damage for Levels 1, 2, and 3. The amount of damage was found to range from moderate to severe levels, with estimated stiffness parameter k_d/d_{ud} ranging from 0.27 to 0.74. The estimated shear wave speeds obtained during dynamic testing were used to quantify the amount of damage, and the level of damage was estimated to be less severe than the values obtained from the stiffness test. The mean values (and standard deviations) of the estimated inter-story lateral stiffnesses immediately beneath the damaged floor for Damage Levels 1, 2, and 3, respectively, were found to be 0.93 (0.03), 0.70 (0.1), and 0.82 (0.23). The mean values (and standard deviations) of the estimated inter-story lateral stiffness immediately above the damaged floor for Damage Levels 1, 2, and 3, respectively, were found to be 0.94 (0.03), 0.67 (0.09), and 0.80 (0.24). The mean values (and standard deviations) of the estimated inter-story lateral stiffness in floors not immediately above or below the damaged floor were calculated to be 0.99 (0.03), 0.95 (0.07), and 0.96 (0.05). The dynamic estimates could be improved by considering a longer portion of the time series. The values could be tested using forward modeling

Damaged Floor	Damage Level	Mode Number 1st	2nd	3rd	4th	5th
-	0	3.25 Hz	9.72 Hz	15.38 Hz	20.10 Hz	22.52 Hz
1	1	2.77 Hz	9.18 Hz	14.77 Hz	18.79 Hz	22.09 Hz
	2	2.64 Hz	9.04 Hz	14.40 Hz	18.41 Hz	22.17 Hz
	3	2.59 Hz	9.07 Hz	14.27 Hz	18.50 Hz	22.32 Hz
2	1	2.86 Hz	9.60 Hz	14.50 Hz	18.95 Hz	22.11 Hz
	2	2.30 Hz	9.49 Hz	13.58 Hz	18.12 Hz	21.44 Hz
	3	2.30 Hz	9.18 Hz	13.44 Hz	16.74 Hz	21.02 Hz
3	1	3.09 Hz	9.13 Hz	14.91 Hz	19.64 Hz	21.19 Hz
	2	2.71 Hz	8.28 Hz	14.14 Hz	19.29 Hz	20.42 Hz
	3	2.50 Hz	7.71 Hz	13.67 Hz	18.63 Hz	20.40 Hz
4	1	3.11 Hz	8.39 Hz	14.44 Hz	18.29 Hz	22.21 Hz
	2	2.84 Hz	7.12 Hz	12.97 Hz	16.84 Hz	21.46 Hz
	3	2.79 Hz	6.79 Hz	12.35 Hz	15.58 Hz	21.27 Hz
5	1	3.25 Hz	9.25 Hz	14.22 Hz	19.00 Hz	22.16 Hz
	2	3.19 Hz	8.22 Hz	12.72 Hz	18.40 Hz	22.01 Hz
	3	3.16 Hz	7.52 Hz	12.30 Hz	18.26 Hz	22.03 Hz

Table 3.4: **Shear Beam: Observed Natural Frequencies (Damaged and Undamaged Frame).** The natural frequencies were determined using the ERA from the IRF generated by inputing a pulse at the base of the structure with a sampling rate of 1000 sps. As expected, there are considerable decreases in the natural frequencies with increasing levels of damage.

by determining the accompanying natural frequencies and mode shapes and comparing those with the observed ones.

4. The modal response of the structure was found to be highly consistent between trials, though the introduction of damage results in the presence of transient signals that generally originate at the damaged floor. A decreased transmission through the damaged floor of the high-frequency motion generated by the shake table was also observed.

Damaged Floor	Damage Level	Mode Number 1st	2nd	3rd	4th	5th
-	0	0.016	0.005	0.004	0.003	0.005
1	1	0.019	0.005	0.007	0.008	0.004
	2	0.019	0.013	0.009	0.006	0.015
	3	0.026	0.016	0.008	0.010	0.022
2	1	0.031	0.010	0.009	0.013	0.011
	2	0.077	0.026	0.022	0.022	0.008
	3	0.076	0.017	0.029	0.015	0.002
3	1	0.010	0.010	0.003	0.006	0.026
	2	0.025	0.020	0.007	-0.003	0.010
	3	0.018	0.028	0.018	0.010	0.012
4	1	0.019	0.017	0.004	0.015	0.015
	2	0.025	0.023	0.022	0.020	0.003
	3	0.028	0.027	0.028	0.034	0.004
5	1	0.017	0.010	0.010	0.001	0.006
	2	0.015	0.025	0.015	0.003	0.002
	3	0.032	0.034	0.022	0.004	0.006

Table 3.5: **Shear Beam: Observed Modal Damping Ratios (Damaged and Undamaged Frame).** The modal damping ratios were computed using ERA from the IRF generated by inputing a pulse at the base of the structure with a sampling rate of 1000 sps. As expected, there are considerable increases in the damping ratios, though the structure is very lightly damped.

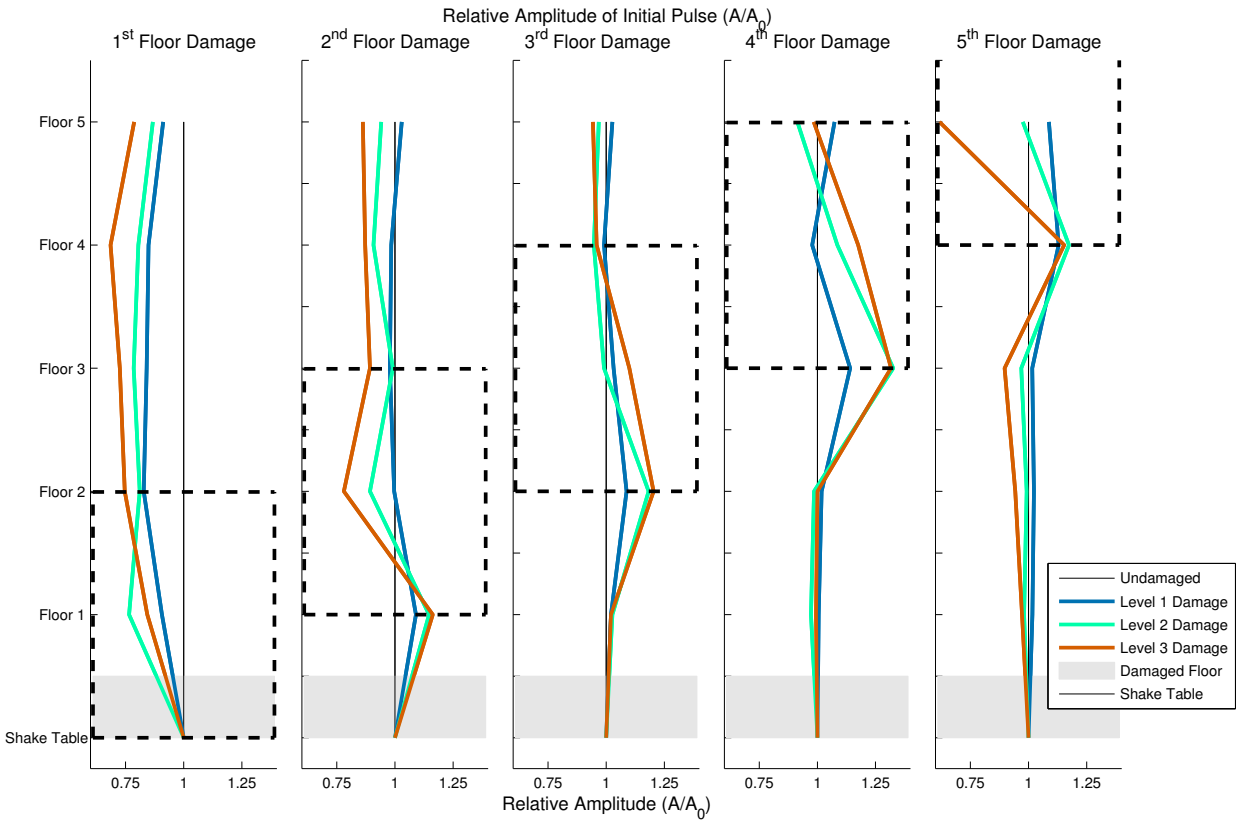

Figure 3.17: **Amplitude of Initial Shear Wave Pulse.**The amplitude of the initial shear wave pulse can be an immediate indicator of loss of stiffness, though it can be difficult to measure due to the presence of the transient signals. The amplitude is estimated from data recorded at 150 ksps.

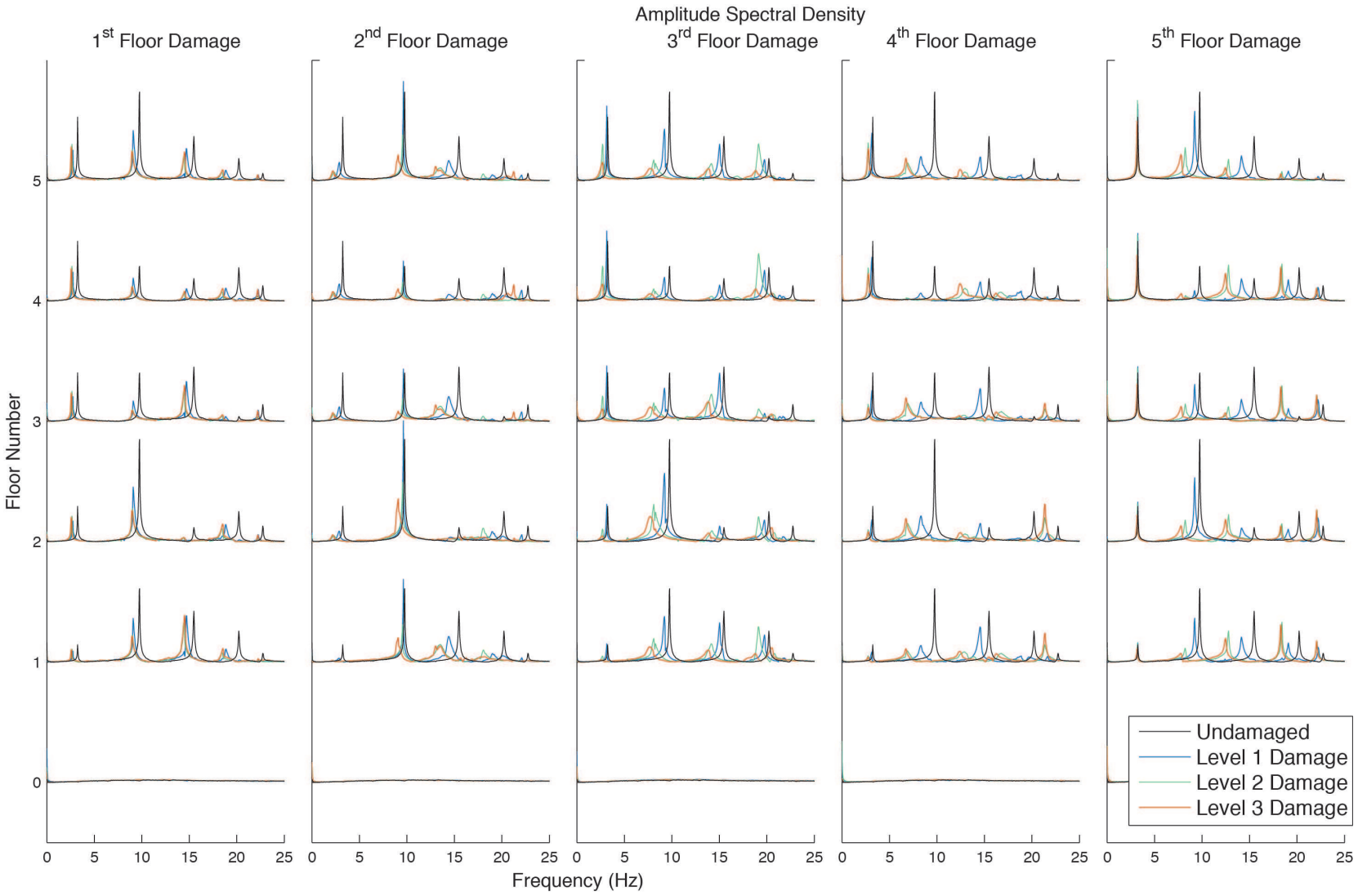

Figure 3.18: **Experimental Shear Beam: Frequency Response Function.** Recorded at 1 ksps.

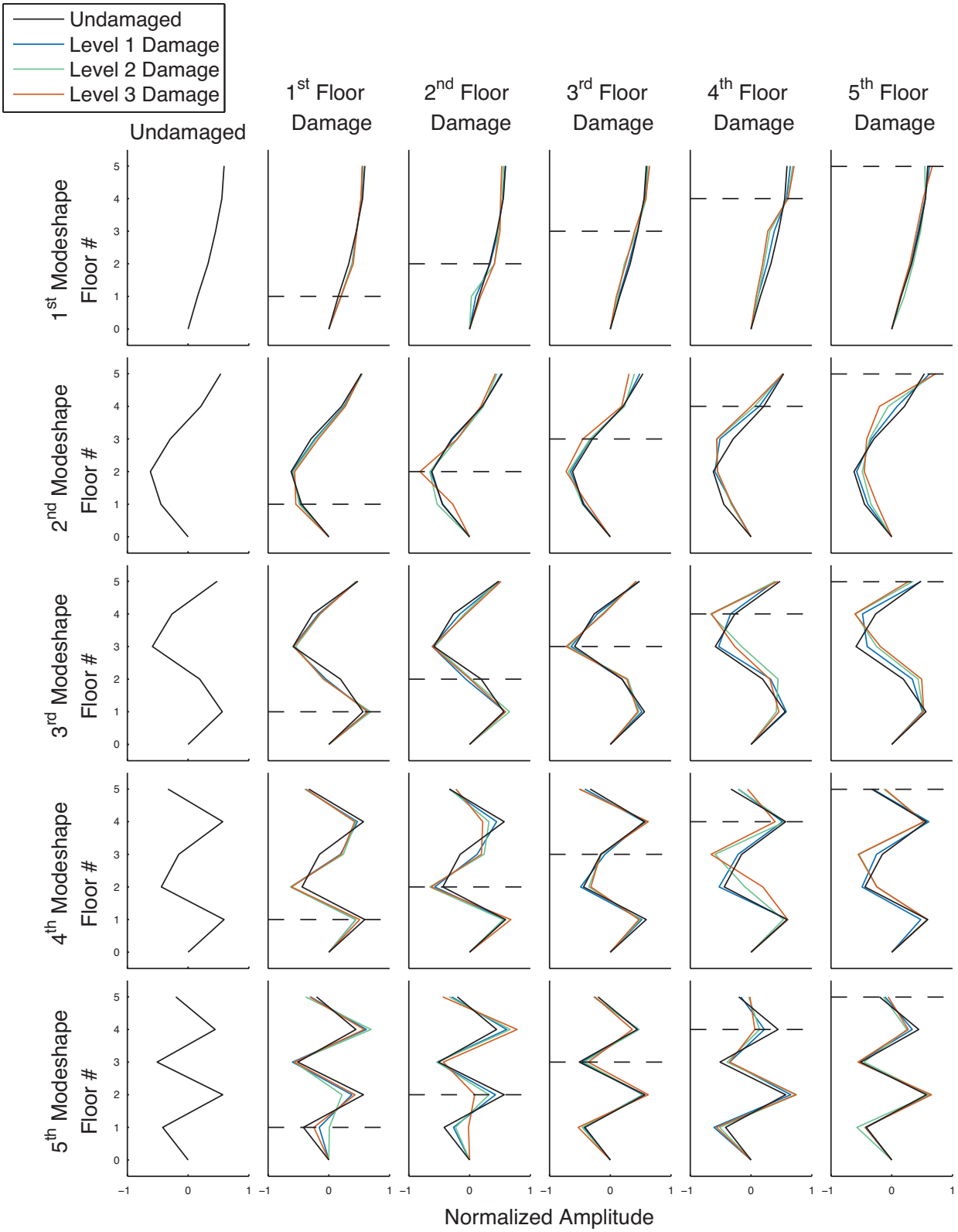

Figure 3.19: **Experimental Shear Beam: Modeshapes (Damaged and Undamaged).** Experimental modeshapes of the undamaged uniform shear beam.

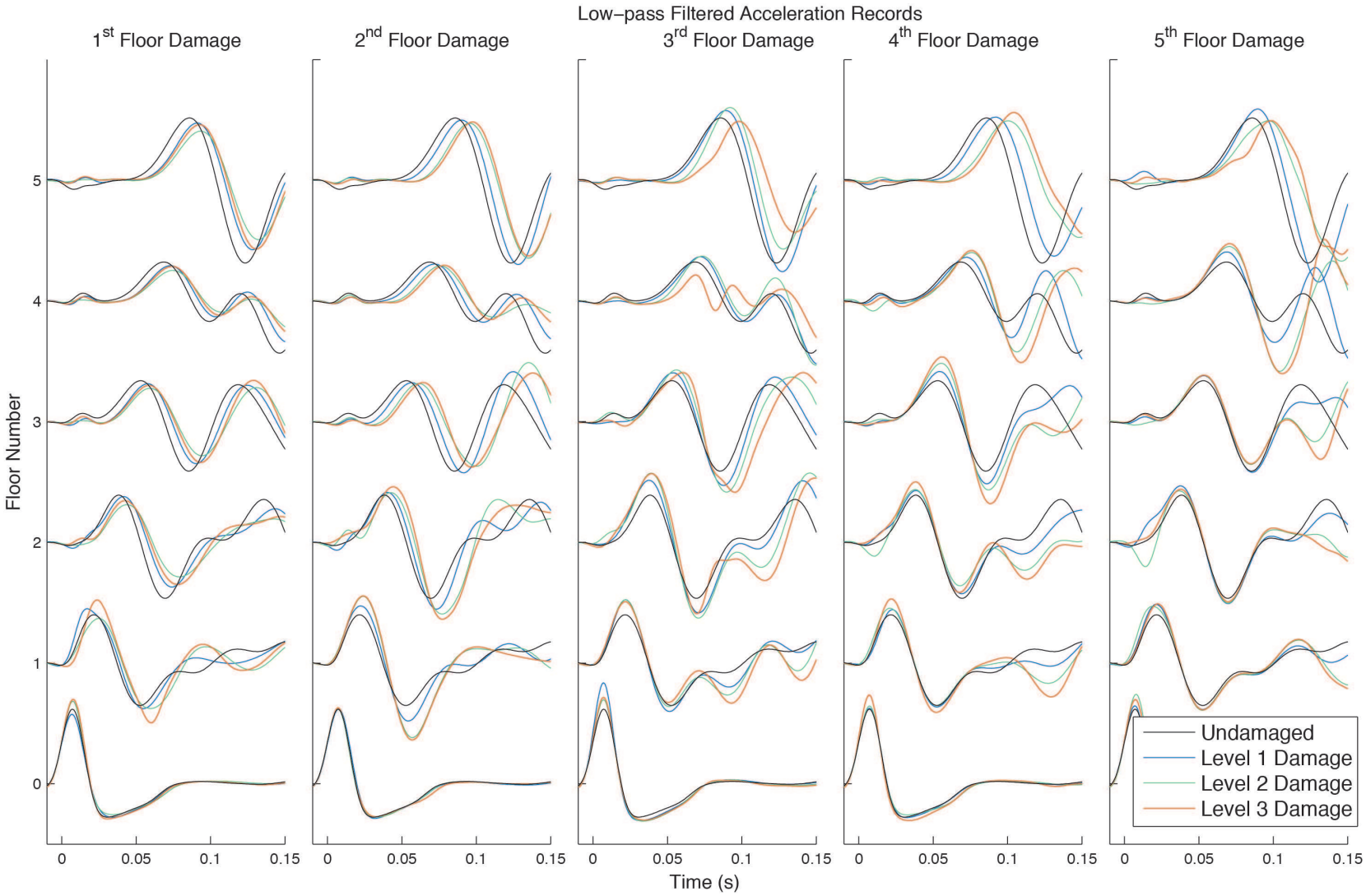

Figure 3.20: **Low-Frequency Component of Accelerations.** Recorded at 1 ksps.

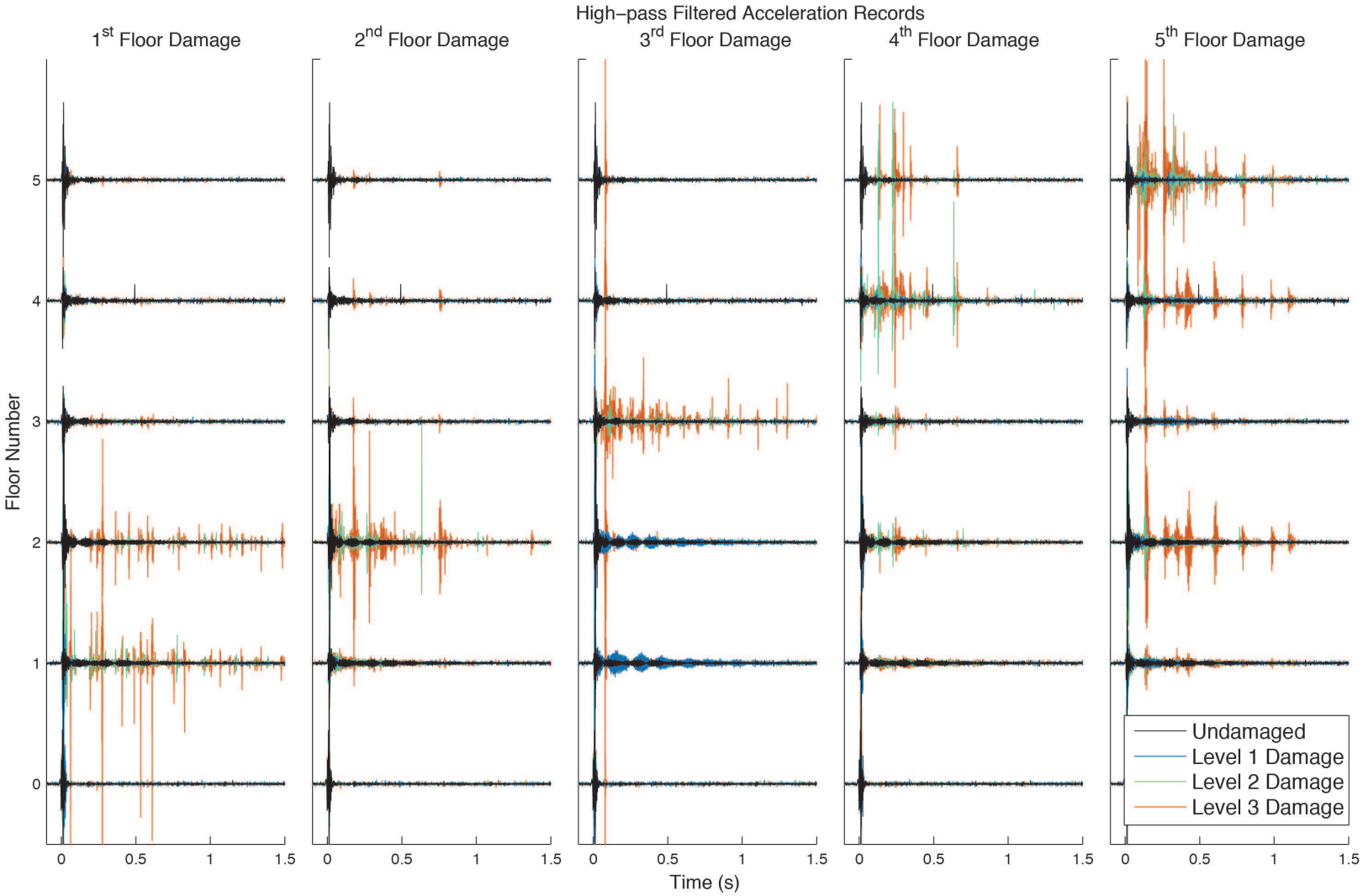

Figure 3.21: **High-Frequency Component of Accelerations.** Recorded at 1 ksps.

Chapter 4

Numerical Study: Time-Reversed Reciprocal Method and Damage Detection Method for Weld Fracture

A numerical study is performed to gain insight into applying the proposed method of detecting high-frequency dynamic failure in steel moment-resisting frame buildings that is outlined in Chapter 2. The method relies on a prerecorded catalog of impulse response functions for instrumented buildings. Structural failure during a seismic event is detected by screening continuous data for the presence of waveform similarities to each of the cataloged building responses.

The motivation for this method is described by Kohler et al. (2009). Weld fracture is represented as an opening tensile crack, with a step-like time history. Following the body-force equivalent source method in seismology, the weld fracture is approximated as a localized region that experiences very large elastic tensile strains, and a seismic moment tensor (for a point tensile crack) is used to characterize the source. The response of the structure is given by convolution of the forcing term with the spatial derivative of the structure's Green's functions. If the response of the structure is represented as a sum of rays, each traveling with a constant velocity, then the spatial derivative of the Green's functions is equal to the time-derivative of the Green's function, multiplied by a constant. Under this assumption, the response of the structure is thus given by a linear combination of delta functions convolved

with the Green's functions. This is a simplification of building behavior, and it must first be determined whether a Green's function can be used to approximate the response to bolt failure.

In the first part of the study, a steel frame's response to two loading cases, an impulse-like force and an opening crack tensile stress (Mode I crack), is computed on a temporal scale of microseconds. Results indicate that the velocity waveform generated by a tensile crack can be approximated by the velocity waveform generated by an impulse-like force load applied at the proper location. These results support the idea of using a nondestructive impulse-like force (e.g. hammer blow) to characterize the building response to high-frequency dynamic failure (e.g. weld fracture). However, the method may not be robust to noise, and may be better suited for damage localization.

In the second part of this numerical study, a time-reversed reciprocal method is applied to the frame. An impulse-like force is applied to a beam column connection in a linear elastic steel frame, and the resulting displacements are then used to determine the absolute time and location of the initially applied force. Time-reversal methods have seen success in other fields as well as for plate-like structures, where the presence of flexural waves renders perfect recovery impossible, but have yet to be applied to full-scale civil structures (Fink, 1992; Tromp et al., 2005; Wang et al., 2004).

4.1 Comparison of Structural Response to Two Different Source Conditions

The responses of a steel frame to two different loading cases, an impulse-like force and an opening crack tensile stress, both shown in Figure 4.1, are compared to determine whether the waveform generated by the nondestructive source can be used to approximate the waveform generated by the structurally damaging source. First, the response of a two-story one-bay steel frame to an impulse-like force applied to a beam-column connection is computed. A cross section of the three-dimensional steel model is shown in Figure 4.3. Each beam and

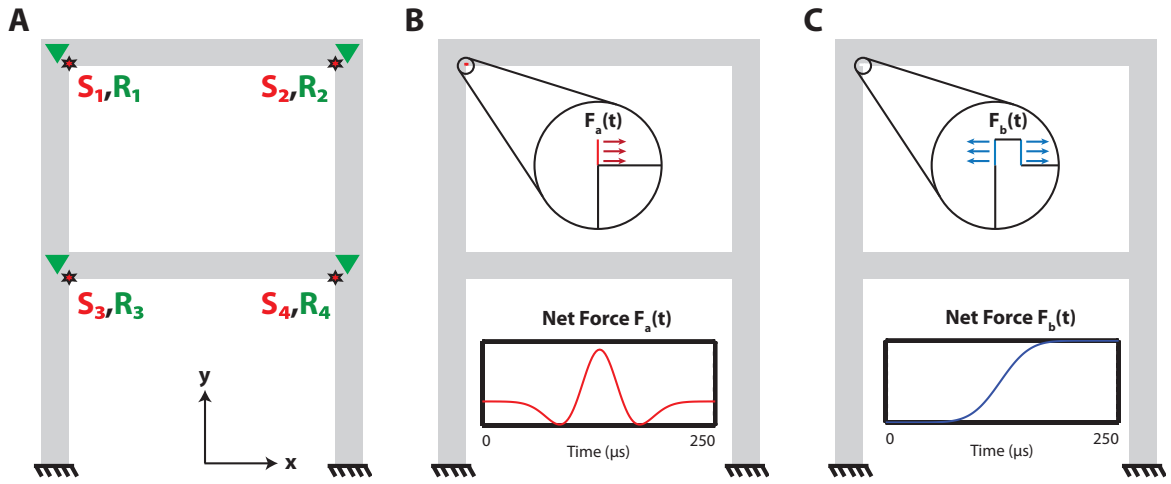

Figure 4.1: **Numerical Setup. A.** Receiver and source locations on the frame. **B.** Impulse-like force using Ricker wavelet force-time history applied to top left beam-column connection in an unnotched frame, and **C**. Opening crack tensile stress using error function force-time history applied to the same connection in a notched frame.

column has a square cross section of length 0.5 m. The model parameters are governed by linear elastic material properties of A36 structural steel ($E = 200GPa$, $\mu = 80GPa$, $\rho = 7850kg/m^3$), which correspond to shear and compression wave velocities of $c_s = 3.2km/s$ and $c_p = 5.6km/s$. The hex 8 mesh elements have a discretization length of 2.5 cm; the total time is 4 ms with a time step of 2 μ s. CUBIT is used for mesh generation, PyLith for physics code, and ParaView for visualization (Aagaard et al., 2008, 2013). A square notch is introduced in the opening crack tensile stress case, to simulate crack initiation at the beam-column connection. The square notch has a length of 0.05 m, consistent with the dimensions used for the unnotched frame.

Resulting displacements and velocities are recorded at four receivers located along the central cross section of the frame, shown in Figure 4.1. The simulation is repeated at each of the four source locations for both a force impulse and a tensile crack.

As seen in Figure 4.2, the displacement records generated by using the nondestructive source differ significantly from the displacement records generated by using the structurally damaging sources, primarily due to the static offset created across the notch. The two sets of

velocity records are more similar to each other than are the two sets of displacement records. The similarities between force impulse and tensile crack velocity waveforms underscore the fact that, for traveling elastic waves, the strains are proportional to their associated particle velocities, regardless of the source mechanism. Thus, the template is created using the velocity record.

4.1.1 Stacked Cross-Correlation Values

A stacked cross-correlation method is used to determine the similarity of velocity waveforms generated by a force impulse at source location S_k and a tensile crack at source location S_l. The summarized method follows:

1. A set of velocities $\{v_1^k(t), v_2^k(t), v_3^k(t), v_4^k(t)\}$ are recorded for a force impulse applied at source location S_k, where $v_i^k(t)$ is the three-component velocity vector recorded at the i^{th} receiver. Due to symmetry and the fact that the receivers are located along the central cross section of the frame, the z-component of the velocity vector is zero.

2. The set of envelopes $\{e_1(t), e_2(t), e_3(t), e_4(t)\}$ is computed using the velocities. The magnitude of each 3-component envelope is passed through a low-pass filter to produce a set of scalar functions of time $e_1^k(t), e_2^k(t), e_3^k(t), e_4^k(t)$. These records are archived as our template signals for damage caused at the k^{th} source location. The duration of our template is time T.

3. Similarly, a set of scalar filtered envelopes for a tensile crack at the lth source location Sl are computed: $\{\tilde{e}_1(t), \tilde{e}_2(t), \tilde{e}_3(t), \tilde{e}_4(t)\}$.

4. For simplicity, pad each record $\{\tilde{e}_1(t), \tilde{e}_2(t), \tilde{e}_3(t), \tilde{e}_4(t)\}$ with a duration of T zeros at both the beginning and end, and compute the cross-correlation value for each receiver

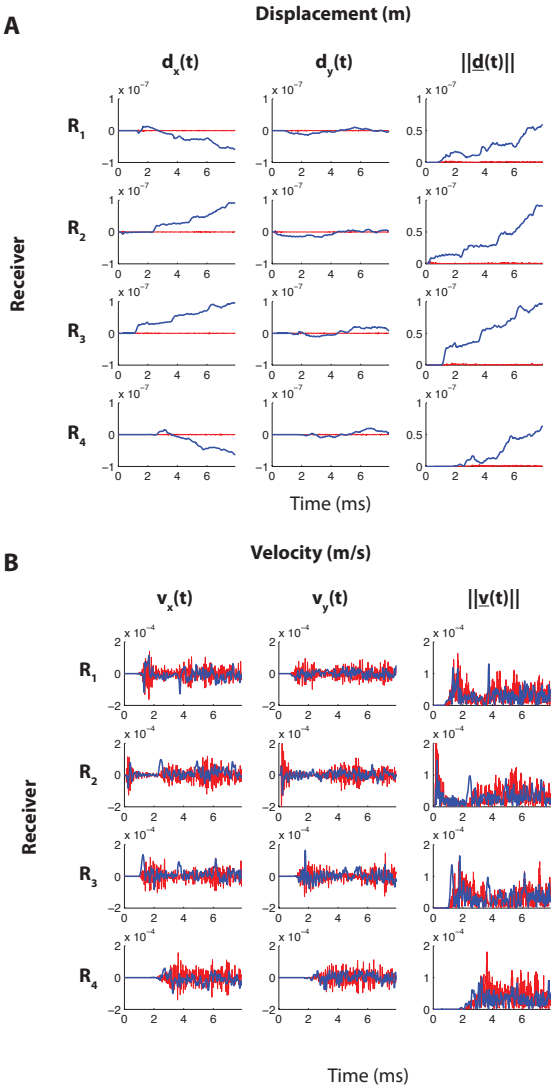

Figure 4.2: **High-Frequency Seismograms A.** Each type of source (impulsive force - red and tensile stress - blue) is applied at source location S_1. Displacements differ significantly between the two cases. **B.** Velocities provide a better agreement, and polarity differences are improved by taking the absolute value or magnitude of the record. Due to symmetry, $d_z = v_z = 0$.

Force Impulse Source Location		Tensile Crack Source Location			
		S_1	S_2	S_3	S_4
	S_1	**0.92**	0.78	0.79	0.84
	S_2	0.78	**0.92**	0.84	0.79
	S_3	0.77	0.92	**0.91**	0.81
	S_4	0.88	0.77	0.81	**0.91**

Table 4.1: **Numerical Steel Frame: Maximum Stacked Cross-Correlation Values.** The response (velocity) of the frame to a hammer blow and to an opening crack are computed, and the envelopes are calculated. The cross-correlations are computed and stacked over the number of receivers, and the maximum values of the stacked cross-correlations are shown here.

location as given by

$$C_i^{kl} = \frac{\max_{t\in(-T,2T)} \int_0^T e_i^k(\tau)\tilde{e}_i^l(t+\tau)\,d\tau}{\sqrt{\int_0^T (e_i^k(\tau))^2\,d\tau \int_0^T (\tilde{e}_i^l(t+\tau))^2\,d\tau}}. \tag{4.1}$$

5. Compute the stacked cross-correlation value by summing over all four receiver locations to obtain

$$C^{kl} = \frac{1}{4}\sum_{i=1}^{4} C_i^{kl}. \tag{4.2}$$

The maximum value of C^{kl} occurs near time t = 0, and is recorded in the k^{th} row and l^{th} column in Table 4.1 below. Correlation values are highest when the location of the tensile crack and the location of the force impulse are the same. However, as the off-diagonal values are also close to unity, the method may not be robust to noise, and may be better suited for damage localization.

4.2 A Time-Reversed Reciprocal Method

A time-reversed reciprocal method is applied to demonstrate that the location of a nondestructive impulse-like force can be determined by using the numerically computed displacement records to time-reverse and retransmit the signal. First, the response of a two-story one-bay steel frame to an impulse-like force applied to a beam-column connection is computed. A cross section of the three-dimensional steel model is shown in Figure 4.3. Each

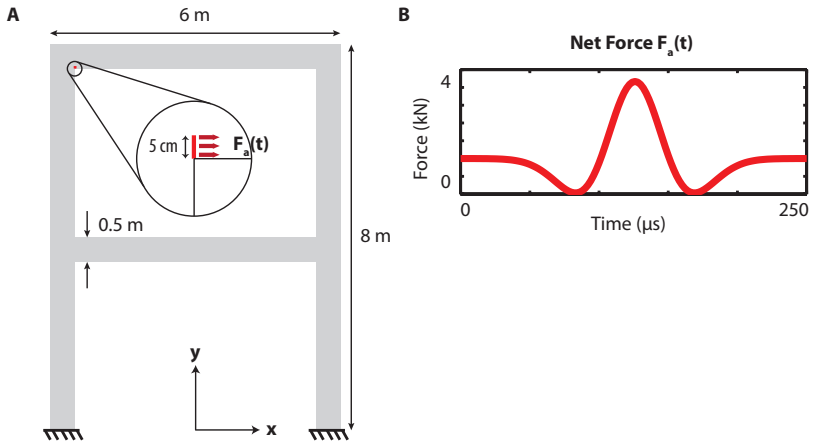

Figure 4.3: **Numerical Setup for Steel Frame.A.** Impulse-like force is applied at beam-column connection in a direction parallel to the x-axis. **B.** Ricker wavelet is used for time-force history.

beam and column has a square cross section of length 0.5 m. The model parameters are governed by linear elastic material properties of A36 structural steel ($E = 200GPa$, $\mu = 80GPa$, $\rho = 7850kg/m^3$), which correspond to shear and compression wave velocities of $c_s = 3.2km/s$ and $c_p = 5.6km/s$. The hex 8 mesh elements have a discretization length of 2.5 cm; the total time is 4 ms with a time step of 2 μs.

4.2.1 Forward Simulation

The response of the steel frame to an impulse-like force applied to a beam-column connection is computed. As can be seen in Figure 4.3, the force is applied along the positive x-axis to the close-up section of the connection. The total force is distributed proportionally over nodes according to the amount of surface area contained by each node. The force-time history is a Ricker wavelet. Waves propagate away from the location of the source, reflecting off the edges of the frame, as shown in Figure 4.4 below. Resulting displacements are recorded at the twelve receiver locations approximately evenly spaced along the central cross section of the frame. A representative sample of displacements is provided in Figure 4.5.

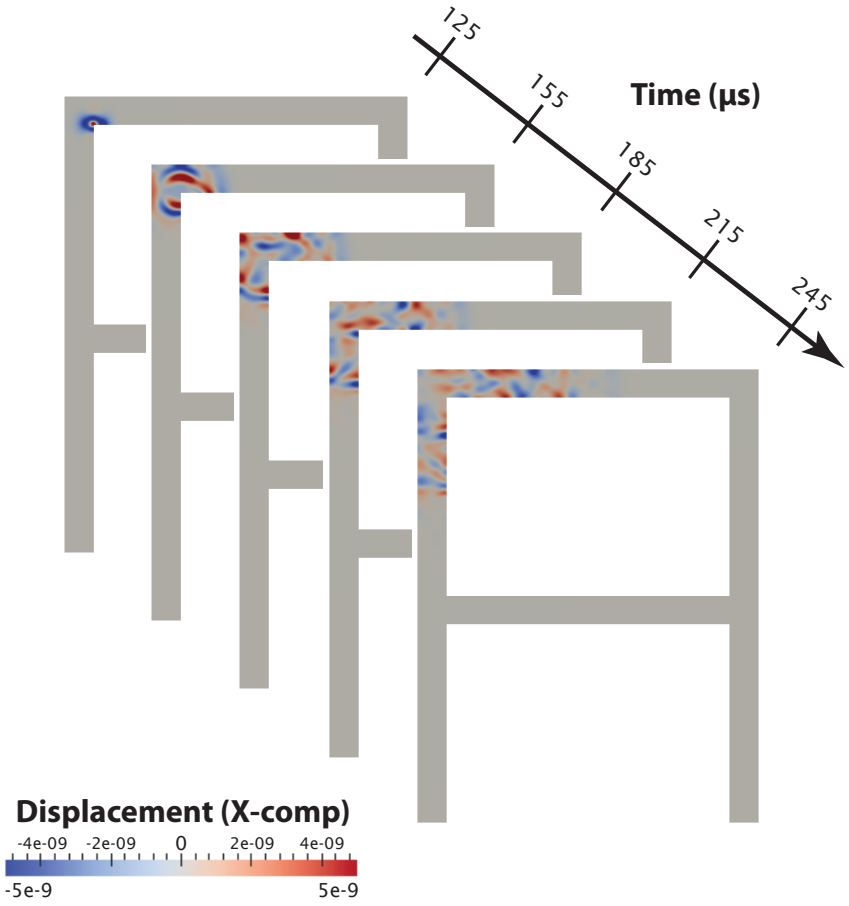

Figure 4.4: **Forward Simulation: Response of Steel Frame to Hammer Blow.** The response of the frame to a hammer blow applied at the upper left corner is computed.

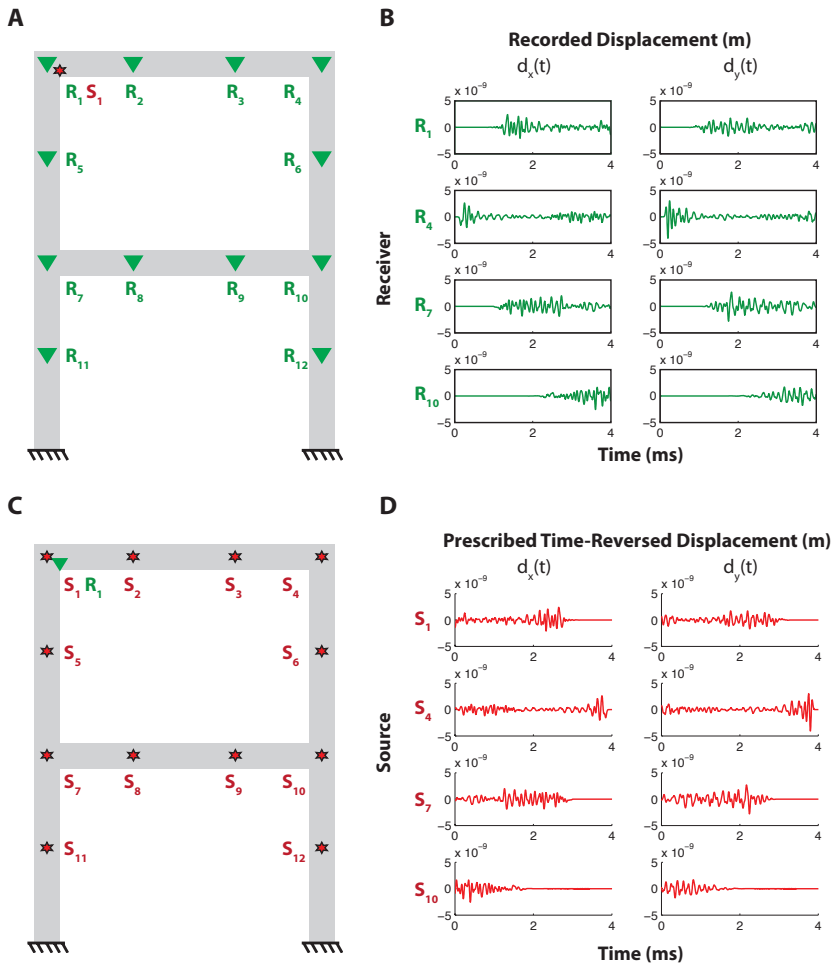

Figure 4.5: **Receivers, Sources, and Displacements A.** Receiver locations and examples of recorded displacements for forward simulation.**B.** Source locations and corresponding prescribed time-reverse displacements for reverse simulation. Due to symmetry, $d_z(t) = 0$.

4.2.2 Reverse Simulation

Following the time-reversed reciprocal method, the receiver and source locations are interchanged, and each of the displacement records is time-reversed and applied at the respective new source location as prescribed Dirichlet conditions, as shown in Figure 4.5 (b) above. The retransmitted signal propagates through the frame, and the waves generated by the twelve new source locations interfere constructively to focus at the original source location S_1, where the nondestructive load was applied, and at the correct time. To simplify timing, the reverse simulation begins at -4 ms and ends at 0 ms, with waves focusing on the beam-column connection at the correct time of -125 μs. Thus, by using a time-reversed reciprocal method, the recorded displacements are used to successfully determine the absolute time and location of the original applied force.

4.3 Conclusions

To numerically test a method for damage detection, a steel frame's response to two loading cases, an impulse-like force and an opening crack tensile stress (Mode I crack), was computed on a temporal scale of microseconds. It was found that the velocity waveform of a tensile crack can be approximated by the velocity waveform of an impulse-like force applied at the same beam-column connection of a steel frame. The results support the use of waveform cross-correlation using a pre-event catalog of impulse response function templates to determine the location and time of occurrence of a subsequent fracture recorded on a network of vibration sensors. However, the damage detection method may not be robust in a real setting, and the method may be better suited for damage localization.

A time-reversed reciprocal method was applied to a two-story one-bay numerical steel frame, as a proof of concept for applying the methodology to a complex structure such as a bridge or building. The signal was not fully recovered, but the location and application time of the impulse-like force were successfully determined. In applying this method to an actual structure, an accurate numerical model would first need to be developed for the structure

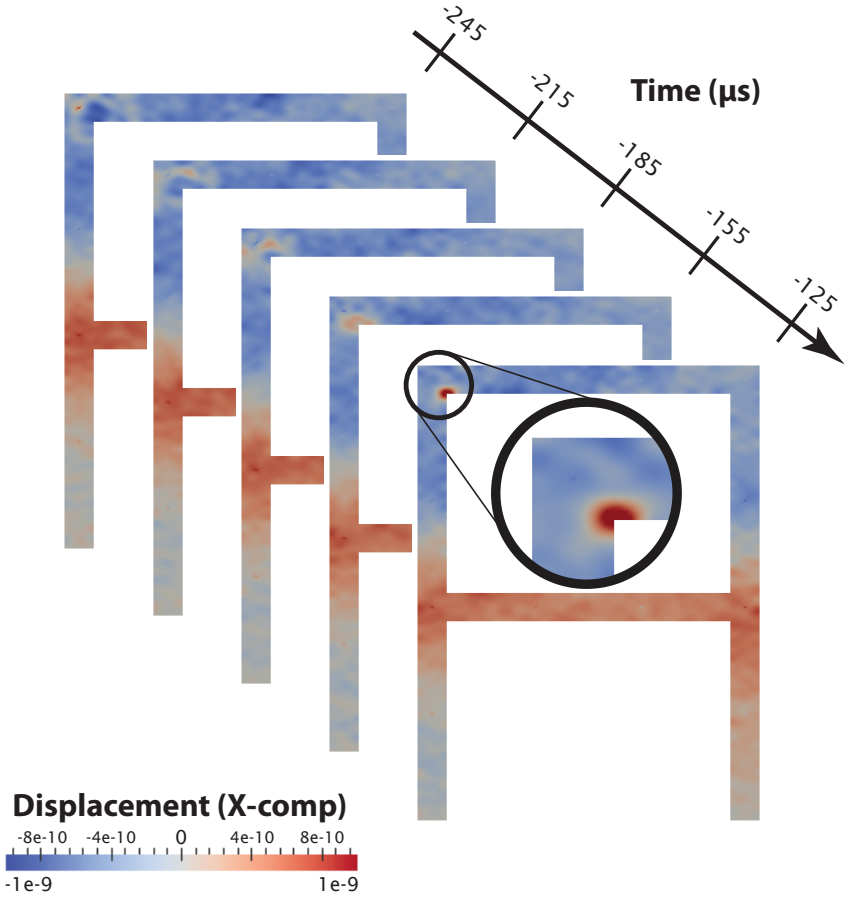

Figure 4.6: **Reverse Simulation: Response of Steel Frame to Prescribed Time-Reversed Displacements.** Waves generated at each of the twelve source locations converge at the correct location at the correct time. There appears to be a low-frequency artifact created whereby the upper story has a net negative displacement and the lower story has a net positive displacement. This might be due to the contribution of waves reflecting off the fixed base of the structure.

in the frequency range of interest, which could be both challenging and computationally-expensive. Once a satisfactory numerical model is obtained, the experimental data, which would contain some elements of noise, would be time-reversed and input to the model at the original receiver locations. It would be interesting to see this method applied to a full-scale experimental structure.

Chapter 5

Application of High-Frequency Damage Detection Methods to Benchmark Problems

To validate the high-frequency damage detection methods developed in previous chapters, the methods were applied to two damage-detection datasets, including a small-scale nonlinear frame made available by the Los Alamos National Laboratory (LANL) and a damaged cable-stayed bridge in China that was made available by the Center of Structural Monitoring and Control at the Harbin Institute of Technology.

5.1 Nonlinear Frame

Nonlinear damage was experimentally studied in a three-story frame with an installed bumper mechanism (Figueiredo and Flynn, 2009). The three-story frame structure (0.6 m tall), shown in Figure 5.1, consists of aluminum columns and plates connected by bolted joints. A shaker excites the base of the structure along a single axis with white noise with an excitation bandwidth of 20-150 Hz. The structure is instrumented with four accelerometers, one at each floor and the base. A sampling frequency of 320 Hz, is used for a duration of 25.6 seconds. The force at the base of the structure applied by the shaker is also recorded.

'Damage' is introduced by a bumper mechanism that creates a repetitive, impact-type nonlinearity. According to Figueiredo and Flynn (2009), the mechanism is intended to

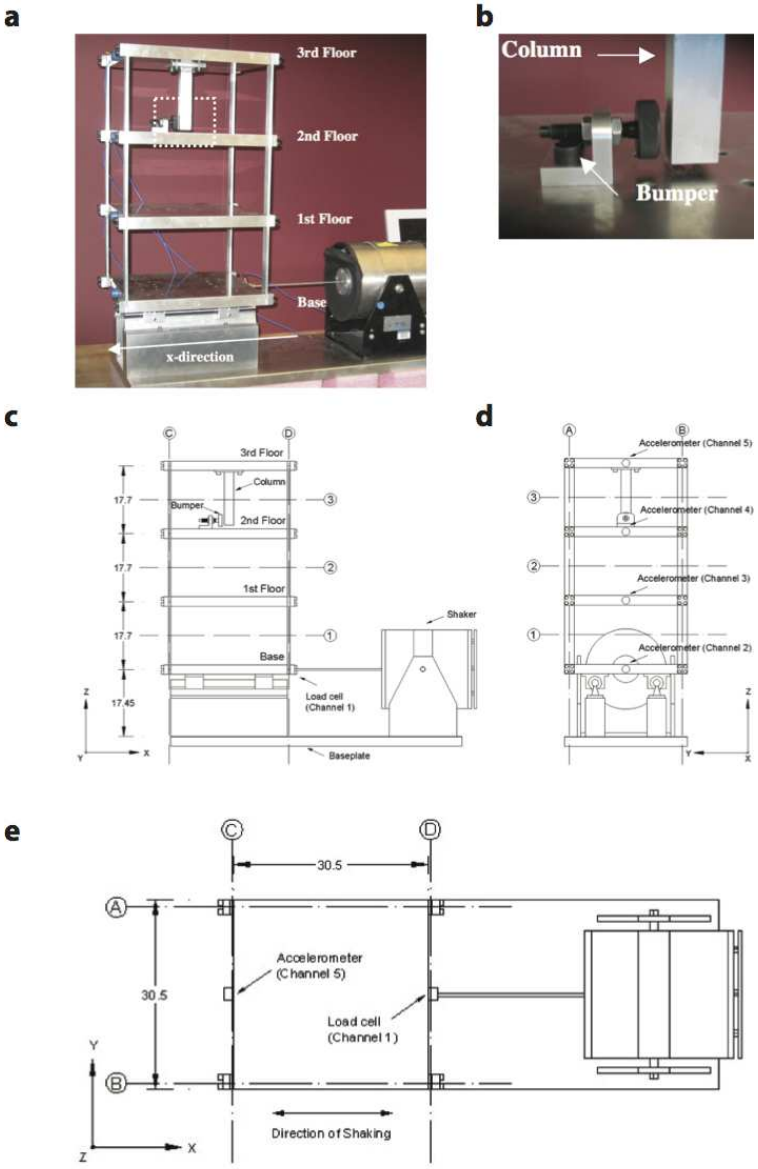

Figure 5.1: **LANL Nonlinear Frame: Experimental Setup. a,** The three-story frame structure (0.6 m tall) consists of aluminum columns and plates connected by bolted joints. **b,** 'Damage' is introduced by a bumper mechanism that creates a repetitive, impact-type nonlinearity. The bumper device is installed between the 2nd and 3rd floors, and consists of a bumper device on the second floor that is able to collide with a center column that extrudes from the base of the top floor. The level of damage is varied by adjusting the distance between the bumper and the column when the structure is in a resting position. **c,** A shaker excites the base of the structure along a single axis with white noise with an excitation bandwidth of 20-150 Hz. **d,** The structure is instrumented with four accelerometers, one at each floor and the base. A sampling frequency of 320 Hz, is used for a duration of 25.6 seconds. **e,** The force at the base of the structure applied by the shaker is also recorded. Images courtesy of Figueiredo and Flynn (2009).

simulate nonlinearities created by damage, such as a crack that opens and closes under dynamic loads (known as a 'breathing crack), or loose connections that rattle. The bumper mechanism is installed between the second and third floors, and consists of a bumper on the second floor that is able to collide with a center column that extrudes from the base of the top floor. The level of damage is varied by adjusting the distance between the bumper and the column when the structure is in a resting position.

The following levels of damage are studied in this section:

Undamaged Baseline condition

Damage Level 1 Gap (0.20 mm)

Damage Level 2 Gap (0.15 mm)

Damage Level 3 Gap (0.13 mm)

Damage Level 4 Gap (0.10 mm)

Damage Level 5 Gap (0.05 mm)

Studies on this data set that have previously been published are mentioned here. Karaiskos et al. (2012) applied outlier methods to modal filtering methods and auto-regressive parameters to detect damage. Hernandez-Garcia et al. (2010) used a MDOF lumped-mass model with additional nonlinear elements to model the behavior of the frame. A correlation was found between the length of the gap created and the magnitude of the observed changes in the nonlinear coefficients (i.e., restoring force coefficients). Figueiredo et al. (2011) applied a few different machine learning algorithms, including neural network, factor analysis, Mahalanobis distance, and singular value decomposition. Bornn et al. (2010) applied an auto-regressive support vector machine algorithm with outlier analysis. Figueiredo et al. (2009) combined support vector machines with outlier analysis to identify and localize damage between the top two stories.

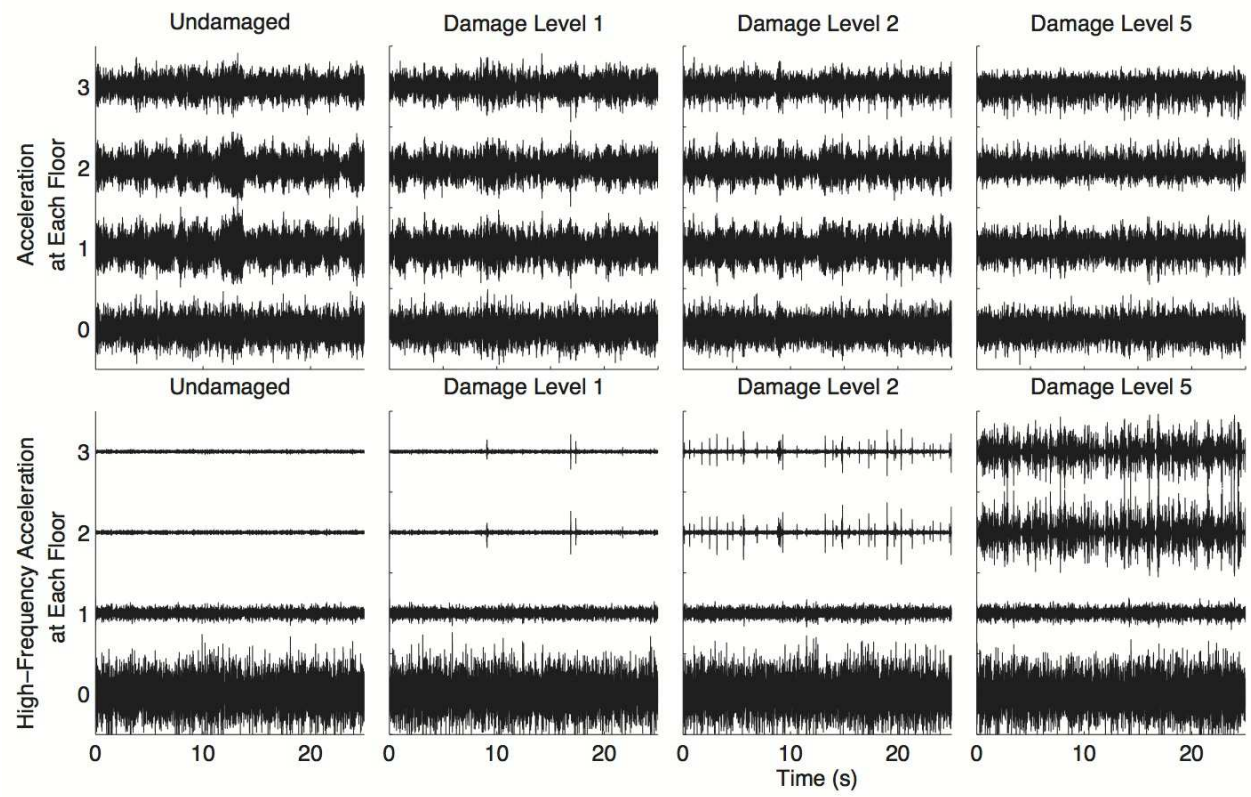

Figure 5.2: **LANL Nonlinear Frame: Recorded Accelerations (Raw and High-Pass Filtered).** By high-pass filtering (8^{th} order Butterworth filter with a cut-off frequency of 88 Hz) the data, the bumper impact events are clearly identified as high-frequency short-duration pulses. The increase in damage results in an increase in the number of impacts. While the impact events are clearly separated in time during Damage Levels 1 and 2, it becomes difficult to distinguish between different damage events for Damage Level 5.

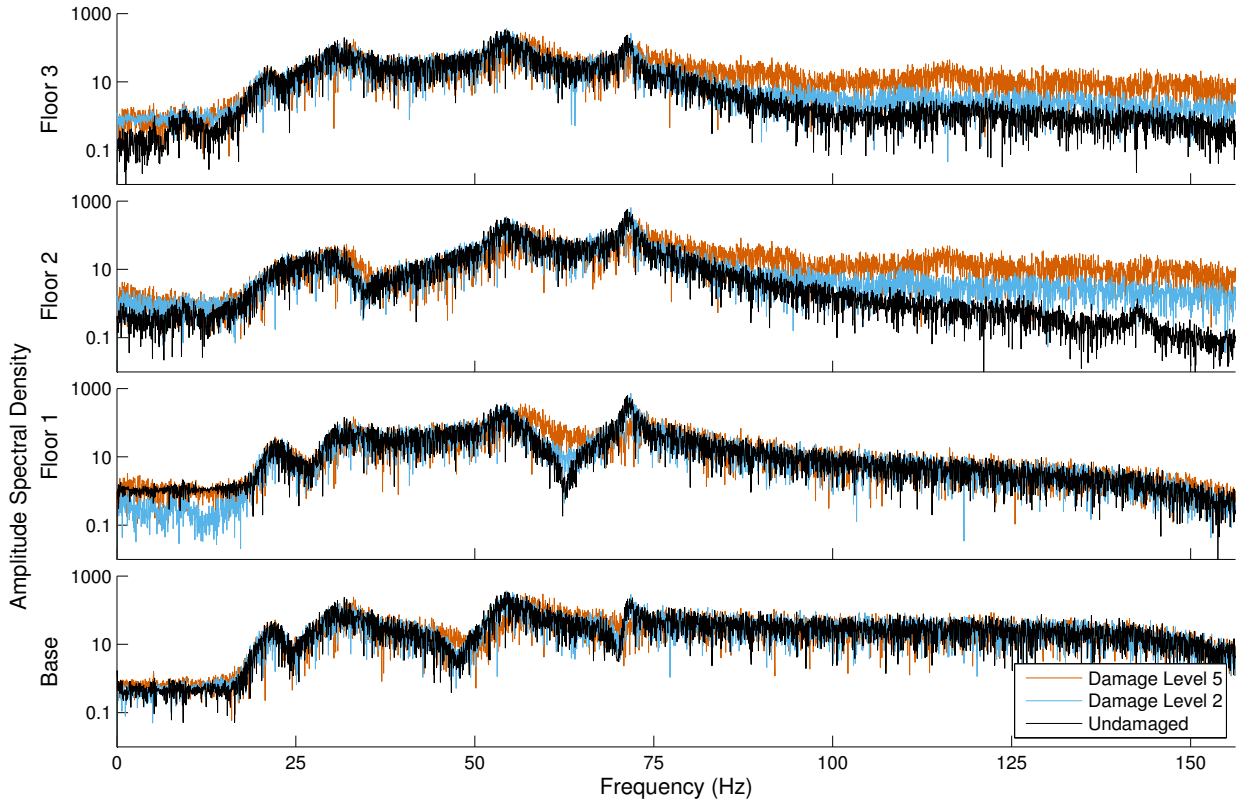

Figure 5.3: **LANL Nonlinear Frame: Amplitude Spectral Density.** The amplitude spectral densities are calculated from the magnitude of the Fourier transform of the raw accelerations. The amplitude spectral densities capture the increase in high-frequency energy that is generated during the bumper impacts between Floors 2 and 3. It appears that there is a significant amount of energy in the system above 160 Hz, and a higher sampling rate could have been used.

5.1.1 Identification of Damage Signals Through Feature Extraction of Pulses

The response of the structure to the impact of the bumper device can be clearly distinguished from the predominant modal response (the first three modes) of the structure by applying a high-pass filter. As the natural frequencies of the first three modes are approximately 30 Hz, 55 Hz, and 70 Hz, an 8^{th} order Butterworth filter with a cut-off frequency of 88 Hz is chosen. Pulses in the resulting high-frequency accelerations, shown in Figure 5.2, capture the motion of elastic waves that are generated by the impact of the column with the bumper. The amplitude and frequency content of these signals make them clearly observable over the predominant modal response, and their relatively sparse occurrence at lower levels of damage make them easy to identify and track. On the other hand, at Damage Level 5, impacts occur so frequently that it becomes difficult to distinguish between individual events. In fact, the high-frequency acceleration recorded on Floors 2 and 3 for Damage Level 5 begins to resemble that recorded at the base of the structure. The motion at the base created by the shaker most likely consists of many tiny stick-slip events, with each event exciting elastic waves that propagate within the base floor. This is presumably what causes the much higher frequency content observed in the base floor (and, arguably, the first floor by proximity). This results in a low signal-to-noise ratio recorded on the first and base floor, making it difficult to detect the propagation of the elastic wave generated from the bumper impacts to the first floor or base in the time-domain. In analyzing the frequency content recorded on each floor for three different damage levels, shown in Figure 5.3, the amplitude spectral densities remain relatively constant between the undamaged and damaged cases. A clear increase in the amplitude spectral density occurs above 75 Hz on Floors 2 and 3, for increasing levels of damage. Hence, it appears that the high-frequency energy generated by the impact of the bumper with the column does not propagate to the first floor.

By using a time-frequency representation of the Floor 3 acceleration records, shown in Figure 5.4, occurrences of the high-frequency impact events clearly stand out from the modal response. A comparison of the spectrograms generated for each floor in Damage Level 2

further confirms that the damage signal is confined to the top two floors. The spectrograms were generated by partitioning the signal in time (a time-window length of 128 points), applying a Hamming window, taking the Fourier Transform, and plotting the logarithm of the power spectral density of each segment. In Figure 5.4, the occurrences of impacts are manifested as vertical stripes, occurring during a very short time span over a burst of frequencies. The events are clearly distinguished from one another at lower levels of damage. At Damage Level 5, the spectrogram begins to resemble white noise at higher frequencies. From Figure 5.5, the bumper impacts are clearly evident on Floors 2 and 3, but not on Floor 1 or the Base. Hence, damage is localized to Floors 2, 3, or both. Additional analysis methods would be needed to localize the source of damage to a more precise location within the top two floors. As hammer-blow data is not available and the low sampling rate does not make for a precise determination of arrival time, forward modeling (i.e., a highly-discretized numerical model) would be needed to estimate the relative amplitudes in acceleration that would occur in response to damage introduced at different locations within Floors 2 and 3.

Following the method described in Section 3.3.4, templates are constructed from the high-frequency impulses that are detected first, namely those in the Damage Level 1 acceleration time series. Shown in Figure 5.6, the high-frequency signals generated by the bumper impacts are not well-characterized at a sampling rate of 320 Hz. The original signals appear to contain a significant amount of energy at higher frequencies. It might be possible to recover some of this information using signal processing techniques, but for now we will use these two templates to try to detect repeating events in subsequent trials. It is worth noting that in an actual building, one might encounter similar technical issues (i.e., decimation and possibly subsampling of a signal generated by damage), and it is better to test the performance of the method for small-scale structures under suboptimal conditions before applying the method to buildings with similar technical limitations.

The high-frequency signals recorded on Floors 2 and 3 are similar to one another in waveform and amplitude, but the polarity is reversed. This can be explained by the force mechanisms of the bumper device. When an impact occurs, an equal and opposite force is generated on each side of the device at the moment of impact, and hence an equal and

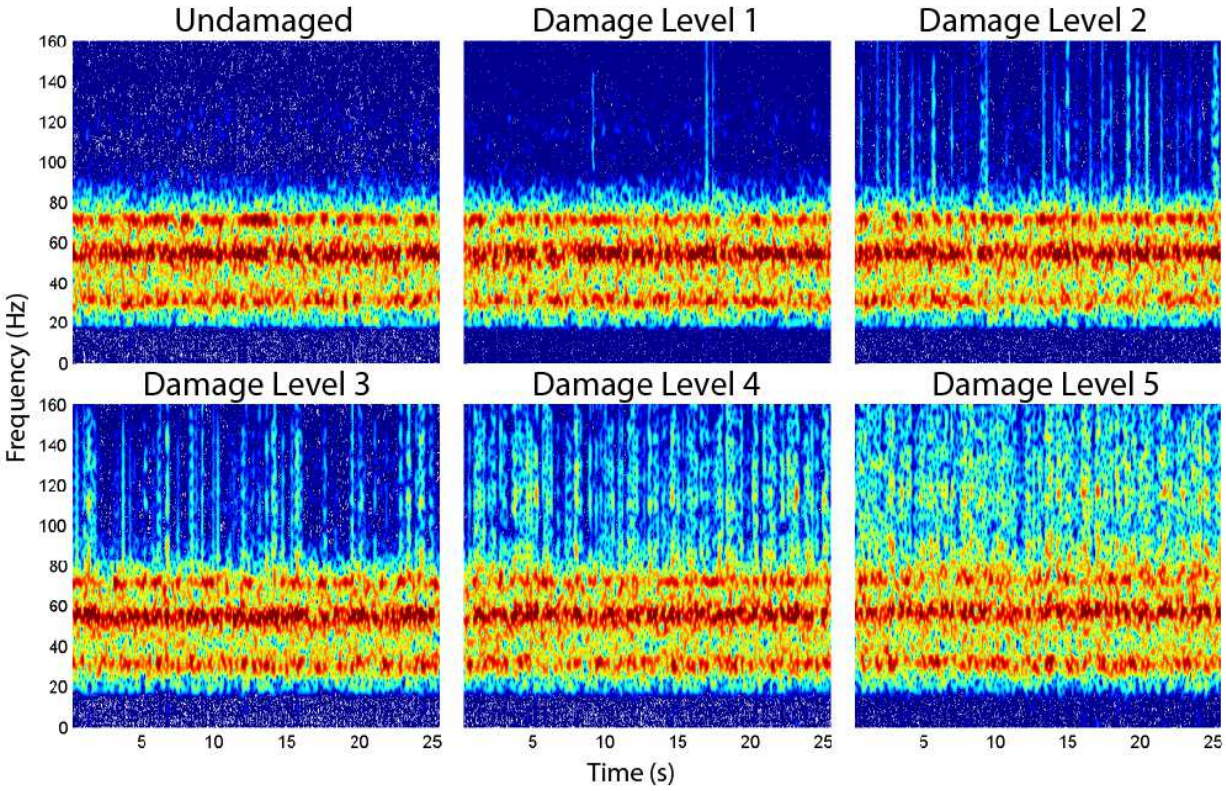

Figure 5.4: **LANL Nonlinear Frame: Spectrograms for Different Damage Levels.** Occurrences of the high-frequency impact events clearly stand out from the modal response and are manifested as vertical stripes, occurring during a very short time span over a burst of frequencies.

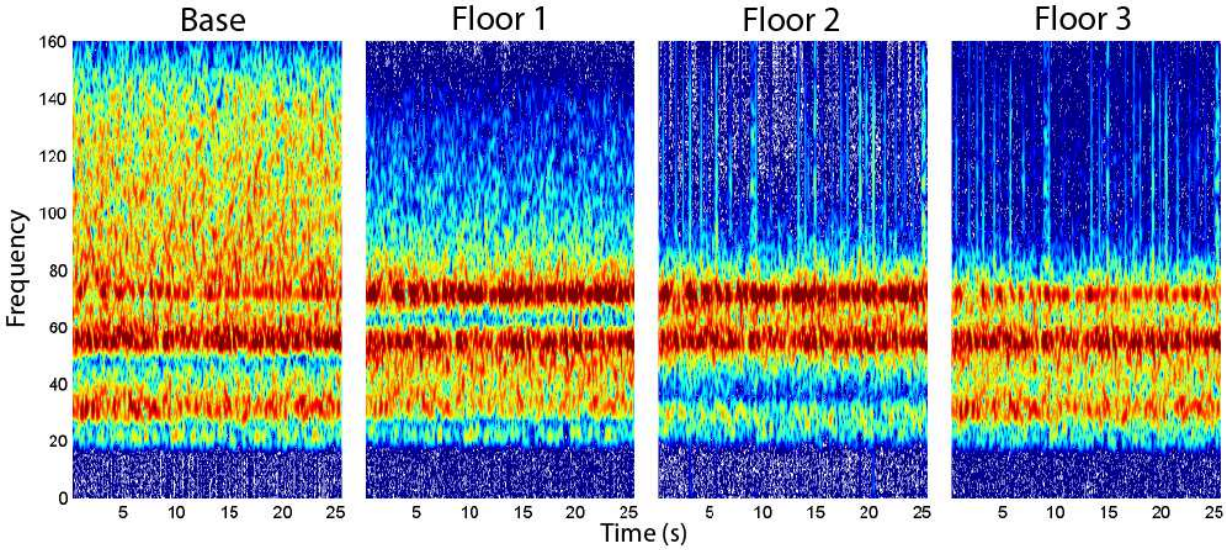

Figure 5.5: **LANL Nonlinear Frame: Spectrograms for Different Floors at Damage Level 2.** Damage events are clearly observed on Floors 2 and 3.

opposite force is applied to Floors 2 and 3. Only the accelerations recorded at the stations on Floors 2 and 3, with a high signal-to-noise-ratio of the detected high-frequency signal, are used to create the templates. For this reason, a high threshold value of 0.9 is chosen, though lower values are observed to work as well. The templates are cross-correlated with the acceleration recorded for Damage Levels 2-5, and detection of repeating signals (i.e., a cross-correlation value above the threshold) is highlighted in Figure 5.7. Despite the issues with the sampling rate, the method still works well, though an increase in false negatives is observed. Template 1 (the blue signal) is detected many more times than Template 2 (the orange signal), as Template 2 appears to consist of two separate events. The total number of detected occurrences of the repeating signals in each record is as follows: Undamaged: 0, Damage Level 1: 3, Damage Level 2: 17, Damage Level 3: 51, Damage Level 4: 49, Damage Level 5: 38. Clearly, there are a number of false negatives in the Damage Level 4 and 5 acceleration records, made evident by the undetected pulses. This reduction in performance seems to be related to the frequent occurrence of pulses, many of which are not well-separated in time. The number of false negatives could be improved on by using a shorter template that has fewer zero-values, using a lower threshold value, or updating the templates.

Finally, in addition to increasing the sampling rate, one potential improvement to this study would be to equip the bumper-column device with an open circuit that closes whenever the bumper and column come into contact. It would then be possible to record exactly when the damage events occurs, and the number of false positives and negatives could be confidently compared to those obtained from the high-frequency analysis.

5.2 Damaged Cable-Stayed Bridge in China

Data recorded on a damaged cable-stayed bridge in China was made available by the Center of Structural Monitoring and Control at the Harbin Institute of Technology. First opened to traffic in 1987, the bridge is one of the first built cable-stayed bridges in mainland China. According to Li et al. (2013), the bridge was repaired between 2005 and 2007 for cracks observed at the bottom of a girder segment over the mid-span, and corroded stay cables

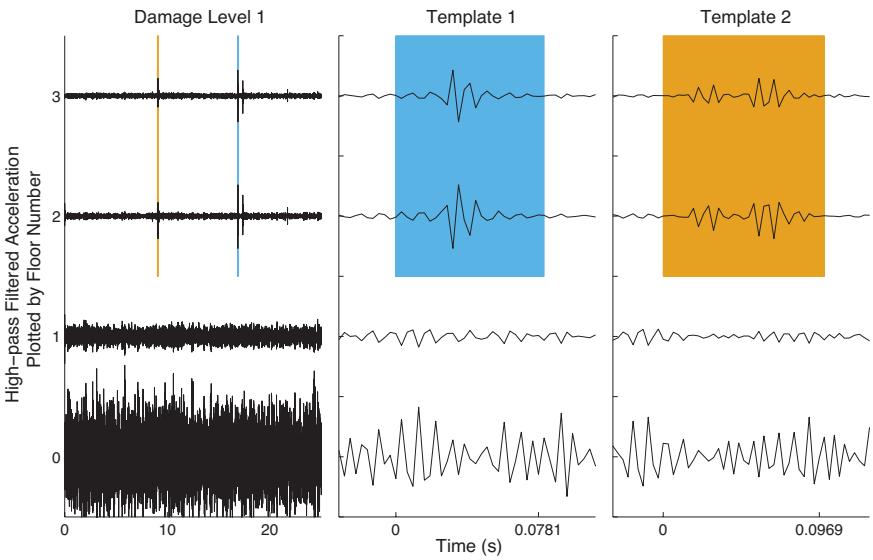

Figure 5.6: **LANL Nonlinear Frame: Damage Signals.** Damage signals are clearly identified in the acceleration records as high-frequency short-duration pulses.

(especially those near the anchors). During this time, the bridge was also upgraded with an SHM system that includes more than 150 sensors, including 14 uniaxial accelerometers, 1 biaxial accelerometer, an anemoscope, a temperature sensor, and optical fiber Bragg grating sensors. Li et al. (2013) presume that the bridge was damaged gradually over a time period from January to August 2008 by overloading.

Acceleration data were recorded continuously by 14 uniaxial accelerometers permanently installed on the deck and 1 biaxial accelerometer fixed to the top of one of the towers to monitor the tower's horizontal acceleration. The dimensions of the bridge as well as the instrument layout are shown in Figure 5.10. Data were recorded between January and August, during which time the bridge transitioned from being in an undamaged state to being in a damaged state. A full day of acceleration data recorded at 100 sps is made available approximately twice a month during this time period. The benchmark problem is to detect, localize, and quantify damage using acceleration measured during this time period. The specific dates are: January 1, January 17, February 3, March 19, March 30, April 9, May 5, May 18, May 31, June 7, June 16, and July 31, 2008.

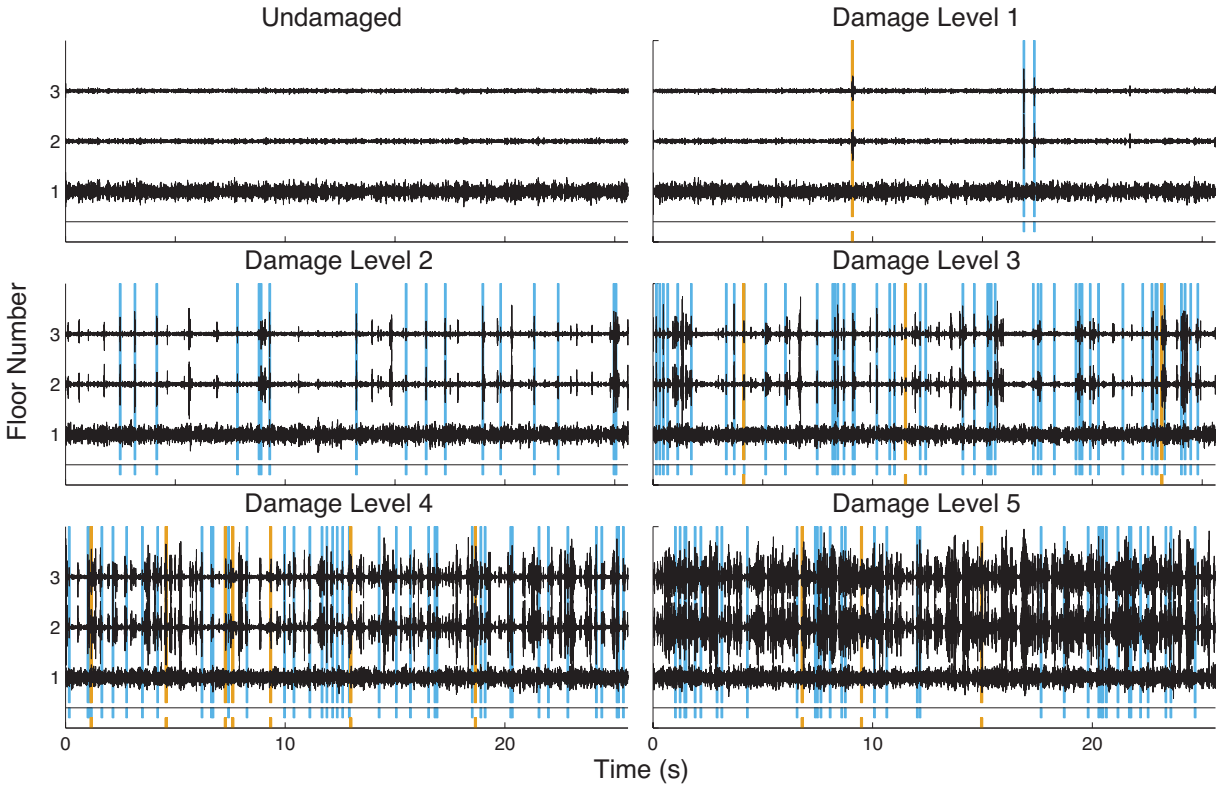

Figure 5.7: **LANL Nonlinear Frame: Damage Detection.** The two damage signals identified in the Damage Level 1 acceleration data are used as templates to detect damage in subsequent records. Only the top two floors are used in the subsequent analysis, with a threshold value of 0.9. A running cross-correlation is performed with auto-correlation normalization, and when the stacked correlation value exceeds the threshold, the signal is said to have been detected. The total number of detected occurrences of the repeating signals in each record is as follows: Undamaged: 0, Damage Level 1: 3, Damage Level 2: 17, Damage Level 3: 51, Damage Level 4: 49, Damage Level 5: 38.

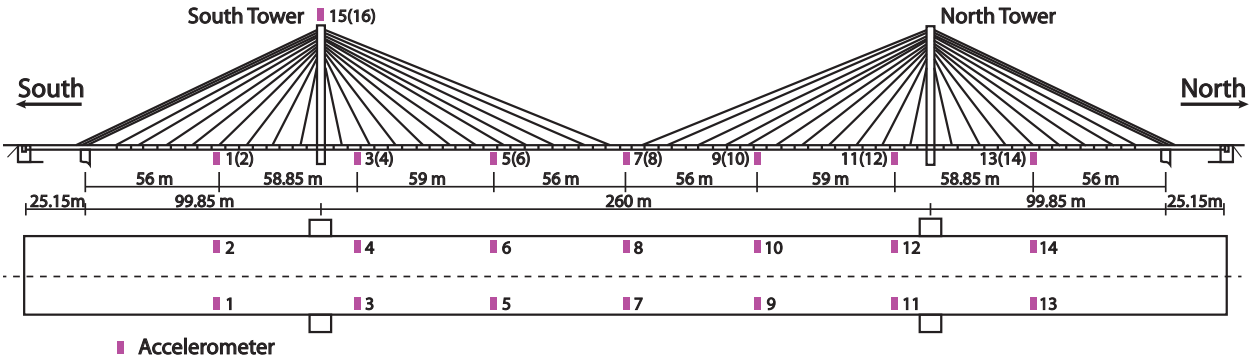

Figure 5.8: **Cable-Stayed Bridge: Dimensions and Instrument Layout.** One of the earliest cable-stayed bridges constructed in mainland China, the bridge consists of a main span of 260m and two side spans of 25.15+99.85 m each. The bridge was upgraded with an SHM system that includes more than 150 sensors, including 14 uniaxial accelerometers, 1 biaxial accelerometer, an anemoscope, a temperature sensor, and optical fiber Bragg grating sensors. This figure was adapted from a similar figure in Li et al. (2013).

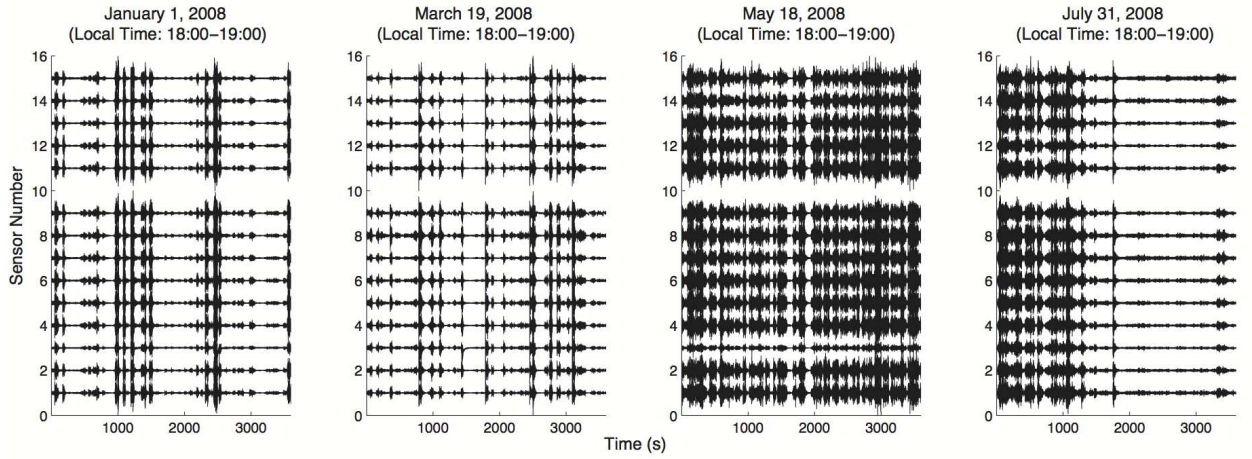

Figure 5.9: **Cable-Stayed Bridge: Sample Deck Accelerations.** Sample accelerations recorded by the accelerometers installed on the deck are shown during seven months when the bridge progressed from being in an undamaged state (in January) to being in a damaged state (in July). An increase in high-frequency short-duration pulses is clearly observed in the acceleration records. The occurrence of these pulses alone might be used to indicate the presence of damage. The abrupt decrease in acceleration levels around 18:30 on July 31 was caused by preventative measures that were taken to limit traffic to prevent the collapse of the bridge (Li et al., 2013). This indicates that the pulses are primarily caused by traffic. The data were high-pass filtered using a 2^{nd} order Butterworth filter with a cut-off frequency of 5 Hz.

5.2.1 Identification of Damage Signals Through Feature Extraction of Pulses

Sample acceleration records from January 1, March 19, March 18, and July 31 during times of heavy traffic are shown in Figure 5.9. The May 18 record is representative of the acceleration time series during the same time of day on June 7 and June 16. The January 1 and March 19 records are representative of records before May 18. The abrupt decrease in acceleration levels around 18:30 on July 31 was caused by preventative measures that were taken to limit traffic to prevent the collapse of the bridge (Li et al., 2013). It is concluded that the presence of damage results in the increased presence of high-frequency short-duration pulses that are primarily generated by vehicle traffic. Indeed, Li et al. (2013) similarly observe that higher magnitude accelerations were observed in the damage state, as well as a significant change in the power spectral density.

By analyzing the acceleration records (Figures 5.11 5.12 5.13, and 5.14) during a time interval (local time of 00:00-01:00) when light traffic is expected on the bridge, an increase in the occurrence of high-frequency short-duration signals with the presence of damage is also observed to have occurred, and fewer pulses are excited during light traffic than are excited during heavy traffic. The pulse events have clear separation in time and appear to be repeating in nature. The feature extraction method is followed. First, a pulse is identified in the undamaged state, T_1^{UD} (yellow), and is shown in Figure 5.10. The undamage signal is a horizontally-propagating wave that has large vertical component, a duration shorter than 1 s, and an apparent velocity of greater than 300 m/s (671 miles per hour). The signal originates at the north end of the bridge, and could be due to the dynamic response of the bridge to the rapid loading generated as a vehicle drives onto or off the bridge, possibly over a location that has increased flexibility. It might be possible to use a simple finite-element model combined with information about the bridge, such as the speed limit and average vehicle load, to determine which mechanism generates the pulse.

The undamage signal is detected multiple times in each subsequent record recorded at the same local time. A threshold value of 0.35 is used. The occurrence of the undamage

signal in the January 1, March 19, March 18, and July 31 acceleration records recorded during a local time of 00:00 - 01:00 is plotted in Figures 5.11 5.12 5.13, and 5.14.

Damage signals are identified using the unidentified pulses in the July 31 acceleration records. The two detected damage signals, T_1^D (blue) and T_2^D (green) are shown in Figure 5.10. T_1^{UD} and T_2^D seem to be caused by the same source and mechanism, vehicle loading at the north end of the bridge. T_2^D seems to consist of higher-frequency energy content than T_1^{UD}. On the other hand, damage signal T_1^D seems to be generated by vehicle loading at the south end of the bridge. The previously recorded data is screened for the presence of the damage signal. Again, a threshold value of 0.35 is used. The damage signal is not detected during the January 1, January 17, February 3, or March 19 acceleration records that were recorded during the same local time. The damage signals are first detected in the March 30 acceleration record, and they are detected in all subsequent records. This indicates that the dynamic response of the bridge to vehicle loading is different in the damaged and undamaged state. The occurrence of damage signal T_1^D might indicate the progression of damage, while an increase in the occurrence of the undamage signal T_1^{UD} might indicate a progression of damage.

Assuming similar traffic loads were encountered on different days at the same local time, it seems that when the bridge was in an undamaged state, a few (presumably heavy) vehicles excited a large dynamic response in the structure. When damage occurred in the bridge, a change in the physical properties of the bridge occurred that resulted in the ability of most vehicles to excite a large dynamic response in the structure, presumably due to an increase in flexibility. If the observed traveling wave is generated by the rapid loading generated as a vehicle drives onto the bridge, this would indicate that the increased flexibility occurred between the outside sensor and the end of the bridge (i.e., between the south end of the bridge and the first sensor, and between the north end of the bridge and the fourteenth sensor). Additional analysis would be needed to determine if the increased flexibility is caused by damage to the stay cables, bridge girders, or other reasons. Low-frequency strain data recorded on the cable stays could be used to assess cable damage. It would be advantageous to combine this method with a traditional vibration method, as decreases in natural frequencies

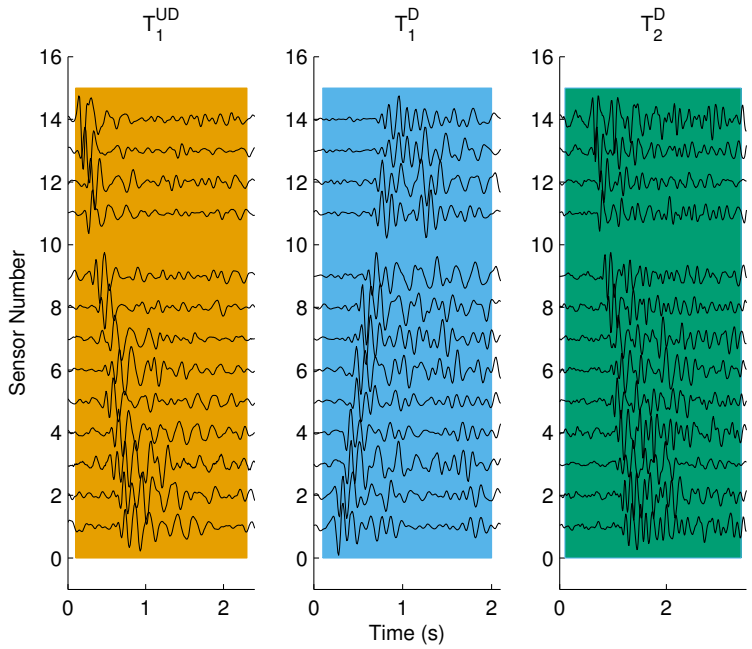

Figure 5.10: **Undamage and Damage Signals.** The undamage signal T_1^{UD} (yellow) is identified in the acceleration data recorded on January 1 between local times of 00:00-01:00. The signal originates at the north end of the bridge, and the source is most likely due to heavy vehicle loading. Two damage signals T_1^D (blue) and T_2^D (green) are identified in the acceleration data recorded on July 31 between a local time of 00:00-01:00. The signal originates at the north end of the bridge, and the source is most likely due to vehicle loading. T_1^{UD} and T_2^D seem to be caused by the same source and mechanism, though T_2^D seems to have higher frequency content. The data were high-pass filtered using a 2^{nd} order Butterworth filter with a cut-off frequency of 5 Hz.

were observed. It might also be possible to stack the detected signals to obtain a high SNR, and to use an updated FEM model to perform a time-reversed reciprocal method.

5.3 Conclusion

The presence of high-frequency short-duration signals in the acceleration records were observed to indicate damage in two benchmark problems, the LANL nonlinear frame and the SMC damaged cable-stayed bridge. In each example, the damage signals were successfully isolated by applying a method to identify potential damage signals through feature extraction of pulses. The method effectively uses the matched filter method to detect the occurrence of repeating signals, and identify new pulses that could indicate damage.

In the LANL nonlinear frame example, the damage signal took the form of elastic waves

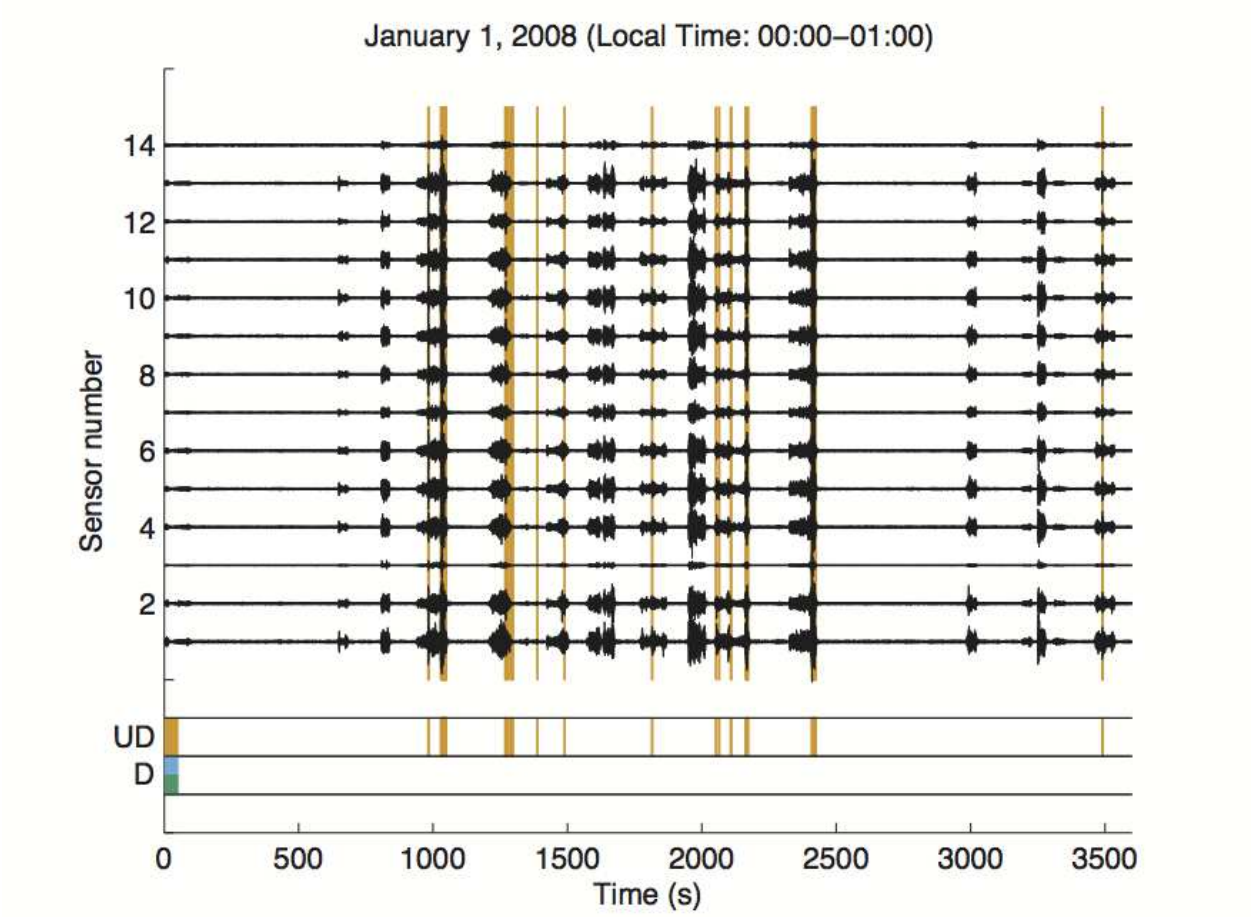

Figure 5.11: **Cable-Stayed Bridge: January 1 Acceleration Records.** The acceleration records are shown when the bridge is known to be in an undamaged state, and during light traffic conditions. The undamage signal T_1^{UD} (yellow) is identified based on pulses in the acceleration data, and a threshold value of 0.35 is used to detect the additional occurrences of the undamage signal.

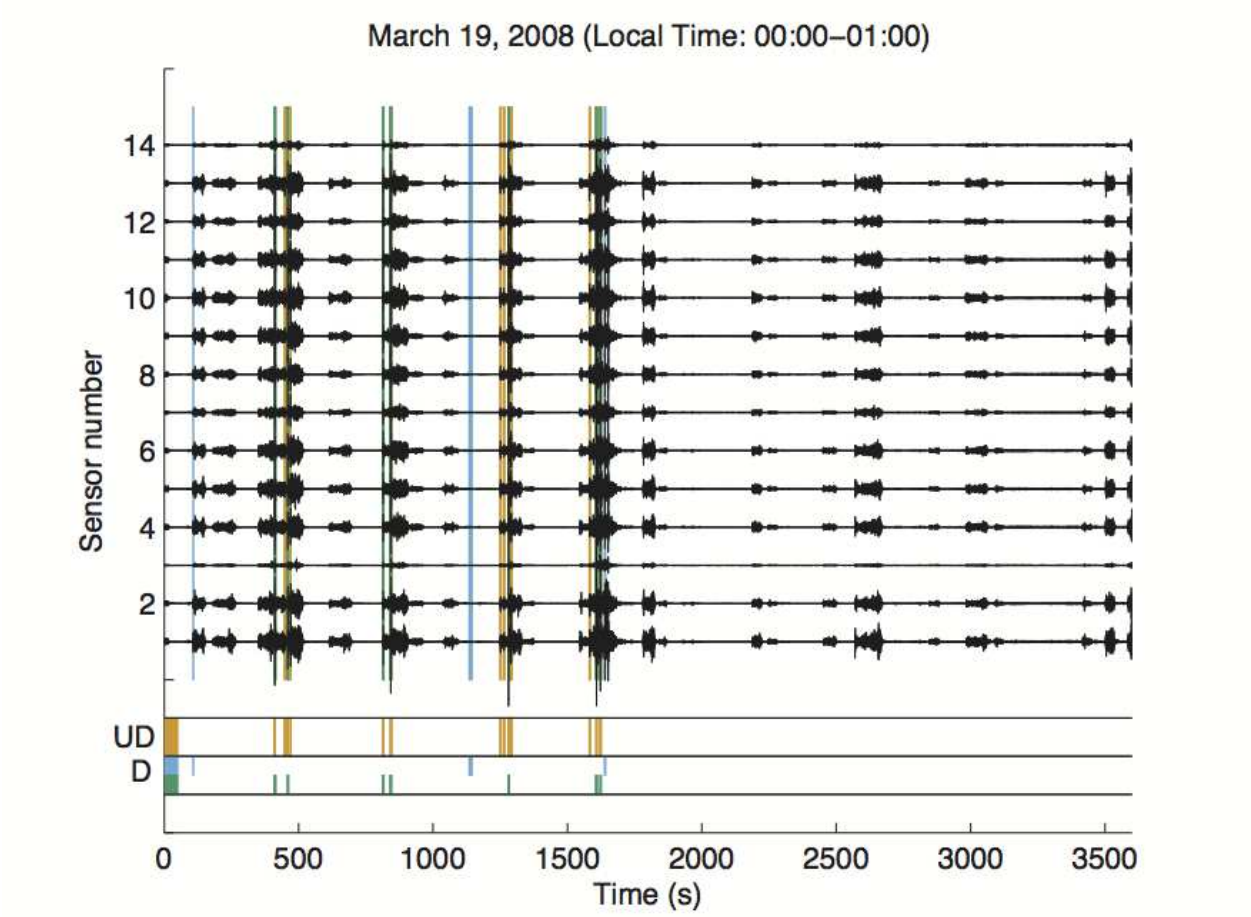

Figure 5.12: **Cable-Stayed Bridge: March 19 Acceleration Records.** The acceleration records are shown when the bridge is not known to be in an undamaged or damaged state, and during light traffic conditions. The undamage signal T_1^{UD} (yellow) is identified multiple times in the data. The first detected occurrences of damage signals T_1^D and T_2^D at this time of day are present in this data set.

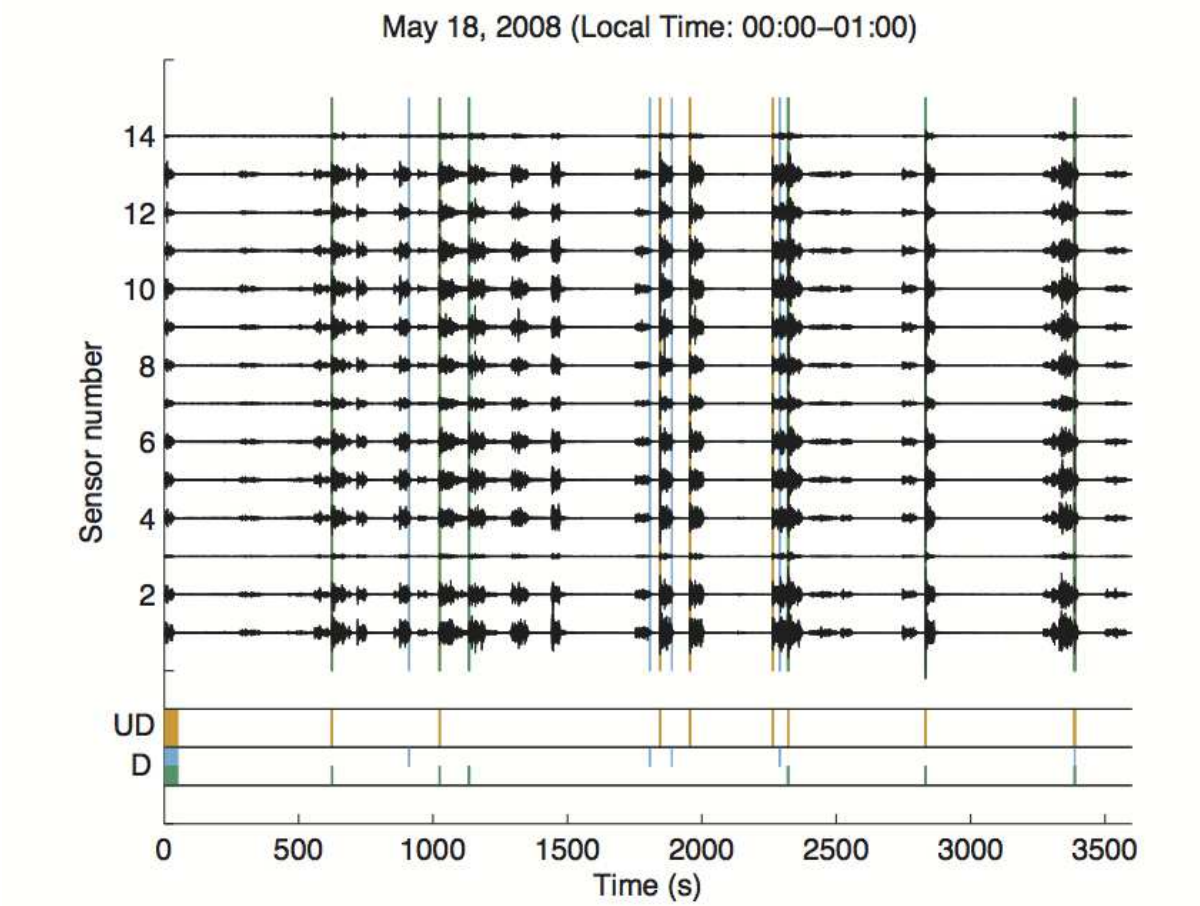

Figure 5.13: **Cable-Stayed Bridge: May 18 Acceleration Records.** The acceleration records are shown when the bridge is not known to be in an undamaged or damaged state, and during light traffic conditions. The undamage signal T_1^{UD} (yellow) and damage signals T_1^D and T_2^D are detected multiple times.

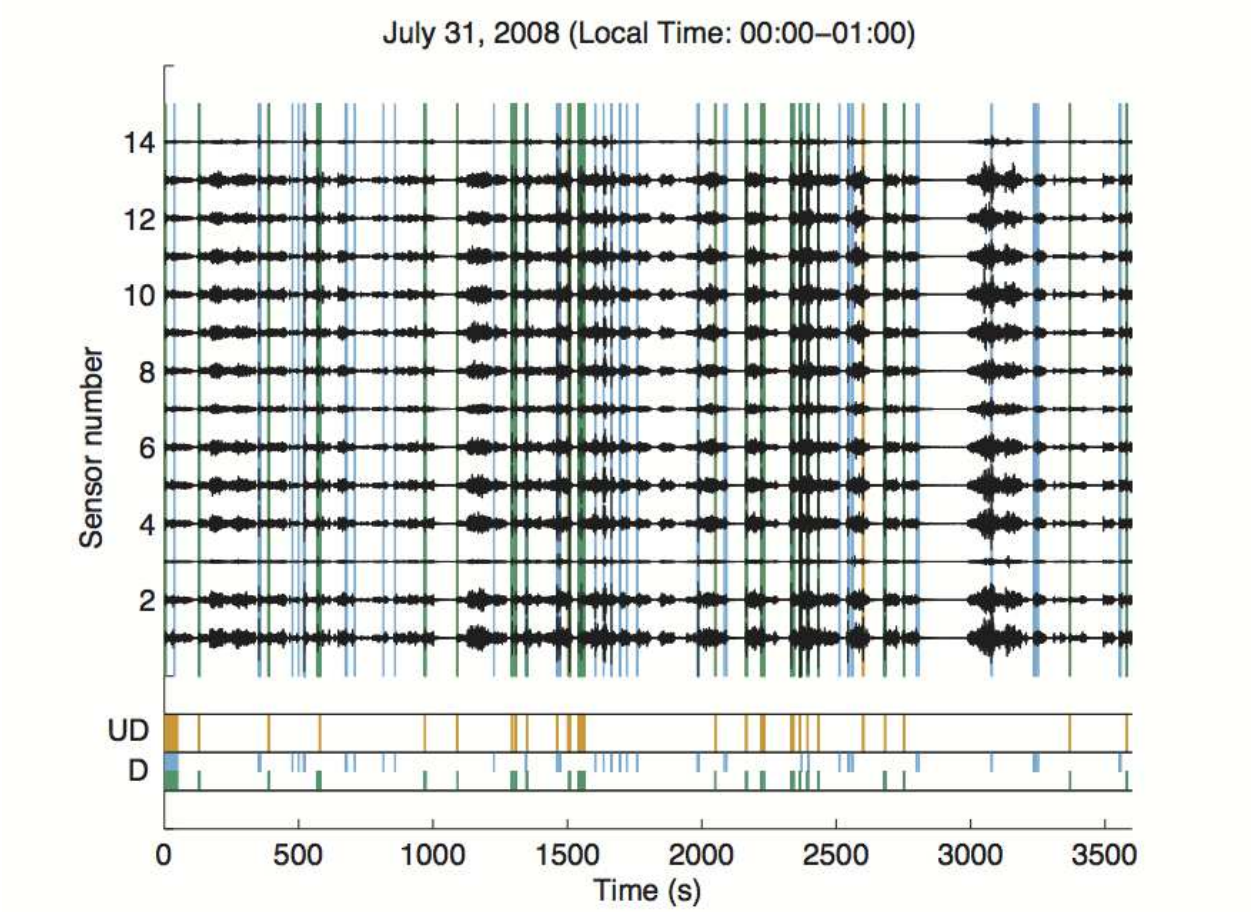

Figure 5.14: **Cable-Stayed Bridge: July 31 Acceleration Records.** The acceleration records are shown when the bridge is known to be in an damaged state, and during light traffic conditions. The undamage signal T_1^{UD} (yellow) is detected multiple times in the record. Two damage signals, T_1^D (blue) and T_2^D (green), are identified based on the unidentified pulses in the July 31 acceleration records. T_1^D seems to be generated by vehicle loading at the north end of the bridge; T_2^D seems to be generated by vehicle loading at the south end of the bridge. T_1^{UD} and T_2^D seem to be generated by the same source and mechanism, with higher-frequency content in T_2^D. The occurrence of damage signal T_1^D might indicate the progression of damage, while the change in the undamage signal T_1^{UD} might indicate a progression of damage. The data were high-pass filtered using a 2^{nd} order Butterworth filter with a cut-off frequency of 5 Hz.

generated by the impact of a bumper mechanism. By using either high-pass filtering or a time-frequency representation, the damage signal could be clearly detected as high-frequency pulses in the acceleration records obtained on the two floors housing the bumper mechanism. The method was observed to be robust despite the low sampling rate, though an increase in false negatives was observed. Additional false negatives occur at high levels of damage when there was little time separation between damage signals. However, the damage signal was successfully isolated, and it was possible to localize the damage, based on the amplitudes of the damage signals, to the top two floors of the structure.

Acceleration data was obtained from a damaged cable-stayed bridge in China. An increase in high-frequency short-duration pulses is clearly observed in the acceleration records, and the occurrence of these pulses alone might be used to indicate the presence of damage. An abrupt decrease in acceleration levels that was caused by preventative measures taken to limit traffic to prevent the collapse of the bridge indicated that the pulses are primarily caused by traffic. One undamage (T_1^{UD}) and two damage signals (T_1^D and T_2^D) were isolated using the feature extraction method. Damage signal T_1^D appears to be generated by vehicle loading on the south end of the bridge; signals T_1^{UD} and T_2^D seem to have been generated by the same source mechanism and location, namely vehicle loading on the north end of the bridge. All acceleration data (recorded during the same time period during light traffic) was screened for the presence of the undamage and damage signals using a threshold value of 0.35. The undamage signal is detected multiple times in each dataset. The damage signals were first detected in the March 30 acceleration record, and they were also detected multiple times in all subsequent records. This is consistent with the occurrence of damage signal T_1^D indicating the progression of damage, and the change in the undamage signal T_1^{UD} indicating a progression of damage. Assuming similar traffic loads were encountered on different days at the same local time, it seems that when the bridge was in an undamaged state, a few (presumably heavy) vehicles excited a large dynamic response in the structure. When damage occurred in the bridge, a change in the physical properties of the bridge occurred that resulted in the ability of most vehicles to excite a large dynamic response in the structure, presumably due to an increase in flexibility. If the observed traveling wave is generated by

the rapid loading event that occurs as a vehicle drives onto a region of increased flexibility on the bridge, this would indicate that the damage location is located between each outside sensor and the closest end of the bridge (i.e., between the south end of the bridge and the first sensor, and between the north end of the bridge and the fourteenth sensor). Additional analysis would be needed to determine if the increased flexibility is caused by damage to the stay cables, bridge girders, or other reasons. Low-frequency strain data recorded on the cable stays could be used to assess cable damage. It would be advantageous to combine this method with a traditional vibration method, as decreases in natural frequencies were observed.

There is some art in choosing the threshold value; too high a threshold value will result in false negatives (missed detections), and too low a threshold value will result in false positives. It might be possible to determine an optimal threshold value by actively exciting the structure using a few known sources (i.e. hammer blow or a known car of a given speed) over the course of a few weeks and experimentally determining an appropriate range based on the analysis of the method using the known signals.

There is also some art in choosing the filtering threshold. It is relatively easier to do this for simple experimental models that are excited along a single axis – a cut-off frequency above the predominant modal frequencies of the structure is desired, and the number of modes to consider is approximately given by the number of floors. For full-scale structures *in situ*, different modes are excited during different environmental conditions, and numerical models typically have a larger number of modes than are excited in the real structure. Model reduction can be used to estimate the highest mode present in the real structure and hence the highest mode above which to filter. Finally, some consideration must be given to the frequency content of the damage signal. Different frequencies are expected to be emitted for different damage mechanisms (e.g. acoustic emission, mechanical impact, generation of a flexural wave).

Finally, while applying the feature detection method can successfully isolate the damage signal in the case of known damage to a structure with a baseline recording, the ability of the technique to quantitatively determine the severity of damage (i.e., loss in stiffness or

increase in flexibility), and hence to definitively determine the presence of damage, is lacking. Changes in the dynamic behavior of the structure can be identified using outlier methods, changes in damage severity can be determined qualitatively, and the damage signal can be used to determine where damage occurred and give an energy estimate, but the damage signal cannot on its own be used to determine the loss in stiffness of the structure, and hence should be combined with knowledge of the structure (e.g., a finite-element model with knowledge of potential damage locations and mechanisms), a statistical approach using data recorded on multiple damaged structures of a similar type (these data would need to be experimentally obtained), or a complementary vibration-based damage detection method.

Chapter 6

Discussion and Conclusion

The application of high-frequency seismograms to damage detection in civil structures was investigated. Two novel methods for SHM were developed and validated using small-scale experimental testing, existing structures *in situ*, and numerical testing.

The first method is developed for pre-Northridge steel-moment-resisting frame buildings that are susceptible to weld fracture at beam-column connections. The method is based on using the response of a structure to a nondestructive force (i.e., a hammer blow) to approximate the response of the structure to a damage event (i.e., weld fracture). In Chapter 2, the method was applied to a small-scale experimental frame, where the impulse response functions of the frame were generated during an impact hammer test. In Chapter 4, the method was applied to a numerical model of a steel frame, in which weld fracture was modeled as the tensile opening of a Mode I crack. Impulse response functions were experimentally obtained for a steel moment-resisting frame building *in situ*. Results indicated that while acceleration and velocity records generated by a damage event are best approximated by the acceleration and velocity records generated by a colocated hammer blow, the method may not be robust to noise. The method seems to be better suited to damage localization, where information such as arrival times and peak accelerations can also provide indication of the damage location. This is of significance for sparsely-instrumented civil structures.

The second SHM method is designed to extract features from high-frequency acceleration records that may indicate the presence of damage. As short-duration high-frequency signals (i.e., pulses) were observed to be indicative of damage, the method relies on the

identification and classification of pulses in the acceleration records. Briefly, pulses observed in the acceleration time series when the structure is known to be in an undamaged state are compared with pulses observed when the structure is in a potentially damaged state. By comparing the pulse signatures from these two situations, changes in the high-frequency dynamic behavior of the structure can be identified, and damage signals can be extracted and subjected to further analysis. It is recommended that, in practice, the method be combined with a vibration-based method that can be used to estimate the loss of stiffness. In Chapter 3, the method was successfully applied to a small-scale experimental shear beam that was dynamically excited at its base using a shake table and damaged by loosening a screw to create a moving part. Although the damage was observed to be aperiodic and nonlinear in nature, the damage signals were accurately identified, and the location of damage was determined using the amplitudes and arrival times of the damage signal. In Chapter 5, the method was also successfully applied to detect the occurrence of damage in a test bed data set provided by the Los Alamos National Laboratory, in which nonlinear damage was introduced into a small-scale steel frame by installing a bumper mechanism that inhibited the amount of motion between two floors. The method was successfully applied and was robust despite a low sampling rate, though false negatives (undetected damage signals) were observed to occur at high levels of damage when the frequency of damage events increased. The method was also applied to acceleration data recorded on a damaged cable-stayed bridge in China, provided by the Center of Structural Monitoring and Control at the Harbin Institute of Technology. Acceleration records recorded after the date of damage showed a clear increase in high-frequency short-duration pulses compared to those previously recorded. One undamage pulse and two damage pulses were identified from the data. The occurrence of the detected damage pulses was consistent with a progression of damage and matched the known chronology of damage. The damage pulse originated between the end of the bridge and the first accelerometer; damage may have occurred within this region.

The findings of each chapter are repeated below.

Chapter 2: Experimental Study: Damage Detection Method for Weld Fracture of Beam-Column Connections in Steel Moment-Resisting-Frame Buildings

An experimental study was conducted to provide insight into a damage detection method that makes use of a prerecorded catalog of IRF templates and a cross-correlation method to detect the occurrence and location of structural damage in an instrumented building. Impulsive hammer blows and bolt fracture were applied to a small-scale steel frame to test the feasibility of applying the method to a building. The similarity between structure responses was evaluated using a cross-correlation method. The main findings of this chapter are:

1. IRFs were successfully obtained for an existing steel moment-resisting-frame building *in situ*. Not only were the IRFs clearly observable over ambient noise, the waveforms were also very consistent between trials with colocated sources, with correlation values typically greater than 0.8. For IRFs generated by hammer blows at different locations, significant differences were observed in arrival times, peak accelerations, and waveforms using eight accelerometers recording at 100 kHz. The data supports the idea of using hammer blow data to localize damage to a single column within a story. A sampling rate of 100 sps, though preferably 500 sps, seems to be high enough to capture the IRFs in the Factor building.

2. The application of the proposed damage detection method to the small-scale frame suggests that the IRF is not a robust approximation of the response to bolt failure. The method may also be suitable for damage localization, especially if it is combined with information about the arrival times and peak accelerations. While the IRFs cross-correlated well with each other and the responses to bolt fracture cross-correlated well with each other when the sources were colocated, the IRFs and responses to bolt fracture did not. However, in all considered cases, the IRF that had the highest correlation value with the response of the frame to bolt failure was the colocated IRF. Improvements in the correlation values were made by using an amplitude-dependent normalization that scaled with the maximum amplitude of acceleration at each receiver in response to bolt fracture. Information, such as arrival times and peak accelerations,

can also be indicators of where damage occurred; this is of significance for sparsely-instrumented structures.

3. The response of the frame to bolt fracture was observed to be surprisingly consistent between trials (correlation values of 0.70-0.85 for responses with colocated sources). This suggests that the mechanism that occurs at the moment of bolt failure is consistent between trials, and a hammer blow does not well-characterize this source. This also implicates that if a building were to undergo damage that resulted in the creation of a repeating source, a repeating high-frequency, short-duration signal might be observed in the acceleration time series. This could be generated by damage cases such as in the case of a breathing crack that repeatedly opens and closes, or a change in boundary conditions that increases the flexibility of a member and allows for the excitation of traveling waves.

4. The pre-recorded IRFs differed significantly from the IRFs that were recorded when the frame was in a damaged state, with typical cross-correlation values of 0.5, as compared to pre-damage values of 0.8. By comparing the generation of waves propagating through the frame, it was seen that the response of the damaged structure to a hammer blow applied at a given location begins to diverge from the response of the undamaged structure only after the elastic waves recorded at a given receiver location passed through the region of damage. This phenomenon is similar to the guided wave methods used in acoustic damage detection methods, and it also has potential to be used for damage detection in larger-scale structures. It would be necessary to use a repeatable mechanism to excite the structure over time, preferably under similar environmental conditions, and differences between the baseline signal and the subsequent recorded signal would be used to indicate damage. Damage might be located through an inverse problem approach that makes use of a finite-element model.

5. The application of a hammer blow to a damaged connection resulted in a low correlation value with the pre-recorded IRF generated by a colocated hammer blow. In this case,

the damaged connection was observed to also act as a high-frequency source, most likely due to motion generated at the interface of the beam and column. Applying a hammer blow to a cracked beam or column in a real building may or may not result in high-frequency energy generated at the crack interface. Presumably, if a beam has a crack and the two sides of the crack are not held firmly together, e.g., a vertical crack in a beam, a hammer blow applied in the vicinity of the crack could result in mechanical slippage and impact caused by the relative motion at the crack interface. If, on the other hand, the crack is firmly held closed, as might be the case for a horizontal crack in a column, high-frequency energy might not be generated at the crack interface in response to a nearby hammer blow.

6. As the responses to bolt fracture correlated just as well with pre-recorded IRFs as they did with the post-damage IRFs, it may be desirable to record the IRFs after an earthquake has occurred, when the building is in a potentially damaged state. In this way, there is an additional chance of detecting any high-frequency energy that is generated within a cracked interface at a damaged connection. (Also, if the building is never subjected to a large earthquake, there will be no need to conduct the hammer blow trials in the first place.) One advantage of having previously-recorded IRFs, however, is that they can be directly compared with post-earthquake IRFs, in order to detect damage in the frame by differences between them.

Chapter 3: Experimental Shear Beam

The effect of damage on the dynamic response of a civil structure was investigated experimentally using a small-scale (0.75 meter tall) shear beam. Damage was introduced into the shear beam by loosening the bolts connecting the columns to the floor, and a shake table was used to apply a consistent pulse at the base of the beam. The main findings of this chapter are outlined below:

1. A dynamic pulse was input at the base of the shake table. High-frequency acceleration records could be used to immediately determine the presence and location of damage,

based on the presence of short-duration high-frequency signals caused by mechanical impact and slippage. Low-frequency acceleration records could also be used to immediately determine the location of damage (i.e., which floor), based on the delayed arrival times and amplitudes of the initial shear wave.

2. A damage detection method that is based on detecting pulses in both the undamaged and potentially damaged acceleration records was found to be successful in detecting the nonlinear, aperiodic occurrences of damage signals. The arrival times and amplitudes were used to determine which floor was damaged. The advantage this strategy has over current strategies is that it can detect early onset damage. It is also based on the physical mechanism of damage in the structure, namely wave propagation, and energy formulations or the combination of the method with a time-reversed reciprocal method could give more information about the damage mechanism. The obvious disadvantage is that if there are no pulses (due not using a high-enough sampling rate, or the absence of such a signal), the method will not work. Another disadvantage is that the method cannot be used to determine the amount of damage (e.g., loss of stiffness), it can only detect the occurrence of signals that may indicate damage. The method could be combined with a vibration-based method.

3. A static tilt test was performed to estimate the severity of damage for Levels 1, 2, and 3. The amount of damage was found to range from moderate to severe levels, with estimated stiffness parameter k_d/d_{ud} ranging from 0.27 to 0.74. The estimated shear wave speeds obtained during dynamic testing were used to quantify the amount of damage, and the level of damage was estimated to be less severe than the values obtained from the stiffness test. The mean values (and standard deviations) of the estimated inter-story lateral stiffnesses immediately beneath the damaged floor for Damage Levels 1, 2, and 3, respectively, were found to be 0.93 (0.03), 0.70 (0.1), and 0.82 (0.23). The mean values (and standard deviations) of the estimated inter-story lateral stiffness immediately above the damaged floor for Damage Levels 1, 2, and 3, respectively, were found to be 0.94 (0.03), 0.67 (0.09), and 0.80 (0.24). The mean

values (and standard deviations) of the estimated inter-story lateral stiffness in floors not immediately above or below the damaged floor were calculated to be 0.99 (0.03), 0.95 (0.07), and 0.96 (0.05). The dynamic estimates could be improved by considering a longer portion of the time series. The values could be tested using forward modeling by determining the accompanying natural frequencies and mode shapes and comparing those with the observed ones.

4. The modal response of the structure was found to be highly consistent between trials, though the introduction of damage results in the presence of transient signals that generally originate at the damaged floor. A decreased transmission through the damaged floor of the high-frequency motion generated by the shake table was also observed.

Chapter 4: Numerical Study: Time-Reversed Reciprocal Method and Damage Detection Method for Weld Fracture

To numerically test a method for damage detection, a steel frame's response to two loading cases, an impulse-like force and an opening crack tensile stress (Mode I crack), was computed on a temporal scale of microseconds. It was found that the velocity waveform of a tensile crack can be approximated by the velocity waveform of an impulse-like force applied at the same beam-column connection of a steel frame. The results support the use of waveform cross-correlation using a pre-event catalog of impulse response function templates to determine the location and time of occurrence of a subsequent fracture recorded on a network of vibration sensors. However, the damage detection method may not be robust in a real setting, and the method may be better suited for damage localization.

A time-reversed reciprocal method was applied to a two-story one-bay numerical steel frame, as a proof of concept for applying the methodology to a complex structure such as a bridge or building. The signal was not fully recovered, but the location and application time of the impulse-like force were successfully determined. In applying this method to an actual structure, an accurate numerical model would first need to be developed for the structure in the frequency range of interest, which could be both challenging and computationally-

expensive. Once a satisfactory numerical model is obtained, the experimental data, which would contain some elements of noise, would be time-reversed and input to the model at the original receiver locations. It would be interesting to see this method applied to a full-scale experimental structure.

Chapter 5: Application of High-Frequency Damage Detection Methods to Benchmark Problems

The presence of high-frequency short-duration signals in the acceleration records were observed to indicate damage in two benchmark problems, the LANL nonlinear frame and the SMC damaged cable-stayed bridge. In each example, the damage signals were successfully isolated by applying a method to identify potential damage signals through feature extraction of pulses. The method effectively uses the matched filter method to detect the occurrence of repeating signals, and identify new pulses that could indicate damage.

In the LANL nonlinear frame example, the damage signal took the form of elastic waves generated by the impact of a bumper mechanism. By using either high-pass filtering or a time-frequency representation, the damage signal could be clearly detected as high-frequency pulses in the acceleration records obtained on the two floors housing the bumper mechanism. The method was observed to be robust despite the low sampling rate, though an increase in false negatives was observed. Additional false negatives occur at high levels of damage when there was little time separation between damage signals. However, the damage signal was successfully isolated, and it was possible to localize the damage, based on the amplitudes of the damage signals, to the top two floors of the structure.

Acceleration data was obtained from a damaged cable-stayed bridge in China. An increase in high-frequency short-duration pulses is clearly observed in the acceleration records, and the occurrence of these pulses alone might be used to indicate the presence of damage. An abrupt decrease in acceleration levels that was caused by preventative measures taken to limit traffic to prevent the collapse of the bridge indicated that the pulses are primarily caused by traffic. One undamage (T_1^{UD}) and two damage signals (T_1^D and T_2^D) were isolated using the feature extraction method. Damage signal T_1^D appears to be generated by vehicle

loading on the south end of the bridge; signals T_1^{UD} and T_2^D seem to have been generated by the same source mechanism and location, namely vehicle loading on the north end of the bridge. All acceleration data (recorded during the same time period during light traffic) was screened for the presence of the undamage and damage signals using a threshold value of 0.35. The undamage signal was detected multiple times in each dataset. The damage signals were first detected in the March 30 acceleration record, and they were also detected multiple times in all subsequent records. This is consistent with the occurrence of damage signal T_1^D indicating the progression of damage, and the change in the undamage signal T_1^{UD} indicating a progression of damage. Assuming similar traffic loads were encountered on different days at the same local time, it seems that when the bridge was in an undamaged state, a few (presumably heavy) vehicles excited a large dynamic response in the structure. When damage occurred in the bridge, a change in the physical properties of the bridge occurred that resulted in the ability of most vehicles to excite a large dynamic response in the structure, presumably due to an increase in flexibility. If the observed traveling wave is generated by the rapid loading event that occurs as a vehicle drives onto a region of increased flexibility on the bridge, this would indicate that the damage location is located between each outside sensor and the closest end of the bridge (i.e., between the south end of the bridge and the first sensor, and between the north end of the bridge and the fourteenth sensor). Additional analysis would be needed to determine if the increased flexibility is caused by damage to the stay cables, bridge girders, or other reasons. Low-frequency strain data recorded on the cable stays could be used to assess cable damage. It would be advantageous to combine this method with a traditional vibration method, as decreases in natural frequencies were observed.

There is some art in choosing the threshold value; too high a threshold value will result in false negatives (missed detections), and too low a threshold value will result in false positives. It might be possible to determine an optimal threshold value by actively exciting the structure using a few known sources (i.e. hammer blow or a known car of a given speed) over the course of a few weeks and experimentally determining an appropriate range based on the analysis of the method using the known signals.

There is also some art in choosing the filtering threshold. It is relatively easier to do this for simple experimental models that are excited along a single axis – a cut-off frequency above the predominant modal frequencies of the structure is desired, and the number of modes to consider is approximately given by the number of floors. For full-scale structures *in situ*, different modes are excited during different environmental conditions, and numerical models typically have a larger number of modes than are excited in the real structure. Model reduction can be used to estimate the highest mode present in the real structure and hence the highest mode above which to filter. Finally, some consideration must be given to the frequency content of the damage signal. Different frequencies are expected to be emitted for different damage mechanisms (e.g. acoustic emission, mechanical impact, generation of a flexural wave).

Finally, while applying the feature detection method can successfully isolate the damage signal in the case of known damage to a structure with a baseline recording, the ability of the technique to quantitatively determine the severity of damage (i.e., loss in stiffness or increase in flexibility), and hence to definitively determine the presence of damage, is lacking. Changes in the dynamic behavior of the structure can be identified using outlier methods, changes in damage severity can be determined qualitatively, and the damage signal can be used to determine where damage occurred and give an energy estimate, but the damage signal cannot on its own be used to determine the loss in stiffness of the structure, and hence should be combined with knowledge of the structure (e.g., a finite-element model with knowledge of potential damage locations and mechanisms), a statistical approach using data recorded on multiple damaged structures of a similar type (these data would need to be experimentally obtained), or a complementary vibration-based damage detection method.

Appendix A

Appendix

A.1 Notation, Definitions, and Properties

These properties were found in Bracewell (1986).

Cross-correlation:

$$\begin{aligned}(x_n \star x_m)(t) &= \int_{-\infty}^{\infty} \overline{x_n(\tau)} x_m(t+\tau) \mathrm{d}\tau, \\ (x_n \star x_m)[p] &= \sum_{q=-\infty}^{\infty} \overline{x_n[q]} x_m[p+q].\end{aligned}$$

Convolution:

$$\begin{aligned}(x_n * x_m)(t) &= \int_{-\infty}^{\infty} x_n(\tau) x_m(t-\tau) \mathrm{d}\tau, \\ (x_n * x_m)[p] &= \sum_{q=-\infty}^{\infty} x_n[q] x_m[p-q].\end{aligned}$$

Fourier Transform and Inverse Fourier Transform:

$$\begin{aligned}
\hat{x}_n(\xi) &= \mathcal{F}\{x_n(t)\} = \int_{-\infty}^{\infty} x_n(t)\mathrm{e}^{-2\pi i t\xi}\mathrm{d}t, \\
x_n(t) &= \mathcal{F}^{-1}\{\hat{x}_n(\xi)\} = \int_{-\infty}^{\infty} \hat{x}_n(\xi)\mathrm{e}^{2\pi i t\xi}\mathrm{d}\xi, \\
\hat{x}_n(\omega) &= \mathcal{F}\{x_n(t)\} = \frac{1}{\sqrt{2\pi}}\int_{-\infty}^{\infty} x_n(t)\mathrm{e}^{-i\omega t}\mathrm{d}t, \\
x_n(t) &= \mathcal{F}^{-1}\{\hat{x}_n(\omega)\} = \frac{1}{\sqrt{2\pi}}\int_{-\infty}^{\infty} \hat{x}_n(\xi)\mathrm{e}^{i\omega t}\mathrm{d}\omega, \\
X_n[p] &= \sum_{q=0}^{N-1} x_n[q]e^{-2\pi i p n/N}, \\
x_n[q] &= \frac{1}{N}\sum_{p=0}^{N-1} X_n[q]e^{2\pi i q n/N}.
\end{aligned}$$

Laplace Transform and Fourier Transform:

$$\begin{aligned}
\mathcal{L}\{x_n(t)\} &= X_n(s) = \int_0^{\infty} x_n(t)\mathrm{e}^{-st}\mathrm{d}t, \\
\mathcal{L}^{-1}\{X_n(s)\} &= x_n(t) = \frac{1}{2\pi i}\lim_{T\to\infty}\int_{\gamma-iT}^{\gamma+iT} X_n(s)\mathrm{e}^{st}\mathrm{d}s, \\
X_n(s)|_{s=i\omega} &= \mathcal{F}\{x_n(t)\}, \\
s &= \sigma + i\omega.
\end{aligned}$$

Fourier Transform of Cross-correlation:

$$\mathcal{F}\{x_n \star x_m\} = \overline{\mathcal{F}\{x_n\}}\mathcal{F}\{x_m\}.$$

Fourier Transform of Convolution:

$$\mathcal{F}\{x_n * x_m\} = \mathcal{F}\{x_n\}\mathcal{F}\{x_m\}.$$

Properties of Convolution and Cross-correlation:

$$\begin{aligned}
x_n * (x_m + x_p) &= (x_n * x_m) + (x_n * x_p), \\
x_n * x_m &= x_m * x_n, \\
x_n * (x_m * x_p) &= (x_n * x_m) * x_p, \\
x_n * \delta &= x_n, \\
\frac{\mathrm{d}}{\mathrm{d}t}(x_n * x_m) &= \frac{\mathrm{d}x_n}{\mathrm{d}t} * x_m = x_n * \frac{\mathrm{d}x_m}{\mathrm{d}t}, \\
x_n \star x_m &= \overline{x_n(-)} * x_m, \\
(x_n * x_m) \star x_p &= x_m(-) * (x_n \star x_p).
\end{aligned}$$

where $x_n(-) = x_n(-t)$ denotes the time-reversed $x_n(t)$, and $\overline{x_n} = \overline{x_n(t)}$ denotes the complex conjugate of $x_n(t)$.

A.2 Publications

Heckman, V. M., Kohler, M. D., and Heaton, T. H. (2011b). A method to detect structural damage using high-frequency seismograms. In *Proceedings of Structural Health Monitoring 2011: International Workshop on Structural Health Monitoring.*

Abstract: "There has been recent interest in using acoustic techniques to detect damage in instrumented civil structures. An automated damage detection method that analyzes recorded data has application to building types that are susceptible to a signature type of failure, where locations of potential structural damage are known a priori. In particular, this method has application to the detection of brittle fractures in welded beam-column connections in steel moment-resisting frames (MRFs). Such a method would be valuable if it could be used to detect types of damage that are otherwise difficult and costly to identify. The method makes use of a prerecorded catalog of Greens function templates and a matched filter method to detect the occurrence and location of structural damage in an in-

strumented building. This technique is different from existing acoustic methods because it is designed to recognize and use seismic waves radiated by the original brittle failure event where the event is not known to have occurred with certainty and the resulting damage may not be visible. The method is outlined as follows. First, identify probable locations of failure in an undamaged building. In pre-Northridge steel MRFs, which are susceptible to brittle failure of welded beam-column connections, those connections would be the locations of probable failure for this type of building. Second, obtain a Greens function template for each identified location of probable failure by applying a short-duration high-frequency pulse (e.g. using a force transducer hammer) at that location. One underlying assumption of this method is that the Greens function template specific to a potential location of failure can be used to approximate the dynamic response of the structure to structural damage at that location. Lastly, after a seismic event, systematically screen the recorded high-frequency seismograms for the presence of waveform similarities to each of the catalogued Greens function templates in order to detect structural damage. This is achieved by performing a running cross-correlation between each Greens function template and a moving window of the continuous data recorded during the earthquake. Damage that occurs at one of the catalogued potential locations is expected to result in a high cross-correlation value when using the correct Greens function template. This method, also known as the matched filter method, has seen recent success in other fields, but has yet to be explored in the context of acoustic damage detection in civil structures. Preliminary experimental results from tap tests performed on a small-scale laboratory frame are presented. Cross-correlation calculations highlight similarities among events generated at the same source location and expose differences among events generated at different source locations. Finally, a blind tap test is performed to test whether cross-correlation techniques and catalogued Greens function templates can be used to identify the occurrence of and pinpoint the location of an assumed-unknown event (Heckman et al., 2011b)."

Heckman, V., Kohler, M., and Heaton, T. (2011a). A damage detection method for instrumented civil structures using prerecorded greens functions and cross-correlation. In

Proceedings of ANCRiSST2011: The 6th International Workshop on Advanced Smart Materials and Smart Structures Technology.

Abstract: "Automated damage detection methods have application to instrumented structures that are susceptible to types of damage that are difficult or costly to detect. The presented method has application to the detection of brittle fracture of welded beam-column connections in steel moment-resisting frames (MRFs), where locations of potential structural damage are known a priori. The method makes use of a prerecorded catalog of Greens function templates and a cross-correlation method to detect the occurrence, location, and time of structural damage in an instrumented building. Unlike existing methods, the method is designed to recognize and use mechanical waves radiated by the original brittle fracture event, where the event is not known to have occurred with certainty and the resulting damage may not be visible. An experimental study is conducted to provide insight into applying the method to a building. A tap test is performed on a small-scale steel frame to test whether cross-correlation techniques and catalogued Greens function templates can be used to identify the occurrence and location of an assumed-unknown event. Results support the idea of using a nondestructive force to characterize the building response to high-frequency dynamic failure such as weld fracture (Heckman et al., 2011a)."

Heckman, V. M., Kohler, M. D., and Heaton, T. H. (2011c). A method to detect structural damage using high-frequency seismograms. In *Proceedings of the 8th International Conference on Urban Earthquake Engineering.*

Abstract: "A numerical study is performed to gain insight into applying a novel method to detect high-frequency dynamic failure in buildings. The method relies on prerecorded catalog of Green's functions for instrumented buildings. Structural failure during a seismic event is detected by screening continuous data for the presence of waveform similarities to each of the cataloged building responses. In the first part of this numerical study, an impulse-like force is applied to a beam column connection in a linear elastic steel frame. A time-reversed

reciprocal method is used to demonstrate that the resulting simulated displacements can be used to determine the absolute time and location of the applied force. In the second part of the study, a steel frame's response to two loading cases, an impulse-like force and an opening crack tensile stress, is computed on a temporal scale of microseconds. Results indicate that the velocity waveform generated by a tensile crack can be approximated by the velocity waveform generated by an impulse-like force load applied at the proper location. These results support the idea of using a nondestructive impulse-like force (e.g. hammer blow) to characterize the building response to high-frequency dynamic failure (e.g. weld fracture) (Heckman et al., 2011c)."

Heckman, V., Kohler, M., and Heaton, T. (2010). Detecting failure events in buildings: A numerical and experimental analysis. In *Proceedings of the 9th U.S. National 10th Canadian Conference on Earthquake Engineering. Earthquake Engineering Research Institute.*

Abstract: "A numerical method is used to investigate an approach for detecting the brittle fracture of welds associated with beam-column connections in instrumented buildings in real time through the use of time-reversed Greens functions and wave propagation reciprocity. The approach makes use of a prerecorded catalog of Greens functions for an instrumented building to detect failure events in the building during a later seismic event by screening continuous data for the presence of waveform similarities to one of the prerecorded events. This study addresses whether a set of Greens functions in response to an impulsive force load can be used to approximate the response of the structure to a localized failure event such as a brittle weld fracture. Specifically, we investigate whether prerecorded Greens functions can be used to determine the absolute time and location of a localized failure event in a building. We also seek to differentiate between sources such as a weld fracture that are structurally damaging and sources such as falling or colliding furniture and other non-structural elements that do not contribute to structural failure. This is explored numerically by comparing the dynamic response of a finite-element cantilevered beam model

structure to a variety of loading mechanisms. A finite-element method is employed to determine the behavior of the resulting elastic waves and to obtain a general understanding of the structural response (Heckman et al., 2010)."

Kohler, M. D., Heaton, T. H., and Heckman, V. M. (2009). A time-reversed reciprocal method for detecting high-frequency events in civil structures with accelerometer arrays. *In Proceedings of ANCRISST 2009 - The Fifth International Workshop on Advanced Smart Structures and Technology.*

Abstract: "A high-frequency experimental method of detecting a failure event in engineered structures is presented that uses the property of wave propagation reciprocity and time-reversed reciprocal Greens functions. The premise is that if a numerical database of pre-event, source-receiver Greens functions can be compiled for multiple locations of potential damage in a structure, that database can subsequently be used to identify the location and time of occurrence of a real failure event in the structure. Once a fracture source emits a wavefield that is recorded on a distributed set of accelerometers in the structure, time-reversed waves can be obtained by convolving the displacements with the database of time-reversed Greens functions and stacking the results. The correct location and time of the fracture source can be inferred from the subset of Greens functions that exhibits the best focus in the form of a delta function. The 17-story, steel moment-frame UCLA Factor building contains a cutting-edge, continuously recording, 72-channel, seismic array. The accelerometers 500 sample-per-second recordings have been used to verify the ability to observe impulse-like sources in a full-scale structure. Application of an impulse-like source on the 3rd and 15th floors of the Factor building shows that the associated displacements serve as useful approximations to the buildings Greens functions in the far field, and can be used in investigations of scenario fracture location and timing (Kohler et al., 2009)."

A.3 Uniform Shear Beam

Consider a simple undamped shear beam model that is fixed at the base with a height H = 100 m, shear wave velocity β = 200 m/s, and with sensors located at each 1/10 of the height of the building recording at 100 sps. The shear wave velocity, β, is proportional to the square root of the stiffness, $\beta = \sqrt{\mu/\rho}$, where μ is the interstory shear modulus, and ρ is the density. The beam is subjected to displacement at the base, $u_0(t)$,

$$\begin{aligned} \frac{\partial^2 u}{\partial^2 t} &= \beta^2 \frac{\partial^2 u}{\partial x^2}, \\ u &= u(x,t), \\ u(0,t) &= u_0(t), \\ \frac{\partial u}{\partial x}(H,t) &= 0. \end{aligned}$$

Its solution at the n^{th} floor is given by the D'Alembert solution to the wave equation with fixed-free boundary conditions (Sasani et al., 2006). The horizontal ground motion generates a vertically propagating shear wave. The fixed-base period, T, is 4H/c. The building motion consists of a sum of upgoing and downgoing waves, and is given by:

$$\begin{aligned} u_n(t) = u_0(t - \frac{nT}{40}) - u_0(t) + \sum_{m=1}^{2t/T+n/20} (-1)^{m+1} u_0(t - \frac{(2m - n/10)T}{4}) \\ + \sum_{m=1}^{2t/T-n/20} (-1)^{m+1} u_0(t - \frac{(2m + n/10)T}{4}). \end{aligned} \tag{A.1}$$

Using this model, one can directly compare the response of the shear beam from applying an impulsive displacement at the base to the impulse response (with simulated noise applied at the base) and cross-correlations (with simulated noise applied at the base), as shown in Figure A.1. To simulate ambient noise at the base of the shear beam, displacements are drawn from a uniform distribution over the range [-0.05, 0.05] meters. Results have been stacked over 10 trials.

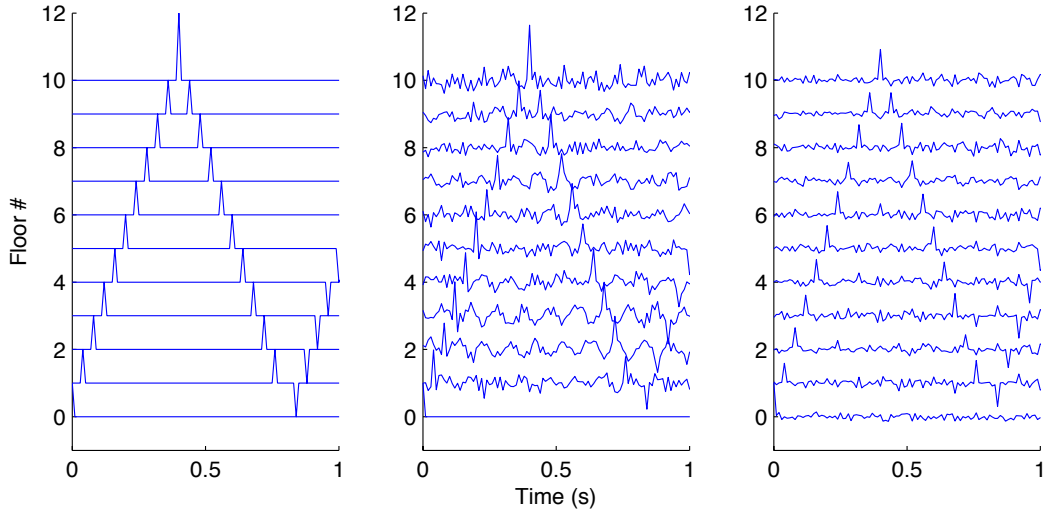

Figure A.1: **Simple Shear Beam Synthetics. A,** An impulsive shear wave travels up the simple shear beam, is reflected at the top floor, and is reflected again at the fixed base. B, Deconvolution is used to obtain the impulse response function from synthetic ambient noise motion at the base. C, Normalized cross-correlation is performed between each record and the base record under ambient noise conditions.

The natural frequencies are:

$$\omega_n = \frac{(2n-1)\pi\beta}{2H}; n = 1, 2, 3, ... \tag{A.2}$$

If an interface is introduced into the shear beam at height $H_{interface}$, so that there are now two separate regions A and B, then the differential equations governing the motion of the beam are as follows:

Region A: $0 <= x_3 <= H_{interface}$,

$$\begin{aligned} \frac{\partial^2 u_A}{\partial^2 t} &= \beta_A^2 \frac{\partial^2 u_A}{\partial x^2}, \\ u_A &= u_A(x_3, t), \\ u_A(0, t) &= u_0(t). \end{aligned}$$

Region B: $H_{interface} <= x_3 <= H$,

$$\begin{aligned} \frac{\partial^2 u_B}{\partial^2 t} &= \beta_B^2 \frac{\partial^2 u_B}{\partial x^2}, \\ u_B &= u_B(x_3, t), \\ \frac{\partial u_B}{\partial x}(H, t) &= 0. \end{aligned}$$

Interface:

$$\begin{aligned} u_B(H_{interface}, t) &= u_B(H_{interface}, t), \\ \frac{\partial u_A}{\partial x}(H_{interface}, t) &= \frac{\partial u_B}{\partial x}(H_{interface}, t). \end{aligned}$$

The reflection and transmission coefficients for a vertically-incident wave generated at the base are:

$$\begin{aligned} T &= \frac{A_T}{A_I} = \frac{2}{1 + \beta_2/\beta_1}, \\ R &= \frac{A_R}{A_I} = \frac{\beta_1/\beta_2 - 1}{\beta_1/\beta_2 + 1}. \end{aligned}$$

A schematic for wave propagation in a shear beam, presented for a variety of boundary conditions, is given in Figure A.2.

The transmission and reflection coefficients for an infinite shear beam with a low-velocity

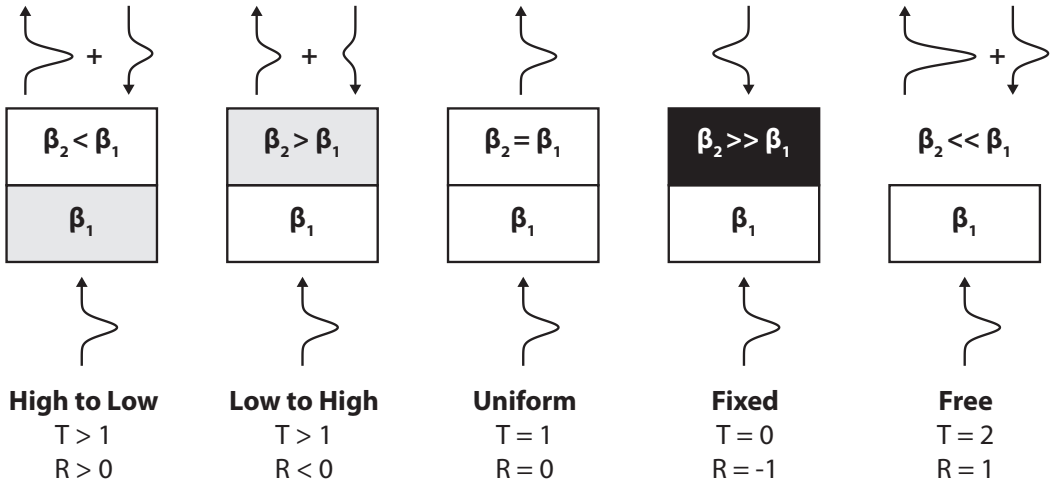

Figure A.2: **Wave Propagation in a Shear Beam: Transmission and Reflection Coefficients for a Variety of Boundary Conditions.** Wave propagation in a shear beam is presented for a variety of boundary conditions.

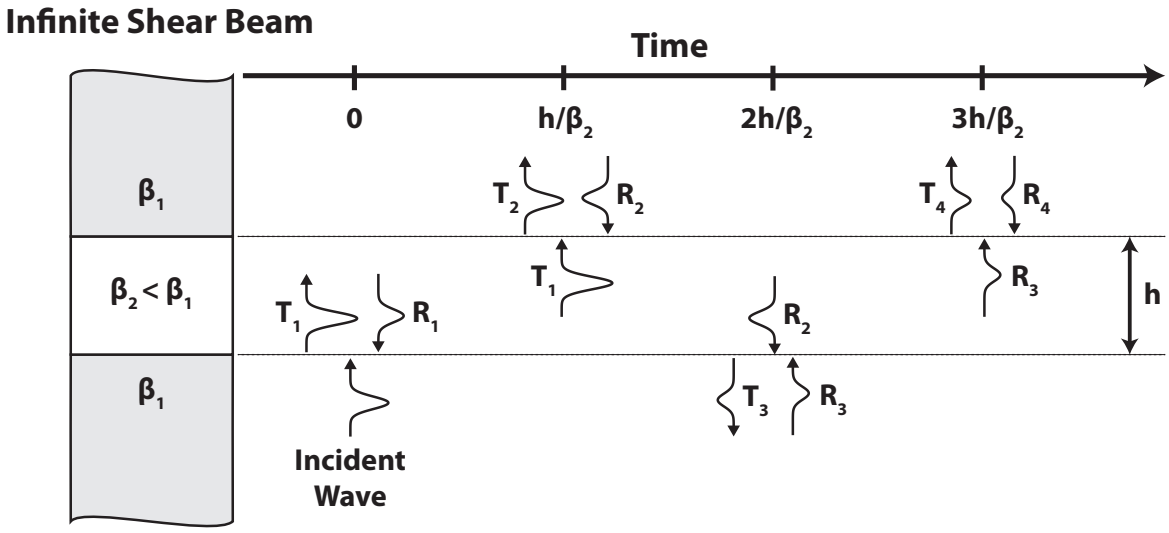

Figure A.3: **Wave Propagation in an Infinite Shear Beam with a Low-Velocity Layer.** A schematic of the different waves is shown.

layer, shown in Figure A.3, are computed as:

$$\begin{aligned}
T_1 &= A_T/A_I \\
&= \frac{2}{1+\beta_2/\beta_1}, \\
R_1 &= A_R/A_I \\
&= \frac{\beta_1/\beta_2 - 1}{\beta_1/\beta_2 + 1}, \\
T_2 &= T_1 \frac{2}{1+\beta_1/\beta_2} \\
&= \frac{2}{1+\beta_2/\beta_1}, \\
R_2 &= T_1 \frac{\beta_2/\beta_1 - 1}{\beta_2/\beta_1 + 1} \\
&= \frac{2}{1+\beta_2/\beta_1} \frac{\beta_2/\beta_1 - 1}{\beta_2/\beta_1 + 1}, \\
T_3 &= R_2 \frac{2}{1+\beta_1/\beta_2} \\
&= \frac{2}{1+\beta_2/\beta_1} \frac{\beta_2/\beta_1 - 1}{\beta_2/\beta_1 + 1} \frac{2}{1+\beta_2/\beta_1},
\end{aligned}$$

$$\begin{aligned}
R_3 &= R_2 \frac{\beta_2/\beta_1 - 1}{\beta_2/\beta_1 + 1} \\
&= \frac{2}{1+\beta_2/\beta_1} \frac{\beta_2/\beta_1 - 1}{\beta_2/\beta_1 + 1} \frac{2}{1+\beta_2/\beta_1} \frac{\beta_2/\beta_1 - 1}{\beta_2/\beta_1 + 1}, \\
T_n &= R_{n-1} \frac{2}{1+\beta_1/\beta_2} \\
&= \frac{2}{1+\beta_2/\beta_1} \frac{\beta_1/\beta_2 - 1}{\beta_2/\beta_1 + 1} \left(\frac{\beta_2/\beta_1 - 1}{\beta_2/\beta_1 + 1}\right)^{n-2}, \\
R_n &= R_{n-1} \frac{\beta_2/\beta_1 - 1}{\beta_2/\beta_1 + 1} \\
&= \frac{2}{1+\beta_2/\beta_1} \left(\frac{\beta_2/\beta_1 - 1}{\beta_2/\beta_1 + 1}\right)^{n-1}.
\end{aligned}$$

A wave is trapped within the lower velocity layer. It takes the wave h/β_2 seconds to travel through the length h of this layer. The amplitude of the wave changes signs each time

it is reflected, and so the period is equal to $T_{trapped} = \frac{2h}{\beta_2}$, and it decays as $(\frac{\beta_2/\beta_1 - 1}{\beta_2/\beta_1 + 1})^2 \frac{\beta_2}{2h}$.

An upgoing shear wave is propagated through an infinite shear beam with a low velocity layer. A series of transmitted and reflected waves are generated. Differences in arrival times and wave amplitudes are observed in the beam with the low velocity layer, compared to a uniform shear beam.

A.4 Application of State Space Method to Acceleration of a High-Rise Building in Osaka

In the dynamic excitation of a structure to a repeating source, the response of the damaged structure does not begin to diverge from the response of the undamaged structure until elastic waves have propagated through the region of damage. Motivated by these findings, the impulse response function of an existing high-rise building in Osaka is generated from the building's response to ambient noise and studied as a means for damage detection.

In dynamically exciting the experimental shear beam studied in Chapter 3, it was observed that the introduction of damage to a single floor of the structure resulted in a slowing of the initial shear wave pulse as it passed through the damaged region, resulting in a clear delay in the arrival time (compared with the arrival time for the undamaged data) on floors above the damaged floor. By using a high sampling rate, the presence and location of damage could be immediately determined, despite the low modal frequencies of the structure (less than 25 Hz) and hence low spatial resolution for damage detection. Motivated by this finding, a numerical study is conducted by introducing damage to a numerical model of an existing high-rise building in the Osaka prefecture. Damage is simulated in the numerical model by reducing the interstory shear stiffness. A horizontal pulse applied at the base of the structure is used as the excitation source. The input pulse at the base of the structure is based on the experimental input pulse obtained by applying correlation methods to the acceleration of the structure during ambient conditions to estimate its IRF. It is found that the low-frequency nature of the noise source generates a broad input pulse that makes damage

detection difficult using this method.

Previous studies have been performed in the context of seismic interferometry of structures. A comparison is made using the simulated IRFs for the damaged and undamaged models. Kohler et al. (2007) deconvolved the subbasement records in UCLA Factor building from upper floor records for 20 earthquakes. The authors developed an ETABS model that agrees with the experimental data. The impulse response function of a building can also be generated using cross-correlation of ambient noise (Prieto et al., 2010). It is common (research) practice in civil engineering to perform modal identification using the cross-correlations of the recorded accelerations of the structure excited by ambient noise (Brincker et al., 2000). Properties of the substructure, such as interstory stiffness, are typically estimated from the modal values.

A.4.1 Experimental Setup

Hayashi et al. (2012) have been monitoring the consecutive vibration characteristics of a high-rise steel building located in the Osaka prefecture. The building, shown in Figures A.4 and A.5, has 21 stories with two stories for the penthouse, and four stories under the ground level. It is a steel moment-resisting frame above ground and a steel-reinforced concrete frame with shear walls under the ground level. It is densely instrumented, with seismometers installed along the center of the structure. Thirteen seismometers (V403BT accelerometers at a sampling interval of 100Hz) are installed on floors B4F and 22F, as well as every other floors from 1F to 21FL. Hayashi et al. have estimated the first three NS natural frequencies to be 0.56 Hz, 1.65 Hz, and 2.97 Hz, and the EW natural frequencies to be 0.56 Hz, 1.65 Hz, 2.91 Hz, from the result of stacking transfer functions recorded for small earthquakes (Hayashi et al., 2012). Impulse responses obtained from earthquake data have been found to be similar to those obtained using microtremor data. The current design analysis models are a multistory shear model and flexure shear model.

The Osaka high-rise building is modeled as a lumped mass system, as shown in Figure A.5. The design parameters were used by Satow Engineers to compute the effective masses

Figure A.4: **Osaka High-Rise: Photo of the Building.** The building, shown in Figures A.4 and A.5, has 21 stories with two stories for the penthouse, and four stories under the ground level. It is a steel moment-resisting frame above ground and a steel-reinforced concrete frame with shear walls under the ground level.

and stiffnesses; they are listed in Table A.6 along with the accompanying floor names and heights (Satow, 1962). The motion of the model is constrained to the horizontal plane; no vertical or torsional motion is incorporated into the model. The N-S and E-W motions are assumed to be independent. For convenience, let **x(t)** denote the N-S component of motion and **y(t)** denote the E-W component of displacement. The lumped model does not account for flexibility at the base; the base is assumed to be perfectly rigid. A state-space formulation is developed to numerically subject the model building to a pulse at its base.

A.5 State Space Formulation

The state of a system is a minimum set of numbers (state variables), which contain sufficient information about the history of the system or process to allow computation of future behavior (Timothy and Bona, 1968).

A.5.0.1 Differential Equations of Motion

The 23-degree-of-freedom lumped mass model is fixed at its base to the ground. Each mass in the model is approximated from the effective mass of the building floors, and is constrained to motion in the horizontal plane. Horizontal springs connect the masses, and their values are approximated from the effective inter-story shear stiffness. We first derive the state space formulation for the N-S direction. As the E-W motion is assumed to be independent, a similar set of equations can be reached by following the same derivation. The differential equations of motion are given by:

$$M\ddot{x}(t) + C\dot{x}(t) + Kx(t) = f(t), \tag{A.3}$$

where displacement vector $x(t)$ contains the generalized coordinates for the system, force vector $f(t)$ defined below in Equation A.7, and the mass, stiffness, and damping matrices (assuming Rayleigh damping) are given by:

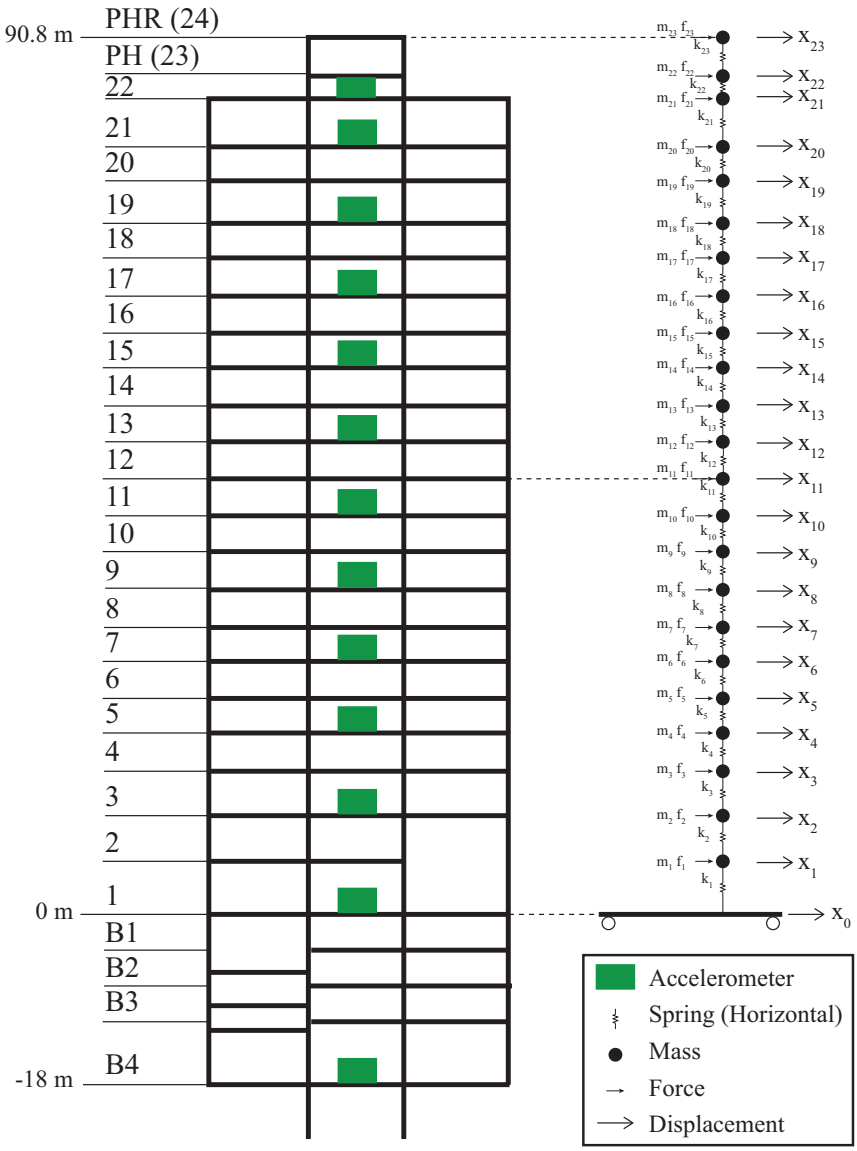

Figure A.5: **Osaka High-Rise: Building Schematic and Model**
The building is modeled as a 23-degree-of-freedom lumped mass system. It is densely instrumented with 13 seismometers located along the center of the building.

$$x(t) = \begin{pmatrix} x_1(t) \\ x_2(t) \\ \vdots \\ x_{23}(t) \end{pmatrix} \qquad M = \begin{pmatrix} m_1 & 0 & \dots & 0 \\ 0 & m_2 & \dots & 0 \\ \vdots & \vdots & \ddots & \vdots \\ 0 & 0 & \dots & m_{23} \end{pmatrix},$$

$$K = \begin{pmatrix} k_1+k_2 & -k_2 & 0 & \dots & 0 & 0 & 0 \\ -k_2 & k_2+k_3 & -k_3 & \dots & 0 & 0 & 0 \\ 0 & -k_3 & k_3+k_4 & \dots & 0 & 0 & 0 \\ \vdots & \vdots & \vdots & \ddots & \vdots & \vdots & \vdots \\ 0 & 0 & 0 & \dots & k_{21}+k_{22} & -k_{22} & 0 \\ 0 & 0 & 0 & \dots & -k_{22} & k_{22}+k_{23} & -k_{23} \\ 0 & 0 & 0 & \dots & 0 & -k_{23} & k_{23} \end{pmatrix} \qquad C = \alpha K + \beta M.$$

These equations can be verified by drawing a free-body diagram for each mass in the mass-spring system. Ground motion is incorporated into the differential equations of motion by replacing it with an equivalent force, $f_0(t)$, applied to mass m_1. There are contributions of $\alpha k_1 x_0$ and $\alpha k_1 \dot{x}_0$ to $f_0(t)$ from the first floor spring and the Rayleigh damper, respectively, that arise from their connection between mass m_1 and the ground. These contributions to the equivalent force can be verified by drawing a free body diagram for m_1 that includes the effects of Rayleigh damping; a schematic for Rayleigh damping can be found in Figure A.6.

$$f_{ext}(t) = \begin{pmatrix} f_1(t) & f_2(t) & \dots & f_{23}(t) \end{pmatrix}^T, \tag{A.4}$$

$$f_0(t) = k_1 x_0(t) + \alpha k_1 \dot{x}_0(t), \tag{A.5}$$

$$B := \begin{pmatrix} k_1 & 0 & \dots & 0 \end{pmatrix}^T, \tag{A.6}$$

$$f(t) = B x_0(t) + \alpha B \dot{x}_0(t) + f_{ext}(t). \tag{A.7}$$

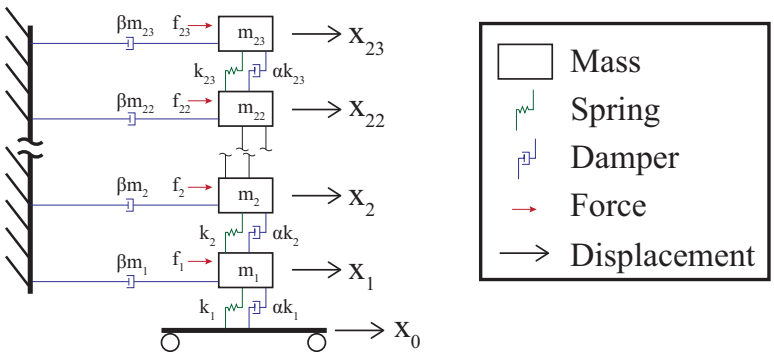

Figure A.6: **Mass-Spring System with Rayleigh Damping**
The model is represented as a mass-spring system with linear viscous damping that is consistent with Rayleigh damping. The contribution from the ground motion can be incorporated into the model as an equivalent force transmitted to the first floor mass via the damper and spring connecting the ground floor to the first floor.

A.5.0.2 Canonical Equations

A change of variables is introduced to transform from the generalized coordinates to the state vector, x_{state}, which contains the state variables, and from the force vector and ground motion to the input vector u. An output vector is denoted by y. The state vector and output vector can be rewritten as:

$$\begin{aligned} x_{state} &= f(x_{state}(t_0), u), \\ y &= g(x_{state}(t_0), u). \end{aligned}$$

A linear differential system characterized by the state equations of the canonical form:

$$\begin{aligned} \dot{x}_{state} &= Ax_{state} + Bu, \\ y &= Cx_{state} + Du, \end{aligned}$$

always has a unique solution for x_{state}.

Single Input System We first consider the case where the source consists purely of ground motion, i.e., $f_{ext}(t) = 0$. During events such as earthquakes, where the building response

is predominantly seismic, the external forces applied to the model contribute a negligible amount to building motion and can subsequently be ignored.

Introduce the state vector x_{state}, state variables $x_{1\,state}$ and $x_{2\,state}$, and input vector u as:

$$\begin{aligned} x_{state} &= \begin{pmatrix} x_{1\,state} & x_{2\,state} \end{pmatrix}^T, \\ x_{1\,state} &= x, \\ x_{2\,state} &= \dot{x} - \alpha M^{-1} B x_0, \\ u &= x_0. \end{aligned}$$

Note that the second term in the equation for $x_{2\,state}$ has been introduced to prevent the dependence of the state variables on $\dot{u}$. Rearranging Equation A.3, we find:

$$\ddot{x} - \alpha M^{-1} B \dot{x}_0 = M^{-1} B x_0 - M^{-1} C \dot{x} - M^{-1} K x.$$

The derivatives of the state variables can now be expressed in terms of the input and state variables:

$$\begin{aligned} \dot{x}_{1\,state} &= \dot{x} \\ &= x_{2\,state} + \alpha M^{-1} B x_0 \\ &= x_{2\,state} + \alpha M^{-1} B u, \\ \dot{x}_{2\,state} &= \ddot{x} - \alpha M^{-1} B \dot{x}_0 \\ &= M^{-1} B x_0 - M^{-1} C \dot{x} - M^{-1} K x \\ &= M^{-1} B u - M^{-1} C \dot{x}_{1\,state} - M^{-1} K x_{1\,state} \\ &= M^{-1} B u - M^{-1} C x_{2\,state} - \alpha M^{-1} C M^{-1} B u - M^{-1} K x_{1\,state}. \end{aligned}$$

Finally, the relation between the state variable and its derivative is expressed in matrix form:

$$\dot{x}_{state} = \begin{pmatrix} 0_{23x23} & I_{23x23} \\ -M^{-1}K & -M^{-1}C \end{pmatrix} x_{state} + \begin{pmatrix} \alpha M^{-1} B \\ (I - \alpha M^{-1} C) M^{-1} B \end{pmatrix} u. \qquad \text{(A.8)}$$

The system is now in expressed in canonical form in Equation A.8. In the canonical state equations, Equations A.9a and A.9b,

$$\dot{x}_{state} = A_{state}x_{state} + B_{state}u, \tag{A.9a}$$

$$y = C_{state}x_{state} + D_{state}u, \tag{A.9b}$$

the matrices C_{state} and D_{state} are defined to give the desired output. For example, to output all of the model displacements, take $C_{state} = \begin{pmatrix} I & 0_{23x23} \end{pmatrix}$ and $D_{state} = 0$. If there is a single output, the system is referred to as a SISO (single-input-single-output) system. If there are multiple outputs, the system is referred to as a SIMO (single-input-multiple-output) system. For our application, C_{state} is selected to output only the model displacements on floors with accelerometers.

Multiple Input System Consider the case where the source consists of an external force (e.g. wind loading) applied to each floor as well as ground motion at the base of the structure. The external forces have a larger impact on the motion of the building during ambient conditions than they do during seismic conditions. We follow the same derivation as in the previous section, while modifying the force vector, Equation A.5, to include the external forces:

$$\begin{aligned} f(t) &= \begin{pmatrix} f_1(t) \\ f_2(t) \\ \vdots \\ f_{23}(t) \end{pmatrix} + \begin{pmatrix} f_0(t) \\ 0 \\ \vdots \\ 0 \end{pmatrix} \\ &= f_{ext}(t) + Bx_0(t) + \alpha B\dot{x}_0(t). \end{aligned} \tag{A.10}$$

The modified state variables are:

$$\begin{aligned} x_{1\,state} &= x, \\ x_{2\,state} &= \dot{x} - \begin{pmatrix} \alpha M^{-1}B & 0_{23x23} \end{pmatrix}, \begin{pmatrix} x_0 \\ f_{ext} \end{pmatrix} \\ u &= \begin{pmatrix} x_0 \\ f_{ext} \end{pmatrix}. \end{aligned}$$

Rearranging Equation A.3, we have:

$$\ddot{x} - \alpha M^{-1}B\dot{x}_0 = M^{-1}Bx_0 + M^{-1}f_{ext} - M^{-1}C\dot{x} - M^{-1}Kx.$$

The derivatives of the state variables are calculated to be:

$$\begin{aligned} \dot{x}_{1\,state} &= \dot{x} \\ &= x_{2\,state} + \begin{pmatrix} \alpha M^{-1}B & 0_{23x23} \end{pmatrix} \begin{pmatrix} x_0 \\ f_{ext} \end{pmatrix} \\ &= x_{2\,state} + \begin{pmatrix} \alpha M^{-1}B & 0_{23x23} \end{pmatrix} u, \\ \dot{x}_{2\,state} &= \ddot{x} - \alpha M^{-1}B\dot{x}_0 \\ &= M^{-1}Bx_0 + M^{-1}f_{ext} - M^{-1}C\dot{x} - M^{-1}Kx \\ &= \begin{pmatrix} M^{-1}B & M^{-1} \end{pmatrix} u - M^{-1}C\dot{x}_{1\,state} - M^{-1}Kx_{1\,state} \\ &= \begin{pmatrix} M^{-1}B & M^{-1} \end{pmatrix} u - M^{-1}Cx_{2\,state} - \begin{pmatrix} \alpha M^{-1}CM^{-1}B & 0_{23x23} \end{pmatrix} u - M^{-1}Kx_{1\,state} \\ &= \begin{pmatrix} (I - \alpha M^{-1}C)M^{-1}B & M^{-1} \end{pmatrix} u - M^{-1}Cx_{2\,state} - M^{-1}Kx_{1\,state}. \end{aligned}$$

And hence,

$$\dot{x}_{state} = \begin{pmatrix} 0_{23x23} & I_{23x23} \\ -M^{-1}K & -M^{-1}C \end{pmatrix} x_{state} + \begin{pmatrix} \alpha M^{-1}B & 0_{23x23} \\ (I - \alpha M^{-1}C)M^{-1}B & M^{-1} \end{pmatrix} u. \tag{A.11}$$

As there are multiple inputs to the system, x_0, it is known as a multiple input system. If there is a single output, the system is referred to as a MISO (multiple-input-single-output) system. If there are multiple outputs, the system is referred to as a MIMO (multiple-input-multiple-output) system.

Alternate Formulation Using Principal Coordinates By converting to principal coordinates and reformulating the state space equations, the numerical accuracy of the solution can be improved. Let λ_n and ϕ_n, n = 1,2,...,23, denote the eigenvalues and normalized eigenvectors of $M^{-1}K$. Then x(t) can be expressed in terms of the principal coordinates p(t):

$$\begin{aligned} \lambda_n &= \omega_n^2 = (2\pi f_n)^2, \\ \Phi &= \begin{pmatrix} \phi_1 & \phi_2 & \dots & \phi_{23} \end{pmatrix}, \\ x(t) &= \Phi p(t), \\ p(t) &= \Phi^{-1} x(t), \\ \Phi^T K \Phi = [\omega^2] &= \begin{pmatrix} \omega_1^2 & 0 & \dots & 0 \\ 0 & \omega_2^2 & \dots & 0 \\ \vdots & \vdots & \ddots & \vdots \\ 0 & 0 & \dots & \omega_{23}^2 \end{pmatrix}, \\ \Phi^T M \Phi &= I. \end{aligned}$$

The differential equations of motion, Equation A.3, are uncoupled by expressing x in terms of the principal coordinates p and multiplying both sides of the equation by Φ^T:

$$\Phi^T M \Phi \ddot{p}(t) + \Phi^T C \Phi \dot{p}(t) + \Phi^T K \Phi p(t) = \Phi^T f(t),$$

$$\ddot{p}(t) + \Phi^T C \Phi \dot{p}(t) + \Phi^T K \Phi p(t) = \Phi^T f(t). \tag{A.12}$$

Single-Input System

If we assume a single input, $x_0(t)$, then we can rewrite Equation A.12 as:

$$\ddot{p} - \alpha \Phi^T B \dot{x}_0 = \Phi^T B x_0 - \Phi^T C \Phi \dot{p} - \Phi^T K \Phi p.$$

The modified state variable is:

$$\begin{aligned} x_{1\,state} &= p, \\ x_{2\,state} &= \dot{p} - \alpha \Phi^T B x_0, \\ u &= x_0. \end{aligned}$$

By taking the derivatives of the state variables, we arrive at the state equation:

$$\dot{x}_{state} = \begin{pmatrix} 0_{23x23} & I_{23x23} \\ -\Phi^T K \Phi & -\Phi^T C \Phi \end{pmatrix} \dot{x}_{state} + \begin{pmatrix} \alpha \Phi^T B \\ (I_{23x23} - \alpha \Phi^T C \Phi) \Phi^T B \end{pmatrix} u. \tag{A.13}$$

To output all of the model displacements, convert back to the original coordinates from the principal coordinates by taking $C_{state} = \begin{pmatrix} \Phi & 0_{23x23} \end{pmatrix}$ and $D_{state} = 0$.

Multiple-Input System

If we assume multiple inputs $x_0(t)$ and $f_{ext}(t)$, then we can rewrite Equation A.12 as:

$$\ddot{p} - \alpha \Phi^T B \dot{x}_0 = \Phi^T B x_0 + \Phi^T f_{ext} - \Phi^T C \Phi \dot{p} - \Phi^T K \Phi p.$$

The state variable becomes:

$$\begin{aligned} x_{1\,state} &= p, \\ x_{2\,state} &= \dot{p} - \alpha \Phi^T B x_0, \\ u &= x_0. \end{aligned}$$

By taking the derivatives of the state variables, we arrive at the state equation:

$$\dot{x}_{state} = \begin{pmatrix} 0_{23x23} & I_{23x23} \\ -\Phi^T K \Phi & -\Phi^T C \Phi \end{pmatrix} \dot{x}_{state} + \begin{pmatrix} \alpha \Phi^T B & 0_{23x23} \\ (I_{23x23} - \alpha \Phi^T C \Phi)\Phi^T B & \Phi^T \end{pmatrix} u. \qquad \text{(A.14)}$$

To output all of the model displacements, convert back to the original coordinates from the principal coordinates by taking $C_{state} = \begin{pmatrix} \Phi & 0_{23x23} \end{pmatrix}$ and $D_{state} = 0$.

State Space Coordinate Change and Transfer Function More generally, a coordinate change can be made for the state space system by introducing the transformation $\tilde{x} = Tx$, where T is a nonsingular matrix (Timothy and Bona, 1968). The state space matrices are also transformed. In the equations below, the subscript "state" has been dropped for convenience:

$$\begin{aligned} \tilde{A} &= TAT^{-1}, \\ \tilde{B} &= TB, \\ \tilde{C} &= CT^{-1}, \\ \tilde{D} &= D. \end{aligned}$$

The coefficent matrix A is transformed by what is known as a similarity transformation; the eigenvalues of the transformed matrix are the same as those of the original matrix. To convert back to the original state space coordinates, take $x = T^{-1}\tilde{x}$.

We can convert to a transfer function representation of the system by taking the Laplace transform of the state space equations. The transfer function $H(s)$ relates the output of the

model to the input. Assuming zero initial conditions, we find that:

$$\begin{aligned} sX(s) &= AX(s) + BU(s), \\ X(s) &= (sI - A)^{-1}BU(s), \\ Y(s) &= CX(s) + DU(s), \\ &= (C(sI - A)^{-1}B + D)U(s). \end{aligned}$$

By considering a change of coordinates, we show that the transfer system remains the same for the new formulation. In changing from a state space representation with state variables defined by the generalized coordinates to a representation with state variables defined by the principal coordinates, as was done in the previous section, we were performing a transformation from one state space to another with $T = \Phi$.

$$\begin{aligned} H(s) &= \frac{Y(s)}{U(s)} \\ &= C(sI - A)^{-1}B + D, \\ \tilde{H}(s) &= \tilde{C}(sI - \tilde{A})^{-1}\tilde{B} + \tilde{D} \\ &= CT^{-1}(sI - TAT^{-1})^{-1}TB + D \\ &= CT^{-1}(T(sI - A)T^{-1})^{-1}TB + D \\ &= CT^{-1}T(sI - A)^{-1}T^{-1}TB + D \\ &= C(sI - A)^{-1}B + D \\ &= H(s). \end{aligned}$$

Consider a state space formulation where D = 0, as it is the case for the lumped mass model. By rewriting the transfer function using the property that for an invertible matrix M, $M^{-1} = \text{adj}\{M\}/|M|$, where 'adj' stands for the adjugate matrix, the denominator of the transfer function can be in terms of the characteristic equation of A. Hence the poles of the

transfer functions are the eigenvalues of the matrix A:

$$\begin{aligned} H(s) &= \frac{Y(s)}{U(s)} \\ &= \frac{C\text{adj}(sI - A)B}{|sI - A|}. \end{aligned}$$

A.5.0.3 State Space Solution

According to Ljung (1987), the general solution for the state vector $x_{state}(t)$ is given by:

$$x_{state}(t) = \Phi(t, t_0)x_{state}(t_0) + \int_{t_0}^{t} \Phi(t, \tau)B(\tau)u(\tau)\,\mathrm{d}\tau,$$

where the state transition matrix $\Phi(t, t_0)$ is the unique solution to:

$$\begin{aligned} x_{state}(t) &= \Phi(t, t_0)x_{0\,state}, \\ \frac{d}{dt}\Phi(t, t_0) &= A(t)\Phi(t, t_0). \end{aligned}$$

Assuming zero initial conditions ($x_{0\,state} = 0$), an initial time of zero ($t_0 = 0$), and that the system is linear and time-invariant, the solution for $x_{state}(t)$ simplifies to:

$$\begin{aligned} \Phi(t, t_0) &= e^{A(t-t_0)}, \\ e^{At} &:= \sum_{k=0}^{\infty} \frac{A^k t^k}{k!}, \\ x_{state}(t) &= \int_0^t \Phi(t, \tau)Bu(\tau)\,\mathrm{d}\tau \\ &= \int_0^t e^{A(t-\tau)}Bu(\tau)\,\mathrm{d}\tau. \end{aligned}$$

This solution can be checked by hand by substituting it into Equation A.9a.

We can choose to numerically solve for x_{state} by computing the difference $x_{state}(t + \Delta t) - x_{state}(t)$, converting from a continuous system to a discrete system, and deriving a recurrence relation for x_{state}. Time step Δt is chosen so that the dynamics of the system are well-constrained (i.e., $\Delta t = \frac{T_{23}}{10}$, where T_N is the modal period of the highest considered mode N

of the model):

$$\begin{aligned} x_{state}(t+\Delta t) &= \int_0^{t+\Delta\tau} e^{A(t+\Delta t-\tau)} Bu(\tau)\,\mathrm{d}\tau \\ &= e^{A\Delta t}\int_0^{t} e^{A(t-\tau)} Bu(\tau)\,\mathrm{d}\tau + \int_t^{t+\Delta t} e^{A(t+\Delta t-\tau)} Bu(\tau)\,\mathrm{d}\tau \\ &= e^{A\Delta t} x_{state}(t) + \int_t^{t+\Delta t} e^{A(t+\Delta t-\tau)} Bu(\tau)\,\mathrm{d}\tau \\ &\approx e^{A\Delta t} x_{state}(t) + \frac{\Delta t}{2} Bu(t+\Delta t) + \frac{\Delta t}{2} e^{A\Delta t} Bu(t). \end{aligned}$$

In the last step, the trapezoidal rule was applied to approximate the integral $\int_t^{t+\Delta t} e^{A(t+\Delta t-\tau)} Bu(\tau)\,\mathrm{d}\tau$. This step can also be worked out by hand to verify. If we denote $x_n = x_{state}(n\Delta t)$ and $u_n = u(n\Delta t)$, we end up with a recurrence relation for x_{state}:

$$x_{n+1} = e^{A\Delta t} x_n + \frac{\Delta t}{2} Bu_{n+1} + \frac{\Delta t}{2} e^{A\Delta t} Bu_n, \tag{A.15}$$

$$q_n = Cx_n + Du_n. \tag{A.16}$$

We can now numerically solve for x_{state} using Equation A.15, by starting at $n = 0$ and incrementally solving for $x_1, x_2 ..., x_N$. Note that matrices A and B are defined in Equation A.8. Once we are done computing x_{state}, we use Equation A.16 to output the displacements in the generalized coordinates. It is also possible to solve for x_{state} in the frequency domain.

In Figure $A.7$, the state-space method was used to generate the impulse response functions to both an impulse applied at the ground floor, and to a force impulse applied at the 15^{th} floor. Note that the force impulse imparts positive net momentum into the system, exciting the rocking response of the building. If the force were being applied inside the building, the net momentum introduced to the system would necessarily sum to zero. A sample frequency response function is shown in Figure A.8. The phase goes to zero near the natural frequency.

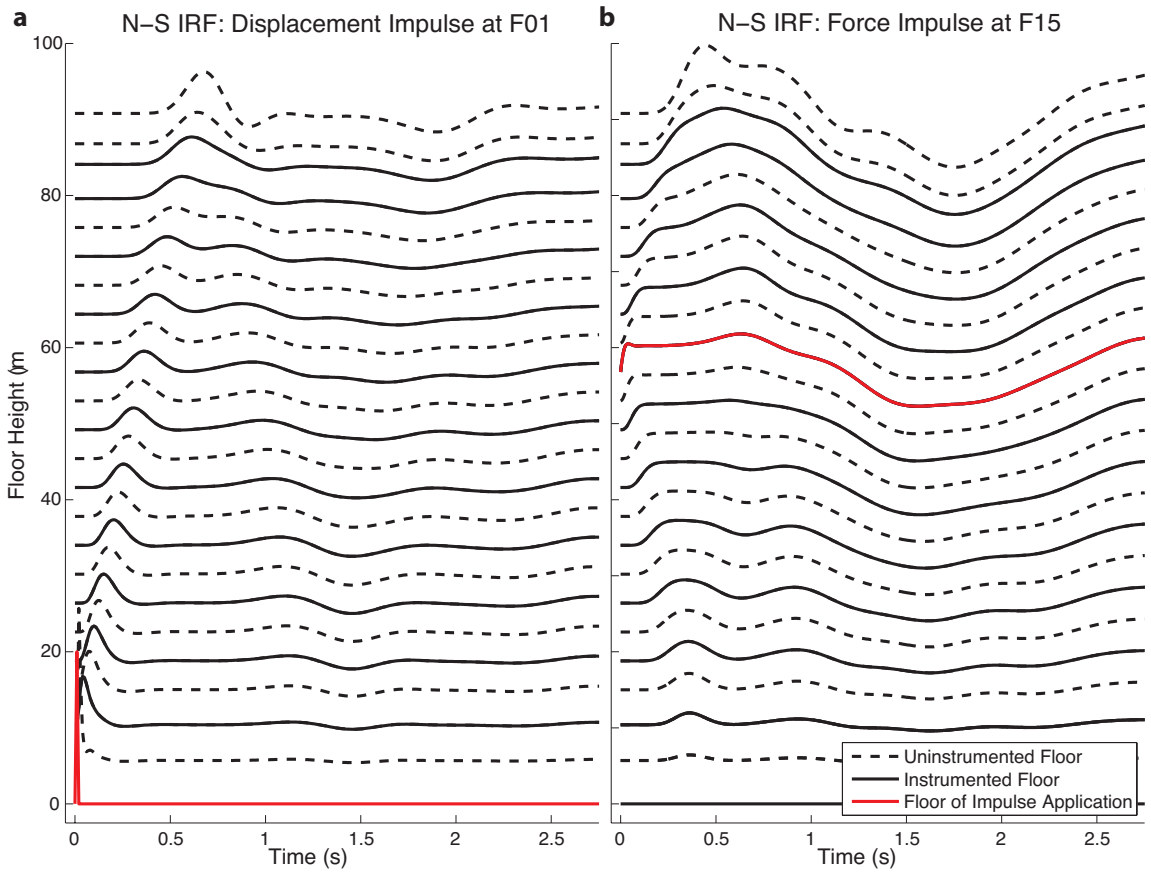

Figure A.7: **Numerical Impulse Response Functions.** The amplitude at each floor has been normalized proportionally to the maximum amplitude of the input floor, thus preserving the relative amplitudes. The floor to which the impulse is applied is highlighted in red. The numerical impulse response functions are calculated using the state space method with the design parameters for the N-S direction.

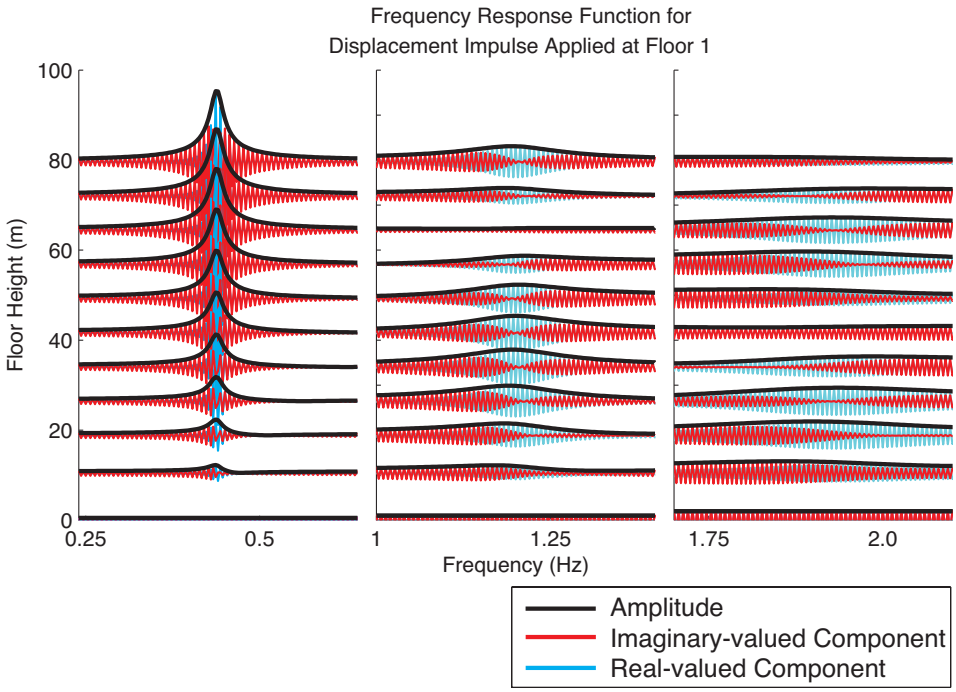

Figure A.8: **Numerical Frequency Response Function.** The frequency response function at the top floor in response to a displacement impulse applied at the first floor was calculated numerically by using the state-space method and the Fourier transform. The amplitude (black), imaginary component (red), and real component (blue) are shown for the first three N-S modes. The amplitudes have been normalized proportionally to the maximum amplitude of the input floor, thus preserving the relative amplitude.

A.5.1 Modal Analysis Using the Laplace Transform Method

We can alternatively use the Laplace transform method to solve for $x(t)$. Consider the uncoupled differential equation for the generalized coordinates, Equation A.12, and take the Laplace transform of each side. Assume zero initial conditions. Let $\zeta_n = (\alpha\omega_n + \beta/\omega_n)/2$ denote the n^{th} modal damping ratio. The damped natural frequency for the n^{th} mode is equal to $\omega_n\sqrt{1-\zeta_n^2}$. Equation A.12 becomes:

$$(s^2 I + s(\alpha[\omega^2] + \beta I) + [\omega^2])P(s) = \Phi^T F(s).$$

Converting back to generalized coordinates using the relation $X(s) = \Phi P(s)$, and inverting the diagonal matrix yields:

$$X(s) = \Phi \begin{pmatrix} (s^2 + 2\zeta_1\omega_1 s + \omega_1^2)^{-1} & 0 & \dots & 0 \\ 0 & (s^2 + 2\zeta_2\omega_2 s + \omega_2^2)^{-1} & \dots & 0 \\ \vdots & \vdots & \ddots & \vdots \\ 0 & 0 & \dots & (s^2 + 2\zeta_{23}\omega_{23} s + \omega_{23}^2)^{-1} \end{pmatrix} \Phi^T F(s).$$

Let us first consider the case with zero external forces, i.e., $f_{ext}(t) = 0$. Then the force acting on the system is equal to the equivalent force $f_0(t)$, given by Equation A.5, acting on the first floor mass m_1. The equation for $X(s)$ simplifies to:

$$X(s) \;=\; k_1(1+\alpha s) \begin{pmatrix} \sum_{p=1}^{23} \phi_p^1 \phi_p^1 (s^2 + 2\zeta_p\omega_p s + \omega_p^2)^{-1} \\ \sum_{p=1}^{23} \phi_p^1 \phi_p^2 (s^2 + 2\zeta_p\omega_p s + \omega_p^2)^{-1} \\ \vdots \\ \sum_{p=1}^{23} \phi_p^1 \phi_p^{23} (s^2 + 2\zeta_p\omega_p s + \omega_p^2)^{-1} \end{pmatrix} X_0(s).$$

This expression gives a vector of transfer functions multiplied by the transformed input ground motion, which is the equivalent of convolution of the impulse response function with the input in the time domain. The 46 distinct poles common to the transfer functions are

given by $\{-\omega_n(\zeta_n \pm i\sqrt{1-\zeta_n^2})\}$. The real parts of the poles are negative, consistent with a stable system. The transfer functions also have a common zero at $\frac{-1}{\alpha}$.

Let us now consider the case where the only source is a force applied at the m^{th} floor, i.e., $f_n(t) = 0\ \forall n \neq m$, and $x_0(t) = 0$. Again, the result is given by a vector of transfer functions multiplied by the transformed input force $F_m(s)$. In the time domain, the solution is equivalent to a vector of convolutions of the impulse response functions with the input force. All transfer functions for the system have the same poles:

$$X(s) = \begin{pmatrix} \sum_{p=1}^{23} \phi_p^m \phi_p^1 (s^2 + 2\zeta_p\omega_p s + \omega_p^2)^{-1} \\ \sum_{p=1}^{23} \phi_p^m \phi_p^2 (s^2 + 2\zeta_p\omega_p s + \omega_p^2)^{-1} \\ \vdots \\ \sum_{p=1}^{23} \phi_p^m \phi_p^{23} (s^2 + 2\mathrm{i}\zeta_p\omega_p s + \omega_p^2)^{-1} \end{pmatrix} F_m(s).$$

The transfer functions and impulse response functions are given by:

$$G_{n0}(s) = \sum_{p=1}^{23} \frac{k_1(1+\alpha s)}{s^2 + 2\zeta_p\omega_p s + \omega_p^2}, \tag{A.17}$$

$$G_{nm}(s) = \sum_{p=1}^{23} \frac{\phi_p^m \phi_p^n}{s^2 + 2\zeta_p\omega_p s + \omega_p^2}, \tag{A.18}$$

$$\begin{aligned} g_{n0}(t) &= \sum_{p=1}^{23} \phi_p^1 \phi_p^n k_1 \mathcal{L}^{-1} \left\{ \frac{1+\alpha s}{s^2 + 2\zeta_p\omega_p s + \omega_p^2} \right\} \\ &= \sum_{p=1}^{23} \frac{\phi_p^1 \phi_p^n k_1 e^{-\zeta_p\omega_p t}}{w_p\sqrt{1-\zeta_p^2}} \left((1 + \alpha\zeta_p\omega_p) \sin(\omega_p\sqrt{1-\zeta_p^2}t) - 2\alpha\omega_p\sqrt{1-\zeta_p^2}\cos(\omega_p\sqrt{1-\zeta_p^2}t) \right), \\ g_{nm}(t) &= \sum_{p=1}^{23} \phi_p^m \phi_p^n \mathcal{L}^{-1} \left\{ \frac{1}{s^2 + 2\zeta_p\omega_p s + \omega_p^2} \right\} \\ &= \sum_{p=1}^{23} \phi_p^1 \phi_p^n \frac{1}{w_p\sqrt{1-\zeta_p^2}} e^{-\zeta_p\omega_p t} \sin\left(\omega_p\sqrt{1-\zeta_p^2}t\right). \end{aligned} \tag{A.19}$$

The inverse Laplace transforms are calculated using complex integration by considering a half-circle contour of a finite radius in the complex plane, taking the limits as the radius tends towards infinity, and applying the Cauchy Residue Theorem (Fokas, 2003).

The transfer functions $G_{n0}(s), G_{nm}(s)$ are expressed in terms of the Laplace variable $s = \sigma + i\omega$. The impulse response functions $\{g_{n0}(t), g_{nm}(t)\}$ are equal to the inverse Laplace transform of the transfer functions, and they give the response of system to an impulse. The frequency response functions $G_{n0}(i\omega) = \hat{g}_{n0}(\omega)$ and $G_{nm}(i\omega) = \hat{g}_{nm}(\omega)$ can be directly computed from the transfer functions by taking $s = \imath\omega$, and they are equal to the Fourier transform of the impulse response functions.

The solution to arbitrary inputs is given by the convolution integral with the impulse response functions:

$$x_n(t) = \int_{-\infty}^{\infty} g_{n0}(\tau) x_0(t+\tau) \mathrm{d}\tau + \sum_{m=1}^{23} \int_{-\infty}^{\infty} g_{nm}(\tau) f_m(t+\tau) \mathrm{d}\tau.$$

As convolution in the time domain is equivalent to multiplication in the frequency domain, the solution could alternatively be calculated by transforming the inputs to the frequency domain, multiplying the transformed inputs with the transfer functions, and taking the inverse transform of the resulting product:

$$x_n(t) = \mathcal{F}^{-1}\{\hat{g}_{n0}\hat{x}_0\} + \sum_{m=1}^{23} \mathcal{F}^{-1}\{\hat{g}_{nm}\hat{f}_m\}.$$

For a number of applications, calculating the solution in the frequency domain is much faster than calculating the solution in the time domain. For example, consider the convolution of two discrete time series of length N. The time-domain solution necessitates performing N multiplications in calculating the sum of the product of the two time series N times, a total of N^2 multiplications. The frequency-domain solution consists in performing N multiplications to calculate the product of the two transformed vectors, and performing two discrete Fourier transforms and two inverse Fourier transforms. As a fast Fourier transform requires $\mathrm{O}(N \log N)$ operations, for large values of N, it is much faster to use a frequency domain solver.

A.5.2 Transfer Functions, Cross-Correlation, Convolution, and Deconvolution

There are three main techniques for obtaining the impulse response function of a system: cross-correlation, deconvolution, and cross-correlation with deconvolution. An investigation of error with each of these methods is presented below.

A.5.2.1 Transfer Functions

As seen in the previous section, the displacement at each floor of our model, $x_n(t)$, can be expressed as sum of convolutions of the impulse response functions with the ground motion and external forces. We are particularly interested in obtaining the set of impulse response functions relating the input displacement at the ground floor to the output displacement at above-ground floors $\{g_{0n}\}$ for $(n = 1, ..., N_{dof})$, as we are interested in obtaining the seismic response of the structure. If, on the other hand, we were more interested in studying the effects of wind on the structure, we would be more interested in obtaining the set of impulse response functions relating the external force applied at each floor to the displacement $\{g_{nm}\}$ for $(n = 1, ..., N_{dof})$ and $(m = 1, ..., N_{dof})$. The displacement on each floor is given by:

$$x_n(t) = (g_{n0} * x_0)(t) + \sum_{m=1}^{N_f} (g_{nm} * f_m)(t). \tag{A.20}$$

A.5.2.2 Cross-Correlation

Express the displacement at the n^{th} floor in terms of the impulse response functions and cross correlate it with the displacement at the ground floor to find:

$$\begin{aligned} C_{0n}(t) &= (x_0 \star x_n)(t) \\ &= x_0 \star (g_{n0} * x_0 + \sum_{m=1}^{N_f} g_{nm} * f_m) \\ &= x_0(-) * (g_{n0} * x_0 + \sum_{m=1}^{N_f} g_{nm} * f_m) \\ &= (x_0(-) * x_0) * g_{n0} + \sum_{m=1}^{N_f} (x_0(-) * f_m) * g_{nm} \\ &= (x_0 \star x_0) * g_{n0} + \sum_{m=1}^{N_f} (x_0 \star f_m) * g_{nm}. \end{aligned} \tag{A.21}$$

The number of external forces in our model, N_f, equals 23. If the source consists of perfectly uncorrelated noise, such that $(x_0 \star x_0)(t) = N\sigma_0^2\delta(t)$ and $(x_0 \star f_m)(t) = 0$, then the cross-correlation between the ground floor displacement and the n^{th} floor displacement yields the relevant impulse response function multiplied by a constant. In this case, we can normalize $C_{0n}(t)$ by $N\sigma_0^2$ to recover the impulse response function:

$$\begin{aligned} C_{0n}(t) &= \frac{(x_0 \star x_n)(t)}{N\sigma_0^2} \\ &= g_{n0}(t). \end{aligned} \tag{A.22}$$

Note that in the above derivations, we cross-correlated displacement time series with displacement time series to uncover the impulse response functions. We could have instead cross-correlated acceleration time series with acceleration time series. In this case,

$$\begin{aligned} C_{0n}(t) &= (\ddot{x}_0 \star \ddot{x}_n)(t) \\ &= (\ddot{x}_0 \star \ddot{x}_0) * g_{n0} + \sum_{m=1}^{M} (\ddot{x}_0 \star \ddot{f}_m) * g_{nm}. \end{aligned}$$

If the source consists of perfectly uncorrelated noise, such that $(\ddot{x}_0 \star \ddot{x}_0)(t) = N\sigma_0^2\delta(t)$ and $(\ddot{x}_0 \star \ddot{f}_m)(t) = 0$, then we could again normalize by $N\sigma_0^2$ to uncover the impulse response function.

We introduce errors to the recorded displacement time series, such that $\tilde{x}_0(t) = x_0(t) + e_0(t)$ and $\tilde{x}_n(t) = x_n(t) + e_n(t)$, where the recorded displacements $\tilde{x}_0(t)$ and $\tilde{x}_n(t)$ are equal to the "true" displacements plus an error term. Assume the errors have zero mean. Then Equation A.22 becomes:

$$
\begin{aligned}
C_{0n} &= \frac{\tilde{x}_0 \star \tilde{x}_n}{N\tilde{\sigma}_0^2} \\
&= \frac{1}{N\tilde{\sigma}_0^2}\left((x_0 \star x_0 + e_0 \star x_0) * g_{n0} + \sum_{m=1}^{N_f}(x_0 \star f_m + e_0 \star f_m) * g_{nm} + (x_0 \star e_n) + (e_0 \star e_n)\right), \\
\tilde{\sigma}_0^2 &= E\left[\left(\tilde{x_0} - E\left[\tilde{x_0}\right]\right)^2\right] \\
&= E\left[\left(x_0 + e_0 - E[x_0 + e_0]\right)^2\right] \\
&= E\left[\left(x_0 + e_0 - E[x_0] - E[e_0]\right)^2\right] \\
&= E\left[\left(x_0 + e_0\right)^2\right] \\
&= E\left[x_0^2 + e_0^2 + 2x_0e_0\right] \\
&= E\left[x_0^2\right] + E\left[e_0^2\right] + E\left[2x_0e_0\right] \\
&= \sigma_0^2 + \sigma_e^2 + 2Cov\left[x_0, e_0\right] \\
&= \sigma_0^2\left(1 + \frac{\sigma_e^2 + 2Cov\left[x_0, e_0\right]}{\sigma_0^2}\right).
\end{aligned}
$$

If the errors are uncorrelated to other errors, forces, and displacements, and $(\ddot{x}_0 \star \ddot{x}_0)(t) = N\sigma_0^2\delta(t)$, this simplifies to:

$$
C_{0n} = \frac{1}{1 + \frac{\sigma_e^2}{\sigma_0^2}} g_{n0} + \frac{1}{N\sigma_0^2}\frac{1}{1 + \frac{\sigma_e^2}{\sigma_0^2}}\left(\sum_{m=1}^{N_f}(x_0 \star f_m) * g_{nm}\right).
$$

We see that in the case of an input error, cross-correlation does not recover the true amplitude of the impulse response function g_{n0}. Instead, its amplitude is reduced by the fraction $\frac{1}{1+\sigma_e^2/\sigma_0^2}$.

A.5.2.3 Deconvolution

Let D_{0n} denote the deconvolution of the displacement of the ground floor from the displacement at the n^{th} floor:

$$\begin{aligned} D_{0n}(t) &= \mathcal{F}^{-1}\left\{\frac{\hat{x}_n}{\hat{x}_0}\right\} \\ &= \mathcal{F}^{-1}\left\{\frac{\hat{g}_{n0}\hat{x}_0 + \sum_{m=1}^{N_f}\hat{g}_{nm}\hat{f}_m}{\hat{x}_0}\right\} \\ &= \mathcal{F}^{-1}\left\{\frac{\hat{x}_0}{\hat{x}_0}\hat{g}_{n0} + \sum_{m=1}^{N_f}\frac{\hat{f}_m}{\hat{x}_0}\hat{g}_{nm}\right\} \\ &= g_{n0}(t) + \sum_{m=1}^{N_f}\left(\mathcal{F}^{-1}\left\{\frac{\hat{f}_m}{\hat{x}_0}\right\} * g_{nm}\right)(t). \end{aligned} \tag{A.23}$$

If an error is added to the recorded displacement time series, Equation A.23 becomes:

$$\begin{aligned} D_{0n}(t) &= \mathcal{F}^{-1}\left\{\frac{\hat{\tilde{x}}_n}{\hat{\tilde{x}}_0}\right\} \\ &= \mathcal{F}^{-1}\left\{\left(\hat{g}_{n0} + \sum_{m=1}^{N_f}\hat{g}_{nm}\frac{\hat{f}_m}{\hat{x}_0} + \frac{\hat{e}_n}{\hat{x}_0}\right)\frac{1}{1+\frac{\hat{e}_0}{\hat{x}_0}}\right\}. \end{aligned}$$

When the error is introduced, a term $\frac{\hat{e}_n}{\hat{x}_0}$ resulting from the added error e_n is added to the transfer function $\hat{g}_{n0}$. The transfer function is also multiplied by the term $\frac{\hat{e}_0}{\hat{x}_0}$, whose amplitude can be bounded by using the triangle inequality. Let us express the complex term $\frac{\hat{e}_0}{\hat{x}_0}$ in polar form as $re^{i\theta}$, with amplitude $r = r(\xi)$ and phase $\theta = \theta(\xi)$. Then we find that the fractional term is bound by the following:

$$\frac{1}{1+\left|\frac{\hat{e}_0}{\hat{x}_0}\right|} \leq \left|\frac{1}{1+\frac{\hat{e}_0}{\hat{x}_0}}\right| \leq \frac{1}{\left|1-\left|\frac{\hat{e}_0}{\hat{x}_0}\right|\right|}, \tag{A.24}$$

$$\frac{1}{1+r} \leq \left|\frac{1}{1+\frac{\hat{e}_0}{\hat{x}_0}}\right| \leq \frac{1}{|1-r|}, \tag{A.25}$$

$$\arg\left\{\frac{1}{1+\frac{\hat{e}_0}{\hat{x}_0}}\right\} = \arg\left\{\frac{1}{1+re^{i\theta}}\right\}. \tag{A.26}$$

If $r \approx 0$, (i.e., a relatively small spectral input error $\hat{e}_0$ compared to $\hat{x}_0$ for a given frequency), then the recovered impulse response function is close to that of the true impulse response function, as the amplitude and phase of the fraction are close to one and zero, respectively. If $r \gg 1$, (i.e., a relatively large spectral input error $\hat{e}_0$ compared to $\hat{x}_0$ for a given frequency), then the amplitude of the recovered impulse response function will be reduced by a factor of about $\frac{\hat{x}_0}{\hat{e}_0}$, and its phase will change by a value of $-\theta$. If $r \approx 1$, then both the amplitude and phase of the recovered transfer function are highly variable and dependent on the phase θ.

A.5.2.4 Cross-Correlation with Deconvolution

Instead of normalizing cross-correlation C_{0n} in the time domain, as in Equation A.22, we can choose to normalize the cross-correlation in the frequency domain, technically combining cross-correlation with deconvolution. By doing so, we can relax the conditions on the type of the source, so that the source does not need to be flat in the frequency domain, merely broadband in the frequency range of interest, while still being uncorrelated with the other

noise sources. The cross-correlation becomes:

$$\begin{aligned} C_{0n}(t) &= \mathcal{F}^{-1}\left\{\frac{\overline{\hat{x}_0}\hat{x}_n}{\overline{\hat{x}_0}\hat{x}_0}\right\} \\ &= \mathcal{F}^{-1}\left\{\frac{\overline{\hat{x}_0}(\hat{g}_{n0}\hat{x}_0 + \sum_{m=1}^{N_f}\hat{g}_{nm}\hat{f}_m)}{\overline{\hat{x}_0}\hat{x}_0}\right\} \\ &= \mathcal{F}^{-1}\left\{\frac{\overline{\hat{x}_0}\hat{x}_0}{\overline{\hat{x}_0}\hat{x}_0}\hat{g}_{n0} + \sum_{m=1}^{N_f}\frac{\overline{\hat{x}_0}\hat{f}_m}{\overline{\hat{x}_0}\hat{x}_0}\hat{g}_{nm}\right\} \\ &= g_{n0}(t) + \sum_{m=1}^{N_f}\mathcal{F}^{-1}\left\{\frac{\overline{\hat{x}_0}\hat{f}_m}{\overline{\hat{x}_0}\hat{x}_0}\right\} * g_{nm}(t). \end{aligned} \tag{A.27}$$

If the noise sources are uncorrelated, this recovers the impulse response function $g_{n0}(t)$, otherwise, there is some contribution from the other impulse response functions. Note that in this case, since we are effectively dividing out the effects of the source in the frequency domain, the source can consist of colored noise. In dividing by $\overline{\hat{x}_0(\xi)}\hat{x}_0(\xi)$, we have implicitly assumed that $\overline{\hat{x}_0(\xi)}\hat{x}_0(\xi) > 0$, i.e., broadband excitation is needed over the frequency range of interest. Signal conditioning techniques, such as waterleveling, can be employed to prevent dividing by zero in the frequency domain. These techniques are touched upon in the following section.

If we add an error to the recorded displacement time series, Equation A.27 becomes:

$$\begin{aligned} C_{0n}(t) &= \mathcal{F}^{-1}\left\{\frac{\overline{\hat{\hat{x}}_0}\hat{\hat{x}}_n}{\overline{\hat{\hat{x}}_0}\hat{\hat{x}}_0}\right\} \\ &= \mathcal{F}^{-1}\left\{\left(\hat{g}_{n0} + \sum_{m=1}^{N_f}\frac{\hat{f}_m}{\hat{x}_0}\hat{g}_{nm} + \frac{\hat{e}_n}{\hat{x}_0}\right)\frac{1}{1+\frac{\hat{e}_0}{\hat{x}_0}}\right\}. \end{aligned}$$

Again, a spectral error term $\frac{\hat{e}_n}{\hat{x}_0}$ is added to the transfer function $\hat{g}_{n0}$, and the entire sum is multiplied by a factor of $\frac{1}{1+\frac{\hat{e}_0}{\hat{x}_0}}$.

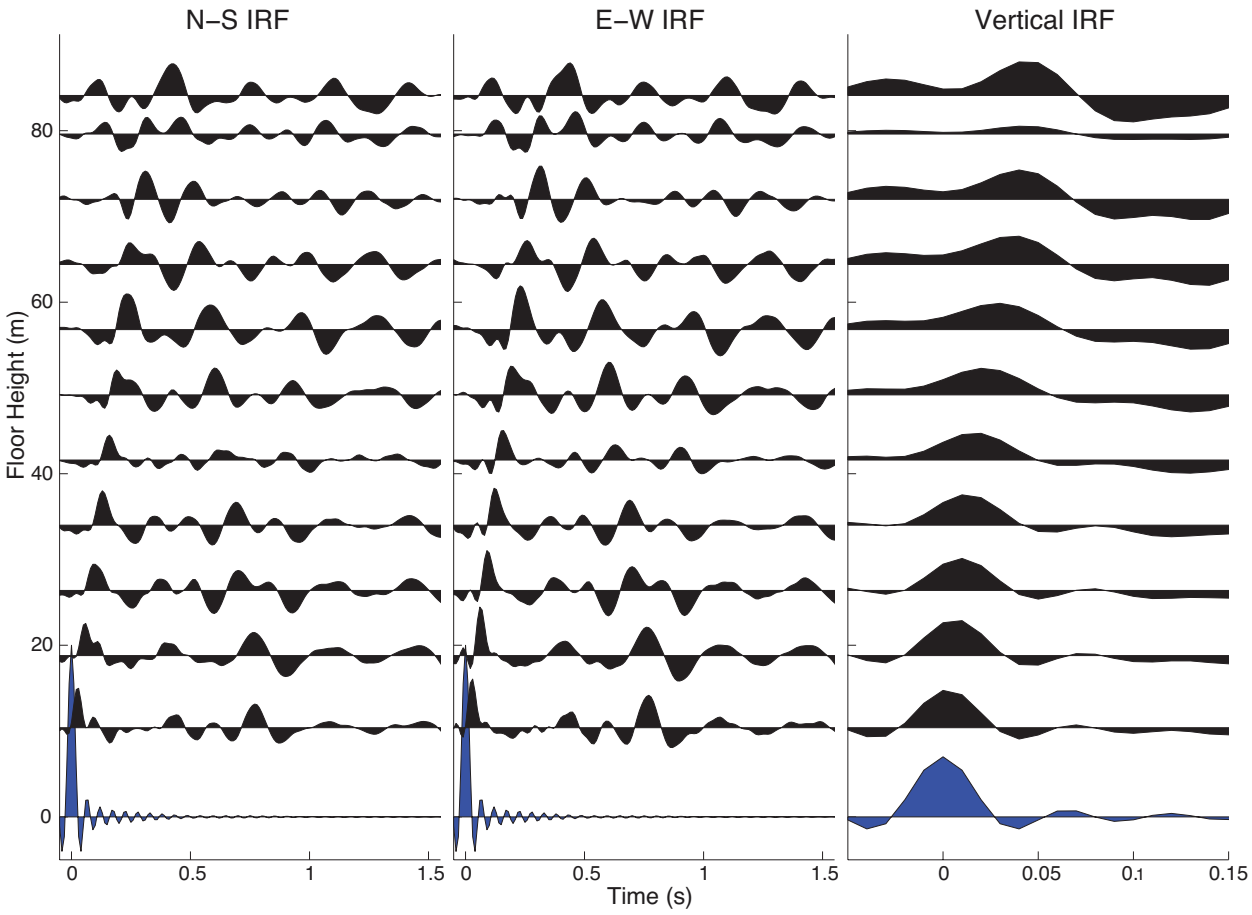

Figure A.9: **Experimental Impulse Response Functions.** The experimental impulse response functions were obtained by applying cross-correlation and convolution to an 8 hour segment of ambient data.

A.5.2.5 Experimental Results

The impulse response functions, shown in Figure A.9, were obtained experimentally by applying cross-correlation with deconvolution (Equation A.27) to an 8 hour segment of ambient data. This method was not observed to excite a strong torsional response (e.g., N-S motion generated by an E-W pulse at the base). The following signal conditioning techniques are employed to improve numerical stability and reduce artifacts:

Hamming Window The time series data is rescaled via a Hamming window before converting to the frequency domain. This is done in order to reduce artifacts that arise from taking the Fourier transform of a signal of finite duration. In this numerical study, the Hamming window is selected to be $0.2N_t$, where N_t is the length of the data. Only the first $0.1N_t$ and last $0.1N_t$ data points are scaled by the Hamming window.

Waterleveling Waterleveling is applied to the Fourier transformed data to prevent dividing by zero when division is performed in the frequency domain. Waterleveling is accomplished by replacing any values that have an absolute value less than a predefined "waterlevel" (chosen to be a fraction of the mean absolute value or max absolute value of the Fourier transformed data) with the phase-preserved waterlevel.

Clipping Clipping is applied to decrease the contribution of an earthquake or other large-amplitude event to a time series. Clipping can be applied either by rescaling a data point that is larger than a predefined amplitude while preserving the sign (or phase). In this sense, it is the opposite of waterleveling.

Whitening Whitening can be applied in either the time domain or the frequency domain to reduce the effect of an earthquake, or to artificially whiten a signal that has colored components. It is performed by rescaling each point inversely proportionally to the sum of amplitudes in a window centered at that point.

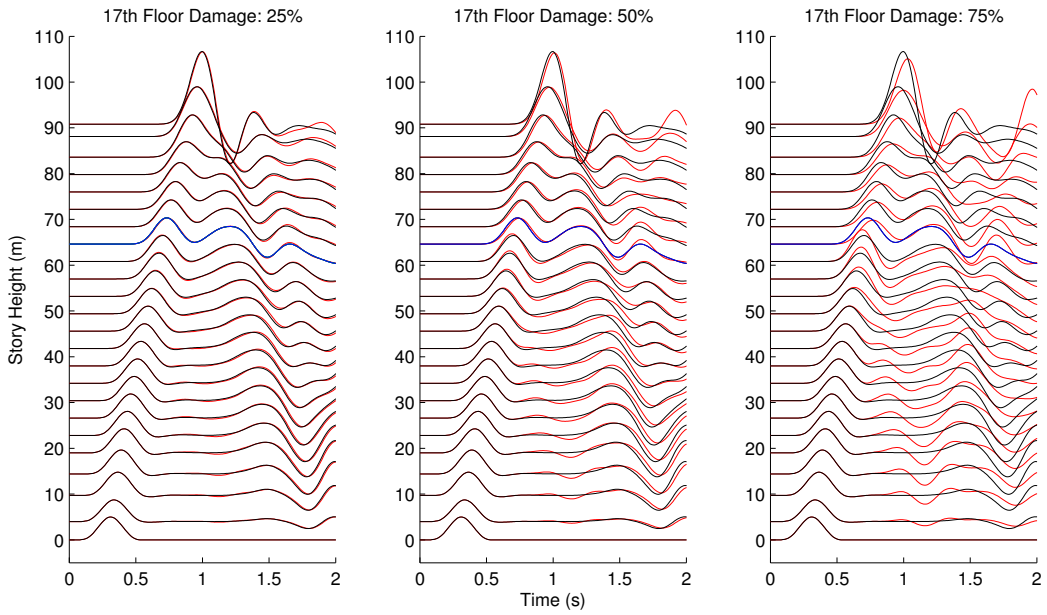

Figure A.10: **Numerically Computed IRFs.** Shear wave propagation in a damaged (red curves) and undamaged (black curves) numerical model of a high rise building. The blue curve indicates the damaged floor.

Filtering A filter (Butterworth) is applied to the resulting data to further separate the targeted signal.

A.5.3 Numerical Results: Damaged vs. Undamaged Building

Damage is created in the numerical model by changing the stiffness between floors, with a reduction of 25% in interstory damage, 50% in interstory damage, and 75% in interstory damage, and only small changes in the IRF are observed. As the source consists of mostly low-frequency energy, as opposed to the shake table used for the experimental shear beam, damage detection based on detecting changes in the arrival time of the initial traveling wave generated in the estimated IRF is difficult. Hence, the frequency content and variable nature of the input signal limits the feasibility of this method for damage detection. Results from these simulated experiments indicate that a 30% reduction in single inter-story stiffness provides a measurable change in the amplification and transmission coefficients of the initial

pulse, and a 50% reduction in inter-story stiffness yields an observable change in the wave speed. The method is limited by the nature of the input signal, which tends to consist of lower-frequency energies and be variable over time.

Floor	Height	Weight	N-S Stiffness	E-W Stiffness	Model	Instrument
PHR	90.8	355080	$1.442e8$	$1.500e8$	x_{23}, y_{23}	–
PHF	86.8	331390	$3.883e8$	$3.697e8$	x_{22}, y_{22}	–
$F22$	84.1	879170	$4.599e8$	$4.129e8$	x_{21}, y_{21}	13
$F21$	79.6	699080	$6.698e8$	$6.090e8$	x_{20}, y_{20}	12
$F20$	75.8	717690	$7.414e8$	$6.718e8$	x_{19}, y_{19}	–
$F19$	72.0	717690	$7.757e8$	$7.188e8$	x_{18}, y_{18}	11
$F18$	68.2	717690	$8.169e8$	$7.532e8$	x_{17}, y_{17}	–
$F17$	64.4	717690	$8.483e8$	$7.934e8$	x_{16}, y_{16}	10
$F16$	60.6	717690	$9.140e8$	$8.678e8$	x_{15}, y_{15}	–
$F15$	56.8	717690	$9.581e8$	$8.934e8$	x_{14}, y_{14}	9
$F14$	53.0	717690	$9.856e8$	$9.208e8$	x_{13}, y_{13}	–
$F13$	49.2	717690	$1.022e9$	$9.9601e8$	x_{12}, y_{12}	8
$F12$	45.4	733900	$1.049e9$	$1.010e9$	x_{11}, y_{11}	–
$F11$	41.6	733900	$1.071e9$	$1.042e9$	x_{10}, y_{10}	7
$F10$	37.8	717690	$1.158e9$	$1.136e9$	x_9, y_9	–
$F09$	34.0	717690	$1.147e9$	$1.164e9$	x_8, y_8	6
$F08$	30.2	717690	$1.139e9$	$1.194e9$	x_7, y_7	–
$F07$	26.4	717690	$1.155e9$	$1.224e9$	x_6, y_6	5
$F06$	22.6	717690	$1.204e9$	$1.274e9$	x_5, y_5	–
$F05$	18.8	717690	$1.320e9$	$1.360e9$	x_4, y_4	4
$F04$	15.0	717690	$1.325e9$	$1.357e9$	x_3, y_3	–
$F03$	10.4	917750	$1.278e9$	$1.251e9$	x_2, y_2	3
$F02$	05.7	1042210	$1.482e9$	$1.411e9$	x_1, y_1	–
$F01$	00.0	362010	$4.176e10$	$5.537e10$	x_0, y_0	2
$B01$	-4.0	2606600	$6.278e10$	$7.148e10$	–	–
$B02$	-7.6	5878800	$8.714e10$	$8.890e10$	–	–
$B03$	-11.2	9170900	$6.427e10$	8.163	–	–
$B04$	-18	12802300	–	–	–	1

Table A.1: **Osaka High-Rise: Design Parameters.** The design parameters used in the model were obtained by Satow Architects, Design, and Engineers, based on the designed structure. The units are: height (m), weight (kg), stiffness (N/m).

A.6 Equipment List

Specifications	Value	Units
Sensor Supply Current	2-20, Adjustable	mA
Number of Sensor Channels	16	
Sensor Excitation Voltage (Compliance Voltage)	+24	VDC
Voltage Gain	UNITY	
Front Panel D'Arsonval Panel Meter		
F.S. DC Volts	+24	VDC
F.S. DC mA	20	mA
Output Coupling Capacitor (Each Channel)	10	μF
Coupling Time Constant		
With 10 Megohm Load	9.0	SEC
With 1 Megohm Load	5.0	SEC
Lower -3db Frequency		
With 10 Megohm Load	0.017	Hz
With 1 Megohm Load	0.032	Hz
High Frequency Response	Determined by Sensor and Cable Length	
Noise, Wideband	150	μV
Sensor Connectors, Rear Panel (16)	BNC	Jack
Output Connectors, Rear Panel (16)	BNC	Jack
Power Cord, 3-Wire with Chassis Ground	3-Wire Plug	6 ft
Power Required Model	13.0	VA
Line Voltage Required (standard model)	115	VAC 50-400 Hz
Line Voltage Required ('E' version)	230	VAC 50-400 Hz
Size, H x W x D	1.75 x 19.0 x 11.1	IN
Weight	5.0/2.3	Lbs./kG.

Table A.2: **Instrument Specifications: Accelerometer Power Rack.** Specifications for the Model 4116 sixteen-channel, rack-mounted power unit with adjustable sensor drive current.

Specifications	Value	Units
Physical		
Weight	3.8	grams
Size (Hex x Height)	.50 x .53	inches
Mounting Provision	10-32, UNF-2B	
Connector, Coaxial, Radially Mounted	10-32, UNF-2A	
Case Material	Anodized Alum.	
Connector Material	Stainless Steel	
Performance		
Sensitivity, +10%/-5% Measured at 100 Hz		
3150A5	500	mV/G
3150A3	100	mV/G
Range F.S. for +/- 4 Volts Out 3150A5	+/- 4	G's
Range F.S. for +/- 5 Volts Out 3150A3	+/- 50	G's
Frequency Response, +/- 5%	1-3000	Hz
Mounted Resonant Frequency, Nom.	8 (12)	kHz
Phase Response, +/- 5 Degrees Phase Shift	1-3000	Hz
Equivalent Electrical Noise (Resolution)	.0001	G, RMS
Transverse Sensitivity, Max.	5	Percent
Strain Sensitivity	.001	G, RMS
Amplitude Non-linearity		
(Zero Based Best Fit St. Line Method)	2.0	% F.S., Max
Transverse Sensitivity, Max.	5	Percent
Strain Sensitivity	.001	250 G's/$\mu\sigma$
Environmental		
Maximum Vibration	50	G's, RMS
Maximum Shock	1000	G's, Peak
Temperature Range	-60 to +250	degF
Thermal Coefficient of Sensitivity	0.1	% / deg F
Electrical		
Excitation (Compliance) Voltage Range	+20 to + 30	VDC
Excitation Current Range	2 to 20	mA
Output Impedance, Nom.	100	OHMS
Output Bias Voltage, +/- Volt	12	VDC
Discharge Time Constant, Min.	1	VDC
Output Signal Polarity for Acceleration Toward Top	Positive Going	

Table A.3: **Instrument Specifications: Accelerometer.** Specifications for the Model 3150A3 and 31250A5 high-sensitivity, low-mass LIVM accelerometer.

Specifications	Value	Units
Dynamic Performance		
Voltage Sensitivity	100	mV/g
Measurement Range	50	±g pk
Frequency Range		
±5%	1-4000	Hz
±10%	0.7-7000	Hz
±3 dB	0.35-12000	Hz
Mounted Resonant Frequency	≥22	kHz
Resolution - Broadband	0.001	g pk
Amplitude Linearity	%	±1
Transverse Sensitivity	%	≤5
Environmental		
Shock Limit (Maximum)	10000	±g pk
Operating Temperature Range	-65 to +250	degF
Strain Sensitivity	≤0.0002	g/$\mu\epsilon$
Electrical		
Excitation Voltage/Constant Current	18-30/2-20	VDC/mA
Output Impedance	<100	ohms
Output Bias	8-12	VDC
Discharge Time Constant	≥0.5	sec
Warm Up Time (within 10% of output bias)	45	μV rms
Broadband Electrical Noise (1-10 kHz)	45	μV rms
Spectral Noise		
1 Hz	320	$\mu g/\sqrt{Hz}$
10 Hz	70	$\mu g/\sqrt{Hz}$
100 Hz	18	$\mu g/\sqrt{Hz}$
1 kHz	6.4	$\mu g/\sqrt{Hz}$
Ground Isolation	None (Optional)	ohms
Mechanical		
Sensing Element	Quartz/Shear	Material/Geometry
Housing	Titanium	Material
Housing	Welded Hermetic	Sealing
Size (hex x height)	0.75 x 0.85	inch
Weight	0.88	oz
Electrical Connector	10-32 Coaxial/Side	Type/Location
Mounting Thread	10-32 Female	Size

Table A.4: **Instrument Specifications: Hammer.** Specifications for the Quartz Shear ICP accelerometer used in the force-transducer hammer.

Model No.		482A	482A04
Specification	Units	Value	Value
Supply Voltage	+V	24	24/Channel
Excitation Current			
(Constant Current Source)	mA	2-20	2-20/Channel
Coupling Capacitor	μF	10	10
DC Offset			
(Max) (w/1 Megohm Load at "Scope" Output)	mV	30	30
Output Noise, Wideband, Pk-Pk (Max)	μF	300	300
Voltage Gain		1:1	1:1
Fault Monitor Meter	V/FS	24	24
Power Required (40 to 400 Hz)	V/A	105 to 125/.12	105 to 125/.12
Power Cord (3-Wire)	ft	6	6
Connectors:			
Input (XDCR) (Microdot)	THD	10-32	10-32
Output (Scope)	Jack	BNC	BNC
Size (H x W x D)	in	4.3 x 1.8 x 6.0	4.3 x 1.8 x 6.0
Weight	lbs	2	2

Table A.5: **Instrument Specifications: Hammer Power Unit.** Specifications for the PCB Piezotronics ICP line power unit.

Specification	Value
Analog Input	
Channels	32, 16
Single-Ended Channels	32
Differential Channels	16
Resolution	16 bits
Sample Rate	2 MS/s
Throughput (All Channels)	1 MS/s
Max Voltage	10 V
Maximum Voltage Range	-10 V, 10 V
Minimum Voltage Range	-0.1 V, 0.1 V
Number of Ranges	7
Simultaneous Sampling	No
Analog Output	
Channels	4
Resolution	16 bits
Max Voltage	10 V
Maximum Voltage Range	-10 V, 10 V
Minimum Voltage Range	-5 V, 5 V
Update Rate	2.86 MS/s
Current Drive Single	5 mA
Digital I/O	
Bidirectional Channels	48
Input-Only Channels	0
Output-Only Channels	0
Timing	Software, Hardware
Clocked Lines	32
Maximum Clock Rate	1 MHz
Logic Levels	TTL
Input Current Flow	Sinking, Sourcing
Output Current Flow	Sinking, Sourcing
Programmable Input Filters	Yes
Supports Programmable Power-Up States?	Yes
Current Drive Single	24 mA
Current Drive All	1 A

Table A.6: **Instrument Specifications: Data Acquisition System.** Specifications for the National Instruments NI USB-6363 X Series multifunction data acquisition.

Bibliography

Aagaard, B., Williams, C., and Knepley, M. (2008). PyLith: A finite-element code for modeling quasi-static and dynamic crustal deformation. In *AGU Fall Meeting Abstracts*, page 1925, San Francisco, CA.

Aagaard, B. T., Knepley, M. G., and Williams, C. A. (2013). A domain decomposition approach to implementing fault slip in finite-element models of quasi-static and dynamic crustal deformation. *Journal of Geophysical Research: Solid Earth*, 118(6):3059–3079.

Aktan, A., Catbas, F., Grimmelsman, K., and Tsikos, C. (2000). Issues in infrastructure health monitoring for management. *Journal of Engineering Mechanics*, 126(7):711–724.

Allemang, R. J. (2003). The modal assurance criterion (MAC): Twenty years of use and abuse. *Sound and Vibration Magazine*, 37(8):14–21.

Anstey, N. A. (1964). Correlation techniques - A review. *Geophysical Prospecting*, 12(4):355–382.

Astroza, M., Ruiz, S., and Astroza, R. (2012). Damage assessment and seismic intensity analysis of the 2010 (M_w 8.8) Maule earthquake. *Earthquake Spectra*, 28(S1):S145–S164.

ATC (2002). *Rapid Visual Screening of Buildings for Potential Seismic Hazards: A Handbook (FEMA 154)*. Applied Technology Council, Federal Emergency Management Agency, National Earthquake Hazards Reduction Program, 2^{nd} Edition.

Atwater, B. F. and Hemphill-Haley, E. (1997). *Recurrence intervals for great earthquakes*

of the past 3,500 years at northeastern Willapa Bay, Washington. U.S. Geological Survey Professional Paper 1576.

Bernal, D. and Beck, J. (2004). Preface to the special issue on Phase I of the IASC-ASCE structural health monitoring benchmark. *Journal of Engineering Mechanics*, 130(1):1–2.

Bernal, D. and Gunes, B. (2004). Flexibility based approach for damage characterization: Benchmark application. *Journal of Engineering Mechanics*, 130(1):61–70.

Binzel, R. P. (2000). The Torino impact hazard scale. *Planetary and Space Science*, 48(4):297–303.

Black, C. and Ventura, C. (1998). Blind test on damage detection of a steel frame structure. In *Proceedings of the 16th International Modal Analysis Conference*, pages 623–629. Society for Experimental Mechanics, Inc.

Boashash, B. (2003). *Time Frequency Signal Analysis and Processing: A Comprehensive Reference*. Elsevier, 1st Edition.

Bornn, L., Farrar, C. R., and Park, G. (2010). Damage detection in initially nonlinear systems. *International Journal of Engineering Science*, 48(10):909–920.

Bracewell, R. N. (1986). *The Fourier Transform and its Applications*. McGraw-Hill New York.

Brincker, R., Zhang, L., and Andersen, P. (2000). Modal identication from ambient responses using frequency domain decomposition. In *Proceedings of the 8th International Modal Analysis Conference*, pages 625–630.

Brockenbrough, R. and Merritt, F. (2006). *Structural Steel Designers Handbook: AISC, AASHTO, AISI, ASTM, AREMA, and ASCE-07 Design Standards*. American Society of Civil Engineers, 4th Edition.

BSSC (2003). *NEHRP Recommended Provisions for Seismic Regulations for New Buildings and Other Structures (FEMA 450)*. Building Seismic Safety Council, National Institute of Building Sciences, Washington, D.C.

Caicedo, J. M., Dyke, S. J., and Johnson, E. A. (2004). Natural excitation technique and eigensystem realization algorithm for Phase I of the IASC-ASCE benchmark problem: Simulated data. *Journal of Engineering Mechanics*, 130(1):49–60.

Cheney, E. E. W. and Kincaid, D. R. (2012). *Numerical Mathematics and Computing*. Cengage Learning.

Cheung, S. H. and Beck, J. L. (2009). Bayesian model updating using hybrid Monte Carlo simulation with application to structural dynamic models with many uncertain parameters. *Journal of Engineering Mechanics*, 135(4):243–255.

Ching, J. and Beck, J. (2004). Bayesian analysis of the Phase II IASC-ASCE structural health monitoring experimental benchmark data. *Journal of Engineering Mechanics*, 130(10):1233–1244.

Cole, H. A. (1971). *Method and Apparatus for Measuring the Damping Characteristics of a Structure*. U.S. Patent No. 3620069 A, U.S. Patent and Trademark Office.

CSSC (1994). *A Compendium of Background Reports on the Northridge Earthquake*. California Seismic Safety Commission, Sacramento, CA.

DesRoches, R., Comerio, M., Eberhard, M., Mooney, W., and Rix, G. J. (2011). Overview of the 2010 Haiti earthquake. *Earthquake Spectra*, 27(S1):S1–S21.

Doebling, S., Farrar, C., Prime, M., and Shevitz, D. (1996). *Damage Identification and Health Monitoring of Structural and Mechanical Systems from Changes in their Vibration Characteristics: A Literature Review*. LANL Report LA-13070-MS. Los Alamos National Laboratory.

Doebling, S. W., Farrar, C. R., and Prime, M. B. (1998). A summary review of vibration-based damage identification methods. *Shock and Vibration Digest*, 30(2):91–105.

Dyke, S. J., Bernal, D., Beck, J., and Ventura, C. (2003). Experimental Phase II of the structural health monitoring benchmark problem. In *Proceedings of the 16th ASCE Engineering Mechanics Conference*.

Eguchi, R. T., Goltz, J. D., Taylor, C. E., Chang, S. E., Flores, P. J., Johnson, L. A., Seligson, H. A., and Blais, N. C. (1998). Direct economic losses in the Northridge earthquake: A three-year post-event perspective. *Earthquake Spectra*, 14(2):245–264.

Engelhardt, M. D. and Sabol, T. A. (1997). Seismic-resistant steel moment connections: Developments since the 1994 Northridge earthquake. *Progress in Structural Engineering and Materials*, 1(1):68–77.

Ewins, D. J. (1984). *Modal Testing: Theory and Practice*. Research Studies Press, Letchworth.

Ewins, D. J. (2000). Model validation: Correlation for updating. *Sadhana*, 25(3):221–234.

Farrar, C. R., Worden, K., Todd, M. D., Park, G., Nichols, J., Adams, D. E., Bement, M. T., and Farinholt, K. (2007). *Nonlinear system identification for damage detection*. LANL Report LA-14353. Los Alamos National Laboratory.

FEMA (2000). *State of the Art Report on Connection Performance (FEMA-355D)*. SAC Joint Venture, Federal Emergency Management Agency.

FEMA (2007). *Welded Steel Moment Frame (Disaster Assistance Policy 9524.1)*. Federal Emergency Management Agency.

Field, E. H., Dawson, T. E., Felzer, K. R., Frankel, A. D., Gupta, V., Jordan, T. H., Parsons, T., Petersen, M. D., Stein, R. S., and Weldon, R. (2009). Uniform California earthquake rupture forecast, Version 2 (UCERF 2). *Bulletin of the Seismological Society of America*, (4):2053–2107.

Figueiredo, E. and Flynn, E. (2009). *Three-Story Building Structure to Detect Nonlinear Effects*. LANL Technical Report. Los Alamos National Laboratory.

Figueiredo, E., Park, G., Farrar, C. R., Worden, K., and Figueiras, J. (2011). Machine learning algorithms for damage detection under operational and environmental variability. *Structural Health Monitoring*, 10(6):559–572.

Figueiredo, E., Park, G., Figueiras, J., Farrar, C., and Worden, K. (2009). *Structural health monitoring algorithm comparisons using standard data sets*. LANL Report LA-14393. Los Alamos National Laboratory.

Fink, M. (1992). Time reversal of ultrasonic fields - Part I: Basic principles. *IEEE Transactions on Ultrasonics, Ferroelectrics, and Frequency Control*, 39(5):555–566.

Fokas, A. S. (2003). *Complex Variables: Introduction and Applications*. Cambridge University Press.

Friswell, M. I. (2007). Damage identification using inverse methods. *Philosophical Transactions of the Royal Society A: Mathematical, Physical and Engineering Sciences*, 365(1851):393–410.

Gibbons, S. and Ringdal, F. (2006). The detection of low magnitude seismic events using array-based waveform correlation. *Geophysical Journal International*, 165(1):149–166.

Giurgiutiu, V. and Cuc, A. (2005). Embedded non-destructive evaluation for structural health monitoring, damage detection, and failure prevention. *Shock and Vibration Digest*, 37(2):83–105.

Goldfinger, C., Nelson, C. H., Morey, A., Johnson, J. E., Gutierrez-Pastor, J., Eriksson, A. T., Karabanov, E., Patton, J., Grcia, E., and Enkin, R. (2012). *Turbidite event history: Methods and implications for Holocene paleoseismicity of the Cascadia subduction zone*. U.S.G.S. Professional Paper 1661F. U.S. Geological Survey.

Gutenberg, B. and Richter, C. F. (1965). *Seismicity of the Earth and Associated Phenomena*. Hafner New York.

Haiti (2010). *Action Plan for National Recovery and Development of Haiti*. Government of the Republic of Haiti.

Hall, J. F., Schmid, B., Comerio, M., Russell, J., Quadri, N. D., Harder, R., Powell, B., Hamburger, R., and Steinberg, R. (1996). Wood buildings. *Earthquake Spectra*, 12(S1):125–176.

Hamburger, R. O., Krawinkler, H., Malley, J. O., and Adan, S. M. (2009). *Seismic Design of Steel Special Moment Frames: A Guide for Practicing Engineers*. National Earthquake Hazards Reduction Program Seismic Design Technical Brief No. 2 (NIST GCR 09-917-3). National Institute of Standards and Technology, U.S. Department of Commerce.

Hayashi, Y., Sugino, M., Yamada, M., Takiyama, N., Onishi, Y., and Akazawa, T. (2012). Consecutive vibration characteristics monitoring of high-rise steel building. In *Proceedings of STESSA 2012: The 7th International Conference on Behaviour of Steel Structures in Seismic Areas*, pages 1065–1070.

Heaton, T. H. and Hartzell, S. H. (1987). Earthquake hazards on the Cascadia subduction zone. *Science*, 236(4798):162–168.

Heckman, V., Kohler, M., and Heaton, T. (2010). Detecting failure events in buildings: A numerical and experimental analysis. In *Proceedings of the 9th U.S. National and 10th Canadian Conference on Earthquake Engineering*. Earthquake Engineering Research Institute.

Heckman, V., Kohler, M., and Heaton, T. (2011a). A damage detection method for instrumented civil structures using prerecorded greens functions and cross-correlation. In *Proceedings of ANCRiSST2011: The 6th International Workshop on Advanced Smart Materials and Smart Structures Technology*.

Heckman, V. M., Kohler, M. D., and Heaton, T. H. (2011b). A method to detect structural damage using high-frequency seismograms. In *Proceedings of Structural Health Monitoring 2011: International Workshop on Structural Health Monitoring*.

Heckman, V. M., Kohler, M. D., and Heaton, T. H. (2011c). A method to detect structural damage using high-frequency seismograms. In *Proceedings of the 8^{th} International Conference on Urban Earthquake Engineering*.

Hera, A. and Hou, Z. (2004). Application of wavelet approach for ASCE structural health monitoring benchmark studies. *Journal of Engineering Mechanics*, 130(1):96–104.

Hernandez-Garcia, M. R., Masri, S. F., Ghanem, R., Figueiredo, E., and Farrar, C. R. (2010). A structural decomposition approach for detecting, locating, and quantifying nonlinearities in chainlike systems. *Structural Control and Health Monitoring*, 17(7):761–777.

ICC (2000). *2000 International Building Code*. International Code Council, Inc., U.S.A.

Jennings, P. C. (2013). Earthquakes and engineers: An international history. *Earthquake Spectra*, 29(2):669–673.

Johnson, E., Lam, H., Katafygiotis, L., and Beck, J. (2004). Phase I IASC-ASCE structural health monitoring benchmark problem using simulated data. *Journal of Engineering Mechanics*, 130(1):3–15.

Juang, J.-N. and Pappa, R. S. (1985). An eigensystem realization algorithm for modal parameter identification and model reduction. *Journal of Guidance, Control, and Dynamics*, 8(5):620–627.

Karaiskos, G., Tondreau, G., Figueiredo, E., Farrar, C., and Deraemaeker, A. (2012). Application of modal filters for damage detection in the presence of non-linearities. In *Proceedings of the 6^{th} European Workshop on Structural Health Monitoring*.

Kaufmann, E., Fisher, J., DiJulio, R., and Gross, J. (1997). *Failure Analysis of Welded Steel Moment Frames Damaged in the Northridge Earthquake (NISTIR 5944)*. Building and

Fire Research Laboratory, National Institute of Standards and Technology, Gaithersburg, MD.

Kohler, M., Heaton, T., and Bradford, S. (2007). Propagating waves in the steel, moment-frame Factor building recorded during earthquakes. *Bulletin of the Seismological Society of America*, 97(4):1334–1345.

Kohler, M. D., Heaton, T. H., and Heckman, V. M. (2009). A time-reversed reciprocal method for detecting high-frequency events in civil structures with accelerometer arrays. In *Proceedings of ANCRISST 2009 - The Fifth International Workshop on Advanced Smart Structures and Technology*.

Krawinkler, H., Anderson, J., Bertero, V., Holmes, W., and Theil Jr, C. (1996). Steel buildings. *Earthquake Spectra*, 12(S1):25–47.

Lam, H., Katafygiotis, L., and Mickleborough, N. (2004). Application of a statistical model updating approach on Phase I of the IASC-ASCE structural health monitoring benchmark study. *Journal of Engineering Mechanics*, 130(1):34–48.

Li, H., Li, S., Ou, J., and Li, H. (2010). Modal identification of bridges under varying environmental conditions: Temperature and wind effects. *Structural Control and Health Monitoring*, 17(5):495–512.

Li, H., Li, S., Ou, J., and Li, H. (2012). Reliability assessment of cable-stayed bridges based on structural health monitoring techniques. *Structure and Infrastructure Engineering*, 8(9):829–845.

Li, S., Li, H., Liu, Y., Lan, C., Zhou, W., and Ou, J. (2013). SMC structural health monitoring benchmark problem using monitored data from an actual cable-stayed bridge. *Structural Control and Health Monitoring*.

Ljung, L. (1987). *System Identication: Theory for the User*. Prentice-Hall Information and System Sciences Series. Prentice Hall, Englewood Cliffs, New Jersey.

Lus, H., Betti, R., Yu, J., and De Angelis, M. (2004). Investigation of a system identification methodology in the context of the ASCE benchmark problem. *Journal of Engineering Mechanics*, 130(1):71–84.

Marwala, T. (2010). *Finite-Element-Model Updating Using Computational Intelligence Techniques: Applications to Structural Dynamics*. Springer.

Moehle, J. P. and Frost, J. D. (2012). Preface: Special issue on the 2010 Maule, Chile, earthquake. *Earthquake Spectra*, 28(S1):vii–viii.

Moore, W. H. (2013). *National Transportation Statistics*. Bureau of Transportation Statistics, Research and Innovative Technology Administration, U.S. Department of Transport.

Osteraas, J., Somers, P., Carpenter, J., Ferner, H., Holmes, W., Krawinkler, H., Longstreth, M., Ryan, P., and Wight, J. (1996). Reinforced concrete buildings. *Earthquake Spectra*, 12(S1):49–74.

Park, H., Sohn, H., Law, K., and Farrar, C. (2007). Time reversal active sensing for health monitoring of a composite plate. *Journal of Sound and Vibration*, 302(1-2):50–66.

Park, J., Song, T.-R. A., Tromp, J., Okal, E., Stein, S., Roult, G., Clevede, E., Laske, G., Kanamori, H., and Davis, P. (2005). Earth's free oscillations excited by the 26 December 2004 Sumatra-Andaman earthquake. *Science*, 308(5725):1139–1144.

Park, S., Stubbs, N., and Bolton, R. (1998). Damage detection on a steel frame using simulated modal data. In *Proceedings of the 16th International Modal Analysis Conference*, pages 616–622. Society for Experimental Mechanics, Inc.

Petersen, M. D., Frankel, A. D., Harmsen, S. C., Mueller, C. S., Haller, K. M., Wheeler, R. L., Wesson, R. L., Zeng, Y., Boyd, O. S., and Perkins, D. M. (2008). *Documentation for the 2008 Update of the United States National Seismic Hazard Maps*. U.S.G.S. Open-File Report 2008-1128. U.S. Geological Survey.

Prieto, G. A., Lawrence, J. F., Chung, A. I., and Kohler, M. D. (2010). Impulse response of civil structures from ambient noise analysis. *Bulletin of the Seismological Society of America*, 100(5A):2322–2328.

Raghavan, A. and Cesnik, C. E. (2007). Review of guided-wave structural health monitoring. *Shock and Vibration Digest*, 39(2):91–116.

Reitherman, R. K. (2012). *Earthquakes and Engineers: An International History*. American Society of Civil Engineers, Reston, VA.

Rodgers, J., Mahin, S., and Celebi, M. (2007). Proposed approaches to fracture damage detection for sparsely instrumented steel moment-framed buildings. *International Journal of Steel Structures*, 7(1):1–10.

Rodgers, J. E. and Mahin, S. A. (2007). Transient response in steel moment frames caused by brittle connection fracture. *Earthquake Engineering and Structural Dynamics*, 36(15):2423–2444.

Rytter, A. (1993). *Vibrational Based Inspection of Civil Engineering Structures*. PhD thesis, University of Aalborg.

SAC (2000). *Recommended Postearthquake Evaluation and Repair Criteria for Welded Steel Moment-Frame Buildings (FEMA-352)*. SAC Joint Venture, Federal Emergency Management Agency.

Sagan, C., Druyan, A., and Soter, S. (1980). *Heaven and Hell*. Cosmos. KCET, Carl Sagan Productions, in association with British Broadcasting Corporation, Polytel International.

Sasani, M., Makris, N., and Bolt, B. A. (2006). Damping in shear beam structures and estimation of drift response. *ASCE Journal of Engineering Mechanics*, 132(8):851–858.

Satow (1962). *Sakai City New Building Construction Work*, Volume 2-4. Satow Engineers and Architects, Tokyo, Japan.

Sharifi, A. and Banan, M. R. (2008). Energy index method: Technique for identification of structural damages. *Journal of Structural Engineering*, 134(6):1061–1064.

Sohn, H., Farrar, C. R., Hemez, F. M., Shunk, D. D., Stinemates, D. W., Nadler, B. R., and Czarnecki, J. J. (2004). *A Review of Structural Health Monitoring Literature: 1996-2001.* LANL Technical Report. Los Alamos National Laboratory.

Somers, P., Campi, D., Holmes, W., Kehoe, B. E., Klingner, R. E., Lizundia, B., and Schmid, B. (1996). Unreinforced masonry buildings. *Earthquake Spectra*, 12(S1):195–217.

SSC (2004). *Status of the Unreinforced Masonry Building Law.* 2003 Report to the Legislature. Seismic Safety Commission, Sacramento, CA.

Thatcher, W., Marshall, G., and Lisowski, M. (1997). Resolution of fault slip along the 470-km-long rupture of the great 1906 San Francisco earthquake and its implications. *Journal of Geophysical Research*, 102(B3):5353–5367.

Timoshenko, S. (1951). *Theory of Elasticity.* Engineering Societies Monographs. McGraw-Hill New York, 2^{nd} Edition.

Timothy, L. K. and Bona, B. E. (1968). *State Space Analysis: An Introduction.* McGraw-Hill New York.

Tromp, J., Tape, C., and Liu, Q. (2005). Seismic tomography, adjoint methods, time reversal and banana-doughnut kernels. *Geophysical Journal International*, 160(1):195–216.

Updike, R. (1996). *USGS Response to an Urban Earthquake - Northridge '94.* U.S.G.S. Open-File Report 96-263. U.S. Geological Survey.

USGS (2012). *Largest Earthquakes in the World Since 1900.* <*http*: *//earthquake.usgs.gov/earthquakes/world/*10*_largest_world.php*>, November 30, 2012 16:21:34 UTC.

Wald, D. J., Kanamori, H., Helmberger, D. V., and Heaton, T. H. (1993). Source study of the 1906 San Francisco earthquake. *Bulletin of the Seismological Society of America*, 83(4):981–1019.

Wang, C., Rose, J., and Chang, F. (2004). A synthetic time-reversal imaging method for structural health monitoring. *Smart Materials and Structures*, 13(2):415–423.

Wang, C. and Rose, L. (2003). Wave reflection and transmission in beams containing delamination and inhomogeneity. *Journal of Sound and Vibration*, 264(4):851–872.

Wilson, E. L. (2004). *Static and Dynamic Analysis of Structures*. Computers and Structures, Inc., Berkeley, CA, 4^{th} Edition.

Wu, J. and Li, Q. (2006). Structural parameter identification and damage detection for a steel structure using a two-stage finite element model updating method. *Journal of Constructional Steel Research*, 62(3):231–239.

Yang, J. N., Lei, Y., Lin, S., and Huang, N. (2004). Hilbert-Huang based approach for structural damage detection. *Journal of Engineering Mechanics*, 130(1):85–95.

Youssef, N. F., Bonowitz, D., and Gross, J. L. (1995). *A Survey of Steel Moment-Resisting Frame Buildings Affected by the 1994 Northridge Earthquake (NISTIR 5625)*. Building and Fire Research Laboratory, National Institute of Standards and Technology, Gaithersburg, MD.

Yuen, K.-V., Au, S. K., and Beck, J. L. (2004). Two-stage structural health monitoring approach for Phase I benchmark studies. *Journal of Engineering Mechanics*, 130(1):16–33.

Zhao, B., Taucer, F., and Rossetto, T. (2009). Field investigation on the performance of building structures during the 12 May 2008 Wenchuan earthquake in China. *Engineering Structures*, 31(8):1707–1723.